CENTRO DE INVESTIGACIÓN Y DE ESTUDIOS AVANZADOS DEL INSTITUTO POLITÉCNICO NACIONAL

Unidad Mérida

DEPARTAMENTO DE FÍSICA APLICADA

" Analysis of the thermal properties of semitransparent materials and characterization of vertical cracks in opaque solids using infrared thermography "

Thesis presented by:

Nelson Wilbur Pech May

To obtain the degree of

Doctor of Science

In the specialty of

Applied Physics

Thesis Directors:

Dr. Juan José Alvarado Gil (CINVESTAV)
Dr. Alberto Oleaga Páramo (UPV/EHU)

Mérida, Yucatán, México September, 2016

CENTRO DE INVESTIGACIÓN Y DE ESTUDIOS AVANZADOS DEL INSTITUTO POLITÉCNICO NACIONAL

Unidad Mérida

DEPARTAMENTO DE FÍSICA APLICADA

“ Análisis de las propiedades térmicas de materiales semitransparentes y caracterización de grietas verticales en sólidos opacos mediante termografía infrarroja ”

Tesis que presenta

Nelson Wilbur Pech May

Para obtener el grado de

Doctor en Ciencias

en la especialidad de

Física Aplicada

Directores de Tesis:

Dr. Juan José Alvarado Gil (CINVESTAV)
Dr. Alberto Oleaga Páramo (UPV/EHU)

Mérida, Yucatán, México septiembre de 2016

eman ta zabal zazu

Universidad del País Vasco
Euskal Herriko Unibertsitatea

“ Analysis of the thermal properties of semitransparent materials and characterization of vertical cracks in opaque solids using infrared thermography ”

Tesis que presenta

Nelson Wilbur Pech May

Directores de Tesis:

Dr. Juan José Alvarado Gil (CINVESTAV)
Dr. Alberto Oleaga Páramo (UPV/EHU)

Esta tesis se ha desarrollado en cotutela internacional entre la Universidad del País Vasco/ Euskal Herriko Unibertsitatea (España) y el Centro de Investigación y de Estudios Avanzados del Instituto Politécnico Nacional Unidad Mérida (México), como requerimiento parcial para obtener el título de

Doctor en Ciencias

en el Departamento de Física Aplicada I, Escuela de Ingeniería de Bilbao, UPV/EHU.

Mérida, Septiembre de 2016

A Doña Berta May Canché y
Don Miguel Pech Pan (†)*,*
queridos padres

Acknowledgements

I would like to thank CONACYT for the national grant (scholar: 243332) supplied over these last four years. It was really helpful for the development of this thesis. Also, I would like to express my gratitude to Becas Mixtas 2013 – mzo2014 Movilidad en el Extranjero (290749) for my scholarship during September 2013 to August 2014, at Universidad del País Vasco (UPV/EHU, Spain), which complemented my support as a visiting research student.

This work was partially supported by the Fund Conacyt-Sener-Energy-Sustainability Grant 207450, within Strategic Project CEMIESol-Cosolpi No. 10 “Solar Fuels & Industrial Processes” as well as by the Project “Fronteras de la ciencia” Grant 192, “Development of theoretical and experimental methodologies for the study and control of heat transport at the nanoscale”

Tengo tanto que agradecer y a tantas personas, que la extensión de mi tesis sería completamente insuficiente para expresarlo todo. Mil gracias a mis padres por su apoyo, sus consejos y su ejemplo. Igualmente, para mis hermanos, hermanas, los aprecio mucho. Mis sobrinos y sobrina,.... son mi alegría!. También a mi txakurra beltxa, 'el cuchito', te llevo en mi recuerdo siempre!.

Muchas gracias a los profesores que contribuyeron al desarrollo de esta tesis, Juan José Alvarado Gil, Alberto Oleaga, Agustín Salazar y Arantza Mendioroz. Agradezco sus enseñanzas, su paciencia y por su entrenamiento. Espero que estén a gusto con los trabajos que hemos desarrollado y que sigamos trabajando en conjunto.

De igual manera, quisiera agradecer a Ricardo Celorrio y Javier Omella; el desarrollo de los elementos finitos discontinuos tipo Galerkin no habría sido posible sin ustedes.

En Bilbao España, a mis compañeros de piso Blanca y Mario, gracias por todo!, la convivencia fue genial. En la ETSI de Bilbao, a los profesores y profesoras del Fisika Aplikatua Saila I, gracias por los cafés, las salidas y excursiones. A las compañeras (os) del despacho, se han librado de mis 'mexicanadas', gracias por todas las experiencias vividas, se les aprecia mucho!. A mis compas del lab, Ángel y Vasyl, чуваки, thanks for the beers and laughs, my best wishes to you!. A mi carnal-vasco, Javier 'firilo' Gorosabel (q.e.p.d.), wey donde sea que estés: Aupa Eibar!. A la pandilla txikitera: Maca, Gorman, Richie, Rubenio y Flatman; las aventuras, las salidas, las cañas, los vinos y pintxos (en espacial el 3.0), todo se ha quedado en nuestras memorias.

En el cinves Mérida, a la gente del lab de espectroscopía: Michel, Manuel, Alex, Cari, Daniel, Bante y Debra, gracias por las experiencias, las salidas, las 'reuniones' con los del lab vecino, muy buenos recuerdos!. También, gracias por sus ideas y recomendaciones para este y otros trabajos, su experiencia es bien valuada. Por último, pero no menos importante, a Yolanda y Zhirnay, muchas gracias por su asistencia para facilitarme los trámites administrativos, de otra forma hubiese sido un caos.

Abstract

In recent decades there has been growing interest in the development of non-invasive, non-destructive methods for studying the physical properties of materials as well as for evaluating defects in samples. Photothermal techniques have proven to be well suited for studying the thermal transport properties and, in some cases, also for the optical properties of solids. In particular, the flash method has been established as a standard for measuring the thermal diffusivity of solids. Moreover, since the development of infrared cameras in the 1990s, infrared thermography has been successfully applied to several fields of science and engineering. Nowadays, it is considered as a novel tool for non-destructive testing of materials and it is a good alternative to the standard ones, such as dye-penetrant, eddy currents, ultrasonics, etc.

In this thesis we have used pulsed infrared thermography to study the thermal transport properties of solid slabs, which can be semi-transparent or opaque to the excitation wavelength. In some cases, it has been shown that infrared thermography is sensitive to the semi-transparency of the studied sample, which allows to identify the optical absorption coefficient of the sample. We have also applied the developed methods to study the thermal conductivity of polymeric nanocomposites based on magnetized carbon nanofibers. Moreover, we have used focused pulsed spot thermography in order to study the principal thermal diffusivities of anisotropic slabs and we have shown that the proposed method is valid for semi-transparent, opaque, thermally thin and/or thermally thick samples. On the other hand, we have used lock-in

(modulated) thermography for studying the thickness of infinite vertical cracks in semi-infinite opaque solids. Additionally, it has been shown that lock-in thermography can be used for studying the geometry of finite and semi-infinite vertical cracks. However, even when this method provides accurate results, we have also studied the width of infinite vertical cracks using focused pulsed spot thermography in order to reduce the measurement time, while maintaining enough accuracy in the determination of the crack width.

Resumen

En décadas recientes ha habido un creciente interés en el desarrollo de métodos no-destructivos y no-invasivos para el estudio de las propiedades físicas de materiales, así como para la evaluación de defectos en muestras. Las técnicas fototérmicas han demostrado ser adecuadas en el estudio de las propiedades de transporte térmico y, en algunos casos, también para las propiedades ópticas de sólidos. Particularmente, la técnica flash ha sido establecida como estándar para la medición de la difusividad térmica de sólidos. Además, desde el desarrollo de las cámaras infrarrojas en los 1990s, la termografía infrarroja ha sido exitosamente aplicada a diversas áreas de la ciencia e ingeniería. Actualmente, es considerada como una novedosa herramienta para ensayos no-destructivos en materiales y es una buena alternativa para los ensayos estándar como aquellos que usan líquidos penetrantes, corrientes parásitas, ultrasonido, etc.

En esta tesis hemos utilizado termografía pulsada para estudiar las propiedades de transporte térmico en bloques sólidos, que pueden ser semi-transparentes u opacos a la longitud de onda de excitación. En algunos casos, se ha mostrado que la termografía infrarroja es sensible a la semi-transparencia de la muestra estudiada, lo que permite determinar el coeficiente de absorción óptica de la muestra. También hemos aplicado los métodos desarrollados al estudio de la conductividad térmica de nanocompositos poliméricos basados en nanofibras de carbono magnetizadas. Además, hemos utilizado termografía pulsada, con haz enfocado, con el fin de estudiar las difusividades térmicas principales en sólidos anisotrópicos, hemos mostrado que el método propuesto es válido

para muestras semi-transparentes, opacas, térmicamente delgadas y/o térmicamente gruesas. Por otra parte, hemos usado termografía lock-in (modulada) para estudiar el espesor de grietas infinitas verticales en sólidos semi-infinitos opacos. Adicionalmente, se ha mostrado que la termografía lock-in puede ser utilizada para estudiar la geometría de grietas verticales finitas y semi-infinitas. Sin embargo, aún cuando este método da resultados precisos, también hemos estudiado el espesor de grietas infinitas verticales utilizando termografía pulsada con haz enfocado con el fin de reducir el tiempo de medida, manteniendo suficiente precisión en la determinación del espesor de las grietas.

Introduction

The discovery of infrared radiation in 1800 by Sir F. W. Herschel attracted the attention of several scientists since it showed that there are other kinds of light that remain invisible to the naked eye. However, a century after Herschel's discovery, the physical principles of infrared radiation were established, when Max Planck published his blackbody radiation theory. Nowadays, Planck's theory is very important not only because its publication date is considered as the birth of quantum physics, but in particular, for thermography science, since Planck's law represents the physical principles that relate infrared thermography to the measurement of a real object's surface temperature.

This thesis is focused on the development of robust infrared thermography applications for the study of thermal transport properties of solids, as well as on the characterization of vertical cracks. In order to make it more comprehensible to the reader, it is presented in two Parts. Part I covers the first six Chapters and is devoted to the study of thermophysical properties in solids (which can be semitransparent or opaque, thin or thick, poor or good thermal conductors), and several heat conduction models, corresponding to the different pulsed thermography setups proposed, are solved. On the other hand, Part II covers the next three Chapters, which present applications of lock-in thermography and pulsed laser spot thermography to the characterization of vertical cracks in opaque solids.

The first Chapter gives a brief, but concise introduction to the fundamental

concepts of infrared thermography since the discovery of infrared radiation in the XIXth century to the development of modern infrared cameras a few decades ago. Modulated or lock-in thermography, which consists in heating periodically a sample with an intensity modulated light beam and at the same time recording its surface temperature variation is presented as a powerful non-invasive non-destructive technique for studying thermal properties and for the characterization of buried defects or delaminations in solids. The principles of the lock-in realization procedure for infrared cameras is exposed. Moreover, the well-known flash method, in both rear-face and front-face configurations, is reviewed in order to show its advantages and disadvantages for studying the thermal properties in opaque solids. Its applicability, as a novel non-destructive testing technique, for the detection of subsurface defects and delaminations in solids is also presented.

In Chapter 2, the experimental setups used for lock-in and pulsed thermographies are presented. Two variants are examined for pulsed thermography: flat illumination and focused illumination. In subsequent Chapters, the applications of those configurations are discussed for the characterization of vertical cracks and for studying thermophysical properties in solids. Moreover, a lock-in thermography setup is introduced that is applicable for the characterization of vertical cracks with good accuracy, as studied in Chapters 7 and 8.

An extension of the front-face flash method to retrieve simultaneously the thermal diffusivity and the optical absorption coefficient of semitransparent plates is presented in Chapter 3. A complete theoretical model that allows calculating the front surface temperature rise of the sample is developed. It takes into consideration multiple reflections of the heating light beam inside the sample, heat losses by convection and radiation, transparency of the sample to the exciting wavelength and to infrared wavelengths, and heating pulse duration. Measurements performed on calibrated solids, covering a wide range of absorption coefficients (from transparent to opaque) and thermal diffusivities, validate the proposed method. Good agreement between the retrieved values and literature is found.

In Chapter 4, a heat conduction study on polyester resin based composites;

loaded with carbon nanofibers decorated with magnetite nanoparticles in several volume concentrations covering from 0 to 3.25 % and oriented applying a constant magnetic field before polymerization, was performed along the direction of the alignment of the fibers, by measuring the in-depth thermal diffusivity and the thermal effusivity using the laser flash method in the front-face configuration. For the maximum volume concentration of aligned nanofibers along the thickness of the sample, an improvement of 80 % of the thermal conductivity above the thermal conductivity of the polyester resin was observed. In contrast, the increase of the thermal conductivity was only of 20 % above the value of the polyester matrix for samples with non-oriented carbon nanofibers. The effects of the magnetized carbon nanofibers and their orientation on the effective thermal conductivity of the composites were analyzed using a simple theoretical model based on the interaction direct derivative, which takes into account the thermal mismatch between the matrix and the fillers, as well as the aspect ratio of the embedded fibers.

The flash method is the most recognized procedure to measure the thermal diffusivity of free-standing opaque plates. However, it fails to simultaneously obtain the thermal diffusivity and thermal effusivity (or thermal conductivity), which are required to completely characterize the thermal properties of a material. This failure is due to the difficulty of knowing the total energy absorbed by the sample surface after the light pulse. Thus, in Chapter 5, it is proposed to use the flash method in the front-face configuration on a two-layer system consisting on the unknown plate and a liquid of known thermal properties, in order to overcome this failure of the classical flash method. It is proven that the surface temperature is sensitive to the thermal mismatch between the plate and the fluid, which is governed by their thermal effusivity ratio. In order to verify the validity of the method and to establish its application limits flash measurements are performed, using a pulsed laser and an infrared camera, on a set of calibrated materials (metals, alloys, ceramics and polymers) covering a wide range of thermal transport properties. The obtained results confirm the ability of the proposed configuration of the flash method to simultaneously retrieve the thermal diffusivity and thermal effusivity in a fast manner in samples whose effusivities are lower than three

times the thermal effusivity of the liquid used as backing fluid.

Chapter 6 presents an extension of the flash method to retrieve simultaneously the principal in-plane and the in-depth thermal diffusivities of anisotropic solids using focused Gaussian illumination. A complete theoretical model allows calculating the temperature rise of an anisotropic and semitransparent sample. The surface temperature distribution has a Gaussian shape along the principal axes, whose radii give the principal in-plane thermal diffusivities. On the other hand, the time evolution of the spatially averaged surface temperature gives the principal in-depth thermal diffusivity. Pulsed infrared thermography measurements performed on opaque and semitransparent samples, covering a wide range of thermal diffusivities, validate the method. It is especially suited to characterize the principal components of the thermal diffusivity tensor of anisotropic plates from a single and fast measurement.

Early detection of cracks is a challenging task to prevent failures in working structures. In the last decades the flying spot method, based on heating the sample with a moving laser spot and detecting the surface temperature with an infrared detector, has been developed to detect cracks in a fast manner. The aim of Chapter 7 is to measure the width of an infinite vertical crack using lock-in thermography. A semi-analytical solution for the surface temperature of a sample containing such a crack when the surface is illuminated by a modulated laser beam focused at a fixed spot close to the crack is obtained. Measurements on glassy carbon and AISI-304 stainless steel samples containing calibrated cracks are performed using an infrared camera. A least square fit of the amplitude and phase of the surface temperature is used to retrieve the thickness of the crack. Very good agreement between the nominal and retrieved thicknesses of fissures is found, even for widths down to 1 μm, confirming the validity of the model.

The purpose of Chapter 8 is to characterize vertical cracks of finite size and arbitrary shape using optically excited lock-in thermography. The direct problem is solved, which consists of calculating the surface temperature distribution when the shape, size and width of the vertical crack are known. In order to do this, a new method based on discontinuous finite elements is proposed, which allows to deal even with very

narrow cracks, for which classical finite element methods fail. The surface temperature of AISI-304 stainless steel samples containing semi-infinite cracks and illuminated with a laser beam focused close to the crack has been measured using a lock-in thermography setup. A least square fit of the amplitude and phase of the surface temperature is used to retrieve the width and depth of the semi-infinite crack. Very good agreement between the nominal and retrieved values of both parameters is found, confirming the validity of the model.

In Chapter 7, a lock in thermography setup with focused laser excitation to characterize the width of infinite vertical cracks accurately is studied. As this method is very time consuming, in Chapter 9 an alternative method to measure the width of an infinite vertical crack using pulsed laser spot infrared thermography is proposed. A semi-analytical solution for the surface temperature of a sample containing such a crack when the surface is illuminated by a pulsed Gaussian laser spot close to the crack is obtained. Measurements of the surface temperature on samples containing calibrated cracks have been performed using an infrared camera. A least square fit of the surface temperature is used to retrieve the thickness of the crack. Very good agreement between the nominal and retrieved thickness of fissure is found, even for widths down to 1 μm, confirming the validity of the model.

Contents

List of Figures

List of Tables

Part I. Study of thermal transport properties

Chapter 1. Infrared thermography for non-destructive testing and evaluation

1.1 Principles of Infrared (IR) radiation

There exists a key experiment, which showed that there is light invisible to the naked eye, that is, the electromagnetic spectrum is wider than just the visible range. This experiment was performed in 1800 by Sir Friedrich Wilhelm Herschel and it consisted in measuring the temperature of the different colors. In order to do this, Herschel used a glass prism to separate the Sun's light into its different wavelength components (the rainbow's colors as thought at that time) and placed thermometers to measure the temperature of various colors in the split spectrum, see Figure 1.1. The famous astronomer found that the temperature increases from blue to red, so he decided to place an extra thermometer just beyond the red color, where apparently no sunlight falls to it, but to his surprise the measured temperature was higher than the obtained for the visible spectrum, thus he concluded that there must be another type of light beyond the red, such that, it is invisible to our naked eye. Herschel named that light as "invisible thermo-metrical spectrum". Nowadays it is commonly called "infrared radiation" [1,2].

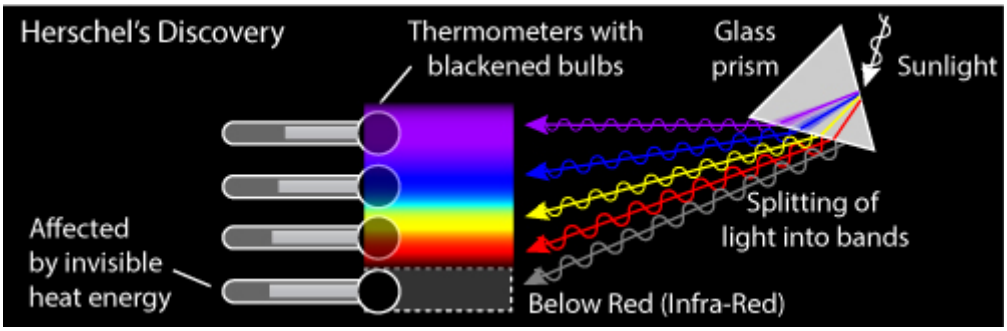

Figure 1.1: Scheme of the Herschel's experiment for measuring the thermal radiation of the Sun's split spectrum, which allowed the discovery of IR radiation.

The electromagnetic radiation emitted by a body as a consequence of its temperature T is called "thermal radiation". In thermal equilibrium, this radiation covers the whole electromagnetic spectrum and the energy emitted at a wavelength λ per unit time, per unit area $E(\lambda, T)$ is a universal function for black bodies. A "blackbody" is a surface that can absorb all the radiation that falls on it and also has the ability to emit the same amount of radiation absorbed (Kirchhoff's law).

During the XIX century many scientists contributed to the understanding of thermal radiation, but it was Max Planck who set the physical principles of this phenomenon. In 1900 he proposed a theory of black body radiation, which is valid for both the short wavelength limit (Wien's law) and the long wavelength limit (Rayleigh-Jeans law).

The power per unit area at a given wavelength emitted by a black body or "spectral radiant emittance" is given by Planck's law,

$$E(\lambda, T) = \frac{2\pi hc^2}{\lambda^5} \frac{1}{\exp\left(\frac{hc/k_B}{\lambda T}\right) - 1}, \tag{1.1}$$

where $h = 6.63 \times 10^{-34}$ Js is the Planck constant, $c = 3.0 \times 10^{8}$ ms^{-1} is the speed of light in vacuum, $k_B = 1.38 \times 10^{-23}$ JK^{-1} is the Boltzmann constant, λ is the wavelength in m and the temperature T is measured in K. Figure 1.2 shows typical curves of the spectral radiant emittance at different temperatures, obtained from numerical simulations of Equation (1.1). A log-log representation has been chosen for clarity in the presentation, also the visible range of the electromagnetic spectrum is

indicated.

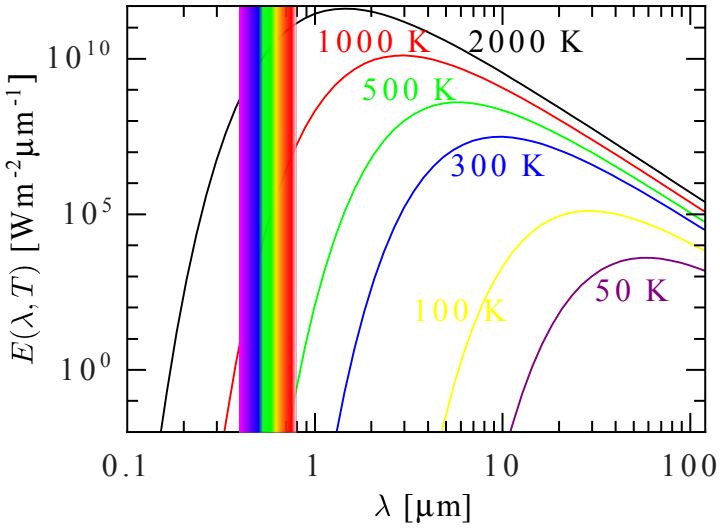

Figure 1.2: Spectral radiant emittance of a black body at different temperatures. Several wavelengths are covered.

It is worthwhile to mention that there is a wavelength (λ_{max}) for which the maximum radiant emittance is reached and this wavelength depends on the temperature of the black body. This is called Wien's displacement law, it can be easily derived from Equation (1.1) and is expressed as

$$\lambda_{max} \approx \frac{2898}{T}. \tag{1.2}$$

In the limit of short wavelengths $hc/k_B \gg \lambda T$, Equation (1.1) becomes the well known Wien's law,

$$E(\lambda,T) = \frac{2\pi hc^2}{\lambda^5 \exp\left(\frac{hc/k_B}{\lambda T}\right)}. \tag{1.3}$$

On the other hand, for long wavelengths $hc/k_B \ll \lambda T$, Planck's law retrieves the so called Rayleigh-Jeans law,

$$E(\lambda,T) = \frac{2\pi hck_BT}{\lambda^4}. \tag{1.4}$$

Moreover, integrating Planck's law over all wavelengths ranging from zero to infinity, the Stefan-Boltzmann law of radiation for black bodies can be deduced, which gives the total power emitted by a black body at a given temperature,

$$E(T) = \sigma_0 T^4, \tag{1.5}$$

where $\sigma_0 = 5.67 \times 10^{-8}$ $Wm^{-2}K^{-4}$ is the Stefan-Boltzmann constant.

The theory of the blackbody radiation is very important, not only because it established a landmark in the history of physics, being Planck's law publication date considered as the born of quantum physics [3], but in particular, for thermography science, since these equations represent the physical principles which relates infrared thermography to the measurement of a real object's surface temperature.

Even when real bodies do not completely follow Planck's radiation law, their radiative properties are described in relation with the corresponding ones of a perfect blackbody. In this way, let E be the total power emitted by an object surface at a given temperature, and E_b the total power emitted by a blackbody surface at the same temperature. The ratio between this two quantities is called the total emissivity (ε),

$$\varepsilon = \frac{E}{E_b}, \tag{1.6}$$

which is a measure of the efficiency of a real body to emit thermal radiation, with respect to a perfect blackbody at the same temperature. Thus, the emissivity is a real number between 0 and 1. Nevertheless, the emissivity of a surface is a function of the observation angle α, wavelength λ, temperature T and even time t [2].

Table 1.1: Classification of physical bodies by their radiative properties.

		$\varepsilon(\lambda, T)$	$\varepsilon(\alpha)$
black body		1.0	1.0
non-black body	gray body	constant	variable
	non-gray (selectively emitting) body	variable	variable
dissipative body		---	constant

A simple classification of physical bodies according to their emissivity is shown in Table 1.1. We have ignored changes in emissivity with time, since they only manifest ultrafast thermal phenomena. In general, when working with infrared cameras, we can

consider objects as gray bodies, since the spectral range of IR cameras is limited (see Section 1.2). However, some objects may act as dissipative ones, like glass [2,4].

1.2 Thermal imaging with IR cameras

Infrared thermography (IRT) is a young non-destructive testing (NDT) technique, which was introduced a few decades ago and keeps attracting the attention of both industrial and scientific branches, because of its versatility for diagnostics, monitoring, measurement of thermal maps on the surface of bodies and because it is, in general, a non-invasive technique.

Practical applications involving infrared technology date from the XIX century. However, it was until the 1930s when many ideas of IR applications emerged: for detection of icebergs, monitoring forest fires, analysis of hot rolled metals, etc. Moreover, in 1937, Vernotte pioneered the idea of the measurement of thermophysical properties in single-sided materials and he also introduced the notion of a thermal transport property, which is known as thermal effusivity nowadays. Nevertheless, it was not until 1959 when Hardy achieved the first single-sided, non-contact thermal characterization by pulsed infrared radiometry; the experiment consisted in measuring the thermal effusivity of the living skin of the forehead of a patient. This work, along with that of J.W. Parker, of the non-contact, double sided, rear-face measurement of thermal diffusivity by active IR pulsed radiometry as well as that of Cowan using modulated heating radiometry, are considered as the milestone works paving the way for active infrared thermography for non-destructive testing and evaluation (NDT&E) [5,6].

In the 1960s, the interest in infrared thermography for NDT&E grew because of the space race and IRT attracted the attention of researchers for the inspection of aerospace materials. However, by the end of the 1970s, the NDT studies performed with IRT were practically qualitative and hence IRT was hardly competitive with other non-destructive tests. However, since those days, a new level on the understanding of IRT

has been achieved after the wider use of heat conduction theory, the introduction of inverse problems for NDT&E, the implementation of efficient numerical algorithms, as well as extensions of IRT to several fields such as, civil engineering, medicine, maintenance, environment, thermo-fluid dynamics, conservation of cultural heritage, among many others [5–7].

A useful classification of IRT is shown in Figure 1.3. Notice the vast possible configurations available for this kind of imaging [6,8]. However, in this work, we have studied just a few of all the possible combinations for active thermography, as indicated by green letters in Figure 1.3.

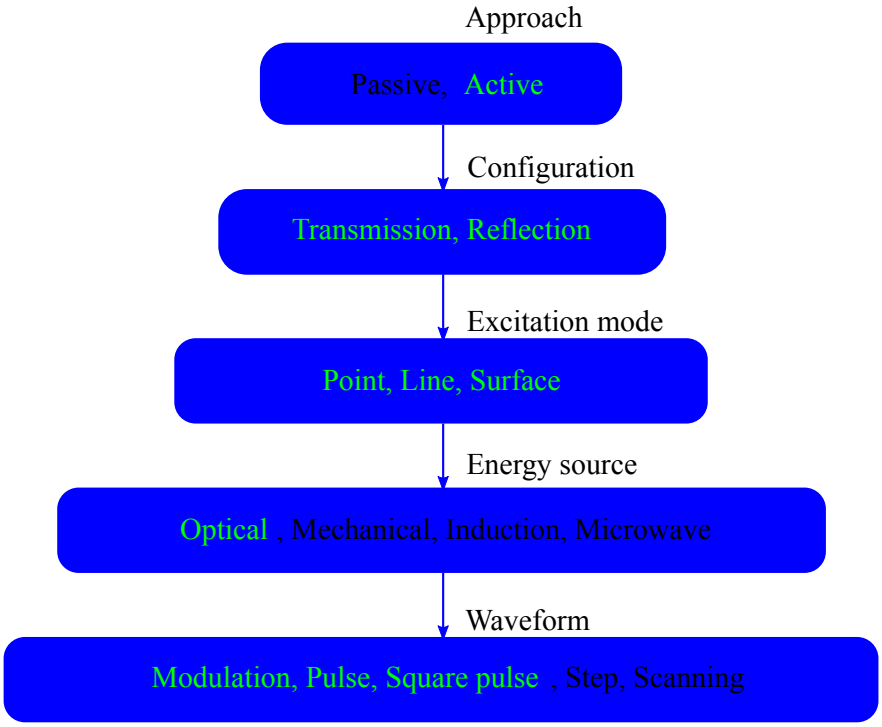

Figure 1.3: A useful classification of infrared thermography. The letters in green indicate the configurations studied in this work.

Thermal imaging or IRT consists in sensing the IR emission of a body and use of this information to build a visible image of its surface temperature field. An infrared camera is the typical device which allows to do this kind of imaging. The principal components of an IR camera are: the optics (lens), IR detectors, a cooling system for the

detectors, electronic and software management for the images.

In the following sub-sections we present a brief description of the main components of an IR camera, as well as some elementary concepts in IR thermography to be taken into account for accurate measurements with an IR camera.

1.2.1 Atmospheric windows

Under typical measurement conditions, we have an object in front of the IR camera, and the atmosphere is between them. It is well known that the atmosphere attenuates the light (radiation) due to absorption by the gases and also due to Rayleigh scattering with suspended particles. Moreover, this attenuation depends on the wavelength of the radiation [2,9]. Thus, not all the radiation emitted by the studied body will reach the IR camera because of the atmospheric absorption through the IR spectrum, as shown in Figure 1.4.

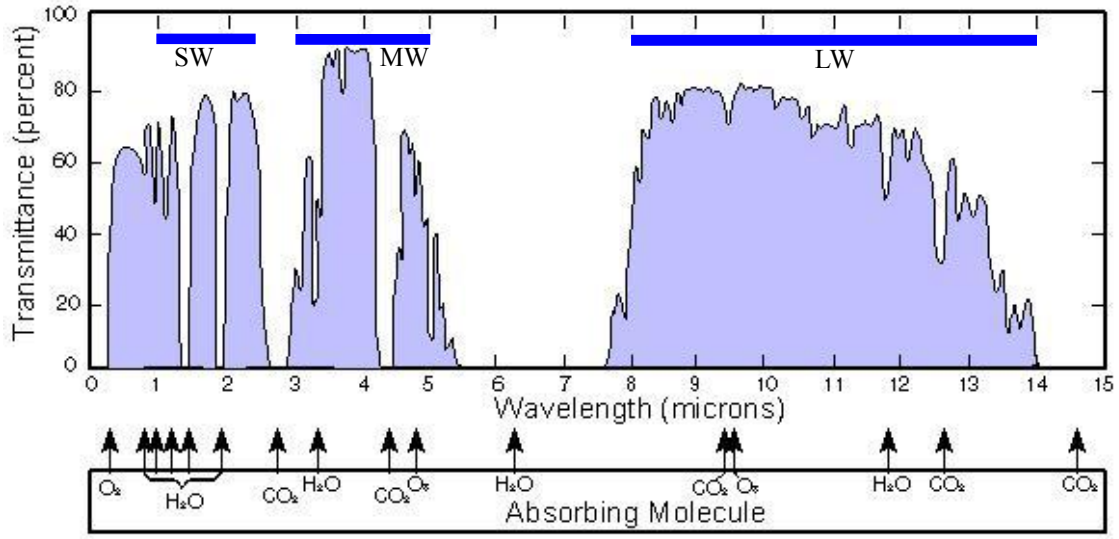

Figure 1.4: Transmittance IR spectrum of the atmosphere. Typical atmospheric windows used in IR cameras are indicated with blue lines.

Typically, three atmospheric windows (range of IR wavelengths with high transmittance) are used in IR cameras: covering from 1 to about 2.5 μm is the short-wave (SW) window; from 3 to about 5.6 μm, the mid-wave (MW) window and from 8

to about 14 μm is the long-wave (LW) window. These LW windows are particularly useful where strong atmospheric attenuation is involved, since atmosphere behaves as a high-pass filter for wavelengths larger than 7.5 μm. On the other hand, mid-wave windows (3 – 5 μm) in combination with highly sensitive detectors, have proven to be very useful for research, development and military applications [2,8].

1.2.2 IR detectors

IR detectors can be classified as: single detectors, linear and focal plane array (FPA) detectors, based on the detector's construction in an IR camera.

Nowadays, IR cameras are mostly provided with FPA detectors, which consists of a two-dimensional pixel matrix, being each pixel a detector of micrometer size. In this kind of cameras, there are no mechanical scanning devices, but the matrix looks at an object by the camera optics, as depicted in Figure 1.5. For example, a typical infrared image (thermogram) of size 320×256 has $81,920$ individual detectors (pixels). Moreover, in modern infrared systems, it is possible to record several hundreds of thermograms per second.

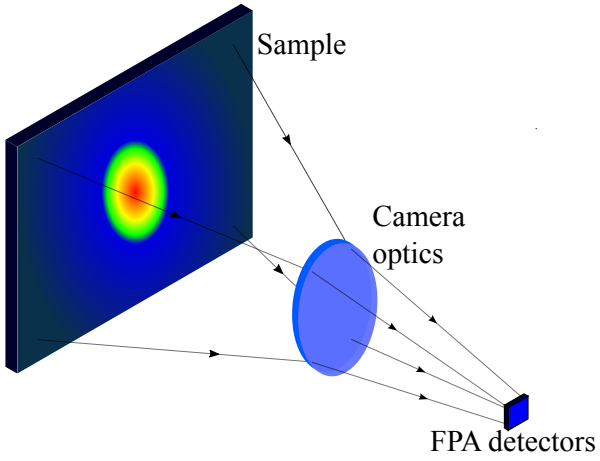

Figure 1.5: Diagram of the acquisition of an IR thermal image by a focal plane array of detectors.

On the other hand, there are several kinds of commercial IR detectors available [10–12]. However, two of them are typically used in modern IR cameras:

microbolometer (thermal) detectors and intrinsic (photon) detectors [2,12].

Microbolometer type detectors are widely used in IR cameras because they do not require cooling (in general), which allows compact camera designs and consequently relatively low production costs. FPA detectors can be manufactured of metals or semiconductor materials and they operate by the bolometer effect, i.e., the incident radiation changes the electrical resistance of the bulk material (bolometric detector). Microbolometers have a flat response curve as a function of wavelength (see Figure 1.6). However, one of their main drawbacks consists in their relatively low detectivity, which is the main parameter characterizing normalized signal to noise performance of detectors, as shown in Figure 1.6. Moreover, they have very slow response time, which is about 12 ms [2,11].

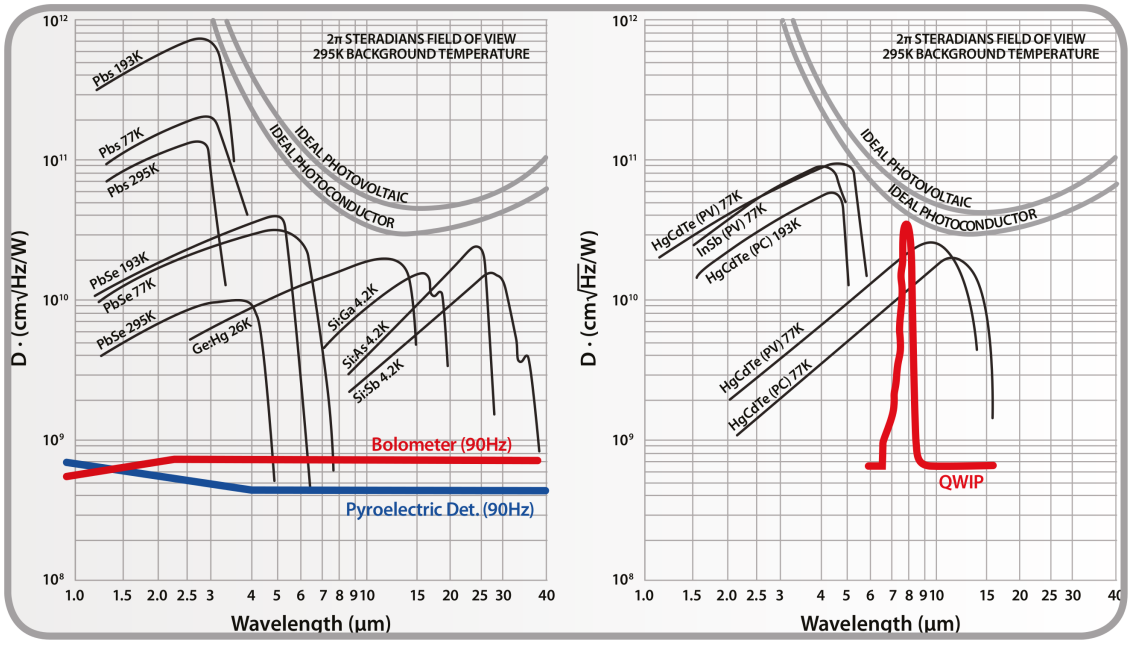

Figure 1.6: Detectivity (D) curves for different detector materials. Bolometer detectivity is flat, while it has strong dependence with wavelength for photon detectors.

Intrinsic detectors operate on the basis of an intrinsic photopyroelectric effect. When these kind of materials are at room temperature, there are some electrons in the conduction band, while most of them are in the valence band. However, this configuration can not be useful for detection of IR radiation, because the electrons

already present in the conduction band can carry an electrical current.

Nevertheless, when the material is cooled at a certain operating temperature (77 K for InSb detectors), the thermal energy is low enough so that all the electrons are found in the valence band, as shown in Figure 1.7a. Under this condition, if the material is exposed to IR radiation and the incident photons have enough energy, the electrons in the valence band can be stimulated to move to the conduction band, as shown in Figure 1.7b. In this way, the material can carry a photocurrent which is proportional to the incident IR radiation beam. Thus, it can be used as an IR detector as long as the incident photon energy (inverse wavelength) is sufficient to overcome the band gap energy (ΔE).

The band gap energy is related to a certain cutoff wavelength (inversely). Accordingly, for detectors in SW or MW windows, the band gap is higher than for detectors in LW windows. Consequently, the operating temperatures are lower for LW detectors than for SW or MW ones [11].

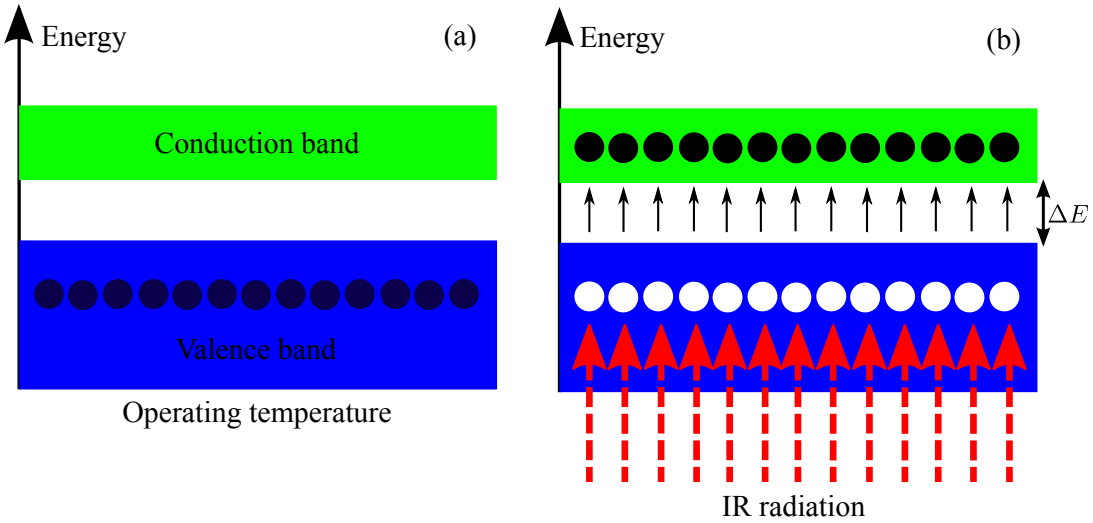

Figure 1.7: Operating principle of quantum detectors. (a) cooled material detector at its operating temperature and (b) effect of the IR radiation incident on the cooled material. The electron on the valence band move to the conduction band.

It is important to remark that cooling this kind of detectors to cryogenic temperatures allow them to be very sensitive to the incident IR radiation (see Figure

1.6). Moreover, these detectors respond very quickly to temperature changes, having a time constant of about 1 ms. Thus, intrinsic detectors are quite good for studying fast transient thermal phenomena and they are used with great success in ultrafast thermography. However, the detectivity must be taken into account, when selecting a photon detector for certain application, since it has a strong dependence on wavelength as shown in Figure 1.5 [2,13].

1.2.3 Cooling methods

The first cooling system developed for infrared detectors consist of a detector attached to a Dewar flask filled with liquid nitrogen, which allows to keep the detector at a low and stable temperature (about 77 K) during the time that it takes the liquid nitrogen to evaporate, limiting the versatility of this very stable system [14].

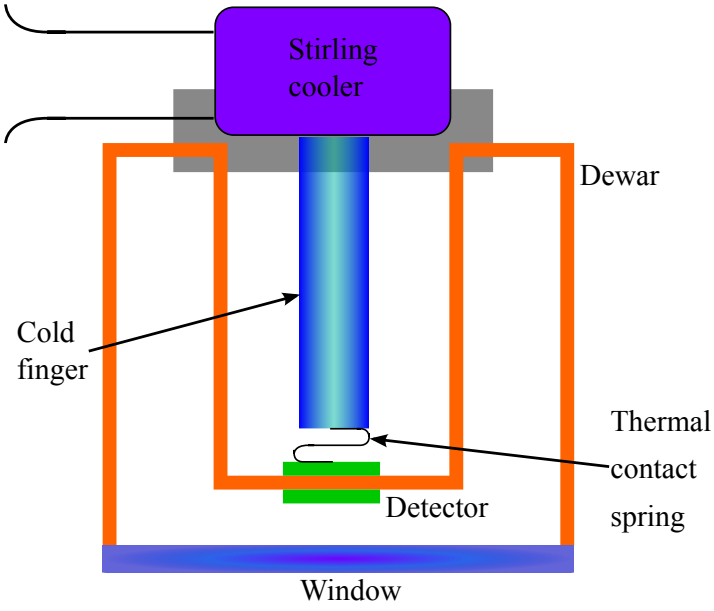

Figure 1.8: Scheme of the Stirling cooling method. The detector is in contact with the cold finger in order to obtain efficient heat conduction.

In 1986 a Peltier based cooling system for a commercial IR camera (Agema, FLIR systems) was introduced. The operation principle consists of a DC current forced through the thermoelectric material, which removes heat from one junction and gives

place to a hot side and a cold one. The hot side is connected to the heat sink and the cold side to the detector [12].

For applications requiring the highest possible sensitivity, an electrical solution to the cryogenic cooling problem has been proposed, the so-called Stirling cooling. In this case, the Stirling motor removes the heat from the cold finger, cooling the detector attached to the cold side, as shown in Figure 1.8. On the other hand, the removed heat is dissipated at the warm side. Even though this cooling method has low efficiency, it is enough for cooling the detector of an IR camera. Moreover, in recent decades, the life time of a Stirling cooler has been increased to more than $8,000$ hours, which is good for an IR camera [12,14].

1.2.4 Temperature resolution

The temperature sensitivity of an IR camera is one of the typical parameters to take into consideration when performing thermographic measurements. The temperature resolution is also known as noise equivalent temperature difference (NETD), which measures the temperature of an object with respect to the ambient that generates a signal equal to the noise level. NETD is usually determined by observation of the area of an technical black body whose temperature is close to that of the background [2,8,12,15].

1.2.5 Spatial resolution

The field of view (FOV) of an IR camera determines the total observation area 'seen' by the detector, at a given distance of the object to the camera optics (see Figure 1.9).

On the other hand, the instantaneous field of view (IFOV) determines the FOV of a single detector (pixel) in an array (FPA). Thus, it is the area that a single pixel 'sees' from the camera optics, as shown in Figure 1.9. In technical data it is referred to as the spatial resolution of the IR camera [2].

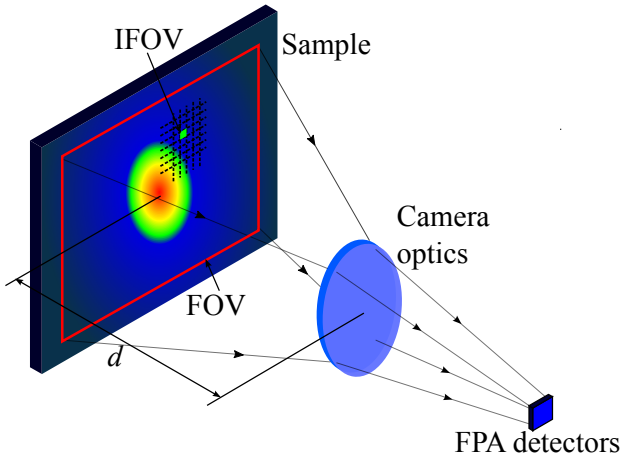

Figure 1.9: Field of view (FOV) and spatial resolution (IFOV) of an IR camera determined by its lens and FPA configuration.

1.2.6 Non-uniformity correction (NUC)

One of the most important functions of the IR camera software is the non-uniformity correction (NUC) of the detector FPA. This correction refines the accuracy of the temperature measurements, since it normalizes the gains and offsets of the individual detectors in the FPA in such a way that all of them have the same electronic characteristics [2,8].

1.3 Lock-in thermography for non-destructive testing and evaluation

Lock-in thermography (LIT) or modulated thermography consists in heating periodically a sample with an intensity modulated light beam and at the same time, to record the temperature variation on its surface with the help of infrared detectors while decomposing the signal with a lock-in amplifier to obtain the amplitude and phase of the modulation. This technique is highly advantageous when we have to extract signal from statistical noise. However, it requires that the excitation source allows to be amplitude-modulated or periodically pulsed at a certain frequency called the lock-in frequency [8,15].

The lock-in realization for thermography was first described by Carlomagno and Berardi in 1976, but it was the work presented by Busse et al in 1992, which inspired AGEMA (now FLIR systems) to create the first lock-in IR camera. This technological advance encouraged the fast development of infrared thermography for non-destructive testing during the last decades. In particular, lock-in thermography has been widely used for characterization of the thermal transport properties in bulk solids, as well as for the detection of delaminations and/or sub-surface defects in opaque solids [7,16,17].

1.3.1 Periodic heat conduction in bulk solids

Heat conduction in bulk solids is described by the heat diffusion equation. In the range of validity of Fourier's law, it establishes that for a point ($\vec{\mathbf{r}}$) in the material the net heat conduction rate in a volume element plus the heat generated inside that volume equals the net rate of change of the thermal energy stored at that point in the material. For a linear, isotropic and homogeneous material, it can be expressed as,

$$\vec{\nabla}^2 T(\vec{\mathbf{r}},t) + \frac{\dot{g}(\vec{\mathbf{r}},t)}{K} = \frac{1}{D}\frac{\partial T(\vec{\mathbf{r}},t)}{\partial t}, \tag{1.7}$$

where K is the thermal conductivity measured in $Wm^{-1}K^{-1}$, which is a measure of the facility for heat conduction inside the material; $D = K/(\rho c_p)$ is the thermal diffusivity of the material in m^2s^{-1}, which indicates the rate at which the heat is distributed into the sample; ρ is the density of the material (kgm^{-3}) and c_p is the specific heat capacity at constant pressure ($Jkg^{-1}K^{-1}$), which is a measure of the energy per unit mass required to increase, in one unit, the temperature of the material. Additionally, $T(\vec{\mathbf{r}},t)$ is the temperature field in K; $\dot{g}(\vec{\mathbf{r}},t)$ is a function related to the internal heat generation measured in $Wm^{-3}K^2$ and t is the time (s). In the case that no internal heat is generated, Eq. 1.7 turns into the so-called Fourier equation [18,19].

In this section we consider the case of a semi-infinite sample (see Figure 1.10) with one surface completely illuminated by a periodic flat light beam, modulated at a frequency f (Hz). The material is such that all light is optically absorbed and converted into heat at the surface of the sample.

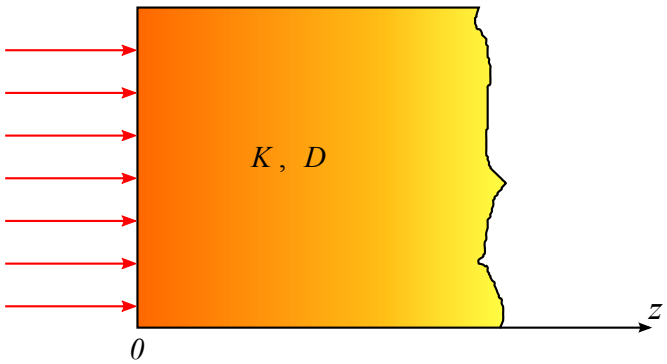

Figure 1.10: Semi-infinite sample periodically heated at its surface by a flat light beam. One dimensional heat conduction is considered.

In this case, one-dimensional heat conduction takes place in the sample along the z-direction and it can be modeled as a boundary value problem using the heat diffusion equation (see Equation (1.7)) with a modulated heat source at the surface $z = 0$ as the boundary condition:

$$\frac{\mathrm{d}^2 T(z,t)}{\mathrm{d}z^2} = \frac{1}{D}\frac{\partial T(z,t)}{\partial t}, \tag{1.8a}$$

$$-K\frac{\mathrm{d}T(z,t)}{\mathrm{d}z}\bigg|_{z=0} = \frac{I_0}{2}\left(1 + e^{i\omega t}\right), \tag{1.8b}$$

where the incident heat flux is the real part of the right hand side of Equation (1.8b). The temperature field $T(z,t)$ can be expressed as a linear combination of the room temperature T_{room}; a time independent temperature $T_{DC}(z,t)$ due to the $I_0/2$ contribution of the incident heat flux and an oscillating temperature $T_{AC}(z,t)$ which is a consequence of the oscillating component of the heat flux $(I_0/2)\mathrm{Re}(e^{i\omega t})$. However, in actual lock-in experiments, we are interested in the oscillating part of the temperature, since $T_{room} + T_{DC}$ is a constant after the transient response and it is usually subtracted from the retrieved temperature signal. Thus, we restrict our analysis to the oscillating part of the temperature. Under this condition, the heat flux is separated in space and time $\left((I_0/2)\mathrm{Re}(e^{i\omega t})\right)$, so we can use the separation of variables technique to express the oscillating temperature as $T_{AC}(z,t) = T_{AC}(z)e^{i\omega t}$. Substituting this expression into Equation (1.8a) and rearranging we obtain

$$\frac{\mathrm{d}^2 T_{AC}(z)}{\mathrm{d}z^2} - q^2 T_{AC}(z) = 0, \tag{1.9}$$

where $q = \sqrt{i\omega/D}$, being i the imaginary unit and $\omega = 2\pi f$ is the angular modulation frequency (rad s^{-1}). Equation (1.9) in combination with the oscillating boundary condition gives the temperature field as,

$$T_{AC}(z,t) = \frac{I_0}{2\epsilon\sqrt{\omega}} e^{-\frac{z}{\mu}} \mathrm{Re}\left\{ e^{i\left(-\frac{z}{\mu} + \omega t - \frac{\pi}{4}\right)} \right\}, \tag{1.10}$$

where $\epsilon = \sqrt{K\rho c_p}$ is the thermal effusivity ($Ws^{1/2}m^{-2}K^{-1}$) of the solid and it measures the ability of the material to exchange heat with its surroundings; it is a surface property. The thermal diffusion length $\left(\mu = \sqrt{D/(\pi f)}\right)$ is the reciprocal real part of q and this is an indicator of the penetration of the temperature field inside the sample. Notice that for a given material of thermal diffusivity D, the smaller the modulation frequency, the larger the penetration of the temperature field inside the sample and for a fixed modulation frequency, the higher the thermal diffusivity of the material, the deeper the penetration of the thermal field into the sample. Moreover, it is worthwhile to mention that the temperature field at $z = \mu$ is $36.8\,\%$ of that at the illuminated surface ($z = 0$) [7,8,18].

On the other hand, it is well known that flat modulated heating on a semi-infinite sample does not allow to retrieve any thermo-physical property of the material, but it has been successfully applied in non-destructive testing for the detection of sub-surface defects [20–23]. Additionally, it serves as an illustrative example to introduce some basic concepts in modulated heat conduction, which is the physical basis of lock-in thermography.

1.3.2 The lock-in process in thermography

The aim of the lock-in process is to evaluate the oscillating part of the detected signal. Since the 1980s, several algorithms have been developed to adapt the conventional lock-in procedures to IR thermography, some of them were reviewed by Krapez 1998, who studied the performance of four different LIT algorithms: standard

lock-in correlation, 4-bucket method, variance method and the least squares method. However, in this work, we restrict ourselves to the study of the standard lock-in correlation because the IR camera used in the experiments (FLIR SC-7500) performs the lock-in process with this algorithm [15,24].

A mathematical description of the lock-in correlation output signal S after averaging over a well-defined integration time t_{int} can be expressed as

$$S = \frac{1}{t_{int}} \int_0^{t_{int}} F(t)W(t)\,\mathrm{d}t, \tag{1.11}$$

where, $F(t)$ is the detected signal and $W(t)$ is the correlation or weighting function. Nevertheless, the digital lock-in correlation uses an analog to digital-converter (ADC), so the acquired signal is digitized into a series of data F_k and the correlation function is replaced by a set of numbers called the weighting factors W_k. Hence, the digital lock-in correlation procedure consists in averaging the product between the measured values F_k and the weighting factors W_k over all the measured events n during a lock-in period. This is similar to the mathematical formulation presented in Equation (1.11), but in discrete variable:

$$S = \frac{1}{n} \sum_{k=1}^{n} F_k W_k. \tag{1.12}$$

In most lock-in thermography systems, the weighting factors are values calculated from a harmonic function. Thus, if this function is symmetric and it is evaluated over a full period, then the summation over all the picked values of W_k is zero, which suppress all DC (direct current) contribution to the output signal S [24].

When doing the measurements, the sampling frequency (rate of digitizing events) and the lock-in frequency might not be synchronized (asynchronous correlation) due to technical limitations or by experimental requirements. Asynchronous correlation gives rise to the so-called “undersampling” technique, which makes possible that the sampling frequency can be lower than the lock-in frequency. However, in this technique there are some “forbidden” lock-in frequencies because of the Nyquist-Shannon sampling theorem, which states that at least two samples per period are necessary for

detecting a certain frequency. Moreover, due to the fact that usually an incomplete number of lock-in periods is performed, the DC suppression will not be as good as the one obtained from a synchronous lock-in correlation, in which the lock-in and sampling frequencies are synchronized. Additionally, the latter does not allow undersampling, so we do not have to worry about forbidden frequencies when working with this configuration.

For simplicity in the presentation, we consider a fixed number of samples n per lock-in period and we average the measurement over N lock-in periods in a synchronous lock-in correlation, so that the weighting factors are the same in each lock-in period and the digital lock-in correlation can be written as

$$S = \frac{1}{nN} \sum_{i=1}^{N} \sum_{j=1}^{n} W_j F_{i,j}. \tag{1.13}$$

In modern IR cameras, the digital lock-in process is performed using a two-channel correlation. This means that there is a set of weighting factors W_j which approximates the sine function and another one which approximates the cosine function. Moreover, the lock-in correlation can be performed during the measurement (on-line or standard lock-in correlation) or with all the data stored after the measurement (off-line correlation). In this work, we only consider the standard lock-in correlation which is the one used by our IR camera.

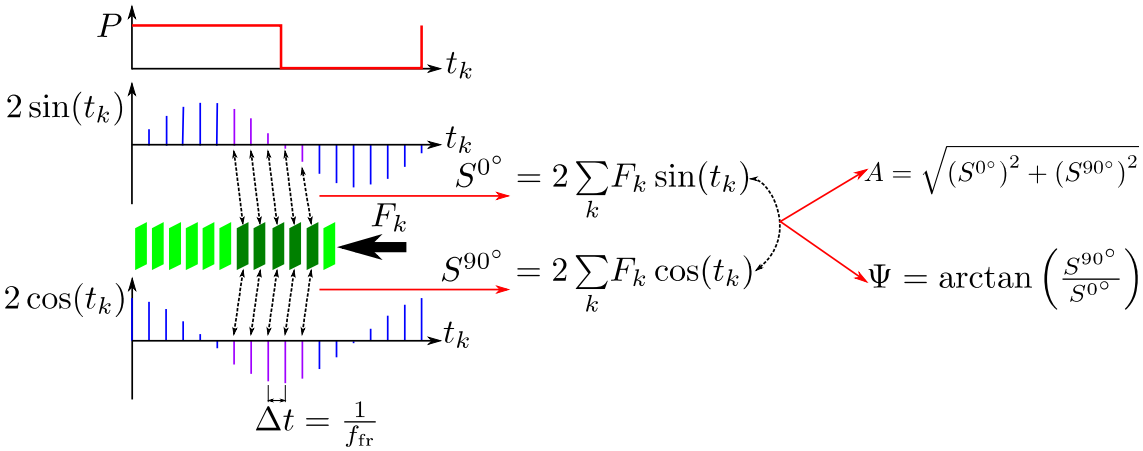

Figure 1.11: Diagram of the principle of lock-in correlation procedure employed in camera-based systems.

Figure 1.11 shows a diagram of the lock-in process as performed with an IR camera: A modulated heat source of intensity P is applied to a sample and the heating process is monitored with an IR camera which records data at a fixed frequency f_{fr}, so that each frame (image) F_k is delayed by $\Delta t = 1/f_{\mathrm{fr}}$ with respect to the previous one. The lock-in correlation is performed twice in parallel using the weighting factors $W_k^{0^\circ} = 2\sin(t_k)$ and $W_k^{90^\circ} = 2\cos(t_k)$, in combination with the acquired frames F_k to obtain the so-called in-phase signal S^{0° and quadrature signal S^{90°, respectively. From these signals, the amplitude A and phase Ψ thermograms (images) can be calculated [15,25].

1.3.3 Noise reduction with LIT

In lock-in thermography, the phase-independent amplitude signal (A) is used to give a measure of the system's noise level. In order to do this, we record a steady-state scene, for example, a blackbody at room temperature, in the lock-in mode and average the amplitude over a certain region. Since the image will be dominated by the system's noise, we obtain a measure of the mean amplitude noise of the system:

$$\langle \mathrm{noise}_A \rangle = \frac{2}{\sqrt{N_{\mathrm{images}}}} \mathrm{NETD}, \tag{1.14}$$

where the NETD is the noise equivalent temperature difference, which is an intrinsic property of the camera (see Section 1.2.4) and the total number of images $N_{\mathrm{images}} = nN$ is given by the number of frames $n = f_{\mathrm{fr}}/f_{\mathrm{lock-in}}$ per lock-in period and the number of evaluated periods $N = f_{\mathrm{lock-in}} t_{\mathrm{acq}}$, being $f_{\mathrm{lock-in}}$ the modulation frequency and t_{acq} the total acquisition time [15].

In the case of an IR camera with a NETD of 20 mK, an acquisition rate (frame frequency) of 350 Hz and recording data during 1 min, a total of $21,000$ images are obtained from the lock-in process, reducing the noise level to 0.28 mK according to Equation (1.14). It is important to mention that increasing the number of images also increases the acquisition time, so a compromise between the acquisition time and noise level is established.

1.4 Pulsed thermography for non-destructive testing and evaluation

Pulsed thermography (PT) consists in heating the surface of a sample by a brief (a few ms) heat pulse of high power (several kW) and monitoring the cooling process of the heated surface using IR detectors or IR cameras. The heating source can be a pulsed laser or a photographic flash-lamp. This technique is fast, versatile and easy to implement, since it only requires the heating source, an IR detector and a synchronization system between the heating pulse and the data acquisition software. Moreover, the processing algorithms available for PT allows to reduce the effects of non-uniform heating, emissivity variations, environmental reflections and surface geometry during the measurements. However, the processing techniques available for PT are more complex when compared with a lock-in correlation [8]. Two applications of PT are very common in NDT&E: detection of sub-surface defects in opaque solids and measurement of the thermal transport properties of solids. The following sub-sections present a brief description of those applications.

1.4.1 Detection of defects in opaque solids

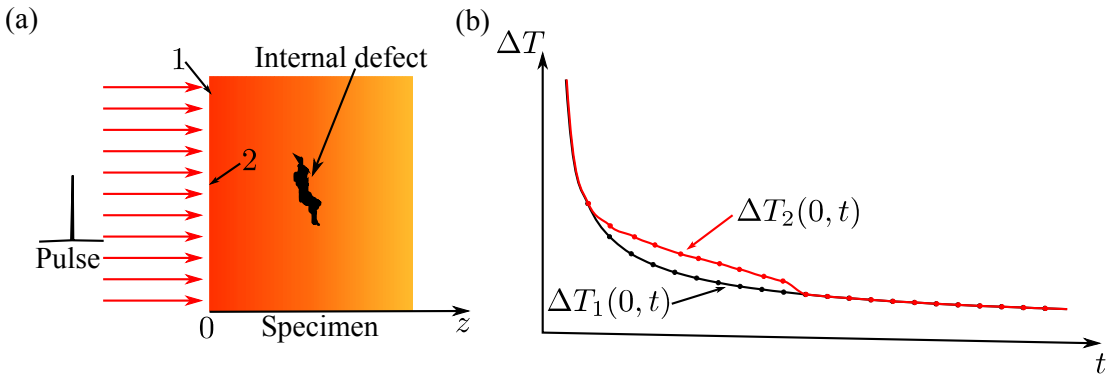

Figure 1.12: (a) Solid specimen containing a buried defect illuminated at its surface $z = 0$ with a Dirac-like pulse and (b) temperature evolution of the heated surface from a point $\Delta T_1(0,t)$ far from the internal defect and from a point $\Delta T_2(0,t)$ contained in the region of the buried defect.

One of the main uses of pulsed thermography in non-destructive evaluation is to reveal the presence of sub-surface defects in samples or devices, even if they are in

service. Furthermore, it is reported that in $80\,\%$ of the applications the main interest is only to detect sub-surface defects on a go/non-go basis. Accordingly, several methodologies have been developed which allow to detect the presence of internal defects in samples by only monitoring the surface temperature evolution after a brief heating pulse [8,26–28].

Studying the heat conduction on an opaque semi-infinite sample, whose surface is illuminated by a brief light pulse, as shown in Figure 1.12a (without the internal defect) is a simple way to understand how is possible to monitor sub-surface defects via IRT and how to estimate their depth inside the sample. Considering ideal conditions, i.e., no heat losses to the surroundings and a Dirac-like pulse, we can write a boundary value problem to describe the phenomenon:

$$\frac{\mathrm{d}^2T(z,t)}{\mathrm{d}z^2} = \frac{1}{D}\frac{\partial T(z,t)}{\partial t}, \tag{1.15a}$$

$$-K\frac{\mathrm{d}T(z,t)}{\mathrm{d}z}\bigg|_{z=0} = Q_0\delta(t), \tag{1.15b}$$

where Q_0 (Jm^{-2}) is the energy per unit area of the heating pulse, $\delta(t)$ is the Dirac's delta function, K and D are the thermal conductivity and thermal diffusivity of the material, respectively. This problem can be solved analytically and the evolution of the temperature rise ΔT after the heating pulse $(t > 0)$ can be expressed as

$$\Delta T(z,t) = \frac{Q_0}{\epsilon\sqrt{\pi t}}e^{-\frac{z^2}{\mu^2}}, \tag{1.16}$$

where ϵ is the thermal effusivity of the material and $\mu = \sqrt{4Dt}$ is the thermal diffusion length, which is a measure of the depth at which the heat has been diffused into the sample at time t. The cooling of the heated surface after the heating pulse can be obtained from an IR measurement by plotting the temperature evolution $\Delta T_1(0,t)$ of a pixel (1) in the thermograms as presented in Figure 1.12b (black curve) and it follows a $t^{-1/2}$ decaying process according to Equation (1.16). However, when the studied sample contains an internal defect (see Figure 1.12a), the predicted cooling behavior deviates from Equation (1.16) and the defect can be detected in the temperature evolution $\Delta T_2(0,t)$ of a pixel (2) as shown in Figure 1.12b (red curve). It is important

to mention that, studying the temperature evolution at $z = 0$, a time $t \sim z^2/D$ is required to detect a defect located at a depth z inside the sample. However, at this time, the temperature signal goes like $\Delta T \sim 1/z$, hence, the detectable defects should be near to the surface $z = 0$ because the temperature signal will be lower as the defect is deeper [8,18].

Although the treatment presented in this sub-section is only a bare approximation of the really complicated 3D heat conduction problem shown in Figure 1.12a, several processing techniques such as thermographic signal reconstruction (TSR) or pulsed phase thermography (PPT) among others, have been based on this simplification to perform qualitative detection of buried defects in opaque solids [28–33].

1.4.2 Measurement of thermal diffusivity in opaque solids

The flash method is extensively used for determination of the thermal diffusivity in solids all over the world and in the last decades, several improvements have been implemented in this methodology. It consists in heating up the front surface of an opaque sample of thickness L, as shown in Figure 1.13a, with a brief light pulse and to monitor the cooling process with an IR detector or camera. This monitoring can be performed on the rear surface (non-illuminated, $z = L$) or on the front surface (heated side, $z = 0$) of the sample, giving rise to two configurations of the method: the classical configuration or Parker's method and the front-face configuration, respectively [34,35].

In Parker's method, the temperature evolution of the surface $z = L$ is monitored by an IR detector and the instant of time $t_{1/2}$ at which the temperature rises to half of its maximum is used to identify the thermal diffusivity D of the material. The temperature evolution at this surface can be calculated by solving the boundary value problem given in Equation (1.15) with an extra boundary condition, which is that the heat flux at the rear surface is zero. Evaluating this temperature at the half value of its maximum, the corresponding time can be obtained as [34]

$$t_{1/2} = 0.139\frac{L^2}{D}. \tag{1.17}$$

A typical temperature evolution curve obtained in the classical configuration of the flash method is presented in Figure 1.13b (black curve), in which red lines indicate the half temperature rise (horizontal line) and its corresponding time (vertical line). The value of D is calculated from Equation (1.17).

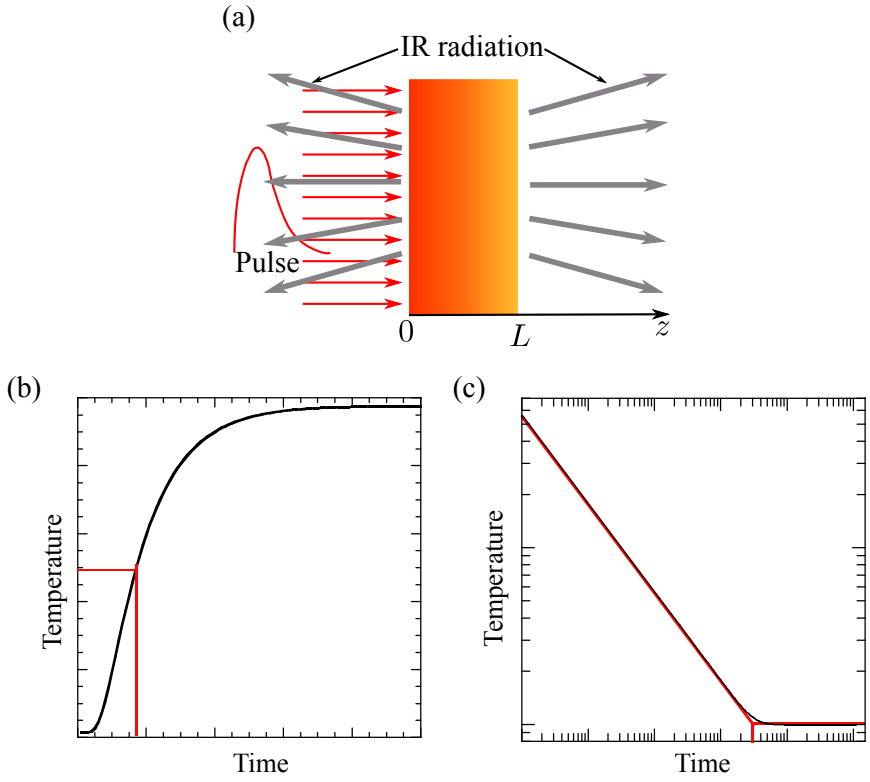

Figure 1.13: (a) Flat slab of thickness L illuminated by a brief light pulse, the IR radiation coming out from both surfaces is shown (gray rays). (b) Temperature evolution of the sample's rear-face used in the Parker's method and (c) front-face temperature evolution as used for identification of the thermal diffusivity.

On the other hand, the front-face configuration became an attractive methodology since the 1980s, probably because of its technical requirements: fast sampling frequencies of the detectors and need for non-contact temperature detection. It consists in monitoring the temperature evolution of the surface $z = 0$ after the heating pulse and it is usually presented in a log-log plot as in Figure 1.13c (black curve). The

first part of the curve is a straight line of $-1/2$ slope and represents the semi-infinite behavior, i.e., the heat is far from reaching the rear surface $z = L$ of the sample. However, for longer times the behavior is a horizontal line and there is a transition zone which reminds of an "elbow" indicating that the heat has reached the rear surface of the sample. Those lines are highlighted in red in Figure 1.13c and their intersection indicates a characteristic time t_1 which is useful for the determination of the material's thermal diffusivity as follows [35]

$$t_1 = 0.318\frac{L^2}{D}. \tag{1.18}$$

This expression can be obtained using the solution of the front-face temperature by equating the semi-infinite regime to the asymptotic one (longer times). It is important to say that t_1 is not the time at which the heat reaches the rear surface of the sample, as can be deduced from the definition of thermal diffusion length in Equation (1.16).

These methodologies provide fast but not so accurate results of the thermal diffusivity of the material, since they do not take into account the presence of effects like the heat losses to the surroundings or the finite duration of an actual pulsed source among others. However, in recent decades, several contributions have been proposed to increase the accuracy of those methods, some of which are presented and discussed in part I of this thesis.

Chapter 2. Instrumentation used for pulsed and lock-in thermographies

2.1 Pulsed thermography setup with flat illumination

In this work, we have used pulsed thermography (PT) in the front-face configuration with plane illumination as a powerful tool for studying the "in-depth" thermal diffusivity and the thermal effusivity of flat slabs, as described in chapters 3 and 4, respectively.

In Figure 2.1a a diagram of the experimental setup used for studying the thermal diffusivity and thermal effusivity of solid slabs is shown: it consists of a pulsed Nd-Glass laser (Quantel) at 1053 nm with "flat-top" spatial profile and adjustable energy (up to 25 J per pulse) used as the heating source. The beam is directed to the sample surface through a gold-coated mirror and its repetition rate is 2 pulses per minute. In order to assure one-dimensional heat conduction and to prevent lateral heat diffusion, the laser beam is defocused with a 20° holographic diffuser, such that the spot covers the whole sample surface. The infrared (IR) radiation emitted by the sample is recorded with an IR camera (FLIR SC7500 working between 3 and 5 μm). A coated Ge window with high transmittance in the $3-12$ μm range is used to protect the camera lens. We record images at frame rates varying from 1 to 3.5 kHz, depending on the thermal diffusivity and thickness of the studied samples. This setup can be used for

determination of the thermal diffusivity of bare slabs (Figure 2.1b), as well as for the thermal effusivity and thermal diffusivity of a slab in contact with a semi-infinite fluid layer, as shown in Figure 2.1c. In the latter case, a window with smaller surface than that of the sample has been drilled into one wall of a metallic box, such that when it is filled with a liquid, both the sample and the fluid will be in direct contact. The sample is glued to the metallic box by applying a belt of molten silicone along the edges of the sample, the silicone is easy to remove and prevents leakages of the fluid during the measurements.

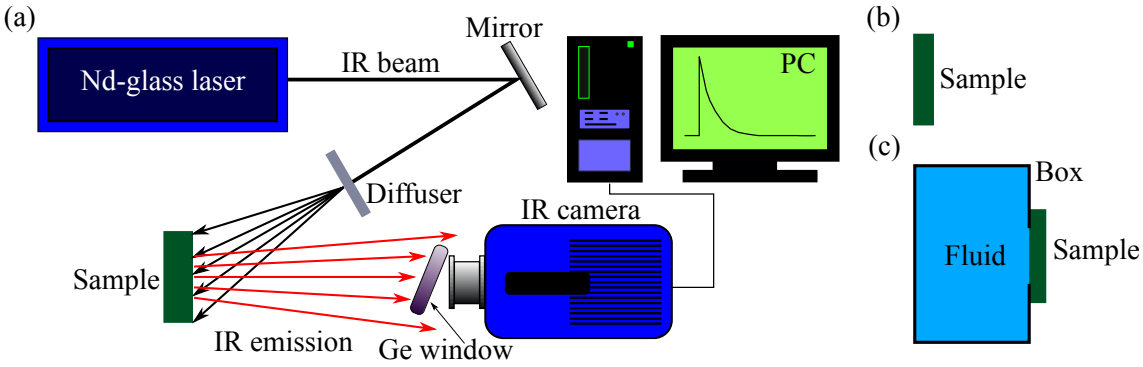

Figure 2.1: (a) Diagram of the PT setup used for studying the thermal diffusivity of (b) flat slabs and for simultaneous determination of the thermal diffusivity and thermal effusivity of (c) a flat slab in contact with a semi-infinite fluid layer.

The noise equivalent temperature difference (NETD) of our IR camera is about 20 mK [36]. This value is obtained for a single pixel working with an integration time of 1.6 ms at 25 °C. Figure 2.2a shows a thermogram (quarter frame, 64×64 pixels) of a black cardboard 1 ms after the heating pulse. The left side of the thermogram (grey-white color), corresponds to the sample, while the right side (black color) is a region without sample. It is worth mentioning that the temperature detected by the IR camera is not the real surface temperature rise of the sample, since neither its emissivity nor its IR transparency are known. However, the "apparent" temperature rise ΔT measured by the IR detectors is proportional to the IR emission exiting the front surface of the sample.

In Figure 2.2b we show by red dots the average temperature evolution over the pixels contained in the red square of the thermogram (Figure 2.2a). As can be observed,

the noise of this signal is ~ 20 mK, but it should be lesser because we are taking the average over 1200 pixels. Moreover, this "noise" is not randomly distributed as it must be, but it has a systematic "wavy" shape with a constant period. It is important to say that this wavy signal is not characteristic of IR cameras, but it appears in our camera due to the back and forth movement of the Stirling motor's piston in the camera cooling system.

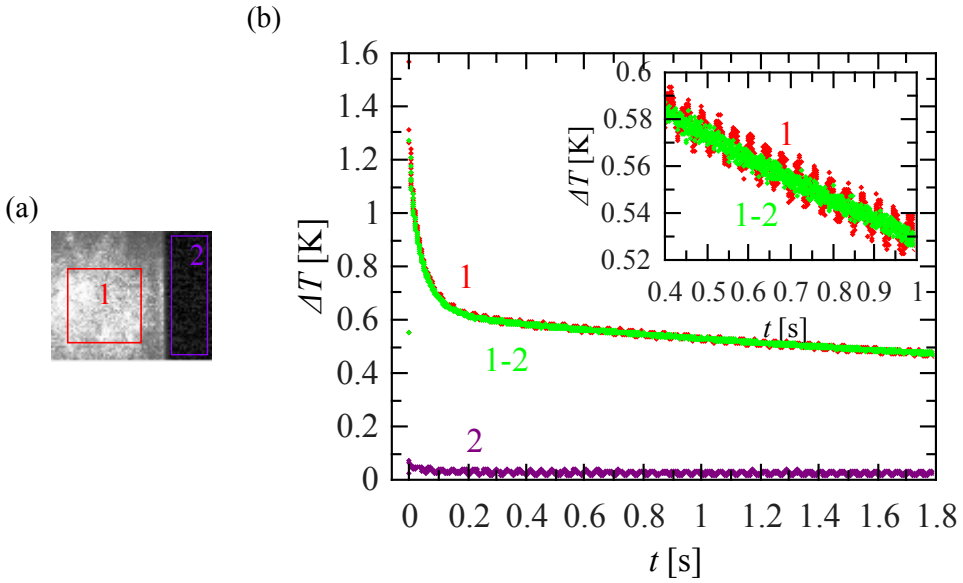

Figure 2.2: (a) Thermogram of a black cardboard after 1 ms of the heating pulse: region 1, inside the sample, is delimited by a red rectangle and region 2, outside the sample, is represented by a purple one. (b) Mean temperature evolution after the heating pulse: in region 1 (red), in region 2 (purple) and their difference (green). The inset shows a zoomed region.

This problem is intrinsic to our camera and it could be really complicated to try a home-made solution. Instead, we propose to suppress the "wavy" signal by taking advantage of its periodic structure and hence reduce the signal noise below the nominal value. In order to do this, we propose the following procedure: we average the temperature over a sample-free zone of the thermogram with the same area as that used for the signal (the purple rectangle in the thermogram). The resulting temperature evolution is the purple "wavy" signal in Figure 2.2b. Finally, we take the difference between those signals (labeled as 1 and 2 in Figure 2.2b, respectively). The resulting "wavy-corrected" temperature is the green signal shown in Figure 2.2b. As can be

observed in the inset, this corrected temperature shows random noise and its amplitude is below 10 mK, which is less than the nominal noise amplitude, as expected. Therefore, in the following, all data presented (collected as a function of time) will correspond to wavy-corrected "apparent" temperature rise.

It is important to mention that in some cases all the thermogram's area is occupied by the sample to be studied, therefore we can no longer apply the presented procedure to obtain a wavy-corrected temperature signal. For those particular cases, we have chosen to implement a fast Fourier transform (FFT) algorithm which allows to clean the wavy signal directly from the measured one, for example, signal 1 in Figure 2.2b. It consists in taking the FFT of the measured signal and to remove the corresponding peak of the Stirling motor (which is about 27 Hz) from the Fourier spectrum, a polynomial interpolation is performed around the suppressed peak in order to recover all other frequencies not related to the Stirling cooling system. The polynomial degree may vary from 3 to 9, depending on the measurement and cooling state of the camera. After that, an inverse fast Fourier transform (IFFT) is applied to the resulting spectrum in order to return to the time domain and to obtain a wavy-corrected temperature signal. However, this procedure is not as effective as the one presented in Figure 2.2b, so whenever possible, we avoid using the FFT based algorithm to obtain a wavy-corrected temperature signal in our measurements.

(a) (b)

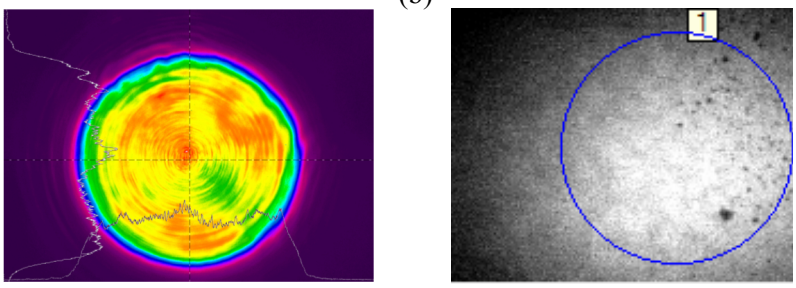

Figure 2.3: (a) Spatial profile of the pulsed laser used in this work and (b) a thermogram 1 ms after the pulse on an AISI-304 sample using a 20° holographic diffuser in front of the sample, uniform heating is achieved on the sample surface.

On the other hand, it is well known that spatial inhomogeneities in the laser beam give rise to nonuniform heating of the sample surface, which affects the temperature evolution after the heating pulse [37,38]. In our case, the spatial profile of the laser beam used, provided by Quantel, is shown in Figure 2.3a and its uniformity is acceptable for our measurements. However, for simulating plane illumination in large samples (about 5×5 cm^2), a $20°$ holographic diffuser has been placed 15 cm away from the sample. Notice that the resulting heated surface is as uniform as if it was illuminated with a flash lamp (see Figure 2.3b).

It is important to say that the duration time of Quantel's laser pulse is about 0.5 ms, as shown in Figure 2.4. The intensity distribution of the laser pulse follows an exponential law of the form $I_0(t) = \frac{Q_0}{N} \frac{t^\gamma}{\tau^{1+\gamma}} \exp(-t/\tau)$, where Q_0 is the energy per unit area delivered by the pulse, γ and τ are parameters which depend on the laser and N is a normalization constant in order to satisfy the condition $\int I_0(t)\,\mathrm{d}t = Q_0$. The intensity distribution of our laser pulse is shown by dots in Figure 2.4 and fits the exponential law (red curve) with $\gamma = 1.46$ and $\tau = 0.132$ ms. For clarity in the presentation, only one in thirty points have been plotted in Figure 2.4, however, all of them have been used in the fitting. Moreover, for a typical flash lamp, its intensity distribution fits the same exponential law with $\gamma = 0.5$ and $\tau = 2.3$ ms [39].

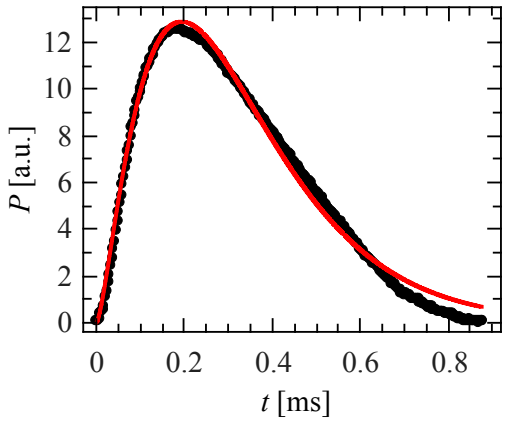

Figure 2.4: Intensity distribution of our Nd-Glass laser pulse. Black dots represent the experimental data and the red curve is the result of fitting to an exponential law.

In some applications, a Dirac's delta like laser pulse may be aggressive or even harmful for the sample surface. Accordingly, a step like laser pulse of finite duration is recommended. In this work, we have used this configuration for studying the thermal transport properties of polymeric composites (see Chapter 4). A diagram of the experimental setup used is shown in Figure 2.5. A continuous wave diode laser (808 nm) with flat-top profile and adjustable power up to 60 W is employed as the heating source. It is synchronized with a function generator in order to control the step pulse duration. The beam is directed onto the sample surface by an optical fiber placed 20 cm away to assure plane illumination. The infrared emission of the sample is collected with an IR camera (FLIR SC7500). A coated Ge window ($3 - 12$ µm) is used to protect the lens of the camera. The images (thermograms) are recorded at 200 Hz with 548 µs integration time in the full frame windowing mode (320×256 pixels). All samples are covered with a thin black paint layer (about 5 µm thick) in order to improve both the laser absorption and IR emissivity.

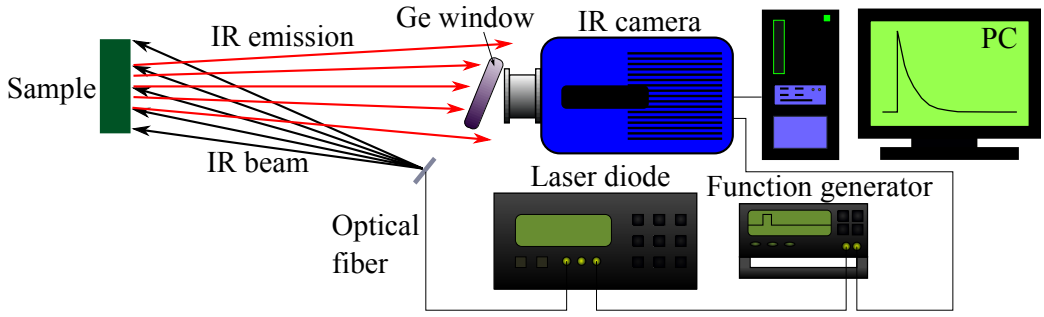

Figure 2.5: Diagram of the experimental setup used for pulsed thermography with a step like laser pulse. It has been applied in the study of thermal transport properties of composites.

In order to reduce the noise level in the measured temperature, we have made an average over 7200 pixels in the thermograms obtained from the IR camera. With this procedure we keep the noise level below 5 mK in the measurements, which is one of the advantages of using an IR camera instead of a monolithic detector.

2.2 Pulsed thermography setup with focused illumination

In some pulsed thermography experiments, it may be useful to focus the spot of the laser beam on the illuminated surface. For example: if we want to determine the in-plane thermal diffusivity of a solid slab or if we want to detect vertical cracks in weldings.

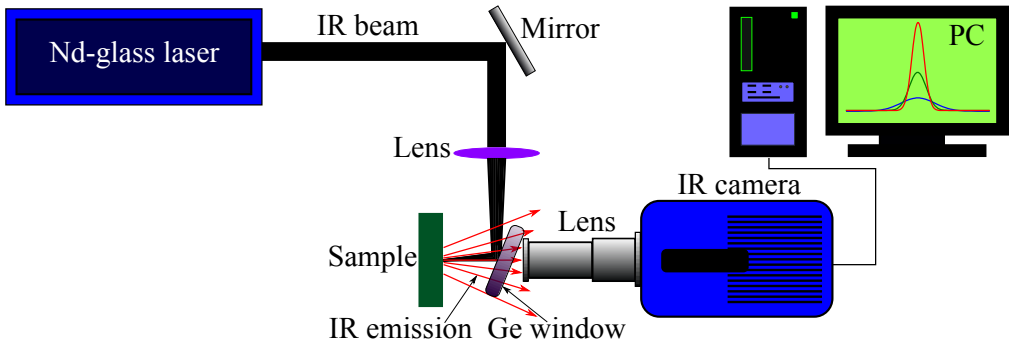

Figure 2.6: Diagram of the experimental setup used for pulsed thermography with focused illumination. The IR camera is provided with a microscope lens.

A diagram of the experimental setup used for pulsed thermography with focused illumination is presented in Figure 2.6. A pulsed Nd-Glass laser at 1.053 μm with "flat-top" spatial profile and adjustable energy (up to 25 J/pulse) is used as the heating source. As the time duration of the pulse is about 0.5 ms, as shown in Figure 2.4, it can be considered as instantaneous (Dirac's delta distribution) if we analyze the temperature profiles at long times after the pulse. The beam is focused by a converging lens of 75 mm focal length and it is directed to the sample surface using a Ge window, which is transparent to mid infrared wavelengths. This Ge window is also used to prevent the laser radiation from reaching the camera lens. The IR radiation emitted by the sample is collected by an infrared microscope lens (x1-MWIR-L0120) and recorded with an IR camera, as in Section 2.1. In this configuration each pixel in the detector averages the infrared emission coming from a 31 μm side square in the sample. Images are recorded at a frame rate of 200 images per second.

In general, when working with focused illumination, a good spatial resolution of the IR camera is needed in order to obtain enough points in the temperature profiles to be analyzed. This can be achieved with a microscope lens, which, in this case, gives a resolution of 31 μm per pixel side and keeps the point spread function (PSF) over 4 pixels on the thermogram. A cheaper alternative consists in using a 50 mm focal length lens with two extension tubes, which provides a comparable resolution of 40 μm per pixel side, but its PSF extends to more than 10 pixels on the thermogram. Thus, if precise temperature profiles are required for measurements, a microscope lens should be used. On the other hand, when just qualitative information of the temperature profiles is needed, the other alternative presented is acceptable and also provides good results.

2.3 Lock-in thermography setup with focused illumination

Lock-in thermography (LIT) with focused illumination has proven to be a powerful and versatile technique for studying the thermal diffusivity of solid slabs and thin filaments. In both cases, the so-called “slopes method” provides accurate results of the thermal diffusivity in opaque solids [5–7]. In this work, we extend the applicability of lock-in thermography with focused illumination to the characterization of vertical cracks in opaque solids (See chapters 7 and 8).

Figure 2.7 shows a diagram of the experimental setup used for characterization of vertical cracks with lock-in thermography in the focused illumination configuration. A continuous wave (CW) laser at 532 nm (COHERENT Verdi 6 W), whose intensity is modulated by an acousto-optic modulator (AOM) ISOMET 1201E-1, is directed to the sample surface by means of a mirror and a silicon window, which is transparent to IR wavelengths. This Si window also prevents laser reflections to reach the camera optics. The laser beam is focused onto the sample surface using a 10 cm focal length lens. The laser power is changed at each frequency ($50 - 200$ mW) in order to obtain a similar temperature rise at the centre of the laser spot of about 5 K. An IR camera (FLIR SC7500) with an InSb detector operating in the $3 - 5$ μm spectral range, records the

sample surface temperature. A microscope lens (x1-MWIR-L0120) has been used to improve the spatial resolution; each pixel measures the average temperature over a square of 31 µm each side.

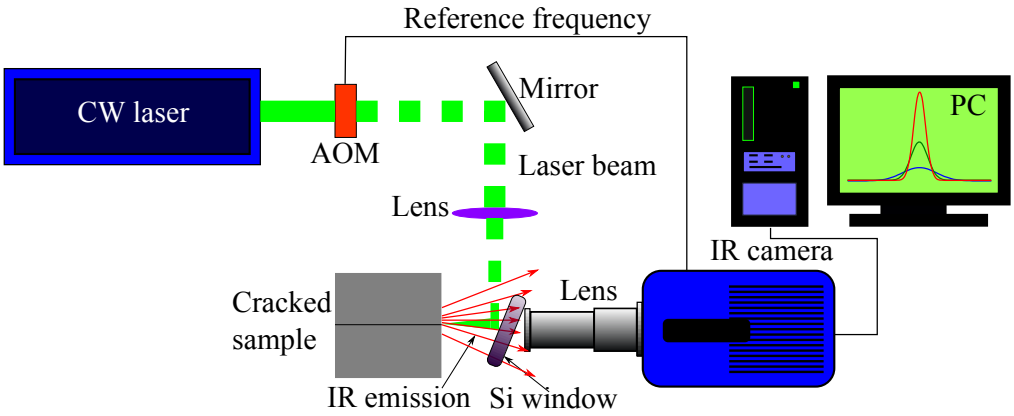

Figure 2.7: Diagram of the experimental setup for lock-in thermography with focused illumination. A microscope lens has been used in order to improve the camera's spatial resolution.

Chapter 3. Measuring the thermal diffusivity of semitransparent solids by the front-face flash method

3.1 Front-face flash method for opaque slabs

There are several photothermal methods useful for the determination of the thermal diffusivity of solids, most of them use a modulated heating source (frequency domain) [1–8]. These methods are popular because they provide good signal to noise ratio (SNR). However, they are also time consuming, which reduces their applicability in some cases. Consequently, pulsed methods are also used, which demands a brief heating pulse (time domain) [9–15]. Although the SNR obtained with pulsed methods is not as good as for modulated methods, time domain measurements have shown to provide accurate results combined with short time consuming measurements, which make these methods very attractive for industry. In this way, Parker et al introduced in 1961 the well known "classical flash method" for measuring the thermal diffusivity of opaque solids, which consists on heating the front face of an opaque plate with a brief light pulse and analyzing the temperature evolution at its rear surface [34]. Alternatively, in the "front-face flash method" a brief light pulse heats up the front surface of an opaque solid slab of thickness L and we record the temperature evolution at the same surface after the heating pulse with an infrared (IR) detector. Considering

ideal conditions, i.e., no heat losses to the surrounding atmosphere and a Dirac-like delta pulse, a series solution of the temperature evolution at the front-face $T(0)$ can be found [19,35].

$$T(0) = \frac{Q_0 \chi}{\epsilon} \frac{\sqrt{D}}{L} \left[1 + 2 \sum_{n=1}^{\infty} \exp\left(-\frac{n^2 \pi^2}{L^2} Dt \right) \right], \tag{3.1}$$

where Q_0 is the energy per unit area delivered by the pulse (Jm^{-2}), χ is the fraction of energy absorbed by the sample surface, D and ϵ stand for the thermal diffusivity and thermal effusivity of the sample, respectively. Usually, the thermal diffusivity was determined from fits to the series solution or by using the time $t_1 = L^2/(\pi D)$, as explained in Section 1.4 of Chapter 1. It is important to say that, under experimental conditions, a laser or flash lamp pulse is not a Dirac-like pulse, but it has a characteristic temporal shape (see Chapter 2, Figure 2.4). Moreover, unless the sample is inside a vacuum chamber, there will be heat losses to the surrounding atmosphere due to radiation mechanisms, which cannot be neglected. In order to improve the accuracy on the identification of the thermal diffusivity in opaque solids, Balageas introduced in 1989 those effects in the modeling of the heat conduction problem for a flash experiment in the front-face configuration [35]. Consequently, this methodology became attractive for studying the thermal transport properties of solids, also encouraged by the development of fast IR detectors. Furthermore, the front-face method has shown to be particularly useful for non-destructive testing of materials since, unlike the rear-face flash method, it only needs access to the free surface of the sample, which improves its versatility for scientific and industrial applications [35,55].

Studies on semitransparent solids used to be preformed by applying a thin opaque coating on the slab surfaces, which allows the use of the classical flash method or the front-face flash method for thermal diffusivity identification. However, in 2014, Salazar et al extended the classical rear-face flash method to deal with semitransparent samples without any coating. In this way, the thermal diffusivity (D) together with the optical absorption coefficient (α) of these materials could be measured [56].

3.2 Front-face flash method for semitransparent slabs

In this chapter we present a generalization of the front-face flash method to accurately retrieve the thermal diffusivity (D) of semitransparent plates without any coating. This issue has been already addressed in the literature for ideal conditions [57,58], i.e., instantaneous light pulse (Dirac-like) and absence of heat losses. Nevertheless, we have calculated the front surface temperature of a semitransparent slab illuminated by a brief light pulse considering additional effects in the model, such as:

(a) the multiple reflection of the light beam at the sample surfaces,

(b) the influence of heat losses by convection and radiation,

(c) the transparency of the sample to IR wavelengths, and

(d) the pulse duration.

Then, in order to verify the validity of the method we have performed experimental measurements, using a pulsed laser and an IR camera, on several calibrated materials (glasses, metallic oxides and cardboard) that are semitransparent to both visible and IR wavelengths. Moreover, we have also tested the model on opaque samples such as metals, composites and graphite. This study clearly establishes the conditions and limits to measurement of the thermal diffusivity on semitransparent samples accurately using the front-face flash method.

Let us consider an uncoated semitransparent slab of thickness L, uniformly illuminated by a flat light beam of wavelength λ and intensity I_0. The geometry of the problem is shown in Figure 3.1. According to the Beer-Lambert law and taking into account the multiple reflections of the incident light beam, the light intensity inside the sample is

$$\begin{aligned} I(z) &= I_0(1-R)e^{-\alpha z} + I_0(1-R)e^{-\alpha L}Re^{-\alpha(L-z)} \\ &\quad + I_0(1-R)e^{-2\alpha L}R^2e^{-\alpha z} + \cdots \\ &= \frac{I_0(1-R)\left(e^{-\alpha z} + Re^{-2\alpha L}e^{\alpha z}\right)}{1-R^2e^{-2\alpha L}}, \end{aligned} \tag{3.2}$$

where R and α are the optical reflection and absorption coefficients of the slab at the

wavelength of the incident light beam (λ), respectively. The Laplace transform of the heat diffusion equation under this illumination is expressed as follows:

$$\frac{\mathrm{d}^2\bar{T}}{\mathrm{d}z^2} - q^2\bar{T} = -\frac{\bar{I}_0\,(1-R)\,\alpha\left(e^{-\alpha z} - Re^{-2\alpha L}e^{\alpha z}\right)}{K\,(1-R^2e^{-2\alpha L})}, \tag{3.3}$$

where $\bar{T}$ is the Laplace transform of the sample temperature, $\bar{I}_0$ (Jm^{-2}) is the Laplace transform of the light intensity, which takes into account the temporal shape of the pulse, K is the thermal conductivity of the sample, and $q = \sqrt{s/D}$, being s the Laplace variable and D the thermal diffusivity of the sample. The general solution of Equation (3.3) can be written as a linear combination of the solution of the homogeneous equation and a particular solution of the non-homogeneous equation

$$\bar{T}(z) = Ae^{qz} + Be^{-qz} + Ce^{-\alpha z} + Ee^{\alpha z}, \tag{3.4}$$

where the coefficients corresponding to the particular solution are given by

$$C = \frac{\bar{I}_0\,(1-R)\,\alpha}{2K\,(q^2-\alpha^2)}, \tag{3.5a}$$

$$E = -\frac{\bar{I}_0\,(1-R)\,\alpha R e^{-2\alpha L}}{2K\,(q^2-\alpha^2)}. \tag{3.5b}$$

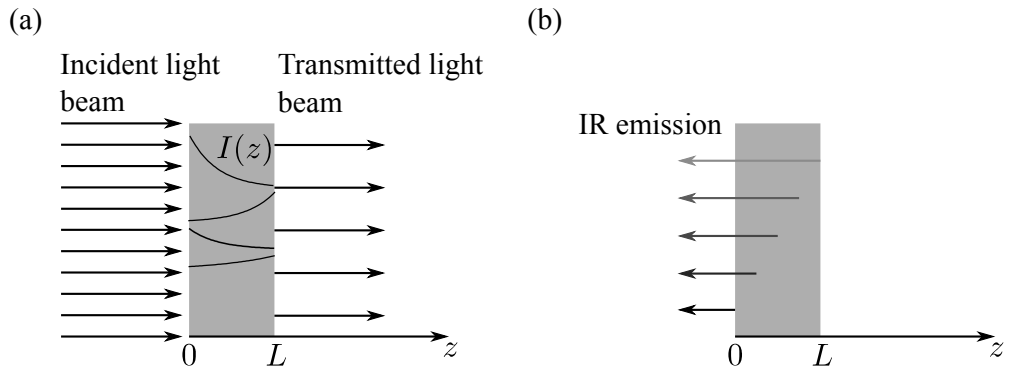

Figure 3.1: (a) Transparency to the incident light: diagram of a semitransparent slab of thickness L, illuminated by a light beam. $I(z)$ shows the multiple reflections of the light beam on the slab's surfaces. (b) Transparency to infrared radiation: the IR emission comes out not only from the slab's surface but also from the inner layers.

On the other hand, the coefficients of the homogeneous solution in Equation (3.4) are obtained from the boundary conditions at the sample surfaces

$$-K\frac{\mathrm{d}\bar{T}}{\mathrm{d}z}\bigg|_{z=0} = -h\bar{T}\left(z=0\right), \tag{3.6a}$$

$$-K\frac{\mathrm{d}\bar{T}}{\mathrm{d}z}\bigg|_{z=L} = h\bar{T}\left(z=L\right), \tag{3.6b}$$

where we have used the linear coefficient of heat transfer (h) to take into account the combined effect of heat losses by convection and radiation. We have also assumed that the value of this coefficient is equal at both surfaces. On the other hand, we have neglected the thermal conduction to the surrounding air (because of its extremely low thermal conductivity). Thus, the Laplace transform of the temperature inside the sample, satisfying the boundary conditions, can be written as

$$\begin{aligned}\bar{T}(z) = C&\left(\frac{A_0 e^{qz} + B_0 e^{-qz}}{E_0} + e^{-\alpha z}\right)\\ &+ E\left(\frac{A_1 e^{qz} + B_1 e^{-qz}}{E_0} + e^{\alpha z}\right),\end{aligned} \tag{3.7}$$

where C and E are given by Equations (3.5a) and (3.5b), respectively and

$$A_0 = e^{-qL}\left(q-h'\right)\left(\alpha+h'\right) + e^{-\alpha L}\left(q+h'\right)\left(-\alpha+h'\right), \tag{3.8a}$$

$$B_0 = e^{qL}\left(q+h'\right)\left(\alpha+h'\right) + e^{-\alpha L}\left(q-h'\right)\left(-\alpha+h'\right), \tag{3.8b}$$

$$A_1 = e^{-qL}\left(q-h'\right)\left(-\alpha+h'\right) + e^{\alpha L}\left(q+h'\right)\left(\alpha+h'\right), \tag{3.8c}$$

$$B_1 = e^{qL}\left(q+h'\right)\left(-\alpha+h'\right) + e^{\alpha L}\left(q-h'\right)\left(\alpha+h'\right), \tag{3.8d}$$

$$E_0 = e^{-qL}\left(q-h'\right)^2 - e^{qL}\left(q+h'\right)^2, \tag{3.8e}$$

where we have defined $h' = h/K$. Notice that, if the sample is semitransparent to the infrared spectrum, the signal recorded by the infrared detector comes not only from the sample surface but also from the bulk. Now, if we define β as the effective infrared absorption coefficient for the sample (averaging the sample behavior from 3 to 5 μm, which is the spectral band of our IR camera) the Laplace transform of the signal recorded by the IR camera placed in front of the sample is given by [59]

$$\bar{S}(0) = F\int_0^L \beta e^{-\beta z}\bar{T}(z)\,\mathrm{d}z, \tag{3.9}$$

where F is a constant which includes the emissivity of the sample, the sensor area and detectivity, and the temperature derivative of the Plank's law at room temperature. Moreover, F also includes the effect of multiple reflections of the IR emission at the sample walls. $\bar{T}(z)$ is the Laplace transform of the sample's temperature as given by Equation (3.7). This means that we are assuming that heat losses associated to the infrared emission from the sample volume are too small in such a way that they do not affect the measured temperature field. By substituting Equation (3.7) into Equation (3.9) and solving the integral analytically, the Laplace transform of the IR signal recorded by the IR camera can be expressed as

$$\begin{aligned}\bar{S}(0) = FC\frac{\beta}{E_0}\Bigg[&-\frac{A_0}{q-\beta}\left(1-e^{-(\beta-q)L}\right)+\frac{B_0}{q+\beta}\left(1-e^{-(\beta+q)L}\right)\\&+\frac{E_0}{\alpha+\beta}\left(1-e^{-(\alpha+\beta)L}\right)\Bigg]\\&+FE\frac{\beta}{E_0}\Bigg[-\frac{A_1}{q-\beta}\left(1-e^{-(\beta-q)L}\right)+\frac{B_1}{q+\beta}\left(1-e^{-(\beta+q)L}\right)\\&-\frac{E_0}{\alpha-\beta}\left(1-e^{(\alpha-\beta)L}\right)\Bigg].\end{aligned} \tag{3.10}$$

In particular, we will consider two temporal shapes for the light pulse: (a) a delta function pulse and (b) a laser or a flash lamp pulse. In the first case, the light intensity distribution is $I_0(t) = Q_0\delta(t)$ and its Laplace transform is $\bar{I}_0 = Q_0$, where Q_0 is the energy per unit area delivered by the pulse and $\delta(t)$ is the Dirac's delta function. The intensity distribution of a flash lamp pulse follows an exponential law of the form $I_0(t) = \frac{Q_0}{N}\frac{t^\gamma}{\tau^{1+\gamma}}\exp\left(-\frac{t}{\tau}\right)$, as explained in Section 2.1 of Chapter 2, and its Laplace transform is given by $\bar{I}_0(s) = \frac{Q_0}{(1+s\tau)^{1+\gamma}}$.

It is worth noting that multiplying both numerator and denominator of Equation (3.10) by L^2 one can rewrite $\bar{S}(0)$ in such a way that it depends on 5 fitting parameters: Q_0/K, $L/\sqrt{D}$, αL, βL and $h'L$. By applying the inverse Laplace transform to Equation (3.10), the IR signal $S(0)$ recorded by the IR camera is obtained. In order to

achieve this, a numerical inverse Laplace transform algorithm has been used: the well-known Stehfest algorithm [60], which gives very accurate results for "smooth" functions [61], as is the case for $\bar{S}(0)$. The Stehfest algorithm can be expressed as

$$f(t;M) = \frac{\ln(2)}{t} \sum_{k=1}^{2M} V_k \bar{f}\left(\frac{k\ln(2)}{t}\right), \tag{3.11}$$

where $f(\cdot)$ is the numerical inverse Laplace transform of the function $\bar{f}(\cdot)$ for $t > 0$, M is a positive integer which establishes the number of functionals involved in the numerical inversion [62]. In this case, we have set $M = 16$ during all calculations of the inverse Laplace transform of Equation (3.10), which has shown stability, accuracy and short time computation. Finally, the coefficients V_k can be computed as follows

$$V_k = (-1)^{M+k} \sum_{j=\|(1+k)/2\|}^{\min(k,M)} \frac{j^{1+M}}{M!} \binom{M}{j} \binom{2j}{j} \binom{j}{k-j}, \tag{3.12}$$

where $\|x\|$ returns the largest integer less than or equal to x and $\min(k, M)$ gives the value of the minimum among k and M.

Accordingly, a fit of the time evolution of the IR signal coming out from the front surface of a semitransparent plate of known thickness allows retrieving D, α, and β. Note that Equation (3.10) also depends on the optical reflection coefficient R, which is an unknown quantity. Numerical calculations indicate that its influence is very small unless the sample is extremely transparent and/or R is very high. As for most semitransparent materials under normal incidence, R is in the range $0.04 - 0.10$, in this work we have taken a fixed value $R = 0.05$ for all the fits.

3.3 Numerical simulations and sensitivity analysis

Numerical simulations showing the time evolution of the normalized signal $S(0)$ for a semitransparent plate illuminated by a delta function pulse are presented in Figure 3.2. Introducing the dimensionless time t/t_c, we obtain a representation of the normalized signal $S(0)$, which is independent of D, L, and K values. The characteristic time $t_c = L^2/(4D)$ was defined taking into account the typical definition of the thermal

diffusion length for transient phenomena [18], $\mu = \sqrt{4Dt}$. It is important to say that the normalization of signal $S(0)$ consists in normalizing the infrared signal to 1 for long times [56].

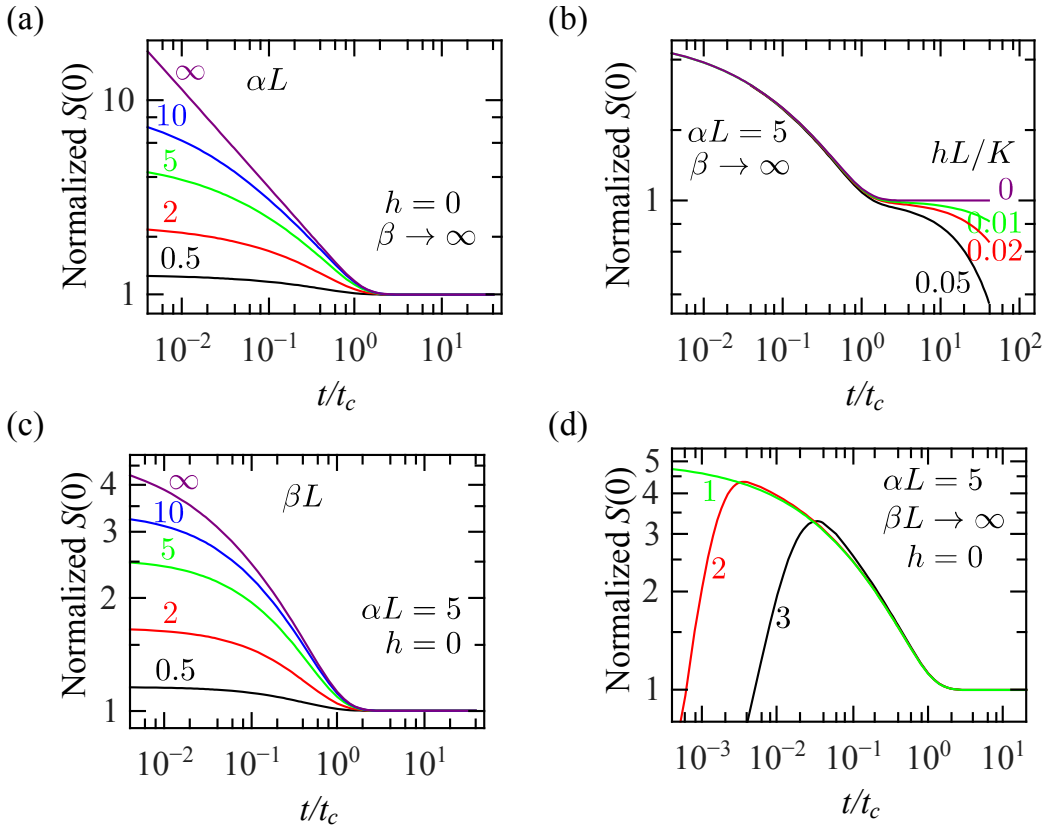

Figure 3.2: Numerical simulations showing the normalized IR signal from the front surface of a semitransparent plate illuminated by a delta function pulse ((a) to (c)) as a function of dimensionless time. (a) Effect of αL value, with $h = 0$ and $\beta \to \infty$, (b) effect of hL/K value, with $\alpha L = 5$ and $\beta \to \infty$, (c) effect of βL value, with $\alpha L = 5$ and $h = 0$. (d) Effect of the time duration of the heating pulse for: (1) a delta function pulse, (2) a laser pulse ($\gamma = 1.46$ and $\tau = 0.132$ ms) and (3), a flash lamp pulse ($\gamma = 0.50$ and $\tau = 2.3$ ms).

In Figure 3.2a we analyze the effect of the sample's transparency at the illumination wavelength on the normalized signal $S(0)$, ignoring the heat losses to the surroundings $(h = 0)$ and considering opacity to IR wavelengths $(\beta \to \infty)$. Notice that in the limiting case of a completely opaque sample $(\alpha L \to \infty)$, the typical shape of the front-face flash method is obtained: a linear behavior at short times with slope $-1/2$

and a horizontal straight line at long times. In fact, the intersection of both straight lines occurs at $t_1 = L^2/(\pi D)$, see Section 1.4 of Chapter 1. As the αL factor decreases, the signal level at short times decreases too, which is due to the transparency of the plate, while at later times the normalized signal remains unaffected [58].

Figure 3.2b shows the effect of heat losses by convection and radiation mechanisms. We have made numerical simulations for a sample that is semitransparent to the incident light beam $(\alpha L = 5)$, but opaque to IR wavelengths $(\beta L \to \infty)$. A typical value for semitransparent samples has been chosen, i.e., neither transparent $(\alpha L < 0.5)$ nor opaque $(\alpha L > 20)$ [49]. Notice that, as the factor hL/K is increased, the normalized signal $S(0)$ is reduced after the time t_c and it decreases faster with time. On the other hand, it is worth noting that heat losses hardly influence the signal behavior at early times after the laser pulse.

The effect of transparency to IR wavelengths is presented in Figure 3.2c, in which simulations have been performed for a semitransparent sample $(\alpha L = 5)$ with negligible heat losses $(h = 0)$. As the transparency to IR increases (smaller βL values) the normalized signal at short times decreases. This means that both transparencies (to illumination and to IR wavelengths) reduce the IR signal collected by the IR detectors, hence the more transparent the sample, the harder will be to characterize its thermal diffusivity with this technique.

Finally, Figure 3.2d shows the effect of the time duration of the heating pulse. Numerical simulations have been performed for a sample that is semitransparent to the incident light $(\alpha L = 5)$, opaque to IR wavelengths $(\beta \to \infty)$ and with negligible heat losses $(h = 0)$. We have considered the laser pulse given in Figure 2.4 of Chapter 2, which is shorter than 1 ms and a typical flash lamp pulse, which takes several milliseconds. As can be seen, for a Dirac pulse there is a sudden jump of the front surface temperature after the pulse. For a finite light pulse, instead, the temperature increases monotonically until it reaches a maximum when the light pulse finishes. It is worth mentioning that at medium and long times the three curves coincide. This means that the duration of the heating pulse has strong a influence on the IR signal just at short

times, but its effect is negligible for long times.

We have also analyzed the sensitivity of the normalized signal $S(0)$ to the parameters of interest (D and α) in order to quantify the ability of the front-face flash method to retrieve these parameters. In Figure 3.3 we show the sensitivity of the normalized $S(0)$ to D, h, and α. Numerical simulations are performed for a typical glass sample ($D = 0.5$ mm^{2}s^{-1}, $K = 1$ Wm^{-1}K^{-1}, $L = 1$ mm, $h = 10$ W m^{2}K^{-1}) that is opaque to IR radiation ($\beta \to \infty$) and illuminated by a delta function pulse. The sensitivity coefficient $Sy(x)$ of the normalized signal $S(0)$ to a given quantity $x = \{D,\, h,\, \alpha\}$ is defined as

$$Sy(x) = \frac{x}{S(0)} \frac{\partial S(0)}{\partial x}. \tag{3.13}$$

In Figure 3.3a the time dependence of the normalized signal $S(0)$ together with the sensitivity to D, h and α are shown for an opaque glass ($\alpha = 103$ mm^{-1}) illuminated by a delta function pulse. This is the expected result for the front-face flash method on opaque samples. The maximum sensitivity to thermal diffusivity occurs at early times, while the sensitivity to heat losses is shifted to later times. Obviously the sensitivity to α is zero over the whole temperature history. In Figure 3.3b the same simulation is performed for a semitransparent glass ($\alpha = 2$ mm^{-1}). Notice that, as the material becomes more transparent the sensitivity to α increases, but the price to be paid is reducing the sensitivity to D with respect to -0.5. It is worth mentioning that the highest sensitivities to D, α and h are well separated in time: very short times for α, intermediate times (around t_1) for D, and long times for h. These uncorrelated (non proportional) sensitivities indicate that the three parameters can be retrieved from the same data set.

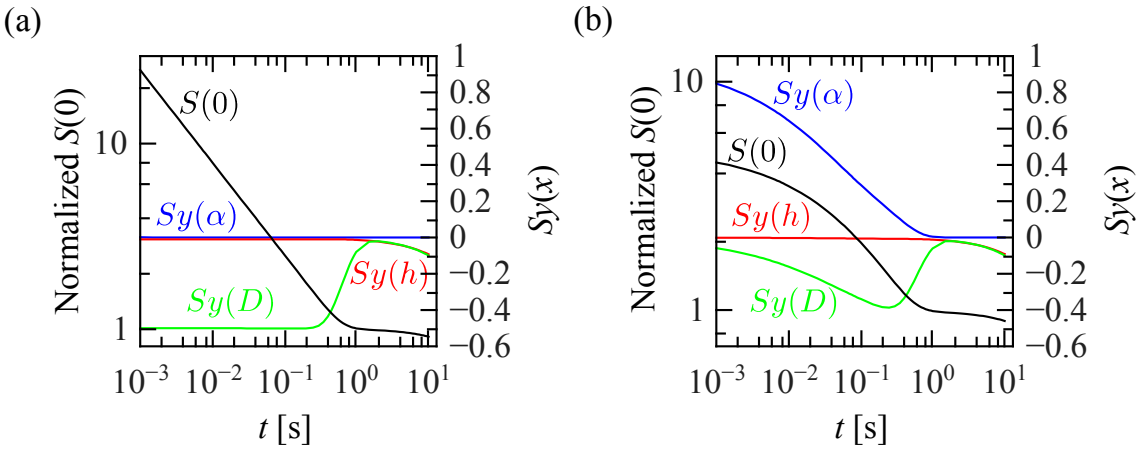

Figure 3.3: Normalized IR signal from the front surface and sensitivity for a glass plate ($D = 0.5$ mm^{2}s^{-1}, $K = 1$ Wm^{-1}K^{-1}, $L = 1$ mm, $h = 10$ Wm^{-2}K^{-1}) illuminated by a delta function pulse. (a) Opaque sample ($\alpha = 103$ mm^{-1}) and (b) semitransparent sample ($\alpha = 5$ mm^{-1}).

3.4 Experimental details and results

In order to validate the proposed generalization of the front-face flash method to measure the thermal diffusivity of semitransparent plates we have performed measurements on samples with different thermal and optical properties: glasses, cardboards and metallic oxides.

The diagram of the experimental set-up used for studying the samples is shown in Figure 2.1a of Chapter 2. In order to prevent lateral heat diffusion, the laser beam is defocused for the spot to reach a diameter of about 2 cm at the sample surface. We record images at a frame rate varying from 1 to 2 kHz, according to the relation $t_1 = L^2/(\pi D)$. The thermograms have been recorded in the quarter windowing mode (64×64 pixels) in order to reach those high frame rates in our camera. It is worth to keep in mind that the temperature detected by our IR camera is not the real surface temperature rise of the sample, since neither its emissivity nor its IR transparency is known. However, the "apparent" temperature rise ΔT measured by the IR detectors is proportional to the IR emission $S(0)$ exiting the sample front surface.

We have performed measurements of the temperature rise as a function of time,

using the Altair software bought from FLIR Systems. The noise level has been reduced down to 10 mK by averaging the temperature over 1200 pixels in the thermograms.

Figure 3.4 shows the results obtained by testing several materials. We have represented the experimental measurements by dots and their corresponding curve fits by continuous lines. A least square fitting procedure has been implemented using the well known Levenberg-Marquardt algorithm [26–28] and the fits have been done with respect to the inverse Laplace transform of Equation 3.10. Five free parameters have been used in the fits: Q_0/K, $L/\sqrt{D}$, αL, βL and h/K.

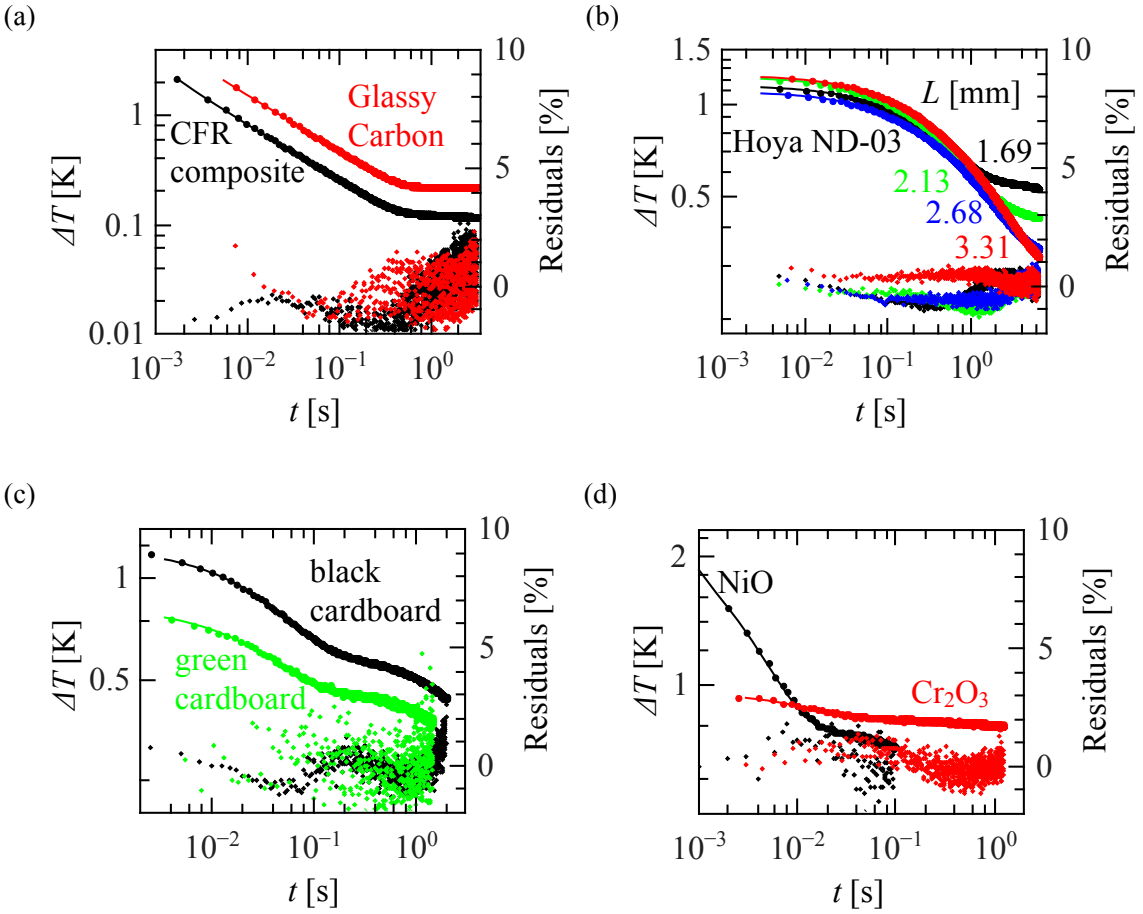

Figure 3.4: Apparent temperature rise above the ambient as a function of time after the heating pulse for different materials. Dots are the experimental data and continuous lines the fit to the theory. (a) Opaque samples. (b) Neutral density filters (ND-03) with several thicknesses. (c) Colored cardboards. (d) Black semitransparent metallic oxides. Residuals are also plotted to visualize the quality of the fits.

Moreover, the finite duration of the laser pulse has been taken into account in the fitting procedure. In order to evaluate the quality of the fits, we have included the residuals in the plots, i.e., the normalized difference between experimental data and fitted values, $(T_{exp} - T_{fit})/T_{exp} \times 100$. They are lower than $2\,\%$ in the whole time range, for all samples. The retrieved quantities of interest are summarized in Table 3.1. Finally, it is important to say that in Figures 3.4a and 3.4d we have plotted only one point of each two measured ones for clarity in the presentation of the fits, while only one point of each ten measured ones have been plotted in Figures 3.4b and 3.4c. However, all points have been included in the fits of all measurements.

In order to calibrate the experimental set-up we have taken data on several opaque plates: glassy carbon, lead (Pb) and carbon fiber reinforced (CFR) composite. The results obtained for two of them are shown in Figure 3.4a. Notice that, at short times the predicted linear behavior with slope $-1/2$ is obtained, while at long times the horizontal straight line is obtained for glassy carbon (intermediate thermal conductor), but the composite (poor thermal conductor) is affected by heat losses. The retrieved thermal diffusivity values are close to the literature values for these materials, confirming the appropriate design and calibration of the experimental set-up.

In order to test the robustness of the method on semitransparent specimens, we have studied four glass plates of the same neutral density filter (ND-03) with different thicknesses: 1.69 mm, 2.13 mm, 2.86 mm and 3.31 mm. The "apparent" temperature rise above the ambient for each of them is shown in Figure 3.4b. Thermal diffusivities fall in the range $D = 0.49 - 0.51$ mm^{2}s^{-1} which is within the uncertainty obtained with the classical flash method [56]. For the optical absorption coefficients, we have obtained the following ranges: $\alpha = 1.21 - 1.39$ mm^{-1} and $\beta = 6.50 - 7.48$ mm^{-1}. The retrieved values for the optical absorption coefficient (α) are close to the value $\alpha = 1.35$ mm^{-1} obtained using a commercial spectrometer at $\lambda = 1053$ nm on the same samples.

In Figure 3.4c the results for two colored cardboards are shown. The retrieved values of D, α and β are summarized in Table 3.1. It is worth mentioning that in these materials there is not only light absorption but light scattering as well. Accordingly, the

Beer-Lambert law does not hold. This means that the retrieved optical absorption coefficient (α) is an effective value combining both absorption and scattering processes inside the material. Note that although a more complete model including light propagation in turbid media should be used [66,67] the obtained thermal diffusivity value is in good agreement with the literature values.

Table 3.1: Thermal diffusivity (D), optical absorption coefficient (α), and IR absorption coefficient (β) of the materials measured in this work. Uncertainty in D is in the range $3\,\% - 6\,\%$ and in α it remains in the range $4\,\% - 8\,\%$.

Material	L [mm]	D, this work [mm^2s^{-1}]	D, literature [a] [mm^2s^{-1}]	α, this work [mm^{-1}]	α, spectrometer [mm^{-1}]	β this work [mm^{-1}]
Pb	2.591	25.4	24.3	---	∞	∞
Glassy carbon	2.935	5.9	6.0	---	∞	∞
CFR composite	0.863	0.57	0.50	---	∞	∞
ND-03 filter	3.31	0.50	0.50–0.60	1.4	1.35	6.5
ND-03 filter	2.86	0.51	0.50–0.60	1.2	1.35	7.7
ND-03 filter	2.13	0.49	0.50–0.60	1.4	1.35	7.7
ND-03 filter	1.69	0.51	0.50–0.60	1.2	1.35	7.5
Black cardboard	0.276	0.14	0.14	8.7	---	2.9
Green cardboard	0.237	0.14	0.14	7.8	---	2.8
NiO	0.643	9.5	8.8	11	11.3	7.4
Cr_2O_3	0.762	3.9	3.2-3.8	5.9	5.94	0.68

[a] References [8,29,31–35].

Finally, in Figure 3.4d we show the experimental results for two metallic oxides: nickel oxide (NiO) and chromium oxide (Cr_2O_3) that are completely black. According to their visual aspect an accurate value of the thermal diffusivity might be expected using the simplified model for opaque samples [35]. However, the departure from the $-1/2$ slope at early times ($t < t_1$) after the heating pulse indicates that these materials are

semitransparent to the heating laser and/or at IR wavelengths. Note that for Cr_2O_3 the temperature evolution is quite flat indicating that the sample is very transparent. Accordingly, the sensitivity to D is small. Anyway, the retrieved value is close to those found in the literature [68,69]. The results of the fits for both oxides are shown in Table 3.1. It is worth mentioning that both thermal diffusivity values are slightly higher than previously reported in the literature [31–33]. One possible reason for this discrepancy is that the samples used in this work are high quality single crystals that improve the heat conduction. As was discussed at the end of Section 3.3, the sensitivity of the normalized temperature to D and α depends on the transparency of the sample. Accordingly, it is not possible to give a unique uncertainty value for all types of samples. Regarding the uncertainty in D, it varies from $3\,\%$ for opaque samples to $6\,\%$ for the most transparent samples we have studied ($\alpha \approx 1$ mm^{-1}). On the contrary, the uncertainty in α is around $8\,\%$ for quite opaque samples ($\alpha \approx 8$ mm^{-1}) but it drops down
to $4\,\%$ for quite transparent samples. In the limit, if the sample is completely transparent to the exciting laser or to IR wavelengths, no information on the thermo-optical properties of the sample can be retrieved.

3.5 Discussion

The main interest of this methodology is to perform straightforward and fast measurements of the thermal diffusivity on semitransparent samples, i.e., without covering the sample with an opaque coating. As by-products, the optical absorption coefficient at the exciting wavelength as well as an effective IR absorption coefficient (3 to 5 μm) are also obtained, which serve to test the reliability of the method. Multiple reflections of the heating light pulse, heat losses by convection and radiation, transparency to infrared wavelengths and the pulse duration have been included in the model. Moreover, in contrast with modulated measurements, which take about 1 hour, pulsed measurements take just a few seconds, as shown in Figure 3.4. Measurements on calibrated samples confirm the validity of the front-face flash method to study the

thermal diffusivity of semitransparent slabs without any coating.

It is important to say that this method is completely applicable for studying the thermal diffusivity and both optical absorption coefficients, simultaneously, as long as one of the "attenuation coefficients" of the specimen satisfies [49]: $0.5 < \alpha L < 20$ or $0.5 < \beta L < 20$. However, if one of the optical absorption coefficients is such that the corresponding attenuation coefficient of the sample is below the lower limit, then the sample is called "transparent" and it would be difficult to determine its thermo-optical properties by the presented method, because the thermographic signal will be drastically reduced due to the transparency. Moreover, when the specimen is transparent to both absorption coefficients, we will not be able to study its thermo-optical properties, because the thermographic signal will be null, for example, germanium or quartz.

On the other hand, when the attenuation coefficient of the specimen is higher than the upper limit, the sample will behave as optically opaque. In this case, the thermographic signal would be maximum according to numerical simulations (see Figures 3.2a and 3.2c). However, it does not mean that we will be capable to study any opaque sample without coating, because we have to keep in mind that those numerical simulations shown in Figure 3 have been done considering highly absorbing surfaces (low reflection coefficient). Consequently, in order to determine the thermal diffusivity of metals (opaque specimens), which are known to have shiny surfaces, the best way would be to cover its surface with a thin opaque layer, for example, a thin graphite layer. Nevertheless, for the lead (Pb) specimen studied in this work, the absorption of its surface was high enough to give a good thermographic signal. Finally, the lower and upper limits established for the attenuation coefficients are not sharp values, but their purpose is only to serve as guidelines for select the thickness of a given sample, whose optical absorption coefficient is already known or an estimation is provided, in such a way that the specimen behaves as semitransparent.

When the condition of one dimensional heat conduction is not satisfied, additional effects will be present in the thermographic signal, such as lateral heat diffusion. Accordingly, in order to assure one dimensional heat transfer during the

measurements, the size of the samples has been taken into account when selecting the laser beam diameter. For small samples, such as NiO and Cr_2O_3, a focusing lens has been used instead of the diffuser shown in Figure 2.1 of Chapter 2. However, for most samples studied in this work, the diffuser has been very useful to generate plane illumination similar to that of a flash lamp.

Chapter 4. Studying the thermal transport properties of polymeric nanocomposites with the front-face flash method

4.1 Thermal properties enhancement of polymeric nanocomposites

During the last decades, research on the improvement of the thermal conductivity of polymer composites has been a topic of great interest and has generated a variety of studies using diverse techniques [73,74]. The aim of these works has been to develop composites which could be lightweight, corrosion resistant and at the same time having acceptable mechanical resistance. In addition the cost of manufacturing should be low, which could make them a competitive option to metallic components [1–4]. These materials are of great interest in the development of microelectronic heat sinks, heat exchangers, electric motor parts, aerospace industry applications, among many others. However, polymeric materials are not generally good heat conductors. This can be modified by orienting the polymer nano and microstructure [77] or by adding high conductivity particles to the polymer [78]. Both approaches have generated interesting results having a great variety of applications [73,79]. Carbon derived fillers such as graphite, carbon nanotubes (CNT), diamond nanoparticles, carbon black, carbon nanofibers (CNF) or graphene flakes are among the most promising fillers, given the

outstanding thermal properties of those materials.

Composites developed on polymeric matrices, using up to $0.4\,\%$ in volume of multi walled carbon nanotubes (MWCNTs) as fillers, showing improvements up to $105\,\%$ on the thermal conductivity with respect to the polymeric matrix have been reported [74,80]. In the case of composite polymers with CNF loadings of $2\,\%$ in weight, a thermal conductivity enhancement of about $115\,\%$ has been found. It has also been reported, in the literature, that larger enhancements of the thermal conductivity can be reached (as high as $200\,\%$) in CNF-polymer composites, but at the expense of an extremely high concentration of CNF ($40\,\%$ in volume) [1,2,9–12]. The variability found in the literature for thermal conductivity of polymeric composites with carbon-based fillers can be understood taking into account that heat transport is strongly dependent on the coupling of the matrix with the filler as well as its dispersion and distribution.

A large variety of methodologies to get high thermal conductivity composites has been focused on minimizing the thermal resistance among the matrix-filler and filler-filler interactions, in reducing internal stresses, gaseous products and induced porosity, as well as optimizing surface wettability, among others. Additionally, sedimentation during the curing process has been a great concern, which can be overcome in several cases by ultrasonic treatments [74,82].

In all cases, it is important to develop methods to increase the thermal conductivity of a given composite, in which the filler content must be maintained below well-defined values even when the main characteristics of the filler interactions with themselves and with the matrix cannot be controlled to sufficient extent. One of those methods, as mentioned above, consists in orienting individual polymeric units or fillers. This option has provided promising results in the enhancement of thermal conductivity [77]. In this chapter, the possibility to improve the thermal conductivity of a polymer, using both mechanisms discussed above, filling the matrix with high conductivity carbon-derived particles and also orienting them is presented. Alignment of this kind of fillers have been achieved using different techniques, such as mechanical stretching,

external electric field, among others. It has been shown that enhancements as high as 4 times the thermal conductivity of aligned CNT composites with respect to non-aligned CNT composites could be reached [80]. In the case of composites with aligned carbon nanofibers, heat transfer has also been studied; however, taking into account that CNF can become easily entangled or broken (diminishing their effective aspect ratio) during the preparation of the composite, additional studies are necessary to determine the key factors required to maximize heat conduction in those systems [83,85,86].

One of the most interesting and simple methods to align particles, without their migration, consists in applying magnetic fields. However, carbon nanofibers do not have a large magnetic moment. Due to this, very strong magnetic fields would be needed to achieve alignment in this kind of fibers. For this reason, in this work we use a method by which nanoparticles of iron are attached to the fibers (*m*-CNF) and as a consequence, when applying a DC magnetic field of low intensity the nanofibers can be aligned along the field.

In order to measure the thermal diffusivity and thermal effusivity of the composite samples and to determine their thermal conductivity in the direction along the oriented fibers, the non-invasive and non-contact technique known as front-face laser flash method was used. This technique consists in heating up the sample's surface with a brief light pulse and record the temperature evolution of the heated surface with an infrared (IR) detector or IR camera. Nowadays, this technique has gained interest of scientists and engineers for its versatility in non-destructive testing of materials, since it only requires access to one surface of the component to be analyzed [35,55], as explained in previous chapters. In this chapter, several concentrations of *m*-CNF have been studied, varying from 0.25 to 3.25 % *m*-CNF in a polyester resin matrix. Each concentration has been prepared in two configurations: non-aligned and aligned *m*-CNF (through the thickness of the samples). Scanning electron microscopy (SEM) has also been used to obtain images of the alignment of the *m*-CNF in the polyester matrix.

Several methodologies have been developed to interpret the effective thermal conductivity in composite systems. In some models, based on the effective medium approach (EMA), it has been assumed that the interaction between the reinforcements

can be neglected, which has provided good agreement with experimental data in the dilute limit (up to 1 % volume for CNT composites) [17–19]. In recent decades, many authors have developed more elaborate models, including additional effects such as thermal resistance at the interface between the matrix and the filler, the effect of coated reinforcements, the role of different geometries of the filler (aspect ratio), the effective conduction path through the reinforcements and phonon heat transport [20–24]. Moreover, in the last years there has been a growing interest in modeling the interaction between the reinforcements of the composite materials [25–27]. This has been done because in many applications high concentration of filler is required, which makes it necessary to take into account the interaction between the fillers in the model. However, in the case of polymeric composites based on CNT or CNF, the interaction between the filler appears at low loading percentages (about 2 % in volume). In those cases, an alternative approach has been proposed, based on the interaction direct derivative (IDD) approach, which includes a second order correction to the effective properties as a function of the filler concentration [28–30]. This model provides explicit analytical expressions for the effective properties, involving simple physical parameters. In this chapter, the IDD model is used to analyze our results for the thermal conductivity of the *m*-CNF composites, and to explore the role and importance of orientation, thermal interface resistance and the effective size of the fibers.

4.2 Preparation of Polyester resin with *m*-CNFs

Carbon Nanofibers (Pyrograf CNF PR-19-XT-HHT) with nominal diameters of 100 – 200 nm and nominal lengths of 30 – 100 μm, have been used for preparing the composites. Magnetic particles were obtained from a ferrofluid (Ferrotec EMG900), which consists of iron nanoparticles with mean size of 10 nm and isoparaffin as solvent.

Carbon nanofibers were dispersed in toluene and then this mixture was vacuum filtered through a polyester nucleopore membrane with pore size of 0.1 μm. After that,

the powder was rinsed with alcohol and filtered again by using a similar polyester membrane. Then, the filtrate was rinsed in water and dried. Chemical oxidation of the CNF was carried out with nitric acid as follows: 1.0 g of CNF were pretreated by immersion in a 25 ml solution of 70 % nitric acid and 30 % water using a three-neck flask and the resultant suspension was refluxed during 30 minutes at 130 ºC with slow agitation. Then, the oxidized CNF were filtered and washed with water until the filtrate was neutral.

After drying the CNF, these fibers and the ferrofluid were mixed at 15 % weight fraction. The solvent was evaporated at room temperature and the sample was rinsed with kerosene and filtered until the liquid was clear. After that, the filtrate was rinsed in alcohol. The sample was kept in vials and was allowed to dry. The magnetic response of these magnetic CNF was easily and quickly visualized, by the attraction of the nanofibers when a magnet is brought close to the sample.

Composites of magnetic carbon nanofibers in a polyester resin matrix (RP RESINMEX) were prepared by dispersing the functionalized *m*-CNF in the polyester resin and mixing slowly for 30 min until a bubble-free homogeneous mixture was obtained. Then, the catalyst was added and the mixture was agitated for two minutes. The mixture was poured onto an aluminum foil surface (placed on a glass plate) and it was covered with another aluminum foil and another glass plate on top. The whole system was pressed with tweezers. In order to obtain samples with magnetic aligned CNF, the samples were placed for 15 min in the center of a pair of Helmholtz coils under the influence of a 600 G magnetic field. All samples were allowed to polymerize during 24 hours at room temperature. Finally, the samples were postcured at 80 °C for 4 hours. The specimens obtained were composite plates of 3 cm × 2.5 cm × 1 mm, one set with randomly arranged fibers and the second with fibers aligned along the thickness of the plate (1 mm).

In order to analyze the orientation of the fibers in the polyester matrix, scanning electron microscopy (SEM) images were obtained on small sections of the samples. These sections were cut perpendicularly with respect to the lateral plane faces of the plates. Specimens of 1 mm × 3 mm surface area and 5 mm thickness were embedded

vertically in an epoxy resin cylinder (in such a way that the surface of 3 mm^2 could be analyzed), whose surface was polished and plasma cleaned during 6 min. Finally, the surface of the sample was covered with a 5 nm thick Cr layer using a sputtering unit (Bal-Tec SCD-004). A SEM system (JEOL JSM-6400) was used to perform the analysis.

4.3 Measurement of thermal diffusivity and relative thermal effusivity by the front-face flash method

The front-face flash method consists of heating up one surface of a slab using a uniform source during a short time interval. The temperature evolution of the heated surface is analyzed to retrieve the thermal diffusivity or thermal effusivity of the material (see Chapters 1 and 2). In Figure 4.1 we show a slab of thickness L, heated up by a uniform pulse of time duration τ. The heat diffusion equation for this problem, with the appropriate boundary conditions, is easy to solve in the Laplace domain and it has analytical solution [101]. Otherwise, it can be deduced from Equation (3.7) of Chapter 3 by taking the limit when the slab is opaque ($\alpha \to \infty$), which leads to:

$$E_0 = e^{-qL}(q-h')^2 - e^{qL}(q+h')^2, \tag{4.1a}$$

$$\frac{CA_0}{E_0} \to -\frac{\bar{I}_0(1-R)e^{-qL}(q-h')}{2KE_0}, \tag{4.1b}$$

$$\frac{CB_0}{E_0} \to -\frac{\bar{I}_0(1-R)e^{qL}(q+h')}{2KE_0}, \tag{4.1c}$$

$$Ce^{-\alpha z} \to 0,\ 0 \le z \le L, \tag{4.1d}$$

$$E \to 0. \tag{4.1e}$$

Substituting these expressions into Equation (3.7) and evaluating at the front surface of the slab ($z = 0$), we obtain:

$$\bar{T}(s) = \frac{\bar{I}_0(1-R)}{\epsilon} \frac{\sqrt{s} + h_r \tanh(qL)}{2h_r\sqrt{s} + (s+h_r^2)\tanh(qL)}, \tag{4.2}$$

where s is the Laplace variable, $q = \sqrt{s/D}$, $h' = h/K$ and $h_r = h/\epsilon$; being K, ϵ and D

D the thermal conductivity, thermal effusivity and thermal diffusivity of the sample, respectively. h is the heat transfer coefficient which takes into account the heat losses from both surfaces to the surroundings due to convection and radiation. $\bar{I}_0$ is the Laplace transform of the light intensity (Wm^{-2}) and takes into account the temporal shape of the pulse, which in the case of a step-like pulse of duration τ is given by $\bar{I}_0 = Q_0 \frac{1-e^{-s\tau}}{s}$, where Q_0 is the energy per unit area of the light step. The value of the reflection coefficient R has been set to 0.05, as in Chapter 3. We have used the well known Stehfest algorithm [60] to obtain the numerical inverse Laplace transform of Equation (4.2), which gives the evolution of the slab's front-face temperature $T(t)$.

Numerical simulations have been performed to show the influence of the thermal diffusivity and thermal effusivity on the surface temperature evolution. Figure 4.2a shows the time evolution of the temperature corresponding to two materials with the same thermal effusivity $\epsilon = 580$ $Ws^{1/2}m^{-2}K^{-1}$, but different thermal diffusivities: $D = 0.11$ mm^2s^{-1} (in black) and $D = 0.28$ mm^2s^{-1} (in red). Both materials have the same thickness $L = 1.0$ mm and are heated up by a step pulse of 5 Wcm^{-2} during $\tau = 30$ ms. Also, a typical value for heat losses at room temperature has been considered ($h = 10$ $Wm^{-2}K^{-1}$) in the simulations.

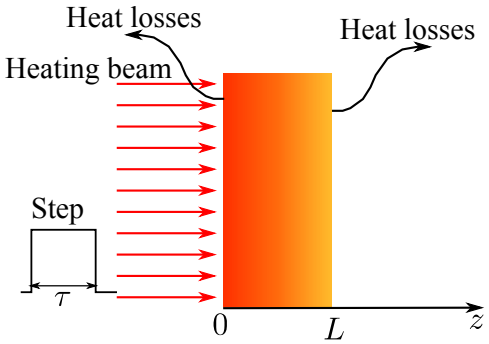

Figure 4.1: Plane slab illuminated by a uniform brief step of duration τ. Heat losses by convection and radiation are taken into account in the model.

Notice that, for early times there is a temperature rise due to the step heating. The maximum temperature at the end of the step duration is the same for both simulations because the materials considered have the same thermal effusivities. During

the cooling of the samples, a linear decline of the temperature occurs on the times for which the slab behaves as a semi-infinite wall. However, when the heat reaches the rear surface of the slab, the slope of the temperature drastically changes, in such a way that the "elbow" that indicates the transition between both regimes is directly related to the thermal diffusivity of the sample. Notice that the heat will reach the back surface of the slab earlier for materials with higher thermal diffusivity than for materials with lower thermal diffusivity, provided that both slabs have the same thickness. This behavior can be observed in Figure 4.2a, in which the time evolution of the temperature of two materials with different thermal diffusivities is compared. The red line corresponds to the time evolution of the temperature for a material with higher thermal diffusivity than the one represented by the black line.

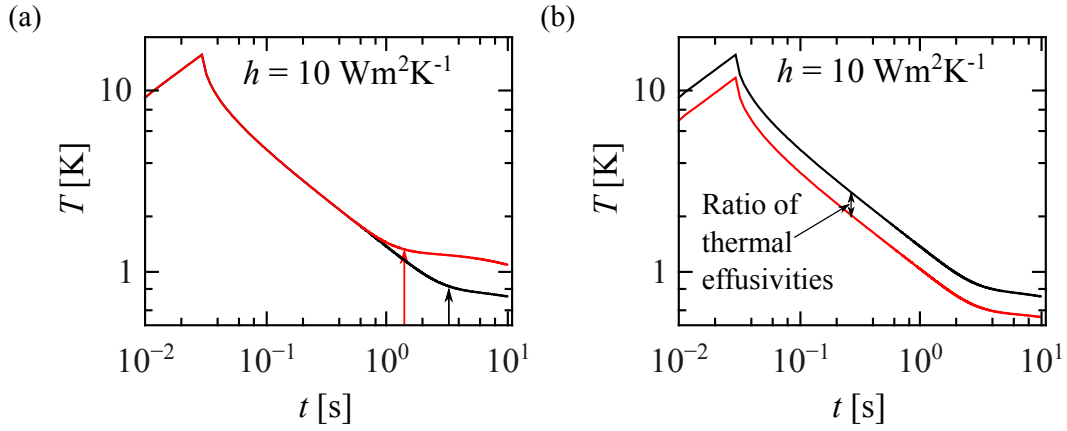

Figure 4.2: Numerical simulations of the temperature evolution on the front surface of the slab illuminated by a light step of 30 ms. (a) Two materials with the same thermal effusivity and different thermal diffusivities have been considered. (b) Two materials with the same thermal diffusivity and different thermal effusivities have been considered. The effect of heat losses by convective and radiative mechanisms is included. The value of the ratio of effusivities is indicated with a double arrow in the linear region.

The arrow on the left indicates that the time at which the heat flux reaches the rear surface in the red curve is shorter than the time at which the back surface of the black curve is reached, as shown by the arrow on the right. Therefore, it can be inferred that a difference in thermal diffusivities introduces a horizontal shift in the 'elbow' of the

time evolution of the temperature.

According to these simulations, a curve fitting of the experimental data is used in order to retrieve the thermal diffusivity of the samples. Three free parameters are used in the curve fittings: $Q' = \frac{Q_0}{\epsilon}$, which takes into account the light pulse duration; $h_r = \frac{h}{\epsilon}$ to consider the heat losses and $x = \frac{L}{\sqrt{D}}$ to retrieve the thermal diffusivity.

On the other hand, Figure 4.2b shows numerical simulations for two materials of the same thermal diffusivity $D = 0.11$ mm^{2}s^{-1}, but different thermal effusivities $\epsilon = 780$ Ws$^{1/2}$m^{-2}K^{-1} (in red) and $\epsilon = 580$ Ws$^{1/2}$m^{-2}K^{-1} (in black). We have used the same thickness, power density, pulse duration and heat losses coefficient as in Figure 4.2a: L = 1 mm, $I_0 = 5$ Wcm^{-2}, $\tau = 30$ ms and $h = 10$ Wm^{-2}K^{-1}. As can be seen, in this case, a difference on thermal effusivities introduces a vertical shift on the temperature evolution graphs. Notice that the temperature rise of the material with higher thermal effusivity (red curve) is always smaller than that of the slab with lower thermal effusivity (black curve). This vertical shift, measured in the semi-infinite zone of the time evolution graph, gives the ratio of the thermal effusivities, when the same energy has been deposited on both slabs. Accordingly, the thermal effusivity of the samples can be obtained by comparison with a reference value.

4.4 Experimental details and results

A diagram of the experimental setup used to study the thermal properties of our composite samples is shown in Figure 2.5 of Chapter 2. Since the emissivity of the samples is unknown, the IR camera only collects data of an apparent temperature rise (ΔT) which is proportional to the actual temperature.

We have performed measurements on a collection of samples, which consists of polyester resin composites loaded with non-aligned *m*-CNFs and composites loaded with aligned *m*-CNFs. For both kinds of composites, concentrations ranging from 0.25 $\%$ $3.25\,\%$ $0.25\,\%$

% to 3.25 % increasing in steps of 0.25 % in volume have been studied. In Figure 4.3, the time evolution graphs obtained from the measurements are presented. The experimental data are represented by dots and continuous lines are used for the curve fits to the model presented in Equation (4.2), in the time domain. The samples correspond to: polyester resin ($D = 0.102$ mm^{2}s^{-1} and $\epsilon = 563.6$ Ws$^{1/2}$m^{-2}K^{-1}, in black), composite loaded with 3.25 % of non-aligned *m*-CNF ($D = 0.141$ mm^{2}s^{-1} and $\epsilon = 638.7$ Ws$^{1/2}$m^{-2}K^{-1}, in blue) and composite loaded with 3.25 % aligned *m*-CNF ($D = 0.189$ mm^{2}s^{-1} and $\epsilon = 738.8$ Ws$^{1/2}$m^{-2}K^{-1}, in red). Notice that when the thermal diffusivity of the sample increases, the 'elbow' of the curves appears at shorter times (samples are of the same thickness, $L = 1$ mm) as discussed in Section 4.3. On the other hand, the higher the thermal effusivity, the lower the temperature rise, as clearly seen in the linear zone (semi-infinite behavior). It is worth to mention that even when the same concentration is used, the alignment of the fibers changes both the thermal diffusivity and thermal effusivity as shown by the blue and red curves in Figure 4.3.

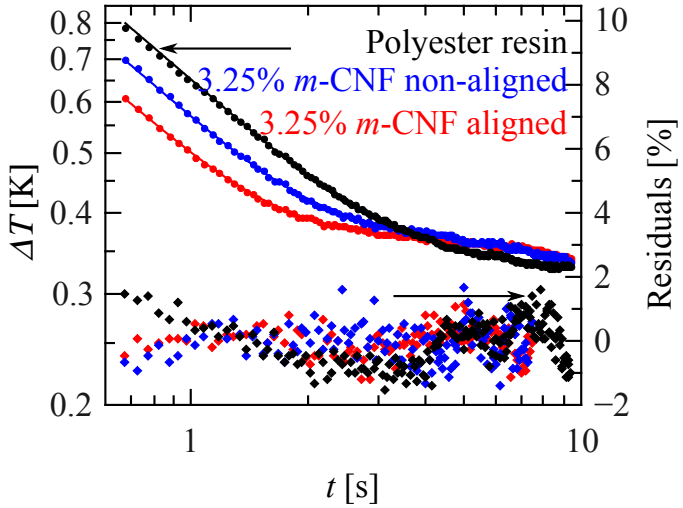

Figure 4.3: Curve fittings (continuous line) of the experimental data (dots) using the numerical inverse Laplace transform of Equation (4.2). The residuals (diamonds) are plotted to show the good agreement between theory and experiment.

A least squares procedure, based on the Levenberg-Marquardt algorithm [63], has been implemented to fit the curve of the experimental data with the inverse Laplace

transform of Equation (4.2). Three parameters (Q', h_r and x) are retrieved from the fits. In order to show the quality of the curve fits, we have also plotted the residuals (diamonds), $(T_{exp} - T_{fit})/T_{exp} \times 100$, whose values are smaller than $2\,\%$ in the whole time evolution graph.

The values obtained for thermal diffusivity are shown in Figure 4.4a as a function of the particle concentration in volume (ϕ). Notice that for aligned *m*-CNF (black) the enhancement on the thermal diffusivity of the composites is higher than for those non-aligned *m*-CNF (red), and this behavior is most remarkable for the highest values of the concentration of particles.

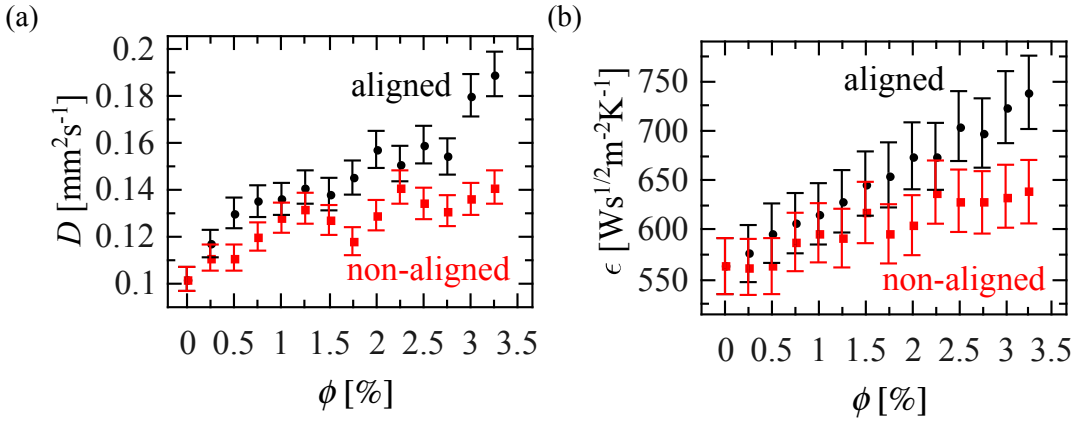

Figure 4.4: Experimental results for the (a) thermal diffusivity and (b) thermal effusivity of the composite samples as a function of the particle concentration in volume (ϕ).

The thermal effusivity of the composite samples has been obtained from the linear zone of the time evolution graphs, since the vertical shift between two fitted lines gives the ratio of thermal effusivities, as shown in Figure 4.2b. In this case we have used the thermal effusivity of the polyester resin ($\epsilon = 545$ $Ws^{1/2}m^{-2}K^{-1}$) as a reference. Notice from Figure 4.4b, that for both kinds of samples, the enhancement on the thermal effusivity of the composites is almost linear, and is better for the aligned *m*-CNF (black) than for non-aligned *m*-CNF (red), as obtained for the thermal diffusivity. In both cases, the uncertainty on the measurement of thermal properties has been obtained from the standard deviation of five measurements and is below $\pm 5\,\%$.

4.5 Effective thermal conductivity models for nanocomposites

In order to verify the alignment of the *m*-CNF in the polyester matrix, we have performed SEM analysis as described in Section 4.2. Figure 4.5 shows the results obtained for concentrations of 0.25 %, 1.25 %, 2.25 % and 3.25 % with non-aligned nanofibers from (a) to (d), respectively and the same concentrations with aligned *m*-CNF, from (e) to (h). Also schematic pictures of the dispersed and aligned nanofibers on the sample's thickness are shown in Figures 4.5a and 4.5e. Backscattered electron images have been used to show even the fibers buried near the surface of the specimens.

It is well known that two thermal properties are needed to characterize (thermally) a given sample, since the three thermal transport properties are related by $\epsilon = K/\sqrt{D}$, where ϵ is the thermal effusivity, D and K are the thermal diffusivity and thermal conductivity, respectively [18].

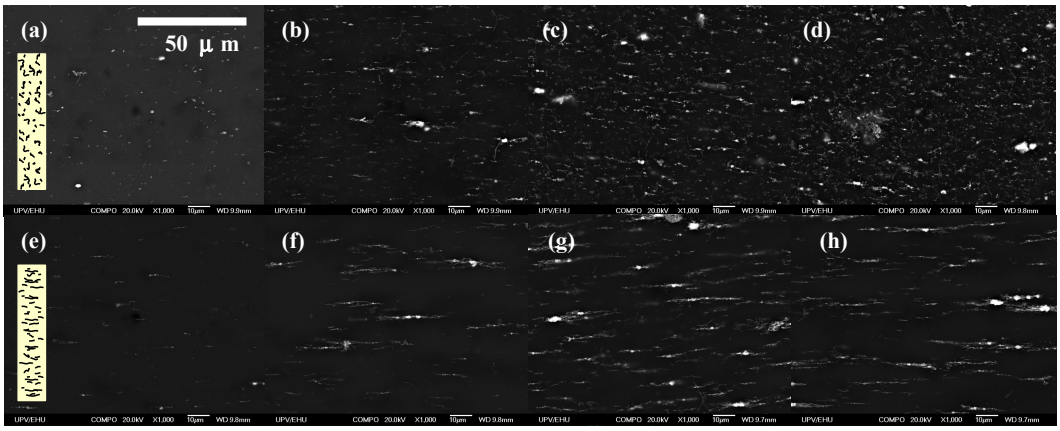

Figure 4.5: SEM images of *m*-CNF on polyester resin. Concentrations of $0.25\,\%$, $1.25\,\%$, $2.25\,\%$ and $3.25\,\%$ for non-aligned (upper row) and aligned (lower row) fibers are shown.

In Figure 4.6 the thermal conductivity obtained from the experimental data of the composites is shown as a function of the *m*-CNF concentration; the uncertainties were obtained according to the error propagation theory [102]. Good enhancement of K is expected, due to the higher thermal conductivity of the carbon nanofibers with respect to that of the polymeric matrix. The enhancement in thermal conductivity is noticeable

for concentrations higher than $1\,\%$ in volume, in which a clear difference between the results obtained for the composites with aligned *m*-CNF and the non-aligned ones is observed. The thermal conductivity of the composite loaded with $3.25\,\%$ of aligned *m*-CNF in volume is 1.8 times the one of the polyester resin. This is a good result considering the low loading percentage of nanofillers. In contrast, thermal conductivity of the composite only reaches 1.2 times for non-aligned nanofibers with respect to the resin matrix. In summary, a remarkable enhancement of the thermal transport properties due to the alignment of magnetized nanofibers has been obtained for polyester-based nanocomposites.

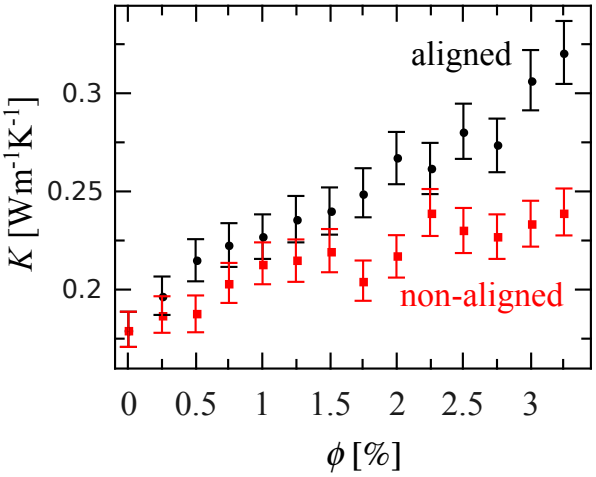

Figure 4.6: Thermal conductivity of the composites samples as a function of the particle concentration in volume.

In order to interpret the results of the enhancement obtained in the thermal conductivity of the polyester resin composites, we have used a theoretical model based on the interaction direct derivative (IDD) micro-mechanics scheme, proposed in the last decades for modeling effective properties of composite systems. This model has the versatility of considering the interaction between the reinforcements, thus it can provide a good approximation of the effective properties up to second order in the filler concentration $o(\phi^2)$. According to this model, the normalized effective thermal conductivity (K_{norm}) of the composite with respect to the thermal conductivity of the matrix can be expressed as [96,100]

$$K_{norm} = 1 + \left[1 - \frac{1}{3}(K_{dlim} - 1)\right]^{-1} (K_{dlim} - 1), \tag{4.3}$$

where K_{dlim} is the effective thermal conductivity in the dilute limit, also normalized by the thermal conductivity of the matrix (K_m). A good choice of the thermal conductivity in the dilute limit is the one obtained from the well-known effective medium approach [90],

$$K_{dlim} = 1 + \frac{\eta\phi\xi}{\frac{K_m\left(1+\frac{2R_{th}K_p}{\eta L}\right)}{\eta K_p} + H(p)}, \tag{4.4}$$

where ϕ is the volumetric fraction of the reinforcements, *m*-CNF in our case, R_{th} is the thermal resistance between the *m*-CNF and the polyester matrix, K_p is the thermal conductivity of the *m*-CNF, ξ is a factor which takes into account if the reinforcements are dispersed in the matrix ($\xi = 1/3$) or they are aligned along the sample's thickness ($\xi = 1$) and $H(p)$ is a function which takes into account the depolarization factor (aspect ratio of the fillers),

$$H(p) = \frac{1}{p^2 - 1}\left[\frac{p}{\sqrt{p^2 - 1}} \ln\left(p + \sqrt{p^2 - 1}\right) - 1\right], \tag{4.5}$$

being $p = \eta l/d$, d is the diameter of the *m*-CNF and η is a correction factor introduced in the actual length (l) of the *m*-CNF due to entanglement effects. It takes into account the non-straightness of the fibers, which affects the thermal conductivity of a fiber in the longitudinal direction, thus affecting the thermal conductivity of the composite [96].

We have performed curve fits of the experimental data using Equation (4.3) with two free parameters (R_{th} and η), as shown in Figure 4.7. The thermal conductivity of the *m*-CNF is 1950 $Wm^{-1}K^{-1}$ [103], and for the polyester resin it is 0.18 $Wm^{-1}K^{-1}$ [104]. Based on the scanning electronic microscopy images taken for the samples, the length of the fibers has been fixed to 30 μm and their diameter to 200 nm in the curve fits. For non-aligned *m*-CNF composites (in red), we have obtained: $R_{th} = 4.6 \times 10^{-8}$ $W^{-1}m^2K$ and $\eta = 0.28$; similarly, for aligned *m*-CNF composites (in black): $R_{th} = 7.5 \times 10^{-8}$ $W^{-1}m^2K$ and $\eta = 0.27$. The results obtained for the thermal mismatch are in good

agreement with theoretical simulations and experimental studies reported in the literature [74,95]. It is worth mentioning that even though the value obtained for the thermal mismatch for aligned fibers is larger than for non-aligned fibers, and that the correction factor η is similar for both types of samples, the thermal conductivity of composites with $3.25\,\%$ volume fraction of aligned *m*-CNFs is 1.4 times the thermal conductivity of composites with non-aligned fibers.

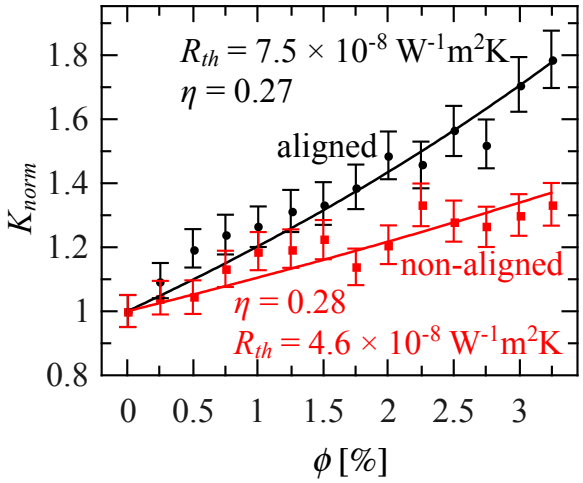

Figure 4.7: Fits of the experimental data results of the normalized thermal conductivity using the theoretical model based on the IDD.

Our results show that the alignment of *m*-CNF in polymeric composites, using external low intensity uniform magnetic fields, is a highly convenient methodology to enhance the heat transport in a given CNF composite. It is especially important to remark that when comparing the increase in thermal conductivity between composites with aligned and non-aligned fibers, twice the amount of fibers is needed to reach the same value of thermal conductivity with non-aligned than with aligned fibers. The proportion of the fibers needed to attain the same thermal conductivity is not the same for all concentrations, but it reduces for higher CNF concentration, as can be seen in Figure 4.7. This behavior agrees with previous results reported in literature [83].

4.6 Summary

The effect in the heat transfer of aligned and non-aligned carbon nanofibers used as fillers in polyester resin has been investigated. It has been shown that the alignment of *m*-CNF in the polymer matrix enhances its thermal conductivity, along the direction of the alignment of the fibers, favoring the use of low concentrations of filler loadings. Accordingly, for a concentration of $3.25\,\%$ in volume, an improvement of $80\,\%$ in the thermal conductivity of the polyester resin was achieved by orienting the *m*-CNF, while only an increase of $20\,\%$ for samples with non-oriented carbon nanofibers was obtained. It was shown that the laser flash method, in the front-face configuration, provides fast, accurate and non-contact measurements of the in-depth thermal diffusivity and thermal effusivity of the composite samples with different concentrations of CNF. A model based on the interaction direct derivative (IDD) scheme has been useful to study the thermal mismatch between the fibers and the polyester matrix. This analysis showed that the thermal interface resistance is larger in samples with aligned carbon nanofibers, and even under these conditions those samples show a higher thermal conductivity than samples with non-oriented fibers. In conclusion, the alignment of *m*-CNF, with the help of a uniform low intensity magnetic field, has shown to be an effective methodology in the enhancement of the in-depth thermal conductivity of polyester nanocomposites. However, more theoretical and experimental research should be done to devise methods to reduce the thermal interface resistance in polymers with oriented *m*-CNF. Additionally a broader range of particles concentrations and intensity of magnetic fields should be analyzed in order to develop a methodology to determine the optimal conditions to maximize the thermal conductivity of a given polymer.

Chapter 5. A two layer system for simultaneous measurement of the thermal transport properties in solids using the front-face flash method

5.1 Thermal transport properties of solids and the flash method

There are two thermal transport properties which characterize a given material: its thermal diffusivity (D) and its thermal effusivity (ϵ) [105,106]. Both are related to the more often acknowledged thermal conductivity (K) through the following relationship: $\epsilon = K/\sqrt{D}$. While steady-state methods are used to measure thermal conductivity, transient methods are sensitive to the couple D and ϵ. In particular, the flash method has become a standard to measure the thermal diffusivity of solids. It consists of heating the front face of an opaque plate by a brief light pulse and analyzing the temperature evolution either at its rear surface, i.e. the classical configuration introduced by Parker et al more than fifty years ago [34], or at the illuminated surface, which is particularly useful for non-destructive testing of materials since it only requires access to the illuminated surface of the sample [35].

However, the flash method applied to free-standing plates only provides the thermal diffusivity, but in most cases fails to give accurate values of the thermal effusivity. The reason for this can be understood by analyzing the temperature history of

the surfaces ($z = 0$ and $z = L$) of an opaque plate of thickness L after being excited by an infinitely brief laser pulse under adiabatic conditions [19]

$$T(0) = \frac{Q_0 \chi}{\epsilon} \frac{\sqrt{D}}{L} \left[1 + 2 \sum_{n=1}^{\infty} \exp\left(-\frac{n^2 \pi^2}{L^2} Dt \right) \right], \tag{5.1a}$$

$$T(L) = \frac{Q_0 \chi}{\epsilon} \frac{\sqrt{D}}{L} \left[1 + 2 \sum_{n=1}^{\infty} (-1)^n \exp\left(-\frac{n^2 \pi^2}{L^2} Dt \right) \right], \tag{5.1b}$$

where Q_0 is the energy per unit area (Jm^{-2}) delivered by the pulse, χ is the energy fraction absorbed by the sample; $T(0)$ and $T(L)$ stand for the temperature at the illuminated and non-illuminated surfaces, respectively. As can be observed, the temperature at each surface depends not only on D and ϵ, but they are correlated with other experimental magnitudes: Q_0 and L. This means that only $Q_0\chi/\epsilon$ and $\sqrt{D}/L$ can be obtained. As the thickness of the sample can be easily measured, the flash method allows retrieval of the thermal diffusivity of the plate. However, the energy fraction absorbed by the sample surface is difficult to determine and therefore the thermal effusivity cannot be obtained accurately. This issue was already pointed out in the pioneering work on the flash method [34] (note that these authors referred to specific heat instead of thermal effusivity, since the multiplying factor in Equations (5.1a) and (5.1b) can be rewritten as $\frac{Q_0 \chi}{\rho c L}$, where ρ is the density and c the specific heat). Since then, several works have been published on retrieving the specific heat using the flash method, but they require an independent measurement of the laser pulse intensity and the reflectivity of the sample at the laser wavelength [6–9], which can be cumbersome in some cases. Alternatively, a relative study of the thermal effusivity on samples with similar reflection coefficient is possible, as shown in Chapter 4.

To overcome the mentioned drawback, putting the rear surface of the plate in contact with a fluid backing has been proposed [45,47]. In this way, the front surface temperature will be sensitive to the thermal mismatch between plate and fluid, which is governed by the ratio of their effusivities. These studies were performed using modulated illumination, registering the amplitude and phase of the surface temperature

as a function of the modulation frequency. Moreover, for normalization purposes (i.e. to eliminate the instrumental frequency dependence) the same frequency scan must be performed twice: with the sample backed by water and with the bare sample. Consequently, this procedure is rather time consuming (around one hour).

Following the idea of using a fluid for thermal effusivity contrast, we propose in this work using the flash method in the front configuration to obtain D and ϵ simultaneously in a fast manner. We have first calculated the front surface temperature of an opaque plate in contact with a fluid after being illuminated by a brief light pulse. The effect of the finite duration of the laser pulse as well as the heat losses by convection and radiation are also included in the model. By studying the sensitivity of the front surface temperature to D and ϵ we show that both quantities are uncorrelated. Then, in order to establish the range of validity of the method we have performed experiments, using a pulsed laser and an infrared (IR) camera, on several calibrated materials (metals, alloys, ceramics and polymers) covering a wide range of thermal transport properties. These experiments show that the thermal effusivity of a sample can be retrieved accurately, provided it is smaller than three times the thermal effusivity of the liquid used as reference.

5.2 One dimensional heat conduction in a two layer system

Let us consider a two-layer system made of an opaque solid slab of thickness L and a semi-infinite fluid backing, as shown in Figure 5.1. The free surface of the plate is illuminated uniformly by a brief laser pulse. The Laplace transform of the temperature rise above the ambient in each medium is

$$\bar{T}_s(z) = Ae^{q_s z} + Be^{-q_s z}, \tag{5.2a}$$

$$\bar{T}_f(z) = Ce^{-q_f (z-L)}, \tag{5.2b}$$

where $\bar{T}$ is the Laplace transform of the temperature, $q = \sqrt{s/D}$, being s the Laplace variable. Subscripts s and f stand for solid and fluid, respectively.

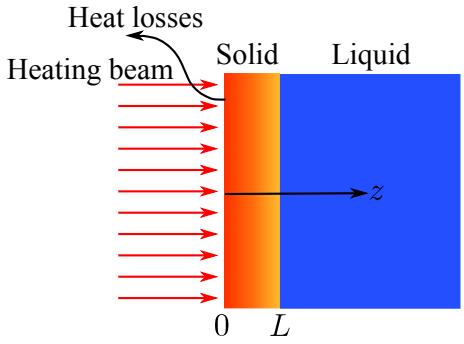

Figure 5.1: Diagram of the two-layer system made of an opaque solid slab and semi-infinite liquid backing. The front surface $(z = 0)$ is uniformly illuminated by a brief laser pulse.

Constants A, B and C are obtained from the boundary conditions at the interfaces

$$K_s \frac{\mathrm{d}\bar{T}_s}{\mathrm{d}z}\bigg|_{z=0} = h\bar{T}_s(z=0) - \bar{I}_0\chi, \tag{5.3a}$$

$$\bar{T}_s(z=L) = \bar{T}_f(z=L), \tag{5.3b}$$

$$K_s \frac{\mathrm{d}\bar{T}_s}{\mathrm{d}z}\bigg|_{z=L} = K_f \frac{\mathrm{d}\bar{T}_f}{\mathrm{d}z}\bigg|_{z=L}, \tag{5.3c}$$

where $\bar{I}_0$ is the Laplace transform of the light intensity, χ is the fraction of energy absorbed by the sample surface and h is the linear coefficient of heat transfer, which takes into account the combined effect of heat convection and radiation. Note that heat transfer by convection at the solid–fluid interface has been neglected since its temperature rise is small. The resulting expression for the Laplace transform of the temperature at the solid surface $(z = 0)$ is

$$\bar{T}_s(0) = \frac{\bar{I}_0\chi}{\epsilon_s\sqrt{s}} \frac{1 + \frac{\epsilon_f}{\epsilon_s}\tanh(q_s L)}{\left(\frac{\epsilon_f}{\epsilon_s} + \frac{h}{\epsilon_s\sqrt{s}}\right) + \left(1 + \frac{h}{\epsilon_s\sqrt{s}}\frac{\epsilon_f}{\epsilon_s}\right)\tanh(q_s L)}. \tag{5.4}$$

In this chapter, we will consider two temporal shapes for the light pulse: (a) a delta function pulse and (b) a laser pulse. In the first case, the light intensity is $I_0(t) = Q_0\delta(t)$ and its Laplace transform is $\bar{I}_0 = Q_0$, where Q_0 is the energy per unit area (Jm^{-2}) delivered by the pulse and $\delta(t)$ is the Dirac delta function. On the other hand,

the light intensity of a laser pulse follows an exponential law of the form $I_0(t) = \frac{Q_0}{N}\frac{t^\gamma}{\tau^{1+\gamma}}e^{-t/\tau}$, whose Laplace transform is $\bar{I}_0 = \frac{Q_0}{(1+s\tau)^{1+\gamma}}$. The parameters γ and τ depend on the pulse shape, while N is a normalization constant which is used to satisfy the condition $\int I_0(t)\mathrm{d}t = Q_0$. The light intensity of our laser pulse fits the exponential law with $\gamma = 1.46$ and $\tau = 0.132$ ms, as shown in Figure 2.4 of Chapter 2.

By applying the inverse Laplace transform to Equation (5.4), the time evolution of the surface temperature above the ambient after absorbing a laser pulse is obtained. However, there is no analytical inverse Laplace transform for the expression in Equation (5.4). Thus, the well-known Stehfest algorithm [60] has been used, which gives very accurate results for 'smooth' functions [111], as in the case of $\bar{T}_s(0)$.

We have written Equation (5.4) in such a way that the degeneracy between parameters is clearly seen. Accordingly, $\bar{T}_s(0)$ depends on four fitting parameters: $Q_0\chi/\epsilon_s$, h/ϵ_s, $L/\sqrt{D_s}$ and ϵ_f/ϵ_s. Therefore, a fit of the time evolution of the front surface of an opaque slab on top of a fluid backing may allow to retrieve simultaneously D_s and ϵ_s, provided the thickness of the slab and the effusivity of the fluid are known. Sensitivity analysis should be performed on the temperature evolution of the front surface of the slab in order to assure that both mentioned parameters can be retrieved from a single fit.

5.3 Sensitivity to thermal diffusivity and thermal effusivity

In Figure 5.2 we present numerical simulations showing the time evolution of the surface temperature $T_s(0)$ of an opaque solid slab with a water backing ($\epsilon_f = 1580$ $\mathrm{Ws^{1/2}m^{-2}K^{-1}}$) illuminated by a brief laser pulse. Ideal conditions are considered: a Dirac pulse $(\tau = 0)$ and absence of heat losses $(h = 0)$. Different values of the thermal effusivity of the solid slab, higher and lower than the thermal effusivity of water, are analyzed. In order to better compare the results, a normalized energy for the laser pulse is used in the simulations $(Q_0\chi/\epsilon_s = 1)$. Moreover, by introducing the dimensionless

time t/t_c, with $t_c = L^2/(4D_s)$, we obtain a normalized temperature $T_s(0)$ which is independent of D_s and L values. As a reference, a simulation for an air backing ($\epsilon_{air} = 5.5$ Ws$^{1/2}$m^{-2}K^{-1}) is also included.

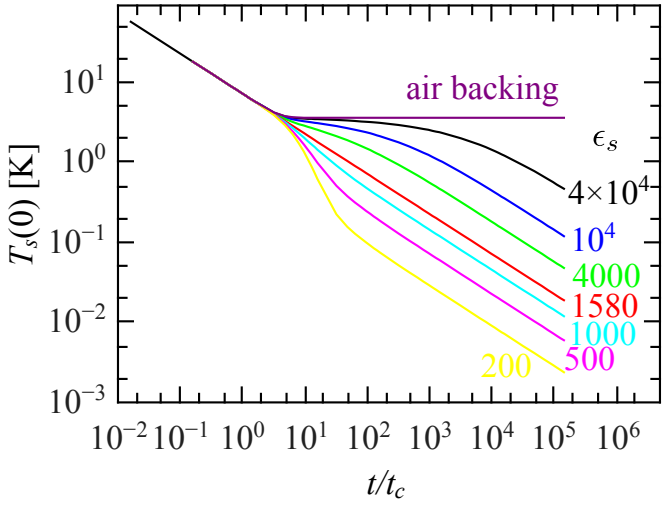

Figure 5.2: Simulation of the surface temperature evolution as a function of the dimensionless time (t/t_c) for an opaque slab on top of water ($\epsilon_f = 1580$ Ws$^{1/2}$m^{-2}K^{-1}) after receiving a brief laser pulse ($Q_0\chi/\epsilon_s = 1$). Ideal conditions are considered: $h = \tau = 0$. Different values of the thermal effusivity of the solid are evaluated. A simulation for air backing ($\epsilon_f = 5.5$ Ws$^{1/2}$m^{-2}K^{-1}) is also plotted for comparison.

As can be seen, at short times after the laser pulse, heat does not reach the rear surface of the solid ($z = L$) and therefore we obtain the response of a semi-infinite sample, which is a straight line with slope -0.5, independently of the thermal effusivities of sample and backing. At longer times, $T_s(0)$ becomes sensitive to the interface between sample and backing. When the backing is air, a horizontal straight line at long times is obtained. In fact, the intersection of both straight lines arises at $t_1 = L^2/(\pi D_s)$, which can be used for thermal diffusivity identification [34]. It is worth mentioning that when the backing is air there is no sensitivity to the thermal effusivity of the sample. When the backing is water the behavior of $T_s(0)$ at very long times is also a straight line of slope -0.5, but the position of this straight line varies depending on the thermal effusivity of the sample. If $\epsilon_s = \epsilon_f$ there is perfect thermal coupling between solid and fluid and accordingly a unique straight line is obtained at

any time. If $\epsilon_s > \epsilon_f$ heat barely crosses the interface at $z = L$ and thermal energy is accumulated inside the solid slab. This explains why the temperature is above the straight -0.5 slope line for $t > t_1$. On the other hand, when $\epsilon_s < \epsilon_f$ heat easily crosses the interface and therefore there is a downwards displacement in temperature with respect to the -0.5 slope line, for $t > t_1$. From a practical point of view, the presence of water in contact with the solid slab may allows us to obtain D_s and ϵ_s, simultaneously from a single measurement. A sensitivity analysis would help us to define under which configurations it is possible to retrieve both parameters with the front-face flash method.

Sensitivity of $T_s(0)$ to a given quantity $x = \{D_s, \epsilon_s\}$ is defined as

$$Sy(x) = \frac{x}{T_s(0)} \frac{\partial T_s(0)}{\partial x}. \tag{5.5}$$

This equation does not have an analytical solution, so numerical methods have been applied to evaluate the local sensitivity of the surface temperature evolution to the thermal diffusivity and thermal effusivity of the solid slab in contact with a semi-infinite liquid layer (water). The sensitivities of $T_s(0)$ to D_s and ϵ_s are shown in Figure 5.3.

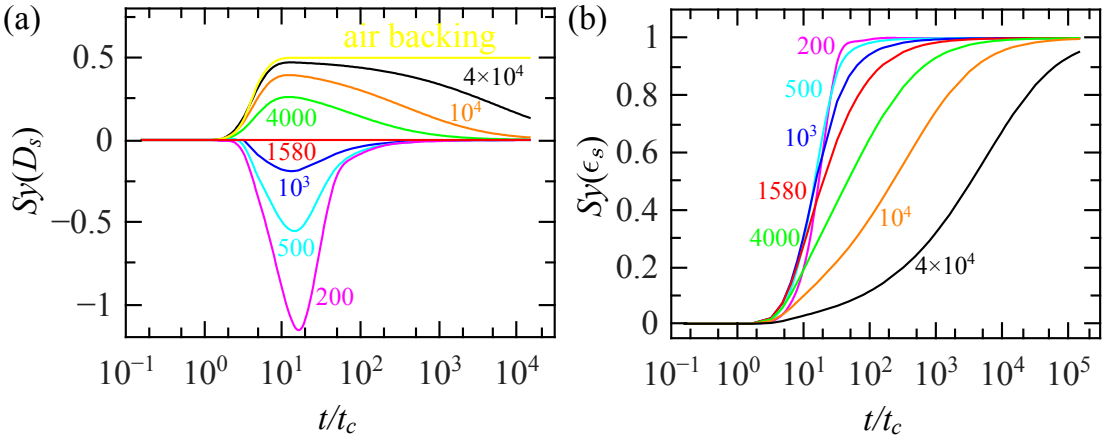

Figure 5.3: Sensitivity to (a) D_s and (b) ϵ_s as a function of the dimensionless time t/t_c for an opaque slab on top of water ($\epsilon_f = 1580$ Ws$^{1/2}$m^{-2}K^{-1}) after receiving a brief laser pulse ($Q_0\chi/\epsilon_s = 1$). Ideal conditions are considered: $h = \tau = 0$. Different values of the thermal effusivity of the solid are evaluated. Sensitivity to D_s for air backing ($\epsilon_f = 5.5$ Ws$^{1/2}$m^{-2}K^{-1}) is also included for comparison.

Numerical simulations have been performed for ideal conditions ($\tau = h = 0$). The sensitivity to thermal diffusivity $Sy(D_s)$ is maximum for air backing, but the price to be paid is the lack of any information on ϵ_s. The use of water as backing produces sensitivity to ϵ_s, at the price of reducing $Sy(D_s)$. It is worth noting that the two sensitivities are not correlated: the highest $Sy(D_s)$ appears at $t \approx 14t_c$, while the highest $Sy(\epsilon_s)$ appears at $t > 80t_c$. From Figure 5.3a we can see that $Sy(D_s)$ is very small for samples with $\epsilon_s \approx \epsilon_f$, while it increases as ϵ_s differs from ϵ_f. This is related to the fact that the elbow in $T_s(0)$ corresponding to the change in slope in Figure 5.2 is barely noticeable for $\epsilon_s \approx \epsilon_f$, but becomes more pronounced as ϵ_s and ϵ_f values separate from each other. In fact, for samples with very low thermal effusivity, $Sy(D_s)$ could reach values even higher using water backing than for air backing, e.g. for $\epsilon_s = 200$ $Ws^{1/2}m^{-2}K^{-1}$, the maximum sensitivity to thermal diffusivity is $Sy(D_s) \approx -1$. In any case, note that for these materials the surface temperature at times corresponding to the highest $Sy(D_s)$, i.e. $t \approx 14t_c$, is very low and therefore it is affected by the experimental noise (in our experimental setup it is about 10 mK). Accordingly, we propose using sample thicknesses verification $L/\sqrt{D_s} \approx 0.5$ $s^{1/2}$, i.e. $t_1 \approx 0.1$ s. In this way, the temperature level just after the elbow, where the sensitivities to D_s and ϵ_s are the largest, is high enough to provide a good signal-to-noise ratio.

On the other hand, Figure 5.3b shows that $Sy(\epsilon_s)$ is always positive, since increasing the thermal effusivity of the sample leads to a temperature rise, as can be seen in Figure 5.2. Moreover, $Sy(\epsilon_s)$ reaches an asymptotic value $Sy(\epsilon_s) = 1.0$ for all materials. However, this value is reached at different times depending on the thermal effusivity of the sample. In particular, for samples with a very high effusivity the highest $Sy(\epsilon_s)$ is obtained only at very long times. This result is related to the fact that the slope of $T_s(0)$ changes slowly for high thermal effusivity materials, while this change is abrupt for materials with low thermal effusivity.

The effects of the finite duration of the laser pulse and heat losses are illustrated in Figure 5.4. Simulations have been performed for a sample with $D_s = 4$ mm^2s^{-1} and $L = 1$ $(Q_0\chi/\epsilon_s = 1)$

$L = 1$ mm, with normalized energy for the laser pulse ($Q_0\chi/\epsilon_s = 1$). The finite duration of the laser pulse appears at very short times, breaking the characteristic straight line with slope -0.5 corresponding to an ideal Dirac pulse. Simulations have been performed for the temporal shape of our pulsed laser, as given in Section 5.2 ($\gamma = 1.46$ and $\tau = 132$ ms). By contrast, the effect of heat losses appears at long times after the laser pulse. For air backing, the temperature behavior deviates from the horizontal straight line predicted for adiabatic conditions.

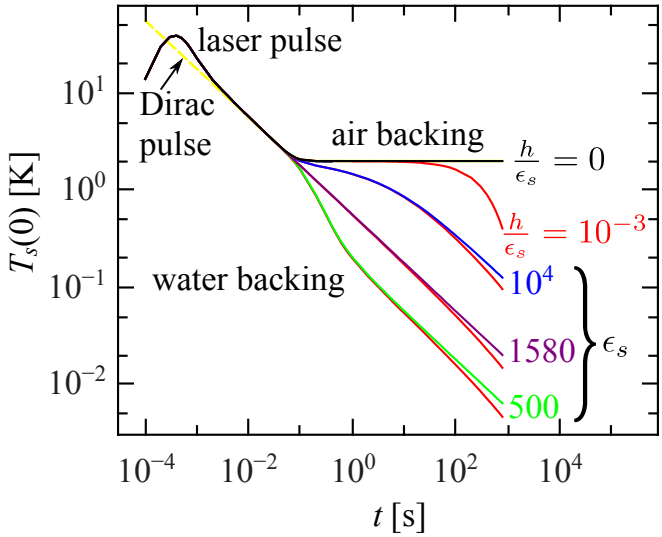

Figure 5.4: Effect of the finite duration of the laser pulse and heat losses. Simulations have been performed for $D_s = 4$ mm^{2}s^{-1} and $L = 1$ mm, with normalized energy for the laser pulse ($Q_0\chi/\epsilon_s = 1$). The effect of the finite duration of the laser pulse has been simulated for the temporal shape of our pulsed laser ($\gamma = 1.46$ and $\tau = 132$ ms). For air backing, the effect of heat losses has been calculated considering $h/\epsilon_s = 0$ and 10^{-3} s$^{-1/2}$. For water backing, simulations have been performed considering no heat losses ($h = 0$) and three different thermal effusivities: $\epsilon_s = 10^4$ Ws$^{1/2}$m^{-2}K^{-1} in blue, $\epsilon_s = 1580$ Ws$^{1/2}$m^{-2}K^{-1} in purple and $\epsilon_s = 500$ Ws$^{1/2}$m^{-2}K^{-1} in green. For each of them, we have also shown results with $h = 10$ Wm^{-2}K^{-1} (lower red curve).

In a similar way, for water backing the temperature behavior deviates from the straight line with slope -0.5. Simulations have been performed keeping the sample thermal diffusivity and thickness constant, but changing its thermal effusivity: (blue curve) $\epsilon_s = 10^4$ Ws$^{1/2}$m^{-2}K^{-1}, (purple curve) $\epsilon_s = 1580$ Ws$^{1/2}$m^{-2}K^{-1} and (green curve) $\epsilon_s = 500$ Ws$^{1/2}$m^{-2}K^{-1}. Results for $h = 0$ (adiabatic conditions) and $h = 10$ Wm^{-2}K^{-1} (in

red) are shown in Figure 5.4. As can be seen, heat losses have a smaller effect when using water than when using air. The reason is twofold: on the one hand, with air backing there are heat losses at both sides of the samples, while with a liquid backing heat losses appear only at the front surface. On the other hand, the temperature is lower for a liquid backing than for air, and therefore the heat flux is also lower since it is proportional to the temperature, as can be seen in Equation (5.3a). According to the results shown in Figure 5.4, both the finite duration of the heating pulse as well as heat losses must be included in the fitting of the experimental results to obtain accurate values of D_s and ϵ_s.

5.4 Experimental limitations and results

In order to validate the method proposed in this work to measure D_s and ϵ_s simultaneously, we have performed measurements on ten reference solid samples covering a wide range of thermal transport properties: metals, alloys, vitreous carbon, ceramics and polymers. A diagram of the experimental setup used for these measurements is shown in Figure 2.1 of Chapter 2. Sample sizes are 5 cm side squares in order to achieve $1D$ heat propagation. The sample is attached to the 4×4 cm^2 window of a metallic box that can be filled with any non-reactive liquid (see Figure 2.1c of Chapter 2). A poor thermal conducting paste (melted silicone) is used to stick the sample edges to the box in order to reduce heat leaks during measurements. The IR radiation emitted by the sample is recorded by an IR camera (FLIR SC7500 working between 3 and 5 μm) provided with a 50 mm focal length lens. At its minimum working distance (about 35 cm) each pixel measures the average IR emission from a 140 mm-side square over the sample surface. Only the pixels placed on a 1 cm-side square at the center of the sample are taken into consideration in order to reduce the influence of heat leaks from the sample to the box. Most samples are covered by a thin graphite layer (about 3 μm thick) in order to improve both the laser energy absorption and the sample

IR emissivity.

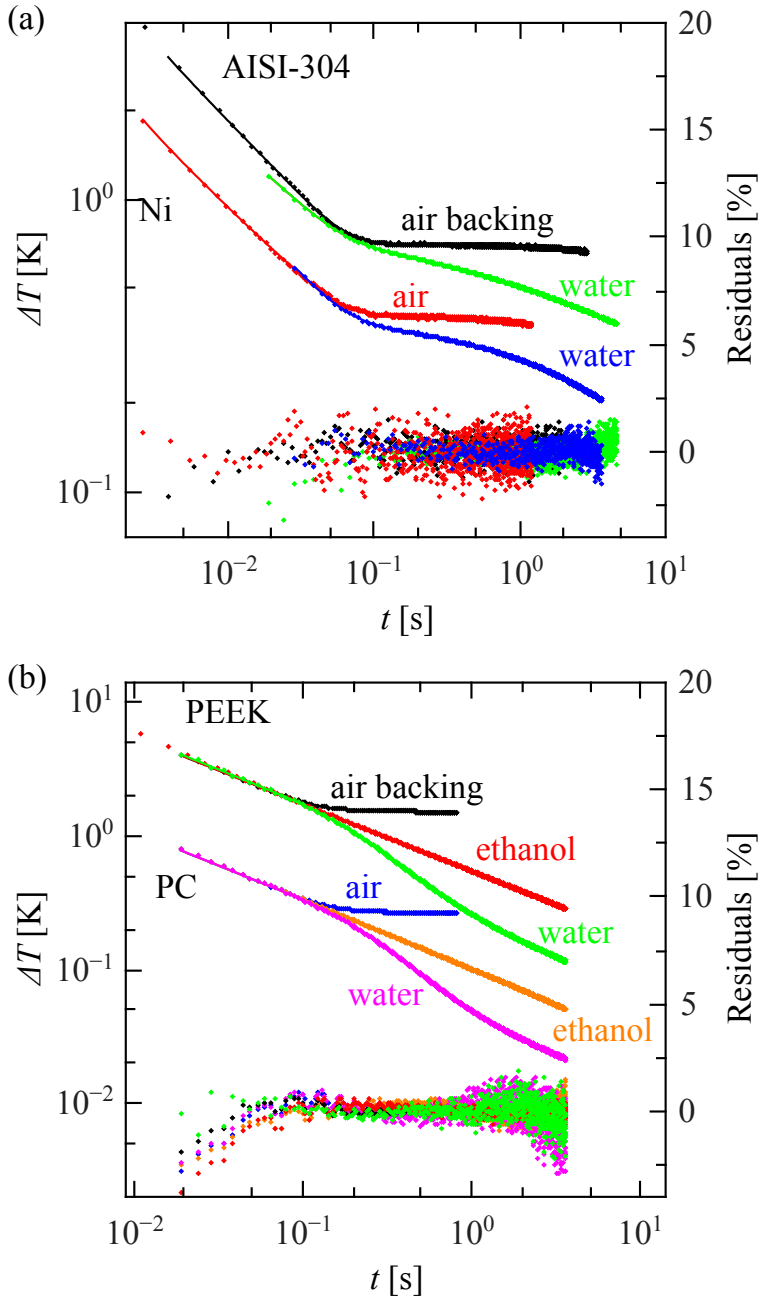

Figure 5.5: Temperature rise above ambient as a function of time after the heating pulse for different materials. Dots are the experimental data and continuous lines the fitting to the theory. Temperature data for Ni and PC are shifted. (a) Metallic samples. (b) Polymers. Polymeric samples were studied with three backings: air, water and ethanol, whereas metallic samples were studied only with air and water backings. Residuals are also plotted to visualize the quality of the fits.

Sample thicknesses were selected in order to verify $t_1 = L^2/(\pi D_s) \approx 0.1$. This particular instant gives the position of the elbow, where the initial straight line with -0.5 slope is modified by the presence of the rear surface of the sample. In this way, we have a long enough time range (up to 6 s in our setup) to obtain the thermal effusivity of the sample before lateral heat flow invalidate the $1D$ model assumed in the theory.

Figure 5.5 shows the results for two metallic (Figure 5.5a) and two polymeric (Figure 5.5b) samples: nickel (Ni), AISI 304 stainless steel, polycarbonate (PC) and polyether-ether-ketone (PEEK). Polymeric samples were studied with three backings: air, water and ethanol, while for the other samples only air and water backings were used. Experimental results are represented by dots and their corresponding curve fittings by continuous lines. For the sake of clarity temperature data for Ni and PC are shifted downwards, also we only have plotted one of each five points in all curves; however, all data collected have been used in the fits. A least-squares fitting procedure has been implemented using the well-known Levenberg–Marquardt algorithm [63,112] and the fits have been done with respect to the inverse Laplace transform of Equation (5.4). Four free parameters have been used in the fits: $Q_0\chi/\epsilon_s$, h/ϵ_s, $L/\sqrt{D_s}$ and ϵ_f/ϵ_s. In order to show the quality of the fits, the residuals, i.e. the normalized difference between experimental data and fitted values, $\left(T_s(0)_{exp} - T_s(0)_{fit}\right)/T_s(0)_{exp} \times 100$, are also plotted. They are lower than $2\,\%$ in the whole time range. The retrieved thermal diffusivity and thermal effusivity data for the ten samples are summarized in Table 5.1, where the materials are listed according to decreasing values of the thermal effusivity. Each result is the average of three consecutive measurements.

As can be observed in Table 5.1, thermal diffusivity values for all the samples agree with the literature values in both configurations: using air or water as backing fluid. On the other hand, the thermal effusivity of polymers is very close to that of ethanol ($\epsilon_{\mathrm{ethanol}} = 560$ $\mathrm{Ws^{1/2}m^{-2}K^{-1}}$). Consequently, no thermal diffusivity can be obtained for these materials using ethanol as backing fluid (since there is no noticeable change in the -0.5 slope, as shown in Figure 5.5b) in agreement with the theoretical prediction. Regarding the thermal effusivity, which is one of the goals of this work, it is

retrieved accurately provided $\epsilon_s \leq 3\epsilon_f$, as is the case for polymers (PEEK and PC), glassy carbon G, glassy carbon K (both bought from Sigradur) and bismuth (Bi), when measured with water backing. For samples verifying $\epsilon_s \gg \epsilon_f$, as is the case of copper (Cu), zinc (Zn), nickel (Ni), lead (Pb), alumina and stainless steel AISI-304 the thermal effusivity is underestimated when using water backing and this error is more pronounced as the thermal effusivity of the sample differs from that of the water. The origin of this drawback arises from the fact that for materials of good thermal effusivity, the sensitivity of $T_s(0)$ to thermal effusivity is low for times close to the 'elbow' and it slowly increases with time. In fact, very long times must be reached in order to obtain a significant sensitivity to thermal effusivity, as can be seen in Figure 5.3b. However, those data corresponding to such long times are affected by lateral heat flux and therefore cannot be used for fitting to Equation (5.4), which assumes $1D$ heat propagation.

Table 5.1: Thermal diffusivity D and thermal effusivity ϵ_s of the materials studied by the proposed two-layer system.

Material	L [mm]	D, air backing [mm^2s^{-1}]	D, water backing [mm^2s^{-1}]	D, literature[(a)] [mm^2s^{-1}]	ϵ_s, water backing [$Ws^{1/2}m^{-2}K^{-1}$]	ϵ_s, literature[(a)] [$Ws^{1/2}m^{-2}K^{-1}$]
Cooper (Cu)	3.248	107	120	117	9100	37140
Nickel (Ni)	2.065	21	21	23.0	12000	18910
Zinc (Zn)	3.116	42	44	41.8	9800	17942
Alumina	1.035	8.4	8.6	7.6-10.3	8600	9430-10900
AISI-304	0.897	3.8	4.1	3.95	6800	7498
Lead (Pb)	2.176	23	24	24.1	6800	7190
Bismuth (Bi)	1.040	6.0	6.1	6.55	3000	3050
Glassy Carbon G	1.088	6.6	6.6	6.2	2300	2530
Glassy Carbon K	1.047	0.74	---	0.73-0.80	1753	---
PEEK	0.259	0.17	0.18	0.145	640	655
PC	0.261	0.14	0.15	0.13-0.15	550	523-563

[(a)]References [45,71,72].

The two polymers studied in this work were also analyzed using ethanol as backing fluid. The obtained thermal effusivity values are: $\epsilon_{\mathrm{PC}} = 550$ $\mathrm{Ws^{1/2}m^{-2}K^{-1}}$ and $\epsilon_{\mathrm{PEEK}} = 640$ $\mathrm{Ws^{1/2}m^{-2}K^{-1}}$. Note that they agree with the values obtained using water backing and with the literature values. The uncertainty in D_s in flash measurements with air backing is in the range $3-5\,\%$, as was obtained in Chapter 3.

Finally, in the case of glassy carbon K (GC-K), it is important to say that its thermal diffusivity cannot be obtained using water as backing fluid, because its thermal effusivity is close to that of water. Consequently, we do not have enough sensitivity to retrieve D_s (see Figure 5.4a). However, we obtained the value 1753 $\mathrm{Ws^{1/2}m^{-2}K^{-1}}$ as the thermal effusivity of GC-K with water backing. Nevertheless, we also performed measurements using ethanol as backing fluid, which provides good contrast to retrieve the thermal diffusivity of glassy carbon K, giving 0.75 $\mathrm{mm^2s^{-1}}$, which is in agreement with literature values. Moreover, the thermal effusivity of GC-K obtained with ethanol backing is 1692 $\mathrm{Ws^{1/2}m^{-2}K^{-1}}$. This value has been confirmed by using the flash method in the front-face configuration, doing a relative measurement as in Chapter 4, considering glassy carbon G, as the reference material.

5.5 Discussion

The uncertainty in D_s with water backing ($\epsilon_w = 1580$ $\mathrm{Ws^{1/2}m^{-2}K^{-1}}$) depends on the effusivity of the sample, as discussed in Section 5.3. It is small (about $3-5\,\%$) for samples verifying $\epsilon_s \gg \epsilon_w$ or $\epsilon_s \ll \epsilon_w$, but it increases as the thermal effusivity of the sample approaches to that of water. In the limit, for samples with thermal effusivity close to that of the water, D_s cannot be obtained since its sensitivity is close to zero (see Figure 5.3a). In these cases, the practical solution is replacing water by another fluid with different effusivity, e.g. ethanol.

On the other hand, as mentioned before, only thermal effusivities satisfying $\epsilon_s \leq 3\epsilon_f$ can be studied with this method. The uncertainty in the retrieved thermal

effusivity is around $5-10\,\%$. Accordingly, our experimental results are given with only two significant figures (see Table 5.1). Notice that only room temperature (RT) measurements have been performed. In any event, there are several liquids with boiling points in the range $200-300$ °C (such as glycerine, 290 °C) that could be used to measure simultaneously D_s and ϵ_s above RT. It is worth mentioning that the eutectic liquid alloy made of gallium (Ga), indium (In) and tin (Sn) has a boiling point higher than 1300 °C. Owing to its low toxicity and wetting ability [113], introducing this liquid metal paves the way to use the method proposed in this work at high temperatures. In this case heat transfer by convection to the backing fluid cannot be neglected. This issue can be overcome by placing both the sample and the backing fluid in a horizontal position. Otherwise this heat transfer by convection should be included in the theoretical model.

In this work, we have addressed the challenging task of measuring, simultaneously, the thermal diffusivity and thermal effusivity of solids in a fast and accurate manner. We have improved the flash method in the front configuration to deal with a two-layer system made of the plate under study and a reference liquid. It is shown that the time evolution of the surface temperature of the solid plate is sensitive to thermal diffusivity and to the thermal mismatch between solid and liquid, which depends on their ratio of thermal effusivities. IR thermography measurements performed on ten samples covering a wide range of thermal effusivities confirm that the thermal effusivity can be retrieved accurately, provided the thermal effusivity of the sample is not higher than three times the thermal effusivity of the reference liquid. Since water is the most accessible liquid with high thermal effusivity, the highest effusivity that can be measured with this technique is about 5000 $Ws^{1/2}m^{-2}K^{-1}$. Although material with good thermal effusivity are out the application range of this technique, the transport properties of many materials of industrial interest such as polymers, composites, ceramics, inorganic oxides and many others can be retrieved.

Chapter 6. Simultaneous measurement of the in-plane and in-depth thermal diffusivity of semitransparent solids using focused pulsed spot thermography

6.1 In-plane and in-depth thermal diffusivity in opaque solids

Several methods have been developed and proposed for the accurate measurement of the thermal diffusivity of solid slabs. Nowadays, the well-known classical rear-face flash method is regarded as a standard technique for thermal diffusivity measurements in opaque solid slabs. It consists of heating the front face of an opaque plate by a brief light pulse and to analyze the temperature evolution of the rear surface, to obtain the thermal diffusivity [34]. Alternatively, in the front-face flash method the temperature is recorded at the illuminated surface [35]. The latter is particularly useful for nondestructive testing of materials since, unlike the rear-face flash method, it only needs access to the free surface of the sample, which improves its versatility for scientific and industrial applications [55,114]. In both configurations, the whole surface is illuminated homogeneously by a flat light beam and the ability of the sample to diffuse heat along the direction perpendicular to the illuminated surface is

tested. Accordingly, the in-depth (through-thickness) thermal diffusivity is obtained.

In order to measure the in-plane (along the illuminated surface) thermal diffusivity, a thermal gradient along the surface must be generated. For this purpose several experimental configurations have been proposed, including different excitation designs and data processing methods. Concerning the methods based on detecting the surface temperature by means of infrared detectors (photothermal radiometry and infrared thermography) it is worth remarking the following illumination schemes: a Gaussian spot [5–10], a disk area [120], an annular area [53,121], a line or a strip [14–16] and a grid-like mask [54].

For a circular Gaussian light pulse, Cernuschi *et al* have demonstrated that, in the case of isotropic and opaque samples, the surface temperature distribution at any time after the pulse has a Gaussian shape whose squared radius has a linear dependence on the in-plane thermal diffusivity [51,119]. In this Chapter, we have generalized this method to deal with anisotropic samples including both opaque and semitransparent materials. In this way, we have developed a complete theoretical model to calculate the surface temperature distribution of an anisotropic semitransparent slab after being illuminated by a focused pulsed laser beam. Moreover, we have included additional effects in the model, such as:

(a) the multiple reflection of the light pulse at the sample surfaces,
(b) heat losses by convection and radiation to the surrounding atmosphere and
(c) the transparency of the sample to IR wavelengths.

We have shown that the surface temperature has a Gaussian profile along the principal axes and the linear relationships between the squared radii and the corresponding principal thermal diffusivities hold for all kinds of sample: isotropic or anisotropic, opaque or semitransparent. Moreover, this linear relationship is not affected by heat losses. On the other hand, the time evolution of the spatially averaged surface temperature is the same as when illuminating the sample with a flat homogeneous light pulse. Therefore, the in depth thermal diffusivity of anisotropic semitransparent

materials can be measured using the same procedure as in isotropic samples (see Chapter 3).

These results indicate that the principal thermal diffusivities of anisotropic samples can be measured by a single and fast experiment. In order to verify the validity of the method and to test its accuracy, we have performed experiments, using a pulsed laser and an IR camera, on several opaque and semitransparent materials covering a wide range of thermal diffusivities from poor thermal conductors (polymers) to good thermal conductors (metals).

6.2 Three-dimensional heat conduction in anisotropic semitransparent slabs

Let us consider an anisotropic semitransparent slab of thickness L, as shown in Figure 6.1, illuminated by a Gaussian laser beam of radius a (at $1/e^2$), wavelength λ and power I_0. We make the Cartesian reference frame coincide with the principal axes of this anisotropic slab.

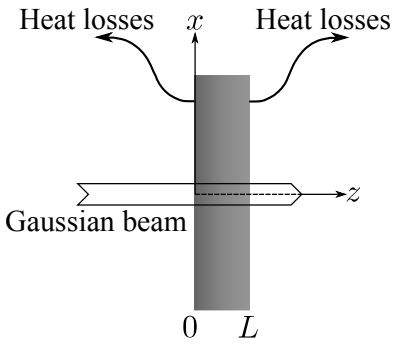

Figure 6.1: Diagram of a semitransparent slab of thickness L illuminated by a Gaussian laser beam.

According to the Beer–Lambert law and taking into account the multiple reflections of the incident laser beam, the power distribution inside the sample is

$$\begin{aligned} I_0(z) &= I_0(1-R)e^{-\alpha z} + I_0(1-R)e^{-\alpha z}Re^{-\alpha(L-z)} + \\ &\quad I_0(1-R)e^{-2\alpha z}R^2e^{-\alpha(L-z)} + \ldots \\ &= \frac{I_0(1-R)(e^{-\alpha z} + Re^{-2\alpha L}e^{\alpha z})}{1-R^2e^{-2\alpha L}}, \end{aligned} \tag{6.1}$$

where R and α are the optical reflection and absorption coefficients of the slab at wavelength λ, respectively. The Laplace transform of the heat diffusion equation for an anisotropic sample under this illumination can be expressed as follows [19]

$$\begin{aligned} K_x\frac{\partial^2\bar{T}}{\partial x^2}+K_y\frac{\partial^2\bar{T}}{\partial y^2}+K_z\frac{\partial^2\bar{T}}{\partial z^2}-s\rho c\bar{T} \\ =-\frac{\bar{I}_0}{2}\frac{e^{-2(x^2+y^2)/a^2}}{\pi a^2}\frac{(1-R)\alpha\left(e^{-\alpha z}-Re^{-2\alpha L}e^{\alpha z}\right)}{(1-R^2e^{-2\alpha L})}, \end{aligned} \tag{6.2}$$

where $\bar{T}$ is the Laplace transform of the sample temperature, s is the Laplace variable, K_x, K_y, K_z are the principal thermal conductivities of the sample and $\rho c = K_j/D_j$ is the heat capacity of the sample, with ρ the density, c the specific heat and the subindex $j=\{x,y,z\}$. $\bar{I}_0$ is the Laplace transform of the light intensity. In this work, we will consider a delta function pulse, $I_0(t)=Q_0\delta(t)$, whose Laplace transform is $\bar{I}_0=Q_0$, i.e., the total energy delivered by the pulse. If we neglect the thermal conduction to the surrounding air (because of its extremely low thermal conductivity), the general solution of Equation (6.2) can be written as the superposition of the solution of the homogeneous equation plus a particular solution of the non-homogeneous equation using the Fourier transform [125]

$$\begin{aligned} \bar{T}(x,y,z,s)= \\ \int_{-\infty}^{\infty}\int_{-\infty}^{\infty}\mathrm{d}\zeta\mathrm{d}\eta e^{-i(\zeta x+\eta y)}\left[Ae^{\beta z}+Be^{-\beta z}+Ce^{-\alpha z}+Ee^{\alpha z}\right], \end{aligned} \tag{6.3}$$

where i is the imaginary unit, $\beta=\sqrt{\frac{D_x\zeta^2+D_y\eta^2+s}{D_z}}$, being ζ and η the Fourier variables and D_j is the thermal diffusivity along the j-*th* principal axis. The coefficients of the particular solution are given by [56]

$$C=\frac{Q_0}{2\pi K_z}\frac{(1-R)\alpha}{(\beta^2-\alpha^2)}\frac{e^{-(\zeta^2+\eta^2)a^2/8}}{1-R^2e^{-2\alpha L}}, \tag{6.4a}$$

$$E=-\frac{Q_0}{2\pi K_z}\frac{(1-R)\alpha Re^{-2\alpha L}}{(\beta^2-\alpha^2)}\frac{e^{-(\zeta^2+\eta^2)a^2/8}}{1-R^2e^{-2\alpha L}}. \tag{6.4b}$$

Constants A and B in Equation (6.3) are obtained from the boundary conditions at the sample surfaces

$$K_z \frac{\mathrm{d}\bar{T}}{\mathrm{d}z}\bigg|_{z=0} = h\bar{T}(z=0), \tag{6.5a}$$

$$K_z \frac{\mathrm{d}\bar{T}}{\mathrm{d}z}\bigg|_{z=L} = -h\bar{T}(z=L), \tag{6.5b}$$

where h is the linear coefficient of heat transfer, which takes into account the combined effect of heat convection and radiation to the surrounding atmosphere. For the sake of simplicity, we have assumed the same h value at both surfaces. The expression of the Laplace transform of the temperature inside the sample is given by

$$\begin{aligned}\bar{T}(x,y,z,s) = \frac{Q_0}{4\pi^2 K_z}\frac{(1-R)\alpha}{1-R^2e^{-2\alpha L}}\int_{-\infty}^{\infty}\int_{-\infty}^{\infty}\mathrm{d}\zeta\mathrm{d}\eta e^{-i(\zeta x+\eta y)}\frac{e^{-(\zeta^2+\eta^2)a^2/8}}{(\beta^2-\alpha^2)} \\ \left[\frac{A_0e^{\beta z}+B_0e^{-\beta z}}{E_0}+e^{-\alpha z}-Re^{-2\alpha L}\left(\frac{A_1e^{\beta z}+B_1e^{-\beta z}}{E_0}+e^{\alpha z}\right)\right],\end{aligned} \tag{6.6}$$

where

$$A_0 = e^{-\beta L}(\beta-h')(\alpha+h') + e^{-\alpha L}(\beta+h')(-\alpha+h'), \tag{6.7a}$$

$$B_0 = e^{\beta L}(\beta+h')(\alpha+h') + e^{-\alpha L}(\beta-h')(-\alpha+h'), \tag{6.7b}$$

$$A_1 = e^{-\beta L}(\beta-h')(-\alpha+h') + e^{\alpha L}(\beta+h')(\alpha+h'), \tag{6.7c}$$

$$B_1 = e^{\beta L}(\beta+h')(-\alpha+h') + e^{\alpha L}(\beta-h')(\alpha+h'), \tag{6.7d}$$

$$E_0 = e^{-\beta L}(\beta-h')^2 - e^{\beta L}(\beta+h')^2, \tag{6.7e}$$

where we have defined $h' = h/K_z$. Notice that these coefficients are equal to those in Equations (3.8) of Chapter 3 by exchanging $q \to \beta$ and $K \to K_z$. Nevertheless, if the sample is semitransparent to the infrared spectrum, the signal recorded by the infrared detector comes not only from the sample surface, but also from the bulk. If we define γ as the effective infrared absorption coefficient of the sample (averaging the sample behavior from 3 to 5 µm, which is the spectral band of our IR camera) the Laplace transform of the signal recorded by the IR camera placed in front of the sample is given by [59]

$$\bar{S}(x,y,s) = A_2\int_0^L \mathrm{d}z\gamma e^{-\gamma z}\bar{T}(x,y,z,s), \tag{6.8}$$

where A_2 is a constant that includes the effects of the emissivity of the sample, the sensor area and detectivity, and the temperature derivative of the Plank function at room

temperature. Moreover, A_2 also includes the effect of the multiple reflections of the IR emission at the sample walls. $\bar{T}(x,y,z,s)$ is the Laplace transform of the sample temperature given by Equation (6.6). This means that we are assuming that heat losses associated to the infrared emission from the sample volume are so small that they do not affect the temperature field. By substituting Equation (6.6) into Equation (6.8) and solving the integral analytically, the Laplace transform of the IR signal recorded by the IR camera writes

$$\bar{S}(x,y,s) = A_3 \int_{-\infty}^{\infty}\int_{-\infty}^{\infty} \mathrm{d}\zeta \mathrm{d}\eta e^{-i(\zeta x+\eta y)} e^{-(\zeta^2+\eta^2)a^2/8} \bar{F}(\beta), \tag{6.9}$$

where

$$A_3 = A_2 \frac{Q_0}{4\pi^2 K_z} \frac{(1-R)\alpha\gamma}{1-R^2 e^{-2\alpha L}}, \tag{6.10}$$

and

$$\begin{aligned}\bar{F}(\beta) = \frac{1}{(\beta^2-\alpha^2)E_0}\Bigg\{ & -\frac{A_0}{\beta-\gamma}\left(1-e^{(\beta-\gamma)L}\right) + \frac{B_0}{\beta+\gamma}\left(1-e^{-(\beta+\gamma)L}\right) \\ & + \frac{E_0}{\alpha+\gamma}\left(1-e^{-(\alpha+\gamma)L}\right) - Re^{-2\alpha L}\Bigg[-\frac{A_1}{\beta-\gamma}\left(1-e^{(\beta-\gamma)L}\right) \\ & + \frac{B_1}{\beta+\gamma}\left(1-e^{-(\beta+\gamma)L}\right) - \frac{E_0}{\alpha-\gamma}\left(1-e^{(\alpha-\gamma)L}\right)\Bigg]\Bigg\}.\end{aligned} \tag{6.11}$$

Note that $\bar{F}(\beta) = \bar{F}(s + D_x\zeta^2 + D_y\eta^2)$, whose inverse Laplace transform is given by $e^{-(D_x\zeta^2+D_y\eta^2)t}F(t)$, where $F(t)$ is the inverse Laplace transform of $\bar{F}(s)$. Accordingly, the inverse Laplace transform of Equation (6.9), i.e. the IR signal recorded by the infrared camera can be written as

$$\begin{aligned} S(x,y,t) &= A_3 F(t) \int_{-\infty}^{\infty}\int_{-\infty}^{\infty} \mathrm{d}\zeta \mathrm{d}\eta e^{-i(\zeta x+\eta y)} e^{-\frac{\zeta^2(a^2+8D_x t)}{8}} e^{-\frac{\eta^2(a^2+8D_y t)}{8}} \\ &= G(t)\exp\left(-\frac{2x^2}{a^2+8D_x t}\right)\exp\left(-\frac{2y^2}{a^2+8D_y t}\right), \end{aligned} \tag{6.12}$$

where $G(t) = \frac{8\pi A_3 F(t)}{\sqrt{(a^2+8D_x t)(a^2+8D_y t)}}$. In particular, considering the case of an isotropic slab ($D_x = D_y = D_z = D$ and $K_x = K_y = K_z = K$), there is cylindrical symmetry

and Equation (6.12) reduces to

$$S(r,t) = G^*(t)\exp\left(-\frac{2r^2}{a^2+8Dt}\right), \tag{6.13}$$

where $G^*(t) = A_2\frac{2Q_0}{2\pi K}\frac{(1-R)\alpha\gamma}{1-R^2e^{-2\alpha L}}\frac{F(t)}{a^2+8Dt}$. This expression is in agreement with previous results in literature [51].

6.3 Limiting cases in time domain

Notice that the IR signal given in Equation (6.12) is not explicit in time domain, but it involves a numerical inverse Laplace transform: $F(t)$. However, it is quite useful in coordinate space, since it consists of Gaussian curves along x and y axis at each instant of time. Moreover, the same $F(t)$ has to be calculated for isotropic samples (see Equation (6.13)), but in this case a simplification appears in the coordinate space, since we only have the r-coordinate due to the cylindrical symmetry.

Nevertheless, For extreme but representative cases, Equation (6.12) has exact analytical solutions in time domain that are analyzed in the following subsections.

6.3.1 Opaque and thermally thick slab

If we consider a sample which is opaque to both heating and mid IR wavelengths ($e^{-\alpha L} \sim e^{-\gamma L} \sim 0$) and it is also thermally thick ($e^{-\beta L} \sim 0$), then under these conditions Equation (6.9) reduces to

$$\bar{S}(x,y,s) \approx A_2\frac{Q_0(1-R)}{2\pi^2 K_z}\int_{-\infty}^{\infty}\int_{-\infty}^{\infty}\mathrm{d}\zeta\mathrm{d}\eta e^{-i(\zeta x+\eta y)}\frac{e^{-(\zeta^2+\eta^2)a^2/8}}{\beta+h/K_z}, \tag{6.14}$$

whose inverse Laplace transform has analytical solution

$$\begin{aligned} S(x,y,t) &\approx A_2 H(t)\frac{Q_0(1-R)}{4\pi^2\epsilon}\int_{-\infty}^{\infty}\int_{-\infty}^{\infty}\mathrm{d}\zeta\mathrm{d}\eta e^{-i(\zeta x+\eta y)} \\ &\times e^{-\frac{\zeta^2(a^2+8D_x t)}{8}}e^{-\frac{\eta^2(a^2+8D_y t)}{8}} \\ &= A_2 H(t)\frac{2Q_0(1-R)}{\pi\epsilon}\frac{\exp\left(-\frac{2x^2}{a^2+8D_x t}\right)}{\sqrt{a^2+8D_x t}}\frac{\exp\left(-\frac{2y^2}{a^2+8D_y t}\right)}{\sqrt{a^2+8D_y t}}, \end{aligned} \tag{6.15}$$

where we have defined $H(t)=\frac{1}{\sqrt{\pi t}}-\frac{h}{\epsilon}e^{(h/\epsilon)^2}\mathrm{erfc}\left(\frac{h}{\epsilon}\sqrt{t}\right)$, being $\epsilon=K/\sqrt{D}$ the thermal effusivity of the sample and $\mathrm{erfc}(\cdot)$ is the complementary error function.

6.3.2 Opaque and thermally thin slab

If the sample is opaque to both heating and mid IR wavelengths and thermally thin, then $e^{-\alpha L}\sim e^{-\gamma L}\sim 0$, and $e^{\pm\beta L}\sim 1\pm\beta L$. Under these conditions Equation (6.9) reduces to

$$\bar{S}(x,y,s)\approx A_2\frac{Q_0(1-R)}{2\pi^2 K_z}\int_{-\infty}^{\infty}\int_{-\infty}^{\infty}\mathrm{d}\zeta\mathrm{d}\eta e^{-i(\zeta x+\eta y)}\frac{e^{-(\zeta^2+\eta^2)a^2/8}}{\beta^2 L+2h/K_z}, \tag{6.16}$$

whose inverse Laplace transform has analytical solution given by

$$\begin{aligned} S(x,y,t) &\approx A_2\frac{Q_0(1-R)}{4\pi^2\rho cL}e^{-\frac{ht}{\rho cL}}\int_{-\infty}^{\infty}\int_{-\infty}^{\infty}\mathrm{d}\zeta\mathrm{d}\eta e^{-i(\zeta x+\eta y)} \\ &\times e^{-\frac{\zeta^2(a^2+8D_x t)}{8}}e^{-\frac{\eta^2(a^2+8D_y t)}{8}} \\ &= A_2\frac{2Q_0(1-R)}{\pi\rho cL}e^{-\frac{ht}{\rho cL}}\frac{\exp\left(-\frac{2x^2}{a^2+8D_x t}\right)}{\sqrt{a^2+8D_x t}}\frac{\exp\left(-\frac{2y^2}{a^2+8D_y t}\right)}{\sqrt{a^2+8D_y t}}. \end{aligned} \tag{6.17}$$

6.3.3 Transparent and thermally thick slab

If the sample is semitransparent to both heating and mid IR wavelengths and thermally thick, then $e^{-\beta L}\sim 0$ and $e^{-\alpha L}\sim e^{-\gamma L}\sim 1$. Under these conditions Equation (6.9) reduces to

$$\bar{S}(x,y,s) \approx A_2 \frac{Q_0(1-R)}{2\pi^2 K_z} \frac{\alpha\gamma}{\alpha+\gamma} \times \int_{-\infty}^{\infty}\int_{-\infty}^{\infty} \mathrm{d}\zeta \mathrm{d}\eta e^{-i(\zeta x+\eta y)} \frac{e^{-(\zeta^2+\eta^2)a^2/8}}{\beta^2}, \tag{6.18}$$

whose inverse Laplace transform has analytical solution and can be expressed as

$$\begin{aligned} S(x,y,t) &\approx A_2 \frac{Q_0(1-R)}{4\pi^2\rho c} \frac{\alpha\gamma}{\alpha+\gamma} \int_{-\infty}^{\infty}\int_{-\infty}^{\infty} \mathrm{d}\zeta \mathrm{d}\eta e^{-i(\zeta x+\eta y)} \\ &\times e^{-\frac{\zeta^2(a^2+8D_x t)}{8}} e^{-\frac{\eta^2(a^2+8D_y t)}{8}} \\ &= A_2 \frac{2Q_0(1-R)}{\pi\rho c} \frac{\alpha\gamma}{\alpha+\gamma} \frac{\exp\left(-\frac{2x^2}{a^2+8D_x t}\right)}{\sqrt{a^2+8D_x t}} \frac{\exp\left(-\frac{2y^2}{a^2+8D_y t}\right)}{\sqrt{a^2+8D_y t}}. \end{aligned} \tag{6.19}$$

In this expression appears the negligible effect of heat losses and also an interchangeable role of α and γ.

6.4 Methodology to measure the thermal diffusivity

In this section we present the procedure to obtain the in-plane and in-depth thermal diffusivities from one single measurement.

6.4.1 Identification of the in-plane thermal diffusivity

Equation (6.12) indicates that the IR signal has always a Gaussian profile along the principal axes (x,y) whose radius b_j (at $1/e^2$) is given by $b_j^2 = a^2 + 8D_j t$, with subscript $j = \{x, y\}$. Following the method proposed by Cernuschi and coworkers for isotropic samples [51,119], the in-plane thermal diffusivities of the sample along the surface principal axes can be obtained as follows. First, the radius b_j of the Gaussian IR signal is measured at different times after the laser pulse has reached the sample. Then, the square of this radius is plotted as a function of time. In this way, a straight line is obtained whose slope $m_j = 8D_j$ allows determining the in-plane thermal diffusivity of

the sample along the j-th principal axis (the intercept gives the square of the laser beam spot radius a^2). According to Equation 6.13, the same linear method applies for isotropic samples. Consequently, from Equations (6.12) and (6.13) we can establish that this linear method is valid for any kind of homogeneous (isotropic or anisotropic) slabs, regardless of their optical properties and thickness. Moreover, it is not affected by the heat losses due to convection and radiation mechanisms.

In order to quantify the ability of this linear method to retrieve the principal thermal diffusivities of the sample, we analyze the sensitivity of b_j^2 to the parameters of interest (D_j and a). The sensitivity Sy to these parameters is defined as

$$Sy(D_j) = \frac{D_j}{b_j^2}\frac{\partial b_j^2}{\partial D_j} = \frac{1}{1+\frac{a^2}{8D_j t}}, \tag{6.20a}$$

$$Sy(a) = \frac{a}{b_j^2}\frac{\partial b_j^2}{\partial a} = \frac{2}{1+\frac{8D_j t}{a^2}}. \tag{6.20b}$$

Equation (6.20a) indicates that $Sy(D_j)$ varies from 0 to 1 as the time after the laser pulse t goes by, while Equation (6.20b) indicates that $Sy(a)$ varies from 2 to 0. This result clearly indicates that both quantities are uncorrelated and that the most accurate diffusivity values are obtained at long times after the laser pulse. Anyway, as the experimental noise increases with t (because of the reduction of the surface temperature), intermediate times after the laser pulse are recommended to obtain D_j accurately.

6.4.2 Identification of the in-depth thermal diffusivity

It is well known that the spatially averaged surface temperature corresponding to a focused heating of an isotropic opaque sample is equivalent to a one-dimensional (flat) excitation [53]. In the case of an anisotropic semitransparent sample, the spatially averaged IR signal is obtained by integrating Equation (6.12)

$$\begin{aligned} S(t) &= \int_{-\infty}^{\infty}\int_{-\infty}^{\infty} \mathrm{d}x\mathrm{d}y S(x,y) \\ &= G(t)\int_{-\infty}^{\infty}\int_{-\infty}^{\infty} \mathrm{d}x\mathrm{d}y e^{-\frac{x^2}{a^2+8D_x t}} e^{-\frac{y^2}{a^2+8D_y t}} = 4\pi^2 A_3 F(t), \end{aligned} \tag{6.21}$$

whose Laplace transform is

$$\bar{S}(s) = 4\pi^2 A_3 \bar{F}(q), \tag{6.22}$$

where $q = \sqrt{s/D_z}$ and A_3 is given by Equation (6.10). Note that both Equations (6.21) and (6.22) only depend on the thermal properties along the z-axis.

$\bar{F}(q)$ is given by the same expression as in Equation (6.11) when exchanging β by q. This result is in agreement with Equation (3.10) in Chapter 3 (remember that the effective IR absorption coefficient is represented by β in Chapter 3, while γ is used here), which represents the Laplace transform of the IR signal corresponding to a uniform (one dimensional) heating along the z-axis. Thus, the in-depth thermal diffusivity of a sample can be identified by recording the time evolution of the spatially averaged IR signal and fitting to Equation (6.21). This is a general equation valid for isotropic and anisotropic samples regardless their thermal and optical properties, and also includes the effect of heat losses to the surroundings.

6.5 Experimental limitations and results

In order to validate the proposed method, we have performed measurements on (an)isotropic plates that are either opaque or semitransparent. Moreover, we have covered a wide range of thermal diffusivity values: metals, ceramics, composites, glasses and polymers.

The diagram of the experimental set-up is presented in Figure 2.6 of Chapter 2. It is worth mentioning that the temperature detected by the IR camera is not the real surface temperature rise of the sample, since neither its emissivity nor its IR transparency are known. However, the "apparent" temperature rise ΔT measured by the IR detectors is proportional to the IR emission (S) exiting the front surface of the

sample.

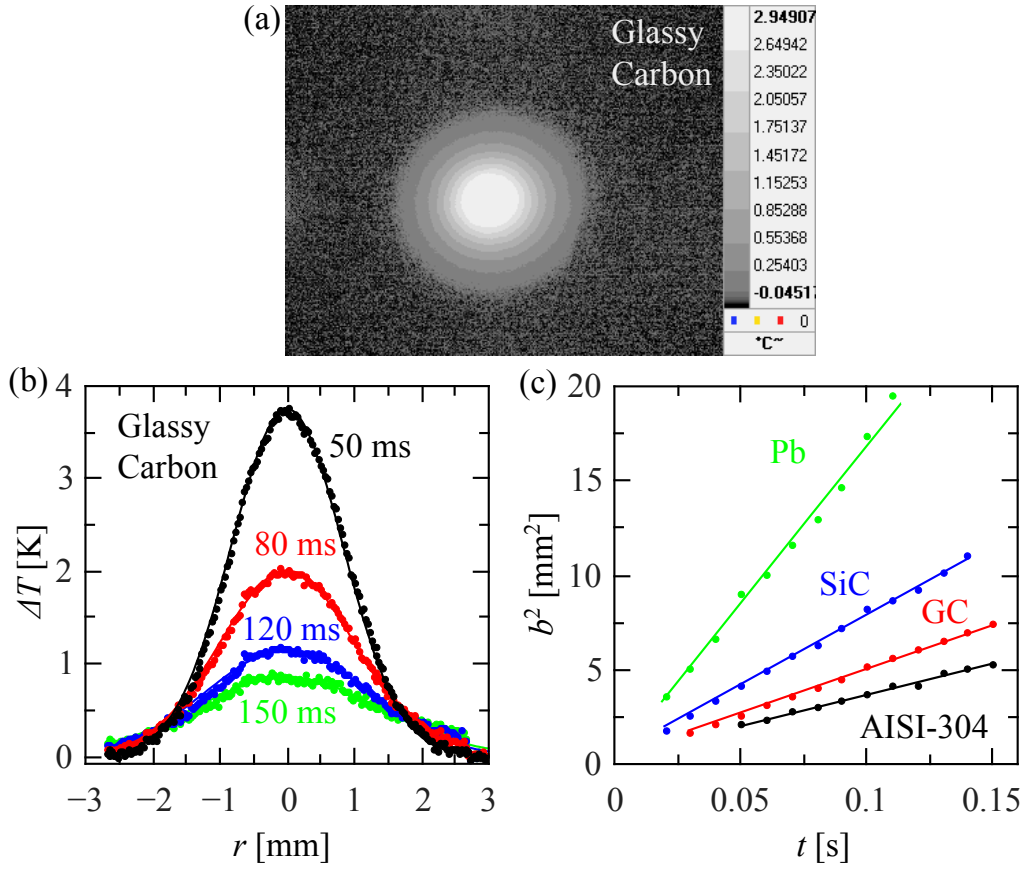

Figure 6.2: (a) Thermogram obtained for GC 50 ms after the laser pulse. (b) Apparent temperature rise above room temperature versus radial position along a line crossing the center of the Gaussian distribution, at several times after the heating pulse. Dots are the experimental data while the continuous lines are the fits to the Gaussian spatial profile given in Equation (6.13). (c) Parameter b^2 versus time. Dots are the experimental data while the continuous lines are the linear fits. Results for four good thermal conducting samples (Pb, SiC, GC and AISI-304 stainless steel) are shown.

Figure 6.2a is a thermogram for a glassy carbon (GC) sample obtained 50 ms after the laser pulse. The circular shape indicates that glassy carbon is isotropic at the surface. Figure 6.2b shows the apparent temperature rise ΔT above the ambient for a sample of glassy carbon along a line crossing the center of the Gaussian distribution. Results for different times after the heating pulse are plotted. Figure 6.2c shows the results of parameter b^2 versus time for several good thermal conducting opaque

samples: Lead (Pb), Silicon Carbide (SiC, 36% porosity), glassy carbon and AISI-304 stainless steel. From the slope m of each straight line the thermal diffusivity of each sample is obtained: $D = m/8$. Their values are given in Table 6.1.

Figure 6.3 shows the same kind of results as in Figure 6.2, but for three low thermal conducting isotropic samples: a polymer (Polyetherether-ketone, PEEK) and two neutral density filters (Hoya ND 03 and Schott NG1). The latter are semitransparent to the exciting laser beam with $\alpha_{ND03} = 1.35$ mm^{-1} and $\alpha_{NG1} = 5.81$ mm^{-1}, as measured by a Cary spectrometer. The retrieved thermal diffusivity values of the three samples are summarized in Table 6.1.

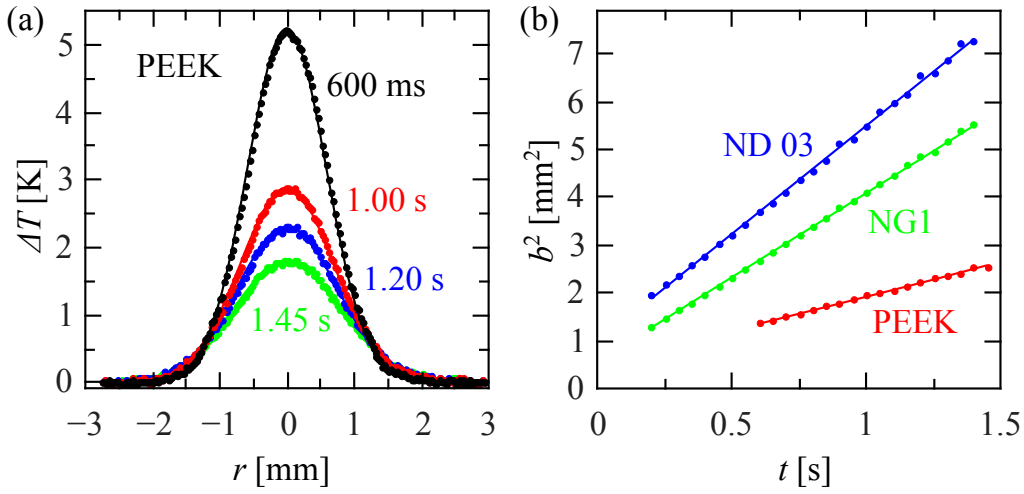

Figure 6.3: The same as in Figures 6.2b and 6.2c for three low thermal conducting samples: a polymer (PEEK) and two neutral density filters (Hoya ND 03 and Schott NG1).

Finally, we studied a unidirectionally oriented carbon fiber reinforced composite (CFR composite) whose matrix is PEEK and the volume fraction of the carbon fibers is about 62%. Figure 6.4a is a thermogram taken 300 ms after the laser pulse. The elliptical shape clearly indicates that this composite is anisotropic, since the heat propagates easily along the fibers (vertical direction). Figure 6.4b shows the results of parameter b^2 versus time for the two principal directions: y (along the fibers) and x (perpendicular to the fibers). Dots are the experimental data and the continuous lines are the linear fits. From their slopes the principal diffusivities $D_x = 0.56$ mm^{2}s^{-1} and $D_y = 3.4$ mm^{2}s^{-1} are obtained.

Figure 6.4c shows the time evolution of the spatially averaged surface temperature rise above the ambient after the heating pulse. Dots are the experimental data and the continuous line the fitting to Equation (6.21) (see Equation (3.10) in Chapter 3), using the Levenberg-Marquardt algorithm [63]. In order to visualize the quality of the fits, the residuals, i.e. the normalized difference between experimental data and fitted values, $(T_{exp} - T_{fit})/T_{exp} \times 100$, are also plotted. They are lower than $5\,\%$ in the whole time range, for all samples. The obtained value of the in-depth thermal diffusivity is $D_z = 0.55$ mm^{2}s^{-1}, which is in agreement with that measured using modulated photothermal radiometry [49].

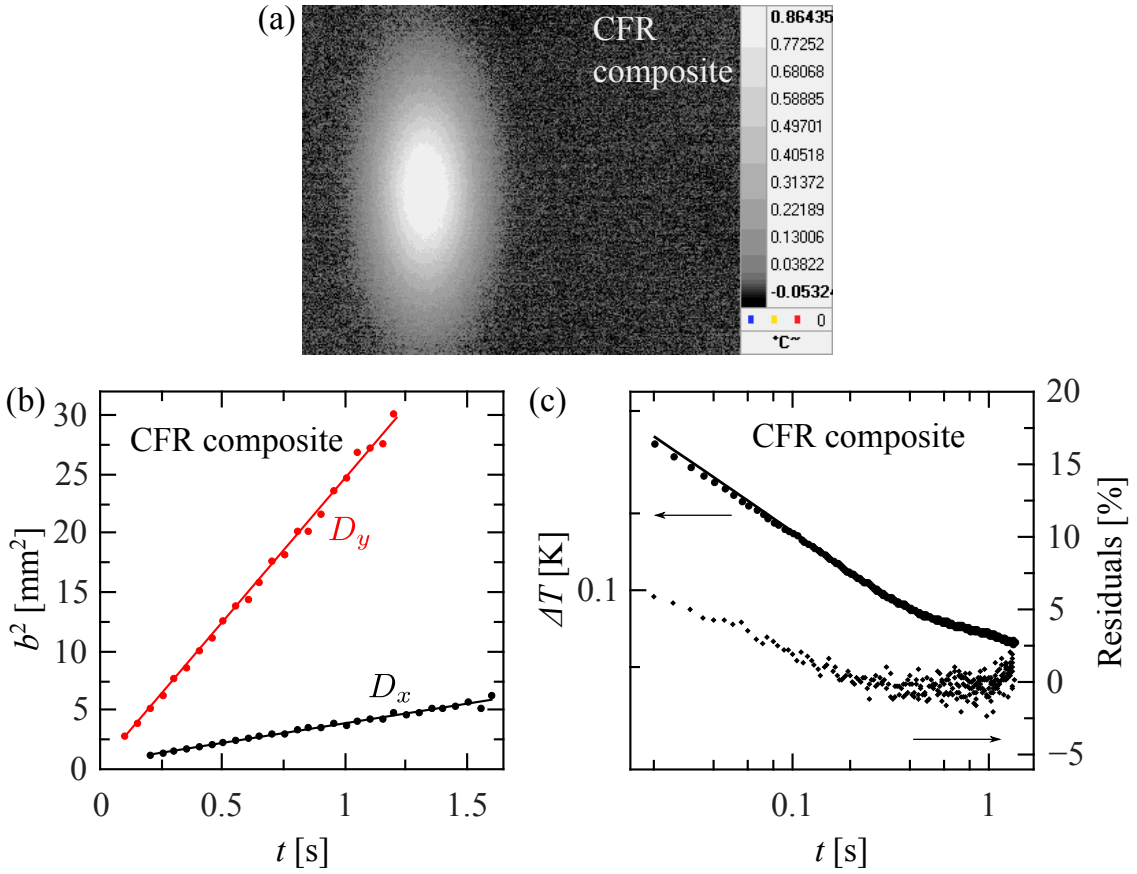

Figure 6.4: (a) Thermogram obtained for an anisotropic CFR composite 300 ms after the laser pulse. (b) Parameter b^2 versus time. Dots are the experimental data while the continuous lines are the linear fits. (c) Spatially averaged temperature rise above the ambient versus time after the heating pulse. Dots are the experimental data and the continuous line corresponds to the fitting to the theory. Residuals are also plotted to visualize the quality of the fit.

The fact that experiments have been performed using a "flat-top" laser while the theory has been developed for a Gaussian one deserves some comments. For the sake of simplicity, let us analyze its effect on an isotropic sample. The Hankel transform of a circular Gaussian beam of radius a (at $1/e^2$) and power P_0 is $P_0/(2\pi)e^{-a^2/8}$, whereas the Hankel transform of a circular "flat-top" beam of radius a and power P_0 is $P_0/(\pi\delta a)J_1(\delta a)$ [126], where J_1 is the Bessel function of first order. Regarding the simple case of an opaque and semi-infinite sample without heat losses, the IR signal for a circular Gaussian spot of radius a (at $1/e^2$) is given by

$$\begin{aligned} S(r,t) &= A_2 \frac{Q_0(1-R)}{2\epsilon\sqrt{\pi^3 t}} \int_0^\infty \mathrm{d}\delta\, \delta J_0(\delta r) e^{-\delta^2(a^2+8Dt)/8} \\ &= A_2 \frac{2Q_0(1-R)}{\epsilon\sqrt{\pi^3 t}} \frac{\exp\left(-\frac{2r^2}{a^2+8Dt}\right)}{a^2+8Dt}, \end{aligned} \tag{6.23}$$

where J_0 is the Bessel function of zero order. On the other hand, the IR signal for a circular "flat-top" spot of radius a writes

$$S(r,t) = A_2 \frac{Q_0(1-R)}{\epsilon a\sqrt{\pi^3 t}} \int_0^\infty \mathrm{d}\delta J_0(\delta r) J_1(\delta a) e^{-\delta^2 Dt}, \tag{6.24}$$

which lacks an analytical solution. It can be verified numerically that at short times after the heating pulse, both spatial temperature distributions are very different, but as times goes by, both temperature fields converge. In fact, when the thermal diffusion length [18] verifies $\mu = \sqrt{4Dt} \geq 1.6a$, the difference between both temperatures is smaller than $1\,\%$ at each point. This means that for times satisfying $t \geq 0.64\frac{a^2}{D}$, predictions from a Gaussian laser and a "flat-top" one are indistinguishable. In all measurements performed in this work and shown in Figures $6.3 - 6.5$ this condition is fulfilled. Moreover, according to the discussion on the sensitivity in Subsection 6.4.1, for times verifying this condition, the sensitivity to the diffusivity is always higher than 0.8.

For statistical purposes, we have run five measurements on each sample under the same experimental conditions. Moreover, for isotropic samples we have evaluated the thermal diffusivity along two perpendicular profiles crossing the center of the laser spot. The uncertainty given in Table 1 is the standard deviation of 10 (5) measurements performed on each isotropic (anisotropic) sample. For all the samples measured in this

work the uncertainty is about 5%. Accordingly, thermal diffusivity values are given with two significant figures. As can be observed, all the results agree with the literature values within the experimental uncertainty.

Table 6.1: Thermal diffusivity of (D) the samples studied in this Chapter.

Material	D, this work [mm^2s^{-1}]	D, literature[(a)] [mm^2s^{-1}]
Lead	24 ± 2	24.3
Porous SiC	9.6 ± 0.5	10.0
Glassy carbon	5.9 ± 0.3	6.0
AISI-304	4.1 ± 0.2	4.0
CFR composite		
x	0.56 ± 0.03	---
y	3.4 ± 0.2	---
z	0.55 ± 0.03	0.51
Hoya ND 03	0.55 ± 0.03	0.51
Schott NG1	0.45 ± 0.02	0.48
PEEK	0.18 ± 0.01	0.18

[(a)]References [49,71,72,127,128].

The theoretical model presented in this Chapter assumes that heat conduction to the surrounding atmosphere is negligible due to the low thermal conductivity of the air. However, for very thin plates (free standing films) this assumption does not hold anymore and the sample should be kept under vacuum in order to use this method.

Before concluding this section, we would like to remark the disturbing Narcissus effect by which the detector sees itself because its own emission is reflected on the sample surface [61]. This effect is specially hurtful in samples with highly reflective surfaces and leads to an underestimation of the obtained thermal diffusivity. Covering the sample surface with a high emissivity paint together with slightly tilting it, removes the Narcissus effect and the right thermal diffusivity is obtained.

6.6 Summary

In this work, we have demonstrated that when illuminating an anisotropic plate by a brief laser pulse of Gaussian profile, the IR signal emitted by the sample also has a Gaussian profile along the surface principal directions at any time after the pulse. The squared radii of these Gaussian IR profiles are linear functions of time. From the slopes of these linear relationships the in-plane principal thermal diffusivities of the sample are obtained. These slopes are independent of the optical properties of the sample and of its thickness. This means that the method applies to all kinds of plate: opaque or semitransparent, thin or thick. Moreover, the slope is not disturbed by heat losses due to convection and radiation. On the other hand, it is demonstrated that the spatially averaged IR signal matching a Gaussian illumination on an anisotropic semitransparent slab behaves as the IR signal obtained with a uniform illumination. Accordingly, by fitting the time evolution of the spatially averaged IR signal to the one-dimensional model, as in the classical front-face flash method on isotropic samples, the in-depth thermal diffusivity of the sample can be obtained from the same trial. Experiments performed on samples that are opaque and semitransparent, covering a wide range of thermal diffusivities confirm the validity of the model. This method is especially interesting to characterize the principal thermal diffusivities of anisotropic plates from one single and fast experiment.

Part II. Characterization of vertical cracks

Chapter 7. Characterization of infinite vertical cracks with lock-in thermography

7.1 State of the art on crack detection and characterization

There are several conventional non-destructive testing methods like dye penetrant, magnetic particles, eddy currents, ultrasonics and x-ray, which have been widely used to detect fissures. However, early detection of both hidden and surface breaking cracks remains a challenging task to prevent failures in working structures. Since the pioneering work by Kubiak [129], infrared thermography (IRT) has been proposed as a non-contact, non-intrusive and health safe method to detect near-surface defects. In particular, vibrothermography, where an ultrasonic wave is launched into the material and the heat dissipated at the defect propagates to the surface indicating the presence of the defect on a cold background, has received increasing attention in the last decade because of its ability to detect and characterize cracks in a wide variety of materials [2–7]. However, in vibrothermography, the ultrasonic transducer must be coupled to the sample surface, thus reducing its versatility. Moreover, open cracks with virtually no rubbing surfaces might be difficult to characterize [136]. On the other hand, optically stimulated thermography is fully non-contact, but the presence of the defect produces just a perturbation of the existing surface temperature field generated by the

external excitation. In addition, the spatial configuration of the illumination strongly affects the detectability of cracks. In the case of vertical cracks, if the sample is excited by a homogeneous illumination producing a heat flux perpendicular to the sample surface, the crack will barely disperse the flux, thus producing a negligible signature on the surface temperature distribution. These kind of cracks can be detected only when an asymmetry in the heat flux is produced. In this way, the so-called *flying spot method* was introduced in the early 1990s [137]. It is based on heating the sample with a moving laser spot or line and detecting the time evolution of the surface temperature with an infrared camera [10–16]. This technique has been implemented for different excitation regimes, mostly continuous wave [9–12] and pulsed illuminations [13–16] and less often, modulated [142] excitations. Using this method, cracks with openings as small as a few micrometers can be detected [141]. In the last years, several approaches to characterize the geometrical parameters of the crack (depth, length, width, orientation…) have been published [145,146]. They take advantage of the asymmetry of the temperature field at both sides of the crack arising from the thermal resistance produced by the crack, which partially blocks heat flux when the laser spot is focused close to the crack.

In this Chapter, we deal with the characterization of infinite vertical cracks using lock-in thermography, which is able to provide surface temperature amplitude and phase images with a very low noise level. First, we have found an analytical expression for the surface temperature of a sample containing such a crack when the surface is illuminated by a modulated laser beam that is focused at a fixed spot close to the crack. In previous works, the surface temperature close to the edge of the sample [147,148] or in samples containing open cracks [21–24] was calculated using Green functions. In this work, we take advantage of the Hankel transform [126] to obtain semi-analytical solutions for infinite vertical cracks. Two geometries of the laser spot are considered: a circular Gaussian spot and a line Gaussian one. The presence of the defect produces an abrupt jump in the amplitude and phase of the temperature profile at the crack position. The influence of the experimental parameters (laser beam radius, distance spot-crack, modulation frequency and width of the crack) on the jump height is analyzed. The goal

is to measure the thermal contact resistance R_{th} of the crack, which is related to the width of the crack.

In order to prepare calibrated infinite vertical cracks, very thin metallic tapes down to 1 µm thick are inserted between two identical blocks under pressure. A modulated laser beam is focused close to the crack. An infrared video camera equipped with a lock-in module provides the amplitude and phase of the surface temperature around the crack. A microscope lens with a spatial resolution of 31 µm is used to collect the infrared emission from the sample. A least square fit of the temperature profile crossing the center of the laser spot and perpendicular to the crack is used to retrieve R_{th}. A very good agreement between the thickness of the metallic tapes and the obtained R_{th} is found, confirming the validity of the model. Moreover, by putting the two blocks directly in contact an extremely narrow crack is obtained that remains undetectable for our thermography setup. We can establish that the upper limit for the thermal resistance of this crack is $R_{th} \leq 10^{-6}$ W^{-1}m^{2}K.

7.2 Temperature field of a semi-infinite sample containing an infinite vertical crack

Figure 7.1 shows a semi-infinite and opaque material with an infinite vertical crack placed at plane $y = 0$. The sample surface is illuminated by a laser beam modulated at a frequency f ($\omega = 2\pi f$). The center of the laser spot is located at a distance d from the crack. We assume adiabatic boundary conditions at the sample surface, i.e. heat losses to the surrounding air are neglected. Two kinds of laser profiles are used:

(a) a circular Gaussian profile of radius a (at $1/e^2$ of the intensity) and

(b) a line Gaussian profile of half-width a.

The aim of this section is to calculate how the crack modifies the surface temperature distribution.

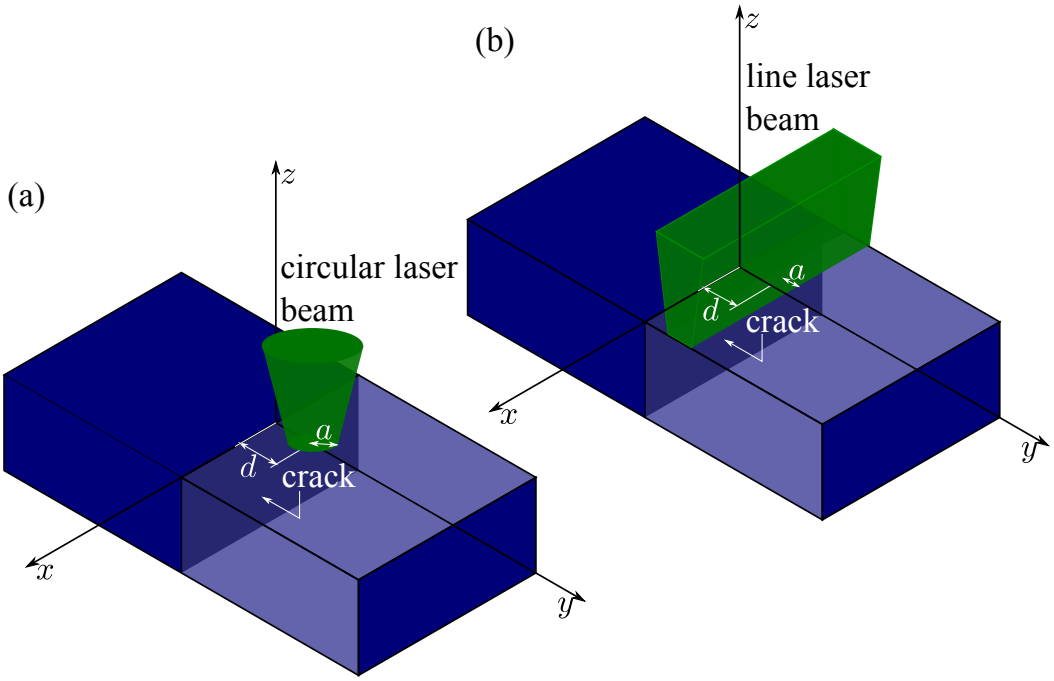

Figure 7.1: Scheme of the infinite vertical crack (in grey) inside a semi-infinite sample. (a) Circular illumination and (b) line illumination.

7.2.1 Circular Gaussian illumination

Consider an infinite material containing an infinite crack at plane $y = 0$, together with a point-like heat source located at $(0, d, 0)$ of modulated intensity $I(t) = \frac{1}{2} I_0[1 + \cos(\omega t)]$, see Figure 7.1a. The expressions for the spherical thermal wave T generated at the heat source and the thermal waves, τ_+ and τ_-, scattered at the crack traveling through $y > 0$ and $y < 0$, respectively, are given by [153]

$$T(x, y, z, \omega) = \frac{I_0}{4\pi K} \frac{e^{-qR}}{R} = \frac{P_0}{4\pi K} \int_0^\infty \mathrm{d}\delta \, \delta J_0(\delta r) \frac{e^{-\beta|y-d|}}{\beta}, \tag{7.1}$$

$$\tau_+(x, y, z, \omega) = I_0 \int_0^\infty \mathrm{d}\delta \, \delta J_0(\delta r) A e^{-\beta y}, \tag{7.2}$$

$$\tau_-(x, y, z, \omega) = I_0 \int_0^\infty \mathrm{d}\delta \, \delta J_0(\delta r) B e^{\beta y}, \tag{7.3}$$

where $q = \sqrt{i\omega/D}$ is the thermal wave vector, K and D are the thermal conductivity and thermal diffusivity of the material, respectively, $J_0(\cdot)$ is the Bessel function of order

zero, $\beta = \sqrt{\delta^2 + q^2}$, δ is the Hankel variable, $R = \sqrt{x^2 + (y-d)^2 + z^2}$ and $r = \sqrt{x^2 + z^2}$. Note that the last expression in Equation (7.1) represents a spherical thermal wave in Hankel space. The temperature of the material at $y > 0$ is given by $T_+ = T + \tau_+$, and the temperature of the material at $y < 0$ by $T_- = T + \tau_-$. Finally, the values of A and B are determined from the boundary conditions at the crack, i.e. heat flux continuity and temperature discontinuity due to the lack of thermal contact:

$$-K \frac{\mathrm{d}T_+}{\mathrm{d}y}\bigg|_{y=0} = -K \frac{\mathrm{d}T_-}{\mathrm{d}y}\bigg|_{y=0}, \tag{7.4a}$$

$$(T_+ - T_-)_{y=0} = K R_{th} \frac{\mathrm{d}T_+}{\mathrm{d}y}\bigg|_{y=0}, \tag{7.4b}$$

where R_{th} is the thermal contact resistance of the crack, which is related to the air gap width L through the equation $R_{th} = L/K_{air}$ [19]. By solving Equations (7.4a) and (7.4b), we obtain

$$A = -B = \frac{R_{th}}{4\pi} \frac{e^{-\beta|d|}}{2 + K R_{th} \beta} \mathrm{sign}(d). \tag{7.5}$$

Accordingly, the temperature inside the material at both sides of the crack is given by

$$T_\pm(x, y, z, \omega) = \frac{I_0}{4\pi K} \frac{e^{-qR}}{R} \pm I_0 \int_0^\infty \mathrm{d}\delta \, \delta J_0(\delta r) A e^{\mp \beta y}. \tag{7.6}$$

As a further step, we consider now a semi-infinite sample whose free surface is located at plane $z = 0$. If we consider adiabatic boundary conditions at the sample surface $(z = 0)$, the effect of this surface is accounted for by introducing a reflected image of the laser spot with respect to the surface (image method). As in our problem the laser spot is located at the sample surface, applying the image method means having a laser spot of double power. Accordingly, the temperature in the material is twice the value given by Equation (7.6) for the infinite material

$$T_\pm(x, y, z, \omega) = \frac{I_0}{4\pi K} \frac{e^{-qR}}{R} \pm 2 I_0 \int_0^\infty \mathrm{d}\delta \, \delta J_0(\delta r) A e^{\mp \beta y}. \tag{7.7}$$

Finally, if we consider not an ideal point-like heat source but a real circular Gaussian spot of total maximum intensity I_0 and radius a (at $1/e^2$ of the intensity), the temperature inside the material is obtained by adding the contribution of each point of the Gaussian spot weighted by its intensity

$$\begin{aligned} T_{\pm}(x,y,z,\omega) = \frac{I_0}{\pi^2 a^2 K} \int_{-\infty}^{\infty}\int_{-\infty}^{\infty} \mathrm{d}x_0 \mathrm{d}y_0 \, e^{-\frac{2\left[x_0^2+(y_0-d)^2\right]}{a^2}} \\ \times \left[\frac{e^{-qR_0}}{R_0} \pm KR_{th}\mathrm{sign}(y_0)\int_0^{\infty} \mathrm{d}\delta \, \delta J_0(\delta r)\frac{e^{-\beta(|y_0|+|y|)}}{2+KR_{th}\beta}\right], \end{aligned} \tag{7.8}$$

where $R_0 = \sqrt{(x-x_0)^2+(y-y_0)^2+z^2}$ and $r_0 = \sqrt{(x-x_0)^2+z^2}$. Equation (7.8) gives the temperature at any point of the semi-infinite material, but its numerical evaluation is rather time consuming since a triple integral is concerned. By considering the surface temperature profile along the y-axis, i.e. perpendicular to the crack and crossing the center of the laser spot, the order of the integrals drops, drastically reducing the computing time.

$$\begin{aligned} T_{\pm}(0,y,0,\omega) = \frac{I_0}{\pi^2 a^2 K} \int_{-\infty}^{\infty}\int_{-\infty}^{\infty} \mathrm{d}x_0 \mathrm{d}y_0 \, e^{-\frac{2\left[x_0^2+(y_0-d)^2\right]}{a^2}} \frac{e^{-qR_1}}{R_1} \\ \pm \frac{I_0}{4\pi K} KR_{th}\int_0^{\infty} \mathrm{d}\delta \, \delta e^{-\frac{(\delta a)^2}{16}} I_0\left[\frac{(\delta a)^2}{16}\right] \frac{e^{\left(\frac{a^2\beta^2}{8}-\beta d-\beta|y|\right)}}{2+KR_{th}\beta} \\ \times \left[\mathrm{erfc}\left(\frac{a^2\beta-4d}{2\sqrt{2}a}\right) - e^{2\beta d}\mathrm{erfc}\left(\frac{a^2\beta+4d}{2\sqrt{2}a}\right)\right], \end{aligned} \tag{7.9}$$

being $R_1 = \sqrt{x_0^2+(y-y_0)^2}$, $I_0(\cdot)$ is the modified Bessel function of order zero and $\mathrm{erfc}(\cdot)$ is the complementary error function [154].

7.2.2 Line Gaussian illumination

The geometry we are dealing with is shown in Figure 7.1b. Let us start considering an infinite material containing an infinite crack at plane $y = 0$. It is heated by an infinitely thin modulated line heat source located at $y = d$, of modulated intensity per unit length $I'(t) = \frac{I'_0}{2}\left[1+\cos(\omega t)\right]$. The expressions for the cylindrical thermal wave T generated at the heat source, and the thermal waves, τ_+ and τ_-, scattered at the

crack traveling through $y > 0$ and $y < 0$, respectively, are

$$T(y,z,\omega) = \frac{I_0'}{4\pi K} K_0(qR_2) = \frac{I_0'}{4\pi K} \int_0^\infty \mathrm{d}\delta \cos(\delta z) \frac{e^{-\beta|y-d|}}{\beta}, \tag{7.10}$$

$$\tau_+(y,z,\omega) = I_0' \int_0^\infty \mathrm{d}\delta \, \cos(\delta z) A e^{-\beta y}, \tag{7.11}$$

$$\tau_-(y,z,\omega) = I_0' \int_0^\infty \mathrm{d}\delta \, \cos(\delta z) B e^{\beta y}, \tag{7.12}$$

where $R_2 = \sqrt{(y-d)^2 + z^2}$ and $K_0(\cdot)$ is the modified Bessel function of the second kind order zero. The last expression in Equation (7.10) represents a cylindrical thermal wave in Fourier space. The temperature of the material at $y > 0$ is given by $T_+ = T + \tau_+$ and the temperature of the material at $y < 0$ by $T_- = T + \tau_-$. Using the boundary conditions at the crack given by Equations (7.4a) and (7.4b), we obtain the same values of A and B given in Equation (7.5). Accordingly, the temperature inside the material at both sides of the crack is given by

$$T_\pm(y,z,\omega) = \frac{I_0'}{4\pi K} K_0(qR_2) \pm I_0' \int_0^\infty \mathrm{d}\delta \, \cos(\delta z) A e^{\mp\beta y}. \tag{7.13}$$

For a semi-infinite material whose free surface is located at plane $z = 0$, the temperature is twice the value given by Equation (7.13), which corresponds to an infinite material,

$$T_\pm(y,z,\omega) = \frac{I_0'}{2\pi K} K_0(qR_2) \pm 2I_0' \int_0^\infty \mathrm{d}\delta \, \cos(\delta z) A e^{\mp\beta y}. \tag{7.14}$$

Finally, if we do not consider an ideal infinitely thin line heat source, but a real line Gaussian spot of total intensity per unit length I_0' and radius a (at $1/e^2$ of the intensity), the temperature inside the material is obtained by adding the contribution of each line of the Gaussian spot weighted by its intensity

$$\begin{aligned} T_\pm(y,z,\omega) = \sqrt{\frac{2}{\pi}} \frac{I_0'}{Ka} \int_{-\infty}^\infty \mathrm{d}y_0 \, e^{-\frac{2(y_0-d)^2}{a^2}} \times \Bigg[\frac{K_0(qR_3)}{2\pi} \\ \pm \int_0^\infty \mathrm{d}\delta \, \mathrm{sign}(y_0) \cos(\delta z) \frac{KR_{th}}{2\pi} \frac{e^{-\beta(|y_0|+|y|)}}{2 + KR_{th}\beta} \Bigg], \end{aligned} \tag{7.15}$$

where $R_3 = \sqrt{(y-y_0)^2 + z^2}$. If we confine the temperature calculations to the surface of the sample ($z = 0$), the order of the integrals is reduced

$$\begin{aligned} T_{\pm}(y,0,\omega) = & \frac{I_0'}{\sqrt{2\pi^3}Ka} \int_{-\infty}^{\infty} \mathrm{d}y_0 \, e^{-\frac{2(y_0-d)^2}{a^2}} K_0(qR_4) \\ & \pm \frac{I_0'}{4\pi K} KR_{th} \int_0^{\infty} \mathrm{d}\delta \, \frac{e^{\left(\frac{a^2\beta^2}{8} - \beta d - \beta|y|\right)}}{2 + KR_{th}\beta} \\ & \times \left[\mathrm{erfc}\left(\frac{a^2\beta - 4d}{2\sqrt{2}a} \right) - e^{2\beta d} \mathrm{erfc}\left(\frac{a^2\beta + 4d}{2\sqrt{2}a} \right) \right], \end{aligned} \tag{7.16}$$

where we have defined $R_4 = \sqrt{(y-y_0)^2}$.

7.3 Numerical simulations of the relative temperature contrast for infinite vertical cracks

In this section we study the influence of parameters d, a and f in the visibility of the crack by analyzing the surface temperature of a semi-infinite sample. All of the simulations are performed for AISI-304 stainless steel ($D = 4.0$ mm^{2}s^{-1} and $K = 15$ Wm^{-1}K^{-1}). Figure 7.2 shows the calculation of the natural logarithm of the temperature amplitude $\ln|T|$ and phase Ψ along the y-axis for a semi-infinite AISI-304 sample containing an infinite vertical crack ($y = 0$) and illuminated by a circular Gaussian spot. Calculations are performed using Equation (7.9) with $d = 1$ mm, $a = 0.75$ mm and $f = 1$ Hz. Four thermal resistances ranging from 10^{-5} W^{-1}m^{2}K (0.26 μm) to 10^{-2} W^{-1}m^{2}K (260 μm) are analyzed. As can be observed, there is an abrupt discontinuity at the crack position in both $\ln|T|$ and Ψ. Note that the same scale level is used in $\ln|T|$ and Ψ in order to clearly show that the jump at the crack is much higher for the former. Regarding $\ln|T|$, the height of the leap increases with R_{th}. However, the behavior of Ψ is more complicated. Whenever the laser spot is very close to the crack and especially when it overlaps the crack ($a > d$), the phase jump is reversed, i.e. the jump is upwards. Besides, the higher the value of R_{th}, the more pronounced the reversal.

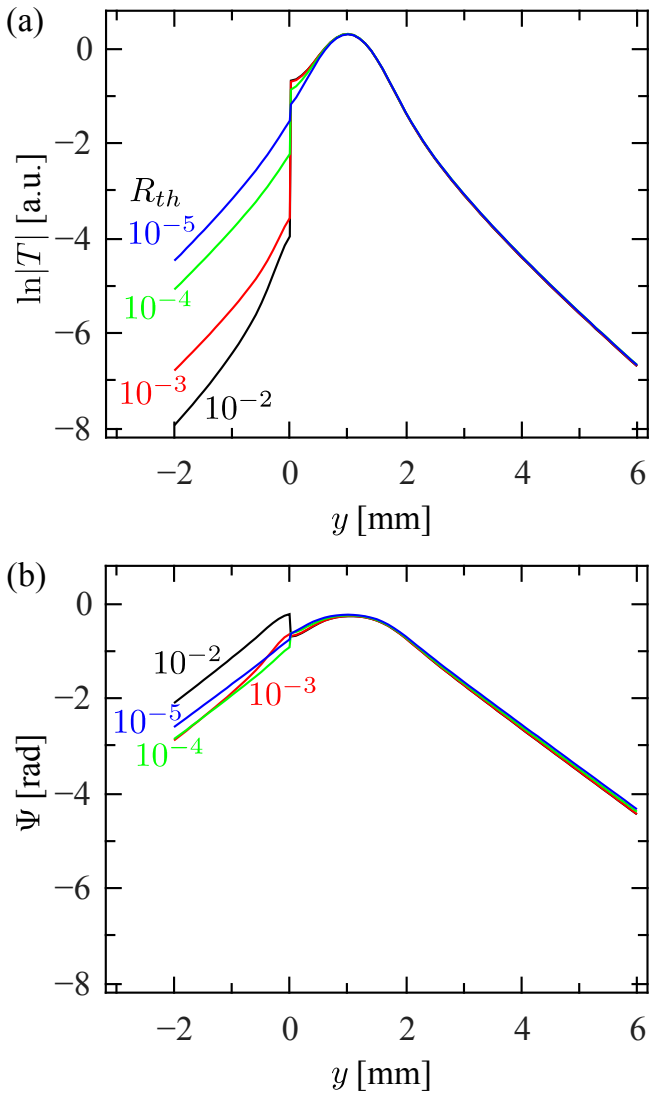

Figure 7.2: Simulation of (a) the natural logarithm of the temperature amplitude and (b) phase along the y-axis for a semi-infinite AISI-304 sample containing an infinite vertical crack. The sample is illuminated at $d = 1$ mm with a circular Gaussian laser with $a = 0.75$ mm modulated at $f = 1$ Hz. The effect of the value of the thermal resistance R_{th} ($W^{-1}m^2K$) is shown.

Figure 7.3 shows the same type of simulations as in Figure 7.2, but for a line Gaussian laser. Calculations are performed using Equation (7.16) with the same parameters as in Figure 7.2. As can be seen, the general trend is similar for both kinds of illumination. The only remarkable difference between both illuminations is that $\ln|T|$ is steeper for circular illumination than for line illumination. This result is related to the

fact that for the former, a spherical thermal wave is generated while for the later the thermal wave is cylindrical. Nevertheless, as the crack jumps are almost the same for both kind of spots, in the remainder of the section only simulations with circular Gaussian illumination are shown.

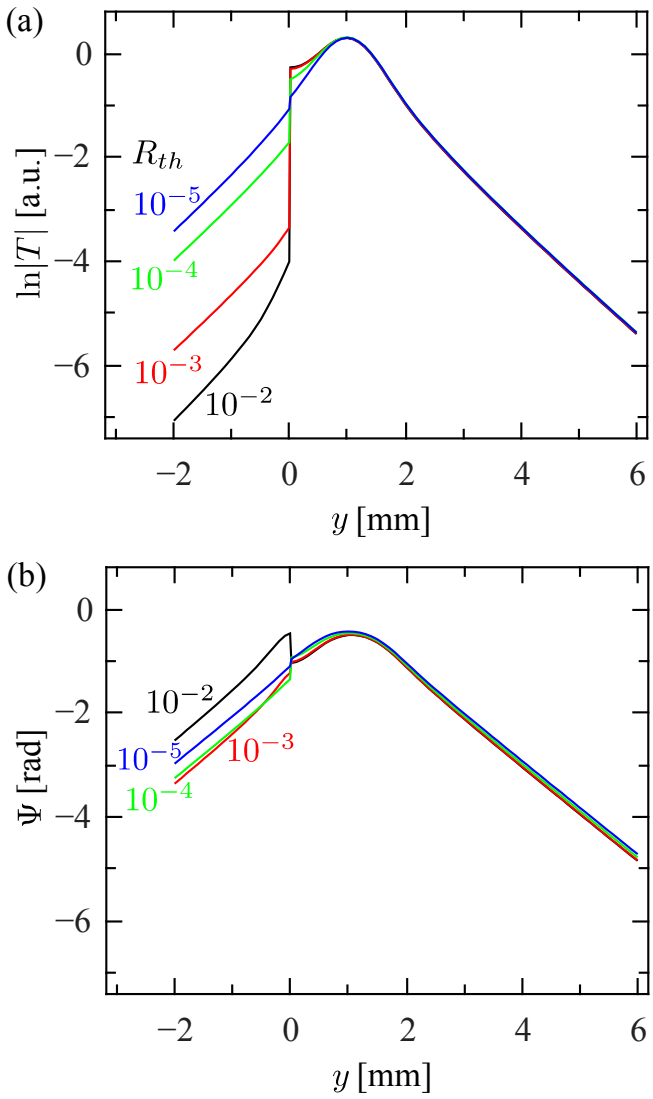

Figure 7.3: Simulation of (a) the natural logarithm of the temperature amplitude and (b) phase along the y-axis for a semi-infinite AISI-304 sample containing an infinite vertical crack. The sample is illuminated at $d = 1$ mm with a line Gaussian laser with $a = 0.75$ mm modulated at $f = 1$ Hz. The effect of the value of the thermal resistance R_{th} ($W^{-1}m^2K$) is shown.

In order to quantify the temperature jump at the crack position, we introduce two parameters: (a) the temperature amplitude contrast at the crack $\Delta_{|T|}$, which is defined as

$$\Delta_{|T|} = \frac{|T_+(0,0,0)| - |T_-(0,0,0)|}{|T_+(0,d,0)|}, \tag{7.17}$$

and (b) the phase contrast Δ_Ψ, defined as

$$\Delta_\Psi = \Psi_+(0,0,0) - \Psi_-(0,0,0). \tag{7.18}$$

Equations (7.9) and (7.16) show that both $\Delta_{|T|}$ and Δ_Ψ depend on the factor KR_{th}. This means that narrow cracks are better detected in high thermal conducting materials (metals, alloys, ceramics…) than in thermal insulators (polymers, composites…). Moreover, both contrasts do not depend on the laser intensity I_0.

First, we analyze the dependence of $\Delta_{|T|}$ (dimensionless) and Δ_Ψ (degrees) on the thermal resistance of the crack. The results are shown in Figure 7.4 for $d = \mu$ and $a = \mu/2$, where $\mu = \sqrt{D/(\pi f)}$ is the thermal diffusion length. Three modulation frequencies are tested: 0.01, 1 and 100 Hz. Continuous lines correspond to $\Delta_{|T|}$ and dashed lines to Δ_Ψ. As can be seen, both contrasts exhibit a sigmoid shape. For low R_{th} (very narrow cracks), there is no temperature contrast and the crack remains undetected. For large R_{th} (wide cracks), the temperature contrast saturates, indicating that these cracks are easy to detect, but R_{th} is difficult to quantify. The highest sensitivity to the thermal resistance appears for intermediate R_{th} values. Note that as the modulation frequency is increased by two orders of magnitude, the sensitivity to R_{th} is displaced to lower values by one order of magnitude. This result means that the high frequencies are better suited to detect and characterize extremely narrow cracks.

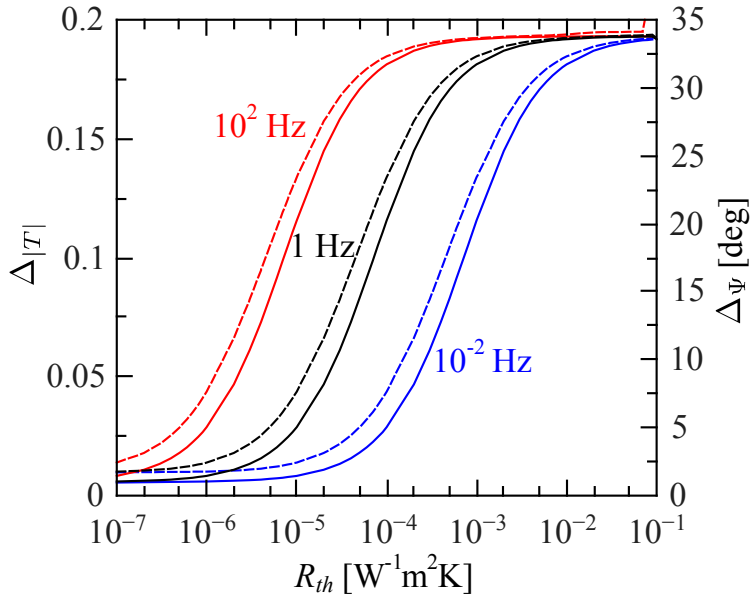

Figure 7.4: Numerical simulation of the dependence of $\Delta_{|T|}$ (left axis, continuous line) and Δ_Ψ (right axis, dashed line) on the thermal contact resistance R_{th}. Calculations are performed for an AISI-304 material ($D = 4$ mm^{2}s^{-1} and $K = 15$ Wm^{-1}K^{-1}) with $d = \mu$ and $a = \mu/2$. Three modulation frequencies are tested.

Anyway, the results shown in Figure 7.4 have no general validity. In Figure 7.5, we shown the same kind of calculations as in Figure 7.4 for $f = 1$ Hz and three combinations of d and a: (1) $d = \mu$ and $a = \mu/2$, (2) $d = \mu$ and $a = \mu$, and (3) $d = \mu/2$ and $a = \mu/4$. As can be seen, the amplitude contrast $\Delta_{|T|}$ is always a sigmoid function, but as a approaches d the shape of the phase contrast Δ_Ψ is no longer a sigmoid. In fact, the phase contrast can be even negative, as has been shown in Figure 7.2b. It is worth noting that for a fixed frequency the region of the highest sensitivity of $\Delta_{|T|}$ to R_{th} (the region with the steepest slope) is independent of the couple (d, a). In fact, it only depends on f.

The dependence of $\Delta_{|T|}$ and Δ_Ψ on the laser spot radius is analyzed in Figure 7.6. Calculations are performed with $d = \mu$. We have studied three thermal resistances: 10^{-5}, 10^{-4} and 10^{-3} W^{-1}m^{2}K. As can be observed, the highest amplitude contrast corresponds to $a \approx 1.25\mu$, i.e. when the laser spot slightly overlaps the crack. This result is independent of R_{th}. On the other hand, the highest phase contrast appears for a

tightly focused laser beam. Note the negative phase contrast for some combinations of R_{th} and a. A negative contrast means that the phase increases at the other side of the crack with respect to the heating spot. This result has already been shown in Figure 7.2b for $R_{th} = 10^{-2}$ W^{-1}m^{2}K.

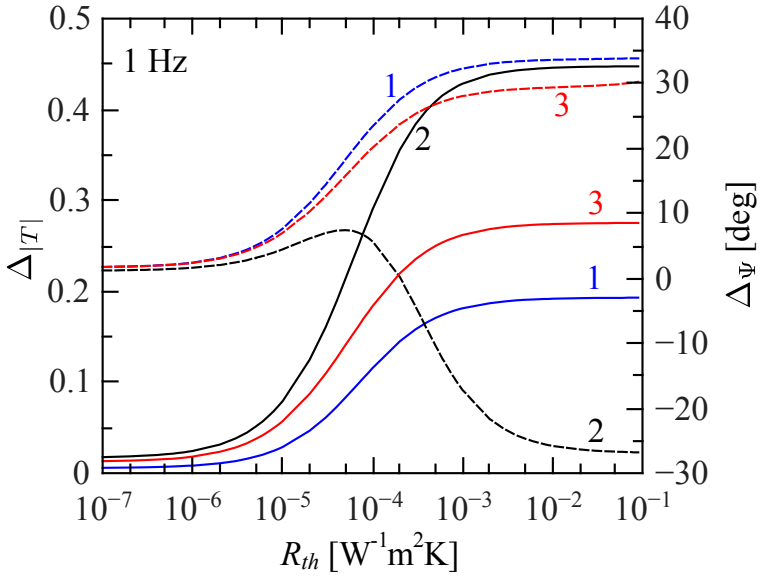

Figure 7.5: Contrasts: $\Delta_{|T|}$ (left axis, continuous line) and Δ_Ψ (right axis, dashed line), calculated at a fixed frequency $f = 1$ Hz, as a function of R_{th}. Three combinations of laser distance and radius are analyzed: (1) $d = \mu$ and $a = \mu/2$, (2) $d = \mu$ and $a = \mu$, and (3) $d = \mu/2$ and $a = \mu/4$.

Finally, in Figure 7.7 the dependence of $\Delta_{|T|}$ and Δ_Ψ on the distance of the laser spot to the crack is analyzed. Calculations are performed for a fixed laser beam radius $a = 0.75\mu$. The same three thermal resistances as in Figure 7.6 are studied. As expected, the highest amplitude contrast is produced when the laser spot overlaps the crack $d \approx 0.5\mu \approx 0.7a$. Note that this result is independent of R_{th}. It is worth mentioning that as the laser spot moves away from the crack the contrast in amplitude decreases, but surprisingly the phase contrast increases until it reaches an asymptotic value.

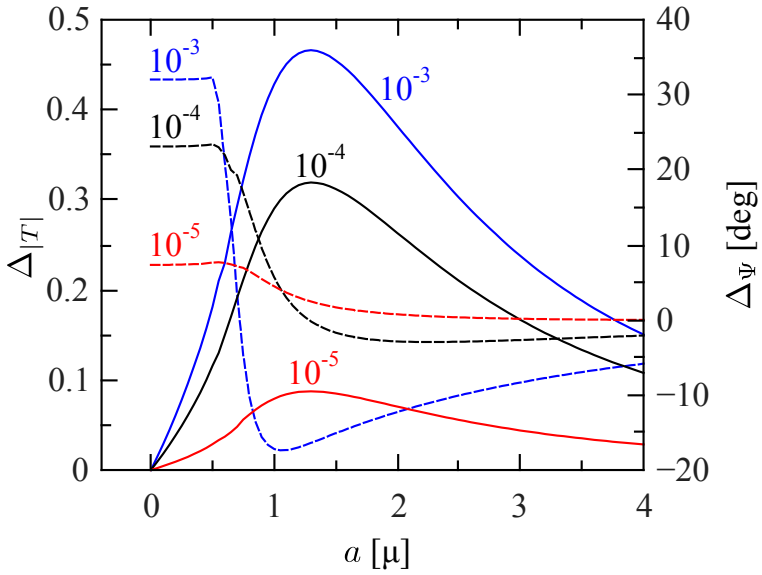

Figure 7.6: Numerical simulation of the dependence of $\Delta_{|T|}$ (left axis, continuous line) and Δ_Ψ (right axis, dashed line), on the laser radius a. Calculations are performed for an AISI-304 sample with $d = \mu$. Three R_{th} values are analyzed: 10^{-5}, 10^{-4} and 10^{-3} W^{-1}m^{2}K.

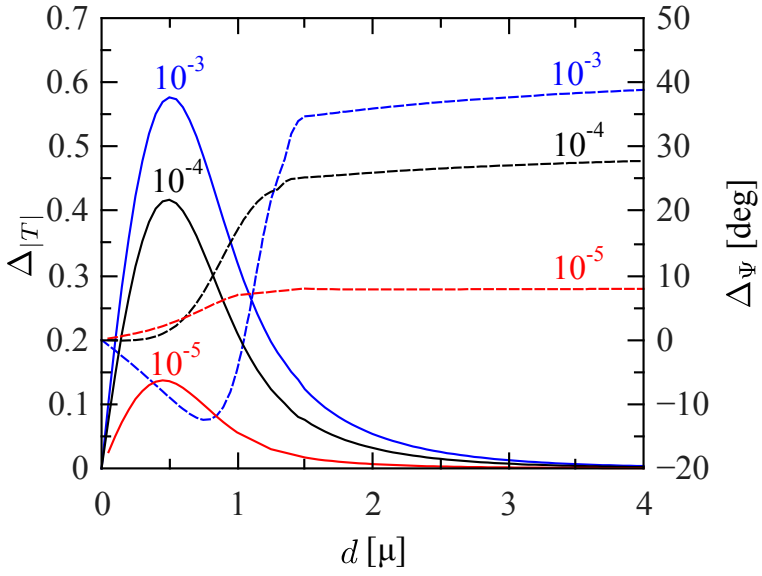

Figure 7.7: Numerical simulation of the dependence of $\Delta_{|T|}$ (left axis, continuous line) and Δ_Ψ (right axis, dashed line), on the distance of the laser spot to the crack. Calculations are performed for an AISI-304 sample with $a = 0.75\mu$ and $f = 1$ Hz. Three R_{th} values are analyzed: 10^{-5}, 10^{-4} and 10^{-3} W^{-1}m^{2}K.

According to the simulations shown in this section, we propose the following guidelines for vertical crack detection and characterization via lock-in thermography:

(a) For a given thermal resistance the largest amplitude and phase contrast are not obtained with the same set of experimental parameters (d, a). The highest amplitude contrast appears when the spot slightly overlaps the crack $a \approx 1.25d$. On the other hand, tightly focused spots $(a < d)$ produce the highest phase contrast. We propose $d \approx \mu \approx 1.25a$ as a rule of thumb to obtain good enough amplitude and phase contrast simultaneously.

(b) In order to detect very narrow cracks the appropriate experimental conditions are a high frequency with $d \approx a \approx \mu$. These conditions mean a tightly focused laser spot. For instance, using $a = d = 0.1$ mm on metallic samples together with a frequency $f \approx 100 - 1000$ Hz allows detection of thermal resistances as low as $10^{-6} - 10^{-7}$ $W^{-1}m^2K$. It is worth noting that under these experimental conditions thicker cracks are also clearly detected.

(c) In order to retrieve R_{th}, frequencies producing the highest temperature amplitude/phase contrast must be avoided, since they are insensitive to R_{th} variations. Instead, lower frequencies which shift the amplitude contrast $(\Delta_{|T|})$ to half of its maximum, are the most sensitive to R_{th} variations.

7.4 Experimental details and results

A diagram of the experimental setup is presented in Figure 2.7 of Chapter 2. In order to increase the signal to noise ratio, a large number of images have been recorded, since in lock-in measurements the average noise level in temperature amplitude decreases as the square root of the number of images [15] and it is proportional to the noise equivalent temperature difference (NETD) of the detector (20 mK in our camera). According to Equation (1.14) of Chapter 1, by processing 2×10^4 images the noise level of the data was kept below 0.3 mK. As our camera (FLIR SC7500) works at a

maximum rate of 350 images/s, collecting 2×10^4 images requires measurements of about 1 min.

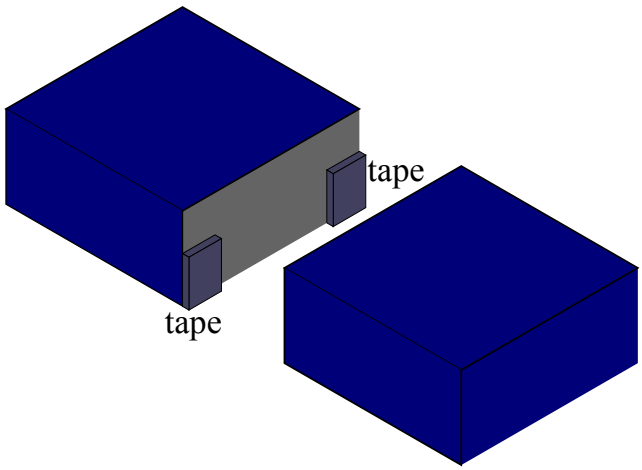

Figure 7.8: Diagram of the infinite vertical crack simulated for the experiment: two thin strips of Ni tape of the same thickness are sandwiched between two AISI-304 stainless steel blocks.

In order to obtain calibrated vertical cracks we have used two glassy carbon plates ($D = 6.0$ mm^{2}s^{-1} and $K = 6.3$ Wm^{-1}K^{-1}) 6 mm thick, which are put together under some pressure. The two large surfaces in contact are mirror-like polished. In order to calibrate the air gap between the plates, strips of nickel tape (Ni) of 25, 10, 5, 2.5 and 1 μm thickness are placed between the carbon layers (see Figure 7.8). They represent thermal resistances of 10^{-3}, 4×10^{-4}, 2×10^{-4}, 10^{-4} and 4×10^{-5} W^{-1}m^{2}K, respectively. The main advantage of using glassy carbon is that this material is at the same time highly absorbing at visible wavelengths and highly emitting at IR wavelengths. This means that its surface does not need to be prepared (painted or coated) in order to obtain a high enough signal to noise ratio, as is the case for metals and alloys.

In Figures 7.9a and 7.9b, the amplitude and phase thermograms corresponding to a 1 μm thick crack obtained with the following experimental parameters are shown: $f = 0.6$ Hz, $d \approx 0.65$ mm and $a \approx 0.35$ mm. Notice that even such a thin crack is detectable using lock-in thermography. In Figures 7.9c and 7.9d, we show by dots the temperature profiles along the y-axis for the five cracks studied.

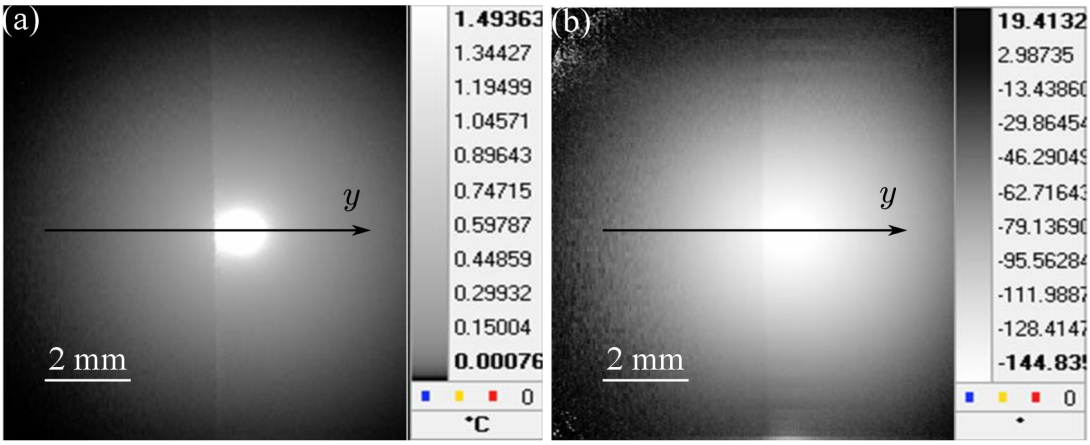
(a)
1.49363
1.34427
1.19499
1.04571
0.89643
0.74715
0.59787
0.44859
0.29932
0.15004
0.00076
0
°C
y
2 mm
(b)
19.4132
2.98735
-13.43860
-29.86454
-46.29049
-62.71643
-79.13690
-95.56284
-111.9887
-128.4147
-144.835
0
y
2 mm

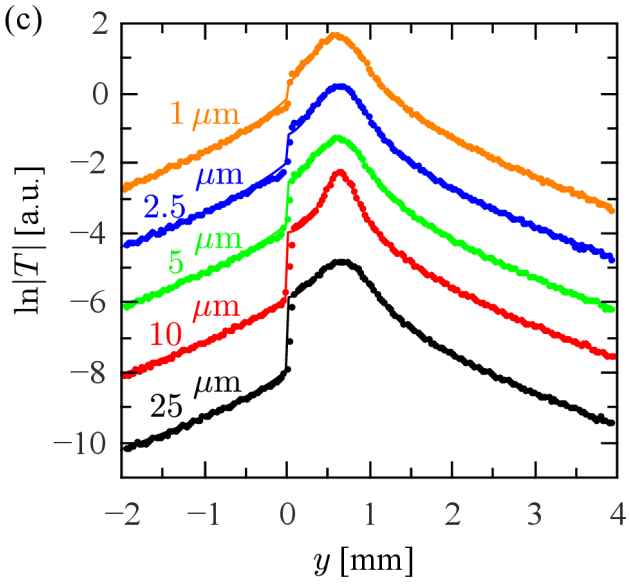
(c)
ln|T| [a.u.]
y [mm]
1 μm
2.5 μm
5 μm
10 μm
25 μm

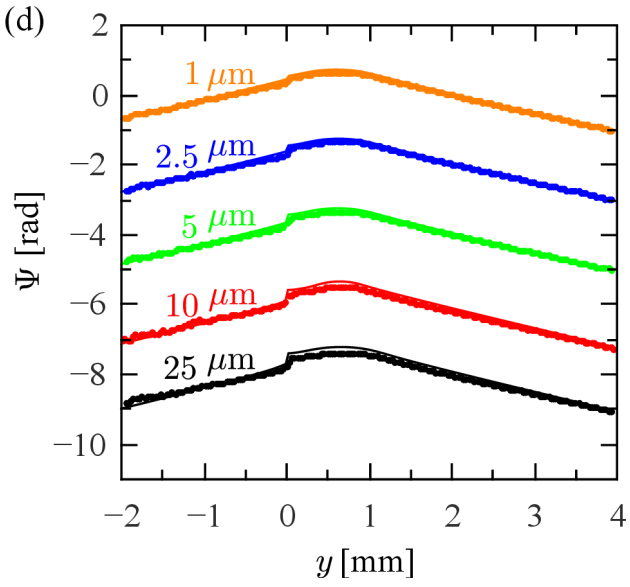
(d)
Ψ [rad]
y [mm]
1 μm
2.5 μm
5 μm
10 μm
25 μm

Figure 7.9: (a) Amplitude and (b) phase thermograms for two glassy carbon plates put in contact to simulate an infinite vertical crack 1 μm thick. The following experimental parameters have been used: $d = 0.65$ mm, $a = 0.35$ mm and $f = 0.6$ Hz. (c) Experimental natural logarithm of the surface temperature amplitude and (d) phase profiles along the y-axis for several crack widths. Dots correspond to experimental data and continuous lines to the fit to Equation (7.9).

The continuous lines are the least squares fits to Equation (7.9) using four free parameters: I_0, a, d and R_{th}. The values of $\ln|T|$ and Ψ of each profile have been shifted to better appreciate the jump at the crack. Note that the fit quality is better for $\ln|T|$ than for Ψ. This is because the jump at the crack is much higher for $\ln|T|$ than for Ψ.

All measurements shown in Figures 7.9c and 7.9d have been performed with $f = 0.6$ Hz, $d \approx 0.65$ mm and $a \approx 0.35$ mm. The retrieved thermal resistances are 8.0×10^{-4}, 4.2×10^{-4}, 2.1×10^{-4}, 9.8×10^{-5} and 4.5×10^{-5} W^{-1}m^{2}K, which correspond to air thicknesses (L) of 21, 11, 5.7, 2.6 and 1.2 μm, respectively. They are very close to the nominal values of the nickel tape thicknesses. On the other hand, in all fits the retrieved values of a and d are in the range $a = 0.35 - 0.37$ mm and $d = 0.63 - 0.66$ mm, which are very close to the values measured optically.

In order to test the consistency of the procedure, we have performed complementary measurements changing the radius of the spot a, the distance of the laser beam to the crack d and the modulation frequency f. As an example, we show in Figure 7.10 the temperature profiles along the y-axis for a 5 μm thick vertical crack keeping $d \approx 0.65$ mm, but changing a and f: (1) $a = 0.20$ mm, $f = 0.3$ Hz, (2) $a = 0.35$ mm, $f = 0.3$ Hz, (3) $a = 0.20$ mm, $f = 0.6$ Hz and (4) $a = 0.35$ mm, $f = 0.6$ Hz. The retrieved thermal resistances are 2.1×10^{-4}, 2.0×10^{-4}, 2.2×10^{-4} and 2.1×10^{-4} W^{-1}m^{2}K respectively, corresponding to an air gap of $L = 5.5 \pm 0.5$ μm. It is worth noting that in our experimental setup, frequencies higher than 1 Hz are not appropriate to size the crack. Increasing the frequency implies getting closer to the crack together with focusing the laser spot more tightly (to maintain the optimal experimental conditions given at the end of Section 7.3). This means that a higher spatial resolution is

needed than what our camera is able to achieve. Besides, the signal to noise ratio decreases as the frequency increases. Accordingly, we use frequencies in the range $1 - 50$ Hz to detect cracks, but not to size them.

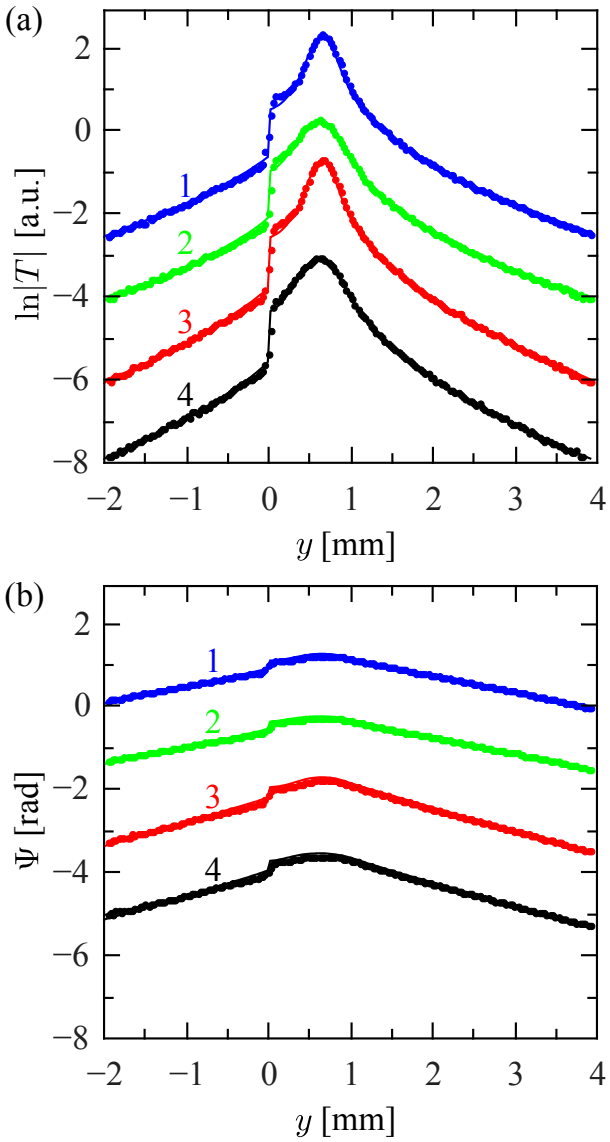

Figure 7.10: (a) Experimental natural logarithm of the surface temperature amplitude and (b) phase profiles along the y-axis for a 5 μm thick vertical crack in glassy carbon. Dots correspond to experimental data and continuous lines to the fit to Equation (7.9). In all measurements $d = 0.65$ mm. (1) $a = 0.20$ mm, $f = 0.3$ Hz, (2) $a = 0.35$ mm, $f = 0.3$ Hz, (3) $a = 0.20$ mm, $f = 0.6$ Hz and (4) $a = 0.35$ mm, $f = 0.6$ Hz.

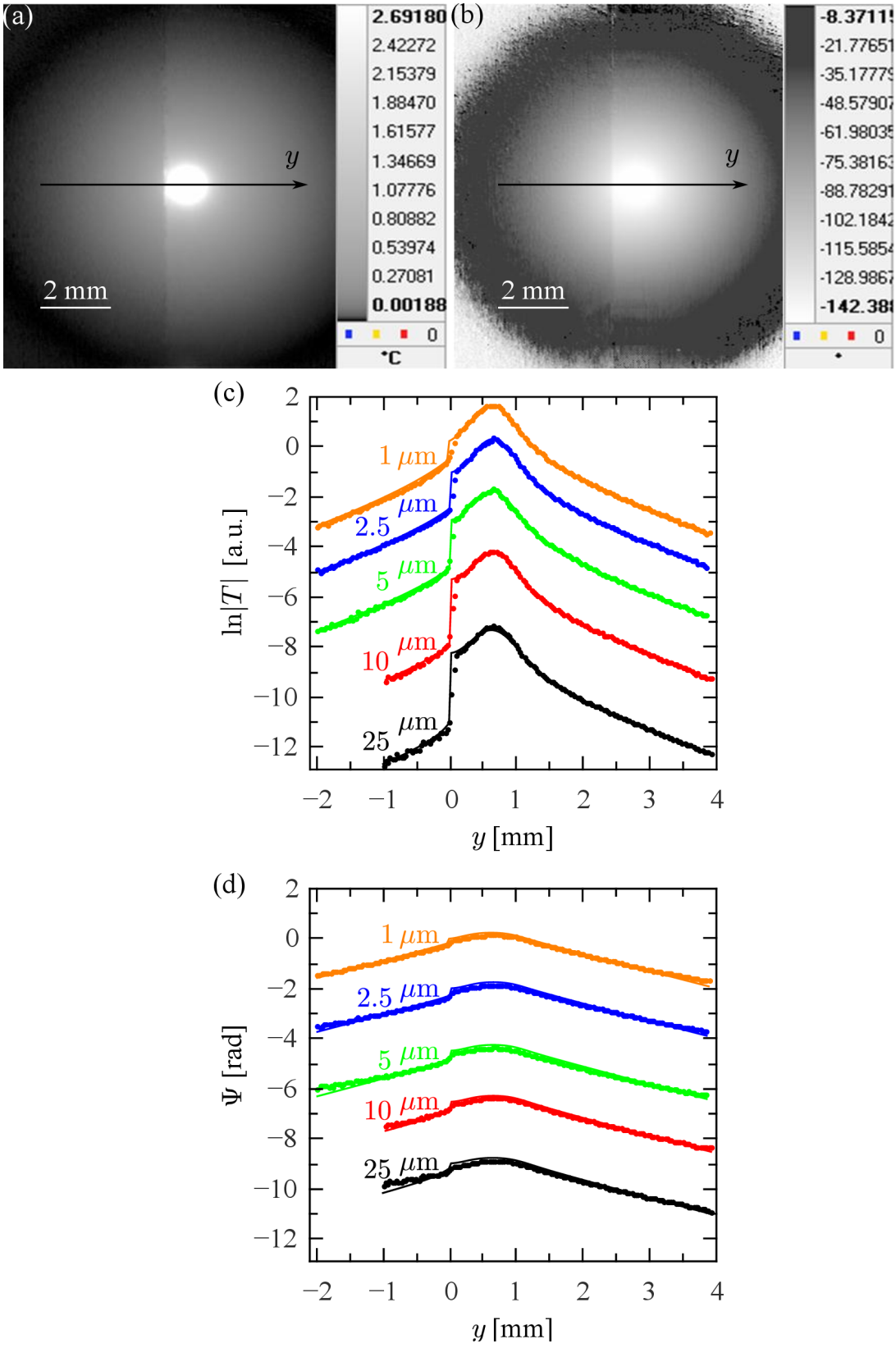
(a)
2.69180
2.42272
2.15379
1.88470
1.61577
1.34669
1.07776
0.80882
0.53974
0.27081
0.00188
0
°C
y
2 mm
(b)
-8.3711
-21.7765
-35.1777
-48.5790
-61.9803
-75.3816
-88.7829
-102.184
-115.585
-128.986
-142.38
0
y
2 mm
(c)
ln|T| [a.u.]
1 μm
2.5 μm
5 μm
10 μm
25 μm
y [mm]
(d)
Ψ [rad]
1 μm
2.5 μm
5 μm
10 μm
25 μm
y [mm]

Figure 7.11: (a) Amplitude and (b) phase thermograms for two AISI-304 stainless steel plates put in contact to simulate an infinite vertical crack 1 μm wide. The following experimental parameters have been used: $d = 0.65$ mm, $a = 0.35$ mm and $f = 0.6$ Hz. (c) Experimental natural logarithm of the surface temperature amplitude and (d) phase profiles along the y-axis for several crack widths. Dots correspond to experimental data and continuous lines to the fit to Equation (7.9).

We have performed the same kind of measurements in two blocks of stainless steel AISI-304, 2 cm thick. As this metallic alloy has a shiny surface, a thin graphite layer about 3 μm thick has been deposited onto the surface in order to increase both the absorption to the heating laser and the emissivity to infrared wavelengths. The amplitude and phase thermograms corresponding to a 1 μm wide crack are shown in Figures 7.11a and 7.11b, respectively.

The same experimental parameters as in Figure 7.9 have been used. The temperature profiles along the y-axis together with the fits to Equation (7.9) are shown in Figures 7.11c and 7.11d. We have obtained the following thermal resistance values: 7.0×10^{-4}, 4.7×10^{-4}, 2.0×10^{-4}, 1.1×10^{-4}, 3.5×10^{-5} $W^{-1}m^2K$, which correspond to air gaps of 27, 12, 5.2, 2.8 and 0.9 μm respectively. They are very close to the thicknesses of the nickel tape. As in the case of the glassy carbon, we have performed complementary measurements changing the experimental parameters a, d, f. We studied the temperature profiles along the y-axis for a 5 μm thick vertical crack keeping $d \approx 0.65$ mm, but changing a and f: (1) $a = 0.27$ mm, $f = 0.3$ Hz, (2) $a = 0.38$ mm, $f = 0.3$ Hz, (3) $a = 0.27$ mm, $f = 0.6$ Hz and (4) $a = 0.39$ mm, $f = 0.6$ Hz. The retrieved thermal resistances are 2.2×10^{-4}, 2.1×10^{-4}, 2.1×10^{-4} and 2.0×10^{-4} $W^{-1}m^2K$ respectively, corresponding to an air gap of $L = 5.5 \pm 0.5$ μm. This result confirms the robustness of the procedure. Then, we put the two glassy carbon plates in direct contact, i.e. without inserting nickel tape. As the surfaces in contact are polished, they simulate an extremely thin crack. The result depends slightly on the position at which the sample is excited. At some positions, we observe neither temperature amplitude contrast nor phase contrast. Moving the positions of the excitation spot on the same sample, we have obtained amplitude and phase contrasts

corresponding to air gaps below 300 nm, probably due to different surface conditions. At the locations where we do not detect the crack, it remains undetectable even when the modulation is increased up to 10 Hz and the laser beam is focused down to 100 μm. This result allows us to conclude that the upper limit for this thermal resistance is $R_{th} \leq 10^{-6}$ W^{-1}m^{2}K.

It is worth noting that detecting very narrow cracks requires using a high frequency together with a laser beam tightly focused close to the crack. However, in our infrared thermography setup the spatial resolution is 31 μm, so measurements with a thermal diffusion length $\mu \leq 100$ μm are not allowed. Under these experimental conditions, thermal resistances verifying $KR_{th} \leq 1$ μm will remain undetectable.

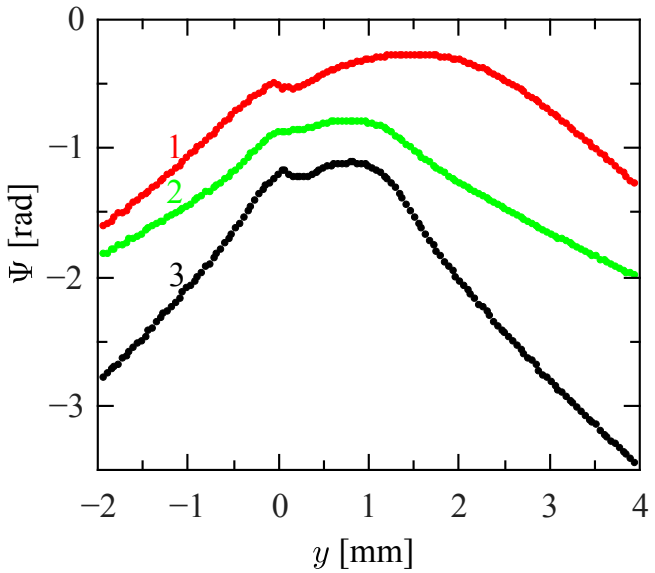

Figure 7.12: Experimental phase profiles of the surface temperature along the y-axis for a 25 μm thick vertical crack in AISI-304. (1) $d \approx 1.5$ mm, $a \approx 2.0$ mm, $f = 0.4$ Hz. (2) $d \approx 0.8$ mm, $a \approx 1.0$ mm, $f = 0.2$ Hz. (3) $d \approx 0.8$ mm, $a \approx 1.0$ mm, $f = 0.8$ Hz. The upwards jump of the phase at the crack position ($y = 0$) can be clearly observed.

Finally, we verify the unexpected reversal (upwards) jump of the phase at the crack position predicted by the model when the laser spot is very close and especially when it overlaps the crack. In Figure 7.12, we show temperature phase profiles along the y-axis for a 25 μm thick vertical crack in AISI-304. Three experimental

configurations satisfying $a > d$ are shown. The predicted reversal of the phase jump at the crack position is confirmed experimentally.

Note that the experimental results shown in Figures 7.9 - 7.11 do not exhibit a sharp discontinuity at the crack but a smooth transition involving around four pixels. This result is due to the imperfect imaging system of the IR camera (diffraction, multiple reflections, flare…). The so-called point spread function (PSF) of the optical system quantifies its effect, which depends on the lens quality. As in our system the effect is only noticeable at the crack position, it has not been taken into account in the fittings of the whole profiles. Nonetheless, it is worth noting that the microscope lens (with a resolution of 31 μm) produces a much smaller PSF than a 50 mm focal length lens with two extension tubes (providing a comparable resolution of 40 μm), with more than 10 pixels affected.

7.5 Summary

In this Chapter, we have dealt with the width characterization of infinite vertical cracks using lock-in thermography with optical excitation. First, we have found a semi-analytical expression for the surface temperature of a material containing such a crack when a modulated and focused laser beam impinges close to the crack. Both circular and line Gaussian spots are studied. The presence of the crack produces an abrupt jump in the amplitude and phase of the surface temperature at the crack position. Numerical simulations indicate that the highest amplitude temperature contrast is produced when a, d and μ satisfy the following condition: $d \approx \mu \approx 1.25a$. The validity of the model has been tested by performing lock-in thermography measurements on stainless steel and vitreous carbon samples containing cracks of calibrated width. By fitting simultaneously the amplitude and phase of the surface temperature to the proposed model, the width of the crack is obtained. The agreement between the optically calibrated width and the retrieved one is very good even for widths as narrow as 1 μm. In Chapter 8, the

characterization of vertical cracks of finite size is addressed. Nevertheless, it is important to say that this work shows the ability of lock-in thermography to characterize vertical cracks, which may occur in welding processes. However, in order to apply this method to retrieve the width of a real crack (for example, in a weld) it is still necessary to work out how to perform measurements without covering the specimen surface, which is a requirement for some non-destructive tests on in-service structures.

Chapter 8. On the characterization of finite vertical cracks with lock-in thermography

8.1 Discontinuous Galerkin solution for vertical cracks under lock-in laser excitation

In this Chapter, we study the propagation of thermal waves across narrow vertical cracks of finite size and arbitrary shape in a homogeneous material. No analytical solution can be found for this problem, thus a numerical approach must be adopted. In classical continuous finite elements methods (FEM), this heat diffusion problem is modeled as a transmission problem in a material consisting of two domains: the bulk and the air filling the crack, together with the corresponding boundary conditions of continuity of temperature and heat flux [155]. In this model it is necessary to use conforming meshes, i.e. tetrahedral subdivisions of the domains, in both the exterior and the interior of the crack, matching at the interfaces. Therefore, for very thin cracks this model requires excessively fine meshes, dramatically increasing memory resources and computing time. In order to overcome this problem, new numerical methods much more efficient than continuous FEM have been implemented [156,157], which allow to calculate the surface temperature of a sample containing thin cracks of any size and shape. These thin cracks are considered as an interface characterized by its

thermal contact resistance R_{th}. The mentioned methods are based on discontinuous Galerkin finite elements methods (DG-FEM [157]). In general, DG-FEM are natural tools to tackle physical problems with discontinuous solutions where classical FEM fail. However, the implementation of DG-FEM is not as straightforward as when dealing with continuous FEM, since DG-FEM require stabilization terms, depending on each particular problem. In particular, an extension of the Bauman-Oden DG-FEM for the Laplace equation [157] is required to model the propagation of thermal waves in cracked materials.

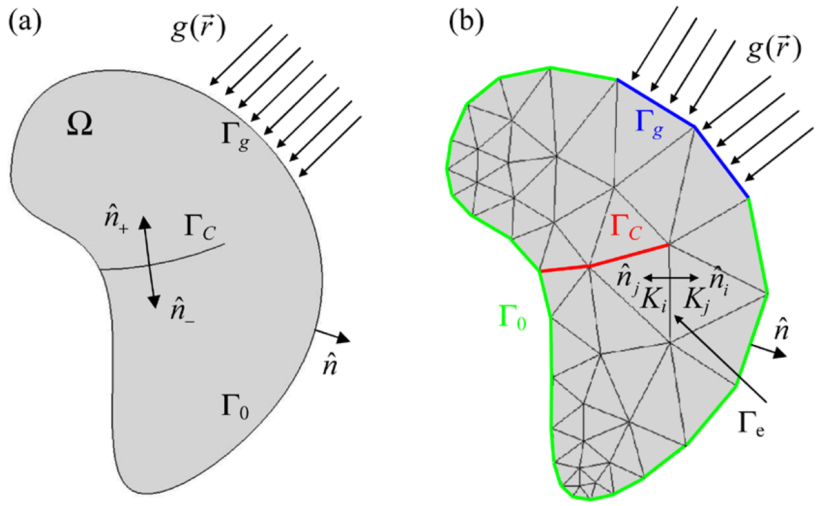

Figure 8.1: (a) Diagram of an opaque material of arbitrary shape containing a finite crack. Γ_g is the illuminated surface, Γ_C is the crack surface, Γ_0 is the non-illuminated external surface of the material and Ω is the sample volume. (b) Diagram of the meshed sample showing tetrahedra conforming with the crack.

In this Section, a brief description of the DG method developed by Omella et al is presented [158,159]. Let's consider a homogeneous and isotropic opaque sample occupying a volume Ω, limited by a surface boundary $\partial\Omega$. The geometry is depicted in Figure 8.1a. The sample contains a narrow crack extending along Γ_C. Since the crack is very thin, we assume that Γ_C is an interface. Some part of the sample surface Γ_g is illuminated by a laser beam modulated at frequency f. The non-illuminated section of the boundary is denoted as Γ_0. The oscillating component of the sample temperature $T(\vec{r})$

$T(\vec{r})$ can be obtained by solving the Helmholtz equation with the appropriate boundary and transmission conditions of temperature and heat flux

$$\nabla^2 T(\vec{r}) + \frac{i2\pi f}{D} T(\vec{r}) = 0,\ \vec{r} \in \Omega \setminus \Gamma_C \tag{8.1a}$$

$$\left(K\frac{\partial T_-}{\partial n_-} + K\frac{\partial T_+}{\partial n_+} \right)\Big|_{\Gamma_C} = 0,\ \vec{r} \in \Gamma_C \tag{8.1b}$$

$$(T_- - T_+)\,|_{\Gamma_C}(\vec{r}) + R_{th}(\vec{r}) K \frac{\partial T_-}{\partial n_-}\Big|_{\Gamma_C} = 0,\ \vec{r} \in \Gamma_C \tag{8.1c}$$

$$\frac{\partial T}{\partial n}\Big|_{\Gamma_0}(\vec{r}) = 0,\ \vec{r} \in \Gamma_0 \tag{8.1d}$$

$$K\frac{\partial T}{\partial n}\Big|_{\Gamma_g}(\vec{r}) = g(\vec{r}),\ \vec{r} \in \Gamma_g \tag{8.1e}$$

where K and D are the thermal conductivity and diffusivity of the sample respectively, subscripts $+$ and $-$ refer to both sides of the crack (no matter which is which), $\hat{n}$ is the outwards unitary normal vector at the sample surface, $\hat{n}_+$ and $\hat{n}_-$ are the outwards unitary normal vectors at the crack sides and $g(\vec{r})$ is the incoming heat flux applied on the illuminated part of the sample boundary.

The first step to apply a DG method to solve Equation (8.1) is to define a 'triangulation' $\{K_j\}_{j=1}^M$ of the total volume, being K_j each of the M tetrahedra, as shown in Figure 8.1b. The faces of the tetrahedra touching the crack must match the crack surface. The second step is to choose simple piecewise functions T_h (for instance polynomials of degree m) to approximate the temperature T in each tetrahedron. For practical purposes, the final step is to write a discrete variational formulation from Equation (8.1) by using Green's formula and defining the so-called *numerical fluxes* [157], i.e. approximations to T and ∇T at the boundaries of each tetrahedron. The flux choices affect the stability and the accuracy of the method and therefore, different choices lead to different methods.

Any variational formulation of a DG method needs the introduction of the so-called *average* and *jump* traces of functions defined on the triangulation [157]. Let $\Gamma = \left(\bigcup_{j=1}^M \partial K_j\right) \setminus (\Gamma_C \cup \partial\Omega)$ be the *skeleton* of the triangulation, that is, all faces of

the tetrahedra that belong neither to the crack nor to the exterior boundary. Let Γ_e be an interior face shared by two tetrahedra K_i and K_j and w any scalar or vector function on Ω, we set the averages $\langle w \rangle$ and jumps $[\![w]\!]$ on Γ_e as:

$$\langle w \rangle = \tfrac{1}{2}(w_i + w_j), \tag{8.2a}$$

$$[\![w]\!] = w_i \cdot \hat{n}_i + w_j \cdot \hat{n}_j, \tag{8.2b}$$

being $\hat{n}_i$ and $\hat{n}_j$ the outwards unitary normal vectors to K_i and K_j respectively, as can be seen in Figure 8.1b.

Thus, applying Green's formula [155] in a standard way in each tetrahedron the DG solution of Equation (8.1) is the m-degree polynomial piecewise function $T_h \approx T$ that satisfies the variational formulation

$$\begin{aligned} \sum_{j=1}^{M} \int_{K_j} \nabla T_h \nabla v_h - \int_{\Gamma} \langle \nabla T_h \rangle [\![v_h]\!] + \int_{\Gamma_C} \frac{1}{R_{th}(\vec{r})K} [\![T_h]\!][\![v_h]\!] \\ - \frac{i2\pi f}{D} \int_{\Omega} T_h v_h = \frac{1}{K} \int_{\Gamma_g} g(\vec{r}) v_h, \end{aligned} \tag{8.3}$$

for all m-degree polynomial piecewise functions v_h in the triangulation $\{K_j\}_{j=1}^{M}$ of Ω.

Unfortunately, the variational formulation in Equation (8.3) is unstable (it amplifies rounding errors). However, it is possible to stabilize it by adding perturbation terms, related to particular choices of the numerical fluxes, that actually are null for the exact solution (but not for the approximate solution) and do not damage the numerical solution at all. A proper DG variational formulation of Equation (8.1), based on the Bauman-Oden choice [157] of the numerical fluxes, is:

$$\begin{aligned} \sum_{j=1}^{M} \int_{K_j} \nabla T_h \nabla v_h - \int_{\Gamma} \langle \nabla T_h \rangle [\![v_h]\!] + \int_{\Gamma} [\![T_h]\!] \langle \nabla v_h \rangle \\ + \int_{\Gamma_C} \frac{1}{R_{th}(\vec{r})K} [\![T_h]\!][\![v_h]\!] - \frac{i2\pi f}{D} \int_{\Omega} T_h v_h = \frac{1}{K} \int_{\Gamma_g} g(\vec{r}) v_h. \end{aligned} \tag{8.4}$$

The third addendum in Equation (8.4) is an anti-symmetric version of the second one and comes from the Bauman-Oden choice of the numerical fluxes. It is introduced in order to stabilize the numerical results of Equation (8.3).

From a practical point of view, the variational formulation is a cornerstone to

introduce the DG model in finite elements packages as FEniCS or FreeFem++ [160,161]. The Bauman-Oden type formulation shown in Equation (8.4) is useful to simulate thermal waves in cracked materials when the location of the crack Γ_C is well known. However, due to the presence of the thermal resistance in the denominator, Equation (8.4) suffers from a computational limitation: the narrower the crack, the larger the computing time required in simulations. Furthermore, it is not possible to plug a zero thermal resistance in the fourth addendum of Equation (8.4). This is a hard impediment when solving inverse problems, in which we attempt to determine the thermal resistance from surface thermograms by a least squares fitting, without previous knowledge of the (eventually null) value of the thermal resistance in the trial location Γ_C. Therefore, it is necessary to develop variational formulations whose computational time is independent of the value of the thermal resistance and that allow zero thermal resistances in a trial location Γ_C, probably larger than the real crack.

Let $h_e = \frac{1}{2}\left(h_{Ki} + h_{Kj}\right)$ be the average linear size of two tetrahedra K_i and K_j that share face Γ_e; that is, the average size of the diameters of the smallest circumscribed sphere around each tetrahedron. The variational formulation of the DG method proposed is:

$$\begin{aligned}
&\sum_{j=1}^{M}\int_{K_j}\nabla T_h\nabla v_h - \frac{i2\pi f}{D}\int_{\Omega}T_h v_h - \int_{\Gamma}\langle\nabla T_h\rangle[\![v_h]\!] + \int_{\Gamma}[\![T_h]\!]\langle\nabla v_h\rangle \\
&\quad - \int_{\Gamma_C}\frac{h_e}{h_e + CR_{th}^2(\vec{r})K}\langle\nabla T_h\rangle[\![v_h]\!] \\
&\quad + \int_{\Gamma_C}\frac{h_e}{h_e + CR_{th}^2(\vec{r})K}[\![T_h]\!]\langle\nabla v_h\rangle \\
&\quad + \int_{\Gamma_C}\frac{h_e R_{th}(\vec{r})K}{h_e + CR_{th}^2(\vec{r})K}\langle(\nabla T_h\cdot\hat{n})\,\hat{n}\rangle\cdot\langle(\nabla v_h\cdot\hat{n})\,\hat{n}\rangle \\
&\quad + \int_{\Gamma_C}\frac{CR_{th}(\vec{r})}{h_e + CR_{th}^2(\vec{r})K}[\![T_h]\!][\![v_h]\!] = \frac{1}{K}\int_{\Gamma_g}g(\vec{r})v_h,
\end{aligned} \tag{8.5}$$

where $\hat{n}$ is the unitary outwards normal vector to the tetrahedral. In fact, Equation (8.5) represents a family of DG methods depending on the value of constant C. We have analyzed the methods corresponding to $C = 0$, $C = 1$ $\mathrm{Wm^{-2}K^{-1}}$ and $C = 1/R_{th}$. The three methods are robust and computationally efficient. However, for the sake of

simplicity and rapidness we have chosen $C = 0$ for the numerical computations in this Chapter. Notice that for $C = 0$ and $C = 1$ $\mathrm{Wm^{-2}K^{-1}}$. Equation (8.5) reduces to the classical Bauman-Oden method [139] for non-cracked materials when R_{th} is null. The computation time of these three methods is independent of the value of the thermal resistance.

Finally, let us remark that both Equations (8.4) and (8.5) require m-degree polynomial piecewise function $T_h \approx T$ with degree $m \geq 2$. This is a purely mathematical requirement for the stability of DG Bauman-Oden type methods and it has to be taken into account just in the selection of the trial functions in finite element packages as FEniCS or FreeFem++ [160,161].

8.2 Numerical simulations for semi-infinite and finite vertical cracks

Figure 8.2a shows the geometry of a vertical crack of arbitrary shape and size. Although the theoretical model developed in the previous section is valid for vertical cracks of any shape and size, we mainly performed numerical simulations for surface breaking semi-infinite cracks (infinite lateral extension and constant depth b), since preparing samples with calibrated cracks of this shape is easier. The geometry of these cracks is given in Figure 8.2b and their discretization is shown in Figure 8.3. As can be seen, the centered and densely discretized area corresponds to the illuminated zone around the center of the laser spot. In order to capture the geometrical characteristic lengths and the natural thermal wavelength $2\pi\mu$ of the solution, the size of the tetrahedra is between $\min(b/2, a/4, \mu/3)$ and 2μ, where $\mu = \sqrt{D/(\pi f)}$ is the thermal diffusion length.

In Chapter 7, when working with infinite cracks, it was found that the highest temperature contrast at the crack position is produced when $d \approx \mu \approx 1.25a$. In this Chapter, we follow these conditions and analyze the influence of the crack depth b on the temperature profile across the crack. Simulations are performed for AISI-304 stainless steel ($D = 4.0$ $\mathrm{mm^2s^{-1}}$ and $K = 15$ $\mathrm{Wm^{-1}K^{-1}}$). As a first test of consistency the

temperature profile corresponding to an infinite crack $(b \to \infty)$ has been calculated both using the analytical solution given by Equation (7.9) in Chapter 7 and using the numerical solution as expressed by Equation (8.5) in Section 8.1. The agreement is excellent for all the thermal resistances tested, ranging from $10^{-7} - 10^{-1}$ W^{-1}m^{2}K.

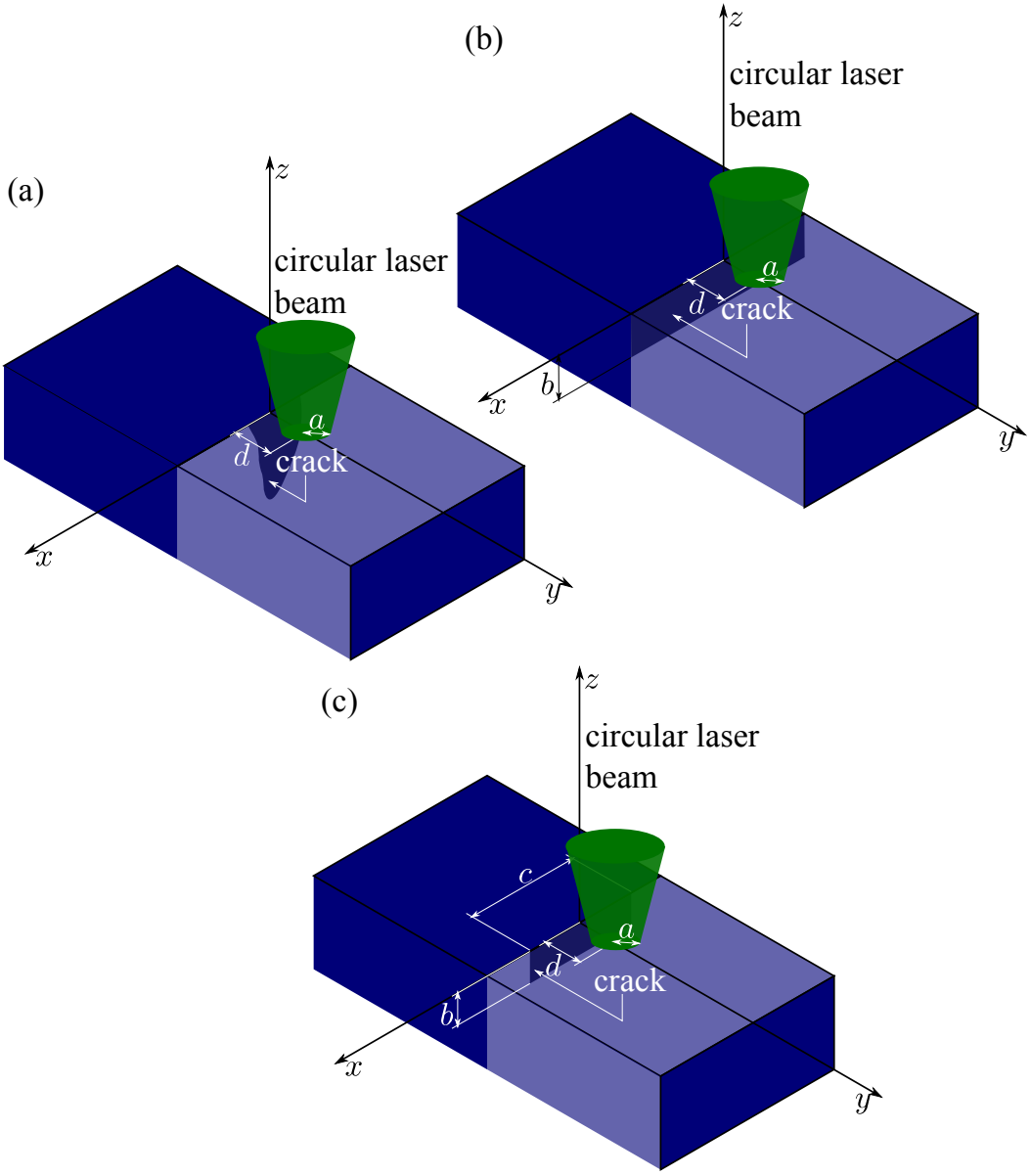

Figure 8.2: Scheme of (a) a finite vertical crack (in grey) of arbitrary shape, (b) a semi-infinite vertical crack (in grey) of height b and (c) a rectangular vertical crack (in grey) of height b and length c.

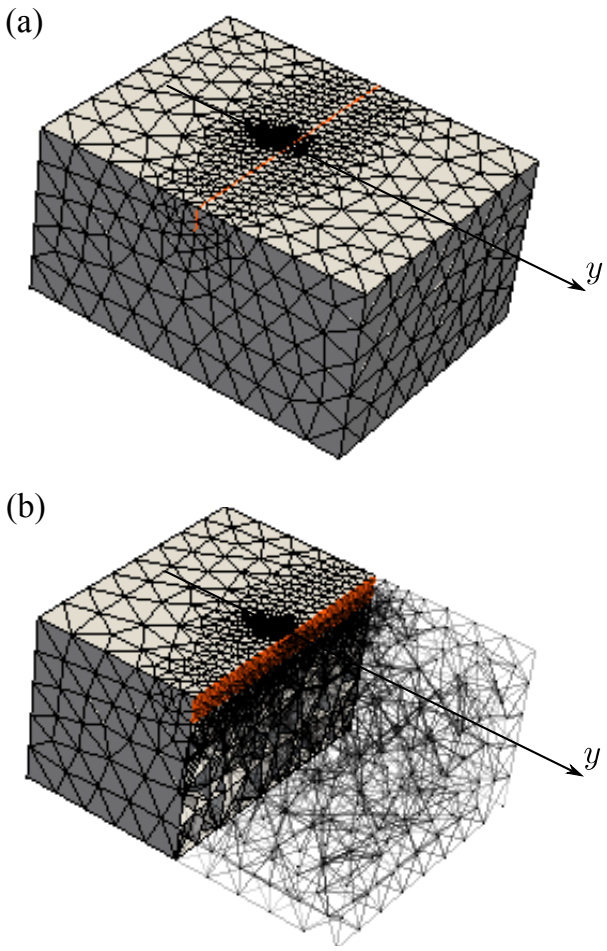

Figure 8.3: (a) Mesh with 6 491 tetrahedra of a cracked thermally thick prism of AISI-304 with dimensions 14.6 mm ×11.6 mm ×7.3 mm ($10\mu \times 8\mu \times 5\mu$) for a modulation frequency $f = 0.6$ Hz. (b) A semi-infinite crack with depth $b = 1$ mm is depicted in red.

Figure 8.4 shows the natural logarithm of the temperature amplitude $\ln|T|$ and phase Ψ along the y-axis for an AISI- 304 sample containing a semi-infinite vertical crack $(y = 0)$ and illuminated by a circular Gaussian spot. Calculations are performed using Equation (8.5) with $d = 1$ mm, $a = 0.75$ mm, $f = 1$ Hz and $R_{th} = 10^{-3}$ W^{-1}m^{2}K (which is equivalent to a crack thickness $L = 25$ µm according to the relation $R_{th} = L/K_{air}$ [19]). Four crack depths are analyzed, i.e. $b = 0.25$, 0.5, 1 and 2 mm besides the infinite one. As can be seen, as the crack depth diminishes the height of the jump of $\ln|T|$ at the crack position $(y = 0)$ is reduced. The phase behavior is more

complicated instead; for the deepest cracks the jump of Ψ at the crack position is reversed, i.e. the jump is upwards.

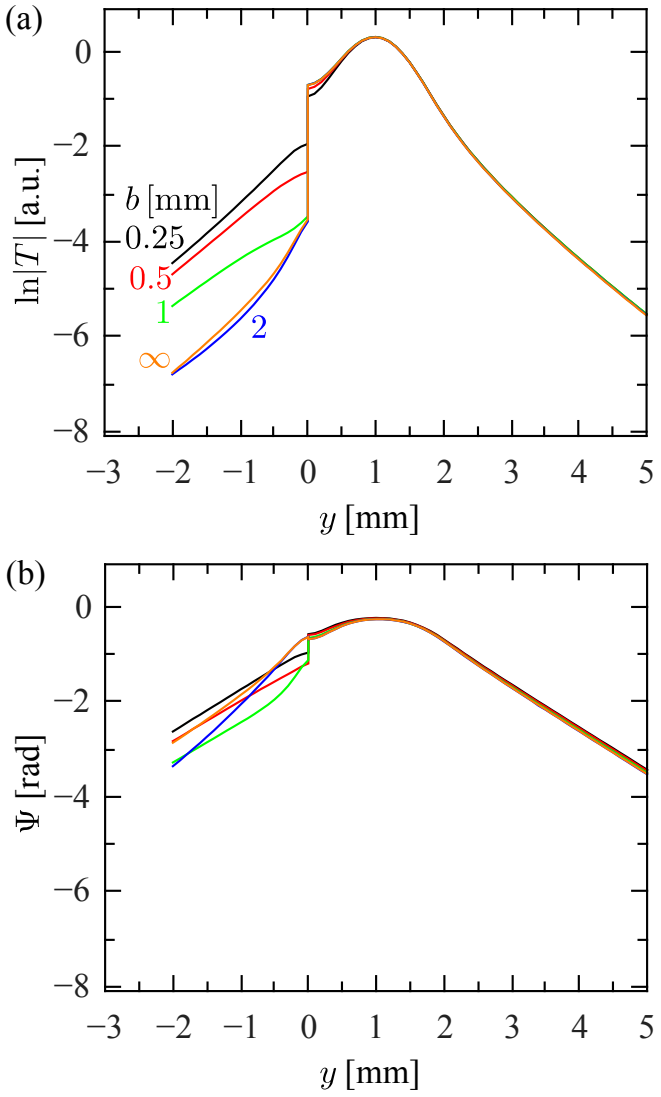

Figure 8.4: Simulation of (a) the natural logarithm of the temperature amplitude and (b) phase along the y-axis for an AISI-304 sample ($D = 4$ mm^{2}s^{-1} and $K = 15$ Wm^{-1}K^{-1}) containing a semi-infinite vertical crack of $R_{th} = 10^{-3}$ W^{-1}m^{2}K. The sample is illuminated at $d = 1$ mm with a Gaussian laser spot of $a = 0.75$ mm modulated at $f = 1$ Hz. Several crack depths b are studied.

In order to quantify the temperature jump at the crack position we introduce the temperature amplitude contrast $\Delta_{|T|}$ and phase contrast Δ_{Ψ}, which are defined respectively as

$$\Delta_{|T|} = \frac{|T(0,\varepsilon,0)| - |T(0,-\varepsilon,0)|}{|T(0,d,0)|}, \tag{8.6}$$

$$\Delta_{\Psi} = \Psi(0,\varepsilon,0) - \Psi(0,-\varepsilon,0), \tag{8.7}$$

where ε represents an infinitesimal distance.

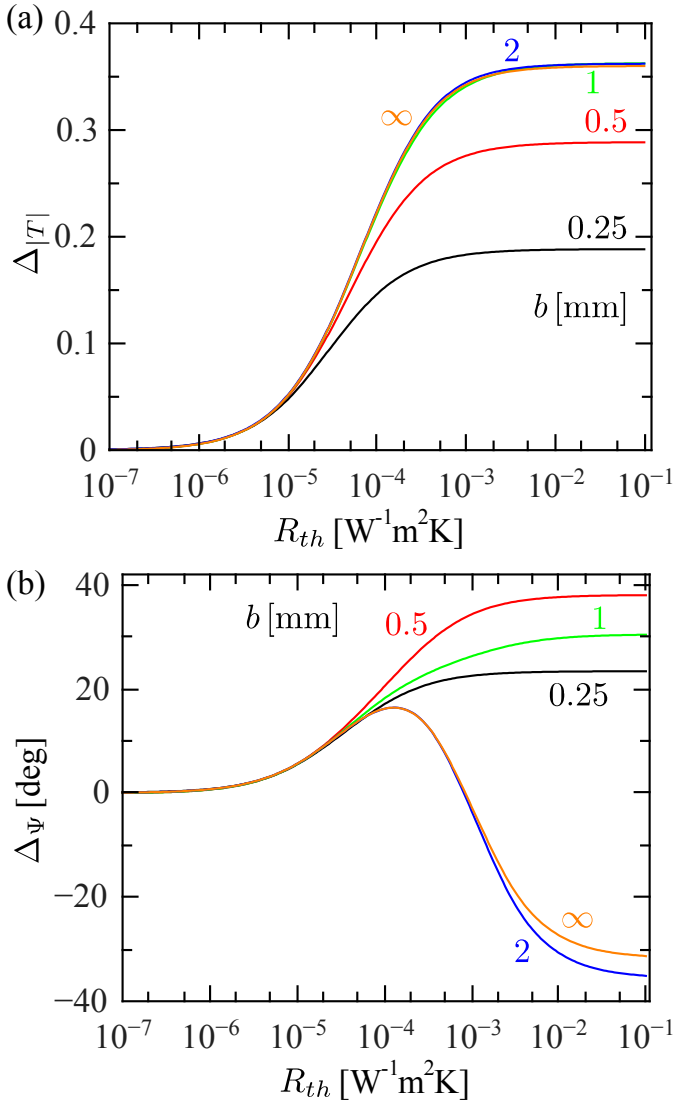

Figure 8.5: Numerical simulation of the dependence of $\Delta_{|T|}$ and Δ_{Ψ} on the thermal contact resistance R_{th}. Calculations are performed for an AISI-304 sample ($D = 4$ mm^{2}s^{-1} and $K = 15$ Wm^{-1}K^{-1}) with $d = 1$ mm, $a = 0.75$ mm and $f = 1$ Hz. Several crack depths b are analyzed.

In figure 8.5 we analyze the dependence of $\Delta_{|T|}$ and Δ_{Ψ} on the thermal resistance of the crack for different crack depths. Calculations are performed with the

same parameters as in Figure 8.4 ($d = 1$ mm, $a = 0.75$ mm, $f = 1$ Hz). For $R_{th} < 10^{-6}$ W^{-1}m^{2}K (crack width narrower than 25 nm), the temperature contrast is negligible and the crack remains undetected. As R_{th} increases, $\Delta_{|T|}$ is enhanced until it reaches an asymptotic value. This value highly depends on the crack depth. For instance, the maximum value of $\Delta_{|T|}$ for $b = 0.25$ mm is half of the value reached for an infinite crack. However, the behavior of Δ_{Ψ} is not monotonous. It changes from negative values for deep crack to positive values for shallow cracks. Anyway, results shown in Figures 8.4 and 8.5 (where the modulation frequency is kept constant, $f = 1$ Hz) indicate that cracks deeper than 1.5 mm are difficult to distinguish from infinite cracks.

To enhance this limit, we tried using lower frequencies which means increasing the thermal diffusion length (μ) and hence, the penetration depth into the sample. Figure 8.6 shows the simulation of $\ln|T|$ and Ψ profiles along the y-axis, similar as in Figure 8.4, but reducing the modulation frequency from 1 Hz to 0.1 Hz. Additionally, Figure 8.7 shows the dependence of $\Delta_{|T|}$ and Δ_{Ψ} on the thermal resistance of the crack as in Figure 8.5, but for a modulation frequency $f = 0.1$ Hz. As expected, by reducing the frequency we can look deeper inside the sample, in such a way that cracks as deep as 3.5 mm can be distinguished from an infinite one. Note that the limiting distinguishable depth verifies the following relation: $b_{limit} \approx \mu$.

Finally, in order to show the usefulness of the discontinuous finite elements to deal with vertical cracks of any shape, we performed simulations for rectangular cracks of depth b and length c, centered on the y-axis (see Figure 8.2c). In Figure 8.8 we show the simulation of $\ln|T|$ and Ψ along the y-axis for an AISI-304 sample containing a rectangular vertical crack. The same parameters as in Figure 8.4 are used ($R_{th} = 10^{-3}$ W^{-1}m^{2}K, $d = 1$ mm, $a = 0.75$ mm and $f = 1$ Hz). The crack depth $b = 0.5$ mm is kept fixed while the effect of changing its length c is studied. Notice that as the crack length decreases the height of the jump of $\ln|T|$ and Ψ at the crack position $(y = 0)$ is reduced. It is worth noting how such a small crack with an area 0.5×0.5 mm^2 is clearly detected by a high enough jump. Anyway, for retrieving the two parameters characterizing a

rectangular crack (b and c) with the highest accuracy we can fit several temperature profiles (not just $x = 0$) and several frequencies for each of them.

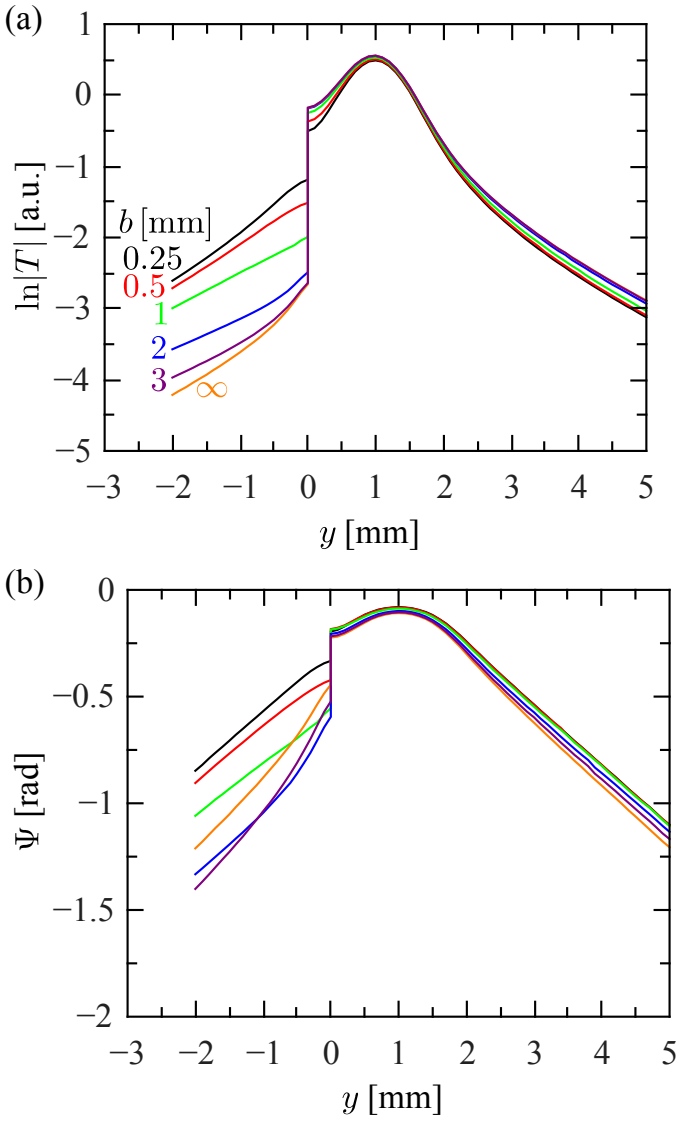

Figure 8.6: Simulation of (a) the natural logarithm of the temperature amplitude and (b) phase along the y-axis for an AISI-304 sample containing a semi-infinite vertical crack of $R_{th} = 10^{-3}$ W^{-1}m^{2}K. The sample is illuminated at $d = 1$ mm with a Gaussian laser spot of $a = 0.75$ mm modulated at $f = 0.1$ Hz. Several crack depths b are studied.

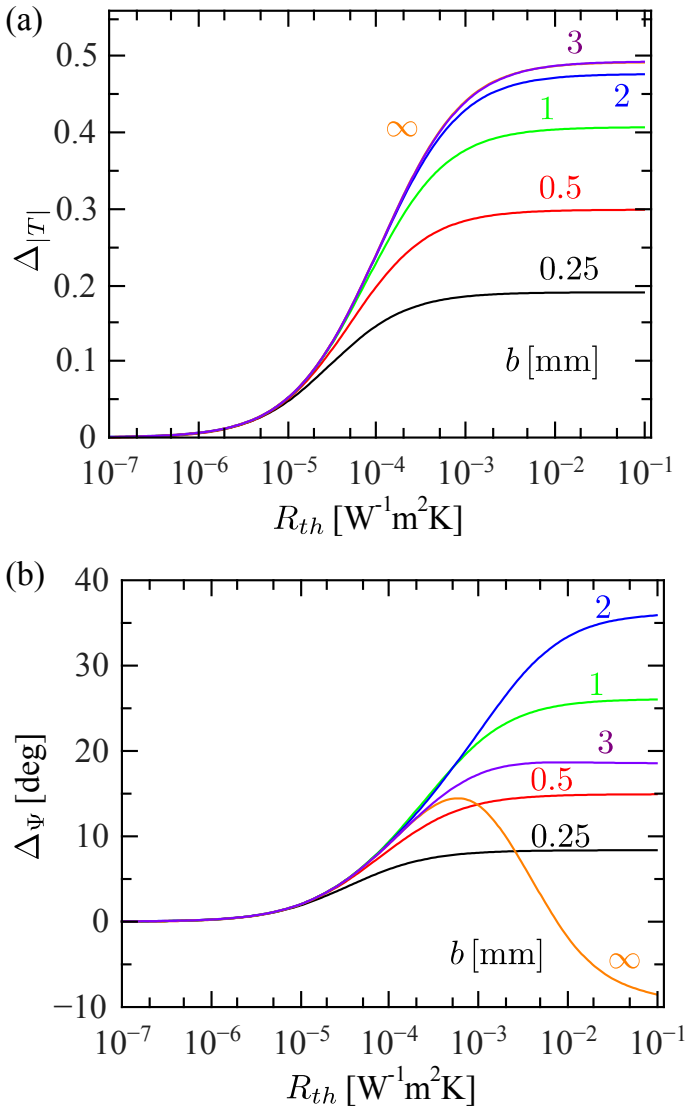

Figure 8.7: Numerical simulation of the dependence of $\Delta_{|T|}$ and Δ_Ψ on the thermal contact resistance R_{th}. Calculations are performed for an AISI-304 sample with $d = 1$ mm, $a = 0.75$ mm and $f = 0.1$ Hz. Several crack depths b are analyzed.

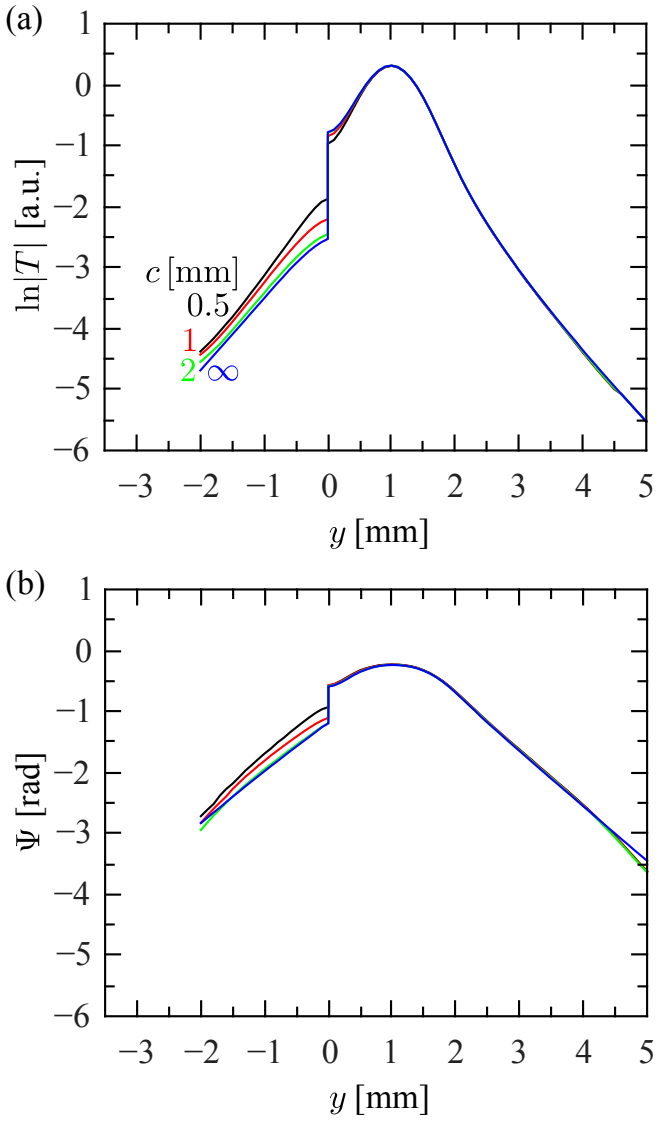

Figure 8.8: Simulation of (a) the natural logarithm of the temperature amplitude and (b) phase along the y-axis for an AISI-304 sample containing a rectangular vertical crack of $R_{th} = 10^{-3}$ W^{-1}m^{2}K. The sample is illuminated at $d = 1$ mm with a Gaussian laser spot of $a = 0.75$ mm modulated at $f = 1$ Hz. The depth $b = 0.5$ mm is kept while several lengths c are studied.

It is worth mentioning that all the numerical simulations presented use polynomial functions of degree 2 and have been performed with an Intel Pentium(R) 4 CPU 3.0 GHz $\times 2$ with a RAM of 1.5 GB. The computing time of a simulation is about 2 min.

8.3 Experimental results and limitations for AISI-304 calibrated cracks

A diagram of the lock-in thermography setup is shown in Figure 2.7 of Chapter 2. In order to prepare calibrated semi-infinite vertical cracks, a thin film of thickness L was inserted between two blocks and buried at a depth b beneath the surface (see Figure 8.9). Both blocks and film are made of AISI-304 stainless steel. Some pressure was applied at the outer edges of the blocks to keep the best thermal contact between them and the film. We picked two films thicknesses, namely $L = 25$ and 12.5 µm. Remembering the relationship between the air gap of the crack and its thermal resistance $R_{th} = L/K_{air}$, they represent thermal resistances of 10^{-3} and 5×10^{-4} $W^{-1}m^2K$ respectively. Moreover, two depths were selected: $b = 0.7$ and 1.1 mm. As the steel blocks have shiny surfaces, a thin graphite layer about 3 µm thick was deposited onto the surface in order to increase both the absorption of the heating laser and the emissivity at infrared wavelengths.

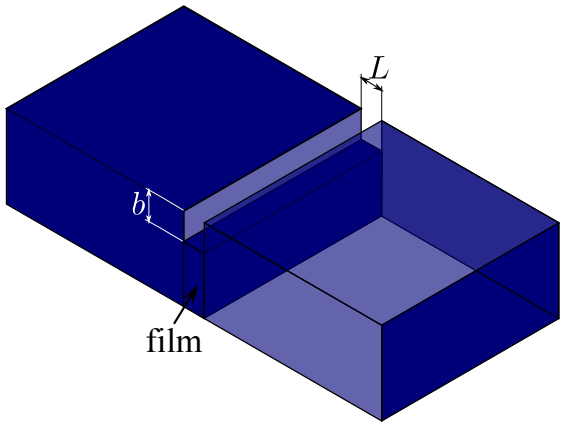

Figure 8.9: Diagram of the semi-infinite vertical crack simulated for the experiment: A thin film of thickness L is sandwiched between two blocks and is buried at a depth b beneath the surface. Blocks and film are made of the same material AISI-304 stainless steel.

The additional thermal resistance due to the lack of perfect thermal contact between film and blocks has been also evaluated. To do this, we put the film just reaching the surface, i.e. $b = 0$. In this way, we have two infinite vertical cracks of approximately the same width, that according to the in-series thermal resistor model

[162] are equivalent to a unique crack with double thermal resistance. We measured the temperature profiles (amplitude and phase) along the y-axis using the following experimental parameters $f = 0.6$ Hz, $d \approx 0.65$ mm and $a \approx 0.50$ mm. By fitting this temperature profile either to Equation (7.9) of Chapter 7 or to Equation (8.5), we obtained a thermal resistance $R_{th} \approx 1 \times 10^{-5}$ W^{-1}m^{2}K, which is equivalent to an air gap $L \approx 0.25$ μm. Such a small value can be neglected if compared to air gaps of the simulated crack ($12.5 - 25$ μm). It is important to say that we applied a thin layer of thermal conductive grease on both touching surfaces in order to improve the adherence of the film to the blocks and also to reduce the thermal resistance at their interfaces. Accordingly, we assume a perfect thermal contact between film and steel blocks.

In Figures 8.10a and 8.10b, we show the amplitude and phase thermograms corresponding to a 25 μm thick crack, buried at depth $b = 0.7$ mm, using the following experimental parameters: $f = 0.6$ Hz, $d \approx 0.65$ mm and $a \approx 0.35$ mm. In Figure 10c, we show by dots the $\ln|T|$ and by diagonal crosses the Ψ profiles along the y-axis corresponding to a film with $L = 25$ μm buried at depths $b = 0.7$ (black symbols) and 1.1 mm (red symbols). Measurements have been performed with $f = 0.6$ Hz, $d \approx 0.65$ mm and $a \approx 0.50$ mm. The continuous lines are the least squares fits to Equation (8.5) using four free parameters: I_0, a, b and R_{th}. Note that the fit quality is better for $\ln|T|$ than for Ψ since the jump at the crack is much higher for the former. The retrieved couples thermal resistance and depth (R_{th}, b) are (0.9×10^{-3} W^{-1}m^{2}K, 0.72 mm) and (1.1×10^{-3} W^{-1}m^{2}K, 1.3 mm), which correspond to air thicknesses of 23 and 28 μm, respectively. Both air gap thickness and depth are very close to the nominal values of the metallic film. On the other hand, in both fits the radius of the laser spot is in the range $a = 0.48 - 0.52$ mm.

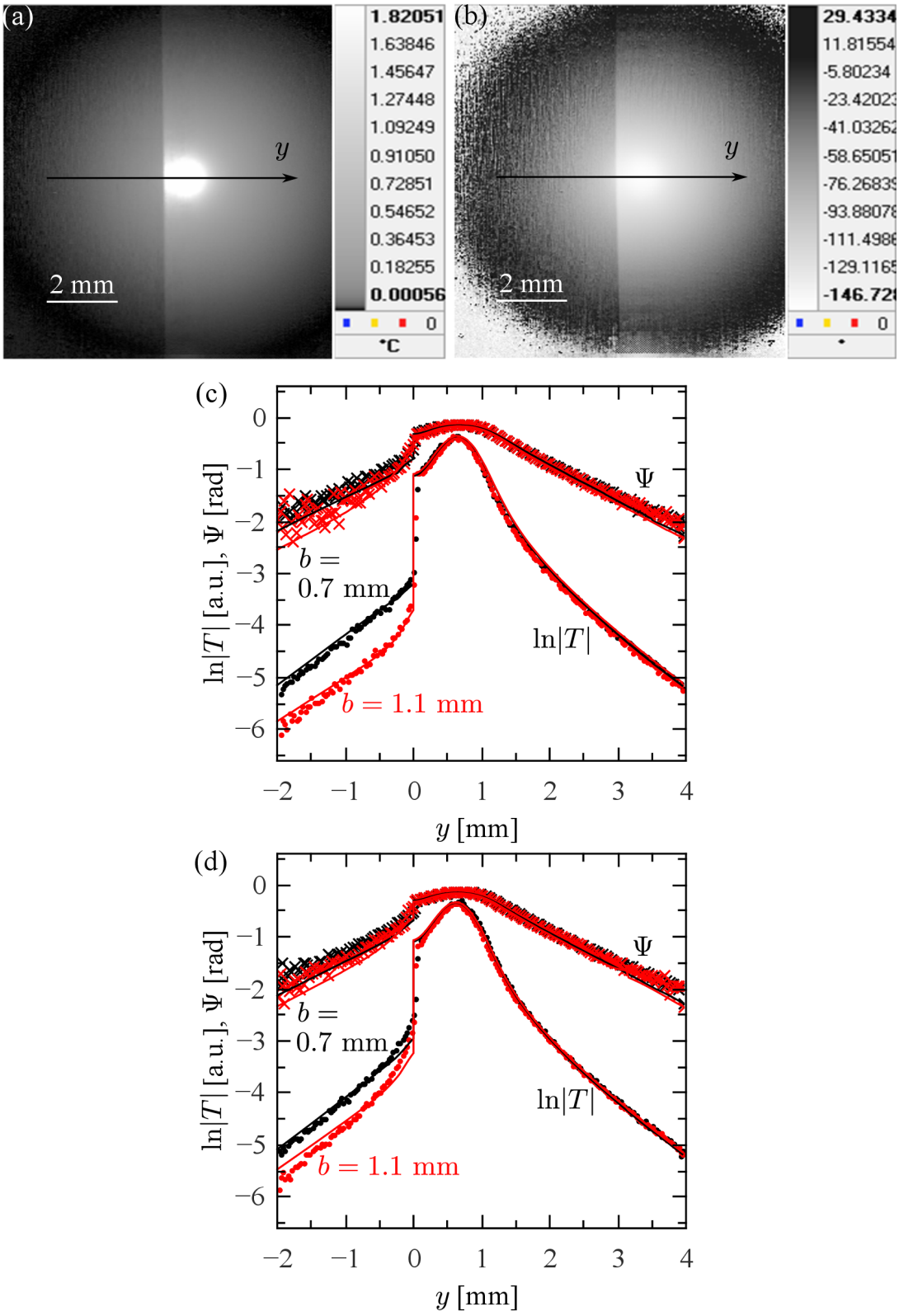
(a)
1.82051
1.63846
1.45647
1.27448
1.09249
0.91050
0.72851
0.54652
0.36453
0.18255
0.00056
°C
y
2 mm
(b)
29.4334
11.81554
-5.80234
y
2 mm
(c)
ln|T| [a.u.], Ψ [rad]
Ψ
b = 0.7 mm
ln|T|
b = 1.1 mm
y [mm]
(d)
ln|T| [a.u.], Ψ [rad]
Ψ
b = 0.7 mm
ln|T|
b = 1.1 mm
y [mm]

Figure 8.10: (a) Amplitude and (b) phase thermograms for two AISI-304 blocks sandwiching a 25 μm thick film of the same material. The film is buried 0.7 mm beneath the surface. The following experimental parameters have been used: $d \approx 0.65$ mm, $a \approx 0.50$ mm and $f = 0.6$ Hz. Experimental $\ln|T|$ (dots) and Ψ (diagonal crosses) of the surface temperature along the y-axis for two thin film thicknesses: (c) 25 μm and (d) 12.5 μm. The thin film is buried at two different depths $b = 0.7$ mm (black) and 1.1 mm (red). Symbols correspond to experimental data and continuous lines to the fit to Equation (8.5).

We have performed the same measurements on an AISI-304 film 12.5 μm thick. The same experimental parameters as before have been used. The experimental data are shown by symbols in Figure 8.10d together with the fits to Equation (8.5), which are represented by the continuous lines. The retrieved couples thermal resistance and depth (R_{th}, b) are $(0.45 \times 10^{-3}$ W^{-1}m^{2}K, 0.69 mm) and $(0.52 \times 10^{-3}$ W^{-1}m^{2}K, 1.1 mm), which correspond to air thicknesses of 11.5 and 13.5 μm, respectively. Both air gap thickness and depth are very close to the nominal values of the metallic film. As before, in both fits the radius of the laser spot is in the range $a = 0.49 - 0.53$ mm.

8.4 Summary

In this Chapter, we have focused our attention on flat vertical cracks because they are difficult to detect and at the same time, it is relatively simple to prepare calibrated samples. The simulations performed on semi-infinite and rectangular vertical cracks indicate that the temperature amplitude and phase profiles along the direction normal to the crack through the center of the exciting spot exhibit jumps at both sides of the crack. The height of these jumps is highly sensitive to the crack parameters (depth, thickness and length). In order to check the ability of the method to retrieve these parameters we have performed lock-in thermography measurements on samples containing calibrated semi-infinite narrow cracks of different thicknesses and depths. Least squares fitting of the data yielded values of the crack thickness and depth in good

agreement with the nominal values. A Bauman-Oden type discontinuous Galerkin finite elements method has been used to numerically solve the surface temperature of semi-infinite samples containing arbitrarily narrow cracks of any shape when the sample surface is illuminated by a modulated and focused laser beam. The main advantage of discontinuous Galerkin finite elements method is that, unlike classical continuous finite elements methods, it allows surface temperature calculations in the presence of very narrow cracks. Moreover, computing time and memory resources are kept down to very reasonable values. This powerful method opens the possibility of characterizing real cracks of arbitrary shape, size and orientation from lock-in thermography measurements. Anyway, this goal requires developing robust inverse algorithms since retrieving complex crack surfaces is a severely ill-posed problem, i.e. very sensitive to data noise. This issue is out of the scope of this thesis, but it is part of the PhD thesis of Ángel Javier Omella at the Department of Applied Mathematics, Universidad de Zaragoza (Spain).

Chapter 9. Characterization of infinite vertical cracks with pulsed spot thermography

9.1 Pulsed thermography for crack detection and characterization

Non-destructive testing and evaluation of surface breaking cracks in a wide variety of in-service devices has been a challenging task for modern industries and laboratories. Several well established methodologies like dye penetrant, magnetic particles, eddy currents and x-ray have been proposed and used to detect fissures as well as defects in materials. Alternative techniques like vibrothermography or optically stimulated thermography have gained attention in recent decades due to their performance in crack detection and characterization [129,131,134,144]. In vibrothermography, the sample is excited by ultrasonic waves and the contacting surfaces of mechanical discontinuities produce heat, that propagates to the sample surface indicating the presence of the defect on a cold background. This technique has received increasing attention in the last decade because of its ability to detect and characterize cracks in a wide variety of materials covering metals, ceramics, polymers and composites [3–10].

However, it might be difficult for this technique to detect open cracks with barely rubbing surfaces. On the other hand, the ultrasonic transducer needs to be in

contact with the sample surface, thus reducing its versatility. Optically stimulated infrared thermography is fully non-contact instead. In this case, the presence of the defect produces just a perturbation of the existing surface temperature field generated by the external optical excitation. Moreover, the spatial configuration of the illumination strongly affects the detectability of cracks. For example, considering vertical cracks, if the sample is excited by a homogeneous illumination which produces a heat flux perpendicular to the sample surface, the crack will barely disperse this flux, thus a negligible signature will be present on the surface temperature distribution, making almost impossible to detect vertical cracks. This kind of cracks can be detected only when an asymmetry in the heat flux is produced. This idea was exploited in the nineties when the so-called *flying spot method* was introduced [137]. It consists of heating the sample with a moving laser spot or line and detecting the time evolution of the surface temperature with an infrared (IR) detector or IR camera [2,11–18]. The excitation can be a continuous wave [11–15], modulated [142] or pulsed laser illumination [2,16–18]. This method allowed detecting cracks with openings of a few micrometers [141].

Once the crack has been detected the interest focuses on the characterization of its geometrical parameters (depth, length, width, orientation, etc.). In the last years, several approaches to perform crack characterization have been proposed [145,146]. They take advantage of the asymmetry of the temperature field at both sides of the crack arising from the thermal resistance produced by the crack, which partially blocks heat flux when the laser spot is focused close to the crack.

Following these ideas, in Chapter 7, we have dealt with the characterization of infinite vertical cracks using lock-in thermography, which is able to provide surface temperature amplitude and phase images with a very low noise level. We found a semi-analytical expression for the surface temperature of a sample containing such a crack when the surface is illuminated by a modulated and focused laser spot close to the crack. By fitting the surface temperature amplitude and phase to the model, the thermal contact resistance R_{th} of the crack, which quantifies the width of the crack, was obtained. This method is very accurate, but the data acquisition is, in some cases, very time consuming (several minutes). That is the reason why we propose working in the

time domain, instead of in the frequency domain, using pulsed laser spot thermography (PLST) to size the width of infinite vertical cracks in a fast manner: the data acquisition radically drops from several minutes to a few seconds. First, we have found a semi-analytical expression for the time evolution of the surface temperature of a sample containing such a crack when the surface is illuminated by a Dirac-like pulsed and focused Gaussian laser spot close to the crack. The presence of the defect produces an abrupt jump in the temperature profile at the crack position. The influence of the experimental parameters (laser beam radius, distance spot-crack, time of measurement and width of the crack) on the jump height is analyzed.

In order to prepare calibrated infinite vertical cracks, very thin metallic tapes down to 1 μm thick are inserted between two identical blocks under pressure. A pulsed laser beam is focused close to the crack. An infrared camera records images of the surface temperature around the crack. A microscope lens with a spatial resolution of 31 μm is used to collect the infrared emission from the sample. A least square fit of the temperature profile crossing the center of the laser spot and perpendicular to the crack is used to retrieve the thermal resistance R_{th}. Very good agreement between the thickness of the metallic tapes and the obtained R_{th} is found, confirming the validity of the model.

9.2 Time domain solution of the temperature field for a Dirac-like pulse

The diagram shown in Figure 9.1 represents the problem of a semi-infinite and opaque material containing an infinite vertical crack placed at plane $y = 0$. The sample surface is illuminated by an infinitely brief (Dirac-like) laser pulse of Gaussian profile and intensity per pulse I_0. The center of the laser spot is located at a distance d from the crack and its radius is a (at $1/e^2$ of the intensity). Adiabatic boundary conditions at the sample surface have been assumed. Under these conditions, the temperature at any point of the material has been already solved in the frequency domain (see Equation (7.9) in Chapter 7), i.e., when the sample surface is heated up by a modulated laser beam of

intensity I_0 and frequency f ($\omega = 2\pi f$):

$$T_{\pm}(x,y,z,\omega) = \frac{I_0}{\pi^2 a^2 K}\int_{-\infty}^{\infty}\int_{-\infty}^{\infty} \mathrm{d}x_0 \mathrm{d}y_0\, e^{-\frac{2\left[x_0^2+(y_0-d)^2\right]}{a^2}} \times \left[\frac{e^{-qR_0}}{R_0} \pm KR_{th}\mathrm{sign}(y_0)\int_0^{\infty}\mathrm{d}\delta\,\delta J_0(\delta r)\frac{e^{-\beta(|y_0|+|y|)}}{2+KR_{th}\beta}\right], \tag{9.1}$$

where $r_0 = \sqrt{x^2+(y-d)^2+z^2}$, $r_1 = \sqrt{(x-x_0)^2+z^2}$, $\beta = \sqrt{\delta^2+i\omega/D}$, J_0 is the Bessel function of zero order, the $\mathrm{sign}(\cdot)$ function is equal to $+1$ for all positive values of its argument and is equal to -1 for the negative ones, K and D are the thermal conductivity and diffusivity of the material, respectively. Finally, R_{th} is the thermal contact resistance of the crack related to the air gap thickness L through the equation $R_{th} = L/K_{air}$ [19].

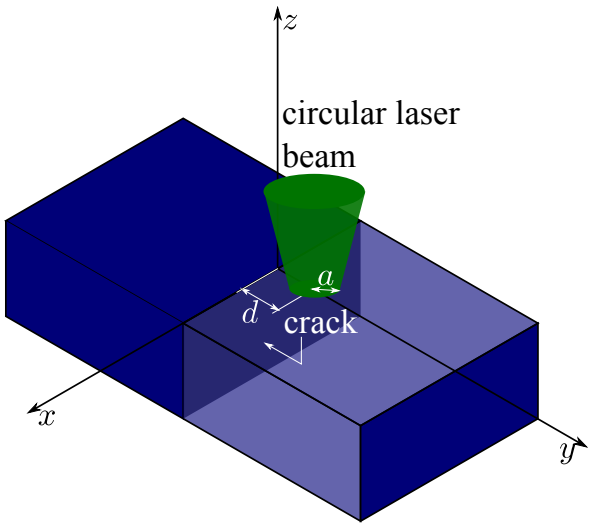

Figure 9.1: Scheme of a semi-infinite sample which contains an infinite vertical crack (in gray) and that is illuminated by a circular Gaussian beam.

Notice that in Equation (9.1) there are two summation terms: the first one corresponds to the temperature field on a semi-infinite material without any crack, whereas the second one represents the contribution of the vertical crack to the temperature field in the material. This phenomenon can be understood in terms of the thermal waves that are reflected and/or transmitted through the vertical crack, as extensively explained in Chapter 7.

It is worth noting that the Laplace transform of the sample temperature in the

time domain after a Dirac-like pulse $\bar{T}(x,y,z,s)$ is obtained from the modulated solution by changing $i\omega$ (that appears implicitly in β) by s and I_0 by $\bar{I}_0$, the intensity of the laser pulse.

$$\begin{aligned}\bar{T}(x,y,z,s) = \frac{\bar{I}_0}{2\pi K}\int_0^\infty \mathrm{d}\delta\, \delta J_0(\delta r_0)\frac{e^{-(\delta a)^2/8}}{\beta_1} \\ + \mathrm{sign}(y)\frac{\bar{I}_0 K R_{th}}{\pi^2 a^2 K}\int_{-\infty}^{\infty}\int_{-\infty}^{\infty}\int_0^\infty \mathrm{d}x_0\mathrm{d}y_0\mathrm{d}\delta\, e^{-\frac{2\left[x_0^2+(y_0-d)^2\right]}{a^2}} \\ \times \delta J_0(\delta r_1)\mathrm{sign}(y_0)\frac{e^{-\beta_1(|y_0|+|y|)}}{2+KR_{th}\beta_1},\end{aligned} \tag{9.2}$$

where $\beta_1 = \sqrt{\delta^2 + s/D}$.

Similarly to Chapter 7, here we focus on the Laplace transform of the temperature profile along the y-axis

$$\begin{aligned}\bar{T}(0,y,0,s) = \frac{\bar{I}_0}{2\pi K}\int_0^\infty \mathrm{d}\delta\, \delta J_0(\delta|y-d|)\frac{e^{-(\delta a)^2/8}}{\beta_1} \\ + \mathrm{sign}(y)\frac{\bar{I}_0 K R_{th}}{\pi^2 a^2 K}\int_{-\infty}^{\infty}\int_{-\infty}^{\infty}\int_0^\infty \mathrm{d}x_0\mathrm{d}y_0\mathrm{d}\delta\, e^{-\frac{2\left[x_0^2+(y_0-d)^2\right]}{a^2}} \\ \times \delta J_0(\delta|x_0|)\mathrm{sign}(y_0)\frac{e^{-\beta_1(|y_0|+|y|)}}{2+KR_{th}\beta_1},\end{aligned} \tag{9.3}$$

which can be written as $\bar{T}(0,y,0,s) = \bar{T}_1(0,y,0,s) + \bar{T}_2(0,y,0,s)$, separating the contribution of the semi-infinite material without crack ($\bar{T}_1$) from the contribution of the crack ($\bar{T}_2$).

The surface temperature evolution in the absence of any crack is obtained through the inverse Laplace transform of $\bar{T}_1(0,y,0,s)$, which is the first term in Equation (9.3). This is achieved by inverting $1/\beta_1$ and solving the resulting integral analytically [51]

$$\begin{aligned}T_1(0,y,0,t) &= \frac{I_0}{2\epsilon\sqrt{\pi^3 t}}\int_0^\infty \mathrm{d}\delta\, \delta J_0(\delta|y-d|)e^{-\delta^2\left(\frac{a^2+8Dt}{8}\right)} \\ &= \frac{2I_0}{\epsilon\sqrt{\pi^3 t}}\frac{\exp\left(-\frac{2(y-d)^2}{a^2+8Dt}\right)}{a^2+8Dt},\end{aligned} \tag{9.4}$$

where $\epsilon = K/\sqrt{D}$ stands for the thermal effusivity of the material. It is worth mentioning that this result agrees with the limiting case (semi-infinite material) of the

series solution obtained by Cernuschi and coworkers for a material illuminated by a Dirac-like laser pulse of Gaussian profile (see Equation (5) in Reference [51]).

The inverse Laplace transform of $\bar{T}_2(0, y, 0, s)$, which is the contribution of the vertical crack to the temperature profile in the time domain, consists of inverting the factor containing β_1, which can be expressed as

$$\bar{F}(s) = \frac{e^{-u\sqrt{\delta^2+s/D}}}{2 + KR_{th}\sqrt{\delta^2 + s/D}}, \tag{9.5}$$

whose inverse Laplace transform can be solved analytically by using partial fractions decomposition and the properties of the Laplace transform [125]

$$\begin{aligned} F(t) = \frac{\sqrt{D}}{KR_{th}} \frac{e^{-Dt\delta^2 - u^2/(4Dt)}}{\sqrt{\pi t}} - \frac{2D}{(KR_{th})^2} e^{-Dt\delta^2 - u^2/(4Dt)} \\ \times \exp\left(\frac{\sqrt{4Dt}}{KR_{th}} + \frac{u}{\sqrt{4Dt}}\right)^2 \operatorname{erfc}\left(\frac{\sqrt{4Dt}}{KR_{th}} + \frac{u}{\sqrt{4Dt}}\right), \end{aligned} \tag{9.6}$$

where $u = |y| + |y_0|$ and $\operatorname{erfc}(\cdot)$ is the complementary error function [165].

On the other hand, the integrals over x_0 and over δ in the second term of Equation (9.3) have analytical solutions

$$\begin{aligned} I_{x_0} &= \int_{-\infty}^{\infty} \mathrm{d}x_0 \, e^{-2x_0^2/a^2} J_0(\delta|x_0|) \\ &= \frac{a\sqrt{\pi}}{\sqrt{2}} e^{-a^2\delta^2/16} I_0\left(\frac{a^2\delta^2}{16}\right), \end{aligned} \tag{9.7}$$

$$\begin{aligned} I_\delta &= \int_0^{\infty} \mathrm{d}\delta \, e^{-a^2\delta^2/16} e^{-\delta^2 Dt} I_0\left(\frac{a^2\delta^2}{16}\right) \\ &= \frac{\sqrt{2}}{\sqrt{Dt}} \frac{1}{\sqrt{a^2 + 8Dt}}, \end{aligned} \tag{9.8}$$

being I_0 the modified Bessel function of zero order.

Using the results obtained in Equations (9.6)-(9.8), we can write an expression for the contribution of the vertical crack to the temperature profile along the y-axis in time domain, which is the inverse Laplace transform of $\bar{T}_2(0, y, 0, s)$:

$$T_2(0,y,0,t) = \frac{I_0 \mathrm{sign}(y)}{\epsilon\pi^2 at\sqrt{D}\sqrt{a^2+8Dt}} \int_{-\infty}^{\infty} \mathrm{d}y_0 \,\mathrm{sign}(y_0) e^{-\frac{2(y_0-d)^2}{a^2} - \frac{u^2}{4Dt}} \times \left[1 - \frac{\sqrt{4\pi Dt}}{KR_{th}} e^{\left(\frac{\sqrt{4Dt}}{KR_{th}} + \frac{u}{\sqrt{4Dt}}\right)^2} \mathrm{erfc}\left(\frac{\sqrt{4Dt}}{KR_{th}} + \frac{u}{\sqrt{4Dt}}\right)\right]. \tag{9.9}$$

Finally, the surface temperature along the y-profile in the time domain is obtained by adding Equations (9.4) and (9.9)

$$T(0,y,0,t) = \frac{2I_0}{\epsilon\sqrt{\pi^3 t}} \frac{\exp\left(-\frac{2(y-d)^2}{a^2+2\mu^2}\right)}{a^2+2\mu^2} + \mathrm{sign}(y) \frac{2I_0}{\epsilon\pi^2 a\sqrt{t}\mu\sqrt{a^2+2\mu^2}} \times \int_{-\infty}^{\infty} \mathrm{d}y_0 \,\mathrm{sign}(y_0) e^{-\frac{2(y_0-d)^2}{a^2} - \frac{u^2}{\mu^2}} \times \left[1 - \frac{\sqrt{\pi}\mu}{KR_{th}} e^{\left(\frac{\mu}{KR_{th}} + \frac{u}{\mu}\right)^2} \mathrm{erfc}\left(\frac{\mu}{KR_{th}} + \frac{u}{\mu}\right)\right], \tag{9.10}$$

where $\mu = \sqrt{4Dt}$ is the so called thermal diffusion length [18]. Note that the thermal resistance is correlated to the thermal conductivity through the factor KR_{th}. This means that narrow cracks are better detected in high thermal conducting materials (metals, alloys, ceramics…) than in thermal insulators (polymers, composites…). Besides, the thermal diffusivity is correlated to the elapsed time after the laser pulse arrives to the sample through the factor Dt. Accordingly, under the same experimental conditions, for low thermal diffusivity samples, the effect of the crack arises later than for materials of good thermal diffusivity.

9.3 Exploring the relative temperature contrast for vertical cracks in the time domain

We have performed numerical simulations of the surface temperature profile along the y-axis of the semi-infinite cracked sample, using Equation (9.10), to illustrate the effect of the thermal resistance as well as the influence of the distance d from the laser spot to the crack, the radius of the Gaussian spot a and the instant of time t, on the visibility of the vertical crack. All the simulations are performed considering AISI-304 stainless steel samples ($D = 4.0$ mm^{2}s^{-1} and $K = 16$ Wm^{-1}K^{-1}) and Dirac-like laser

pulse illumination. It is important to mention that for very small cracks ($KR_{th} < 10^{-4}$ m), the numerical evaluation of the integral term in Equation (9.10) is more stable when using an asymptotic expansion of $e^{z^2}\mathrm{erfc}(z)$ [154].

Figure 9.2 shows the temperature rise, above the ambient, along the y-axis for an AISI-304 sample containing an infinite vertical crack at $y = 0$. The laser spot is centered at $d = 1.0$ mm with radius $a = 0.75$ mm. We show the effect of the value of the thermal resistance R_{th}, ranging from 10^{-3} to 10^{-6} W^{-1}m^{2}K, at four different times after the heating pulse.

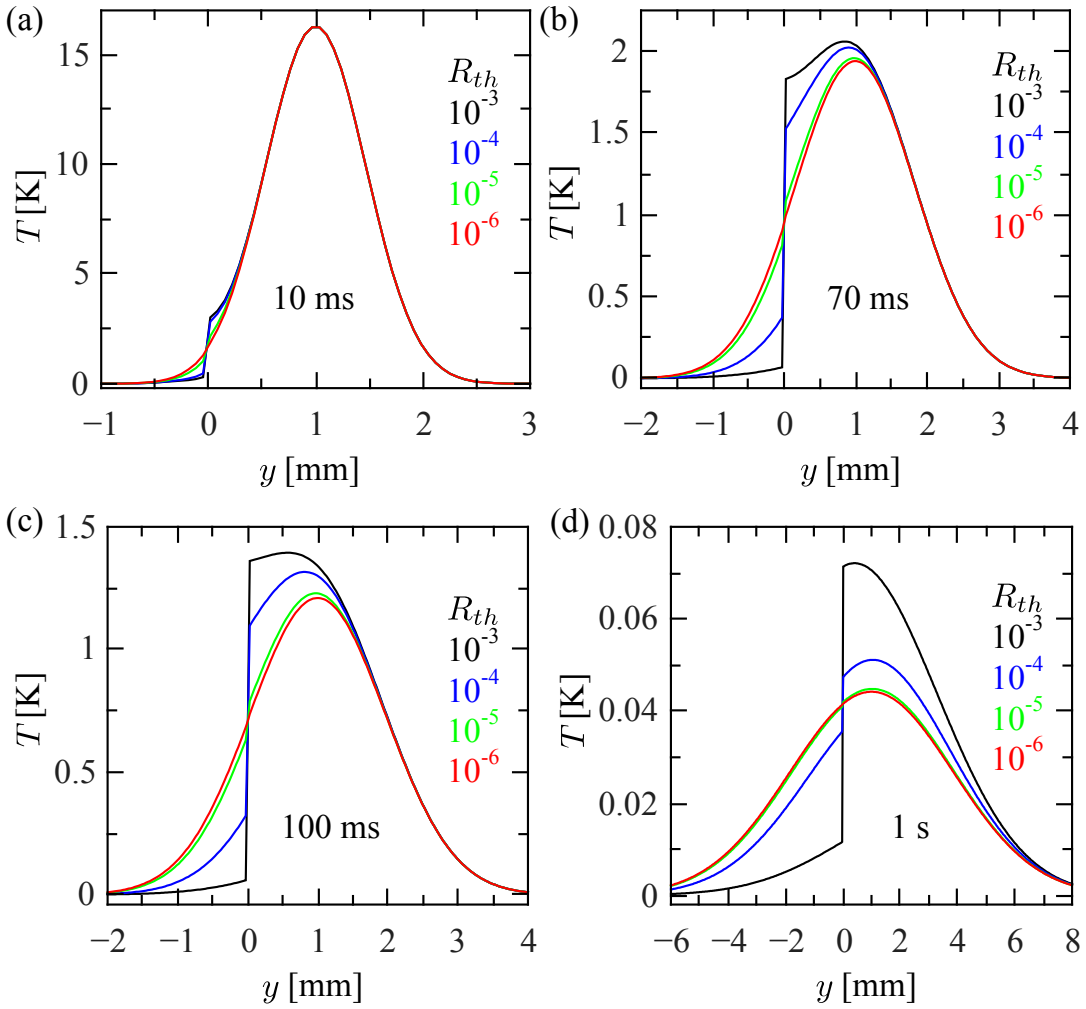

Figure 9.2: Numerical simulations of the temperature profiles along the y-axis for an AISI-304 sample containing an infinite vertical crack $(y = 0)$. The sample is illuminated at $d = 1.0$ mm by a Dirac-like pulse of Gaussian profile with $a = 0.75$ mm. The effect of the thermal resistance R_{th} (W^{-1}m^{2}K) at four times: (a) 10 ms, (b) 70 ms, (c) 100 ms and (d) 1 s after the heating pulse is analyzed.

Notice that there is a discontinuity at the crack position. The larger the thermal resistance, the larger the temperature jump at any time. However, the normalized temperature contrast, i.e., the ratio of the temperature jump and the maximum temperature value, is low for early times (see Figure 9.2a) and grows for medium times (see Figures 9.2b and 9.2c) to a maximum value, then it starts decreasing for longer times (see Figure 9.2d). Moreover, for long times the temperature rise is too low and hence it will be affected by noise in real experiments.

The normalized temperature contrast at the crack position Δ_T is useful to quantify the strength of the temperature jump at the crack position and is defined as

$$\Delta_T(t) = \frac{T(0,0^+,0,t) - T(0,0^-,0,t)}{T(0,d,0,t)}. \tag{9.11}$$

According to Equation (9.10), the relative temperature contrast Δ_T depends on the factor KR_{th}, on the distance d and on the radius of the laser beam a. However, Δ_T does not depend on the intensity I_0 of the laser pulse.

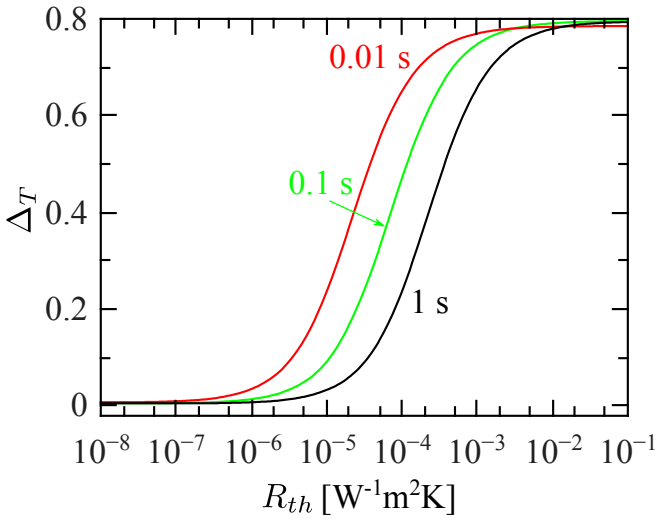

Figure 9.3: Numerical simulation of the dependence of Δ_T on the thermal contact resistance R_{th}. Calculations are performed for a cracked AISI-304 sample with $d = \mu$ and $a = \mu/2$. Three different instants of time after the laser pulse arrival to the sample are evaluated.

Figure 9.3 shows numerical simulations of Δ_T as a function of the thermal

resistance performed on AISI-304 with $d = \mu$ and $a = \mu/2$. Three times after the laser pulse are considered: 10 ms (red curve), 100 ms (green curve) and 1.0 s (black curve). According to the definition of the thermal diffusion length $\mu = \sqrt{4Dt}$, in the simulations of Figure 9.3, early times using a small laser spot impinging the sample very close to the crack, while long instants of time mean using a large laser spot far away from the crack. As can be seen, the temperature contrast Δ_T exhibits a sigmoid shape. For low thermal resistances R_{th} (very narrow cracks) there is no temperature contrast and the vertical crack remains undetected. For large values of R_{th} (thick cracks), the temperature contrast saturates $(\Delta_T \to 0.8)$, indicating that although these large cracks are easy to detect, it is difficult to quantify R_{th}. In fact, the highest sensitivity to the thermal resistance appears for intermediate R_{th} values. Nevertheless, notice that increasing the measurement time by two orders of magnitude, the sensitivity to R_{th} shifts to higher values by one order of magnitude. This result means that using early times after the heating pulse (together with the laser spot tightly focused near the crack) is better to detect and characterize narrow cracks. In order to be able to state guidelines for the characterization of vertical cracks by pulsed spot thermography, the effect of the other parameters involved in Δ_T is explored.

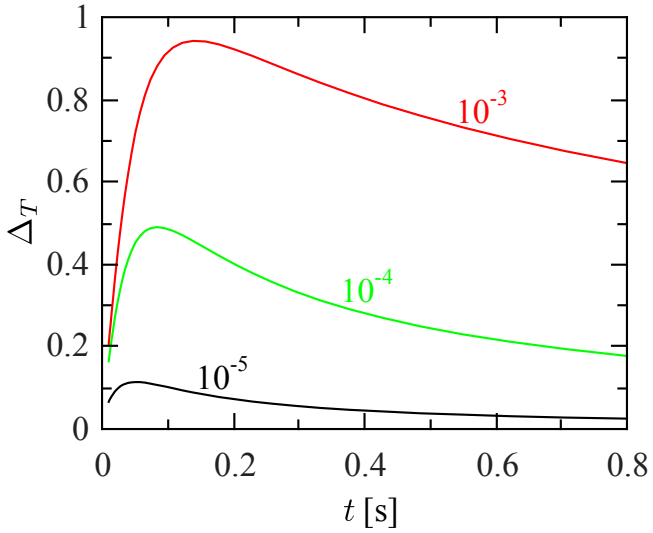

Figure 9.4: Numerical simulation of the dependence of Δ_T on the measurement time t. We have considered a cracked AISI-304 sample with $d = 1.0$ mm and $a = 0.75$ mm. Three different thermal resistances: 10^{-5}, 10^{-4} and 10^{-3} $W^{-1}m^2K$ are studied.

Figure 9.4 shows numerical simulations of the temperature contrast as a function of time. Calculations are performed for $d = 1.0$ mm and $a = 0.75$ mm. We have studied three different values of R_{th}: 10^{-5}, 10^{-4} and 10^{-3} W^{-1}m^{2}K. These results indicate that as time goes by, the contrast increases until it reaches a maximum value, which is higher for larger thermal resistances, in agreement with Figure 9.2, and then it starts decreasing slowly for later times. Moreover, the maximum appears at longer instants of time for larger thermal resistances.

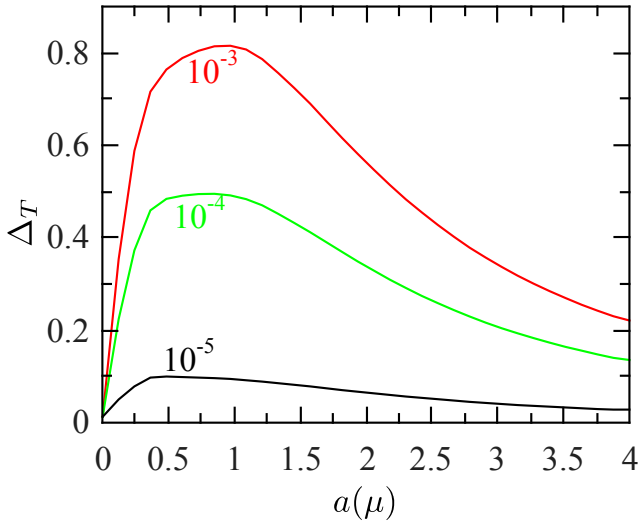

Figure 9.5: Numerical simulations of Δ_T as a function of the radius of the spot. We have considered a cracked AISI-304 sample with $d = \mu = 1.26$ mm ($t = 100$ ms). Three thermal resistances: 10^{-5}, 10^{-4} and 10^{-3} W^{-1}m^{2}K are studied.

In Figure 9.5 we show the dependence of Δ_T on the laser spot radius. Numerical calculations are performed for $d = \mu = 1.26$ mm, which means $t = 100$ ms for AISI-304 samples. Three thermal resistances are studied: 10^{-5}, 10^{-4} and 10^{-3} W^{-1}m^{2}K. As can be observed, the maximum temperature contrast corresponds to $a \approx 0.9\mu$ for the thermal resistance of 10^{-3} W^{-1}m^{2}K, i.e., when the laser spot radius almost reaches the vertical crack. However, this result depends on the thermal resistance: the maximum of the contrast is reached for lower radius spot sizes as the thermal resistance decreases. Nevertheless, there is a good contrast for radii in the range $0.5\mu - 1.5\mu$.

Finally, in Figure 9.6 we analyze the dependence of Δ_T on the distance of the laser spot to the crack. Calculations are performed for fixed laser beam radius $a = 0.9\mu$ and measurement time $t = 100$ ms. We consider three values of thermal resistance R_{th}: 10^{-5}, 10^{-4} and 10^{-3} W^{-1}m^{2}K. As can be observed, the maximum temperature contrast is produced when the laser spot impinges the sample surface at $d \approx 0.75\mu$ and it quickly decreases as the laser spot moves away from this position. Note that this result is valid for all R_{th} values. On the other hand, the relative contrasts for $d = \mu$ are equal to those ones obtained in Figure 9.5 for each thermal resistance, as expected.

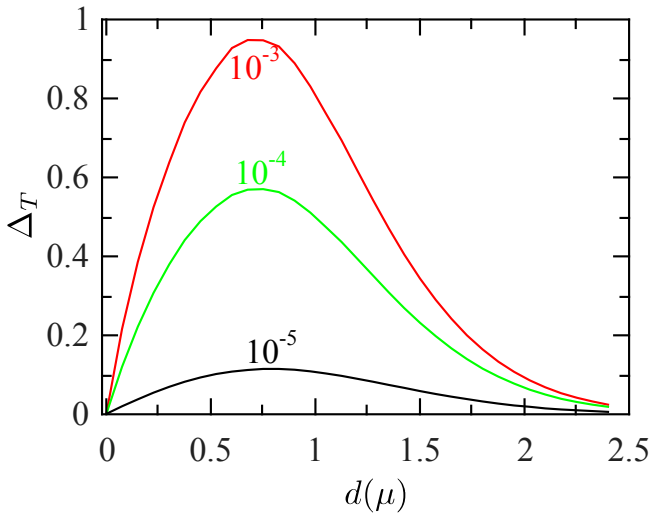

Figure 9.6: Numerical simulation of Δ_T as a function of the position the spot with respect to the crack. We have considered a cracked AISI-304 sample with $a = 0.9\mu$. Three thermal resistances: 10^{-5}, 10^{-4} and 10^{-3} W^{-1}m^{2}K are studied at $t = 100$ ms.

According to the obtained results, we propose the following guidelines for vertical crack detection using pulsed laser spot thermography:

(a) For a given thermal resistance, the largest temperature contrast at the crack position is obtained for $d \approx 0.75\mu \approx 0.85a$, i.e., when the laser spot slightly overlaps the crack. However, in order to avoid light entering the crack and remembering that the maximum of Δ_T as a function of a is not very sharp, we propose the following experimental condition: $d \approx 0.75\mu \approx 1.1a$.

(b) In order to detect very narrow cracks, early times after the Dirac heating pulse

should be used. This condition together with $d \approx 0.75\mu \approx 1.1a$, implies using a tightly focused laser spot very close to the crack. For instance, using $d = 0.1$ mm on metallic samples together with $t \approx 1$ ms allows to detect thermal resistances as low as $10^{-6} - 10^{-7}$ W^{-1}m^{2}K. Note that these experimental conditions are also valid to detect thicker cracks, but not to size them accurately, since the temperature contrast saturates, as shown in Figure 9.3.

(c) In order to retrieve R_{th} accurately, measurement times showing a contrast about half of the maximum one are proposed since they are the most sensitive to R_{th} variations.

9.4 Experimental details and results for vertical cracks

A diagram of the experimental setup is shown in Figure 2.6 of Chapter 2. It is worth mentioning that the temperature detected by our IR camera is not the real surface temperature rise of the sample, since neither its absorptivity to the laser wavelength nor its IR emissivity are known. However, the "apparent" temperature rise ΔT measured by the IR detectors is proportional to the real temperature rise of the sample surface.

According to Equation (9.10), the spatial profile of the temperature at each measurement time depends on five parameters (I_0/ϵ, D, KR_{th}, a and d). However, in the experimental measurements we fix the distance between the laser spot and the crack position ($d \approx 0.8 - 1$ mm) in order to improve the sensitivity and the contrast as described in Section 9.3. On the other hand, the radius of the laser spot (a) and the thermal diffusivity of the sample (D) are measured far away from the crack position by making a curve fitting of the temperature profile along the y-axis to Equation (9.4) for several instants of time. In fact, Equation (9.4) indicates that the temperature profile has a Gaussian profile with radius $b = a^2 + 8Dt$. Accordingly, by measuring b at several times a straight line is obtained whose slope gives D and the intercept provides a [51]. Finally, the only parameters involved in the curve fittings of the temperature y-profiles using Equation (9.10) are KR_{th} and I_0/ϵ.

We have prepared calibrated vertical cracks using two blocks of AISI-304 stainless steel 2 cm thick. As this metallic alloy has a shiny surface, a thin graphite grey layer of about 3 µm thick has been sprayed onto the surface of the sample to increase both the absorption to the heating laser and the emissivity to infrared wavelengths. In order to calibrate the air gap between the two AISI-304 blocks, we placed strips of nickel tape of 25, 10, 5, 2.5 and 1 µm thick between them, which produces thermal resistances of 10^{-3}, 4×10^{-4}, 2×10^{-4}, 10^{-4} and 4×10^{-5} W^{-1}m^{2}K, respectively ($R_{th} = L/K_{air}$, with $K_{air} = 0.26$ Wm^{-1}K^{-1}).

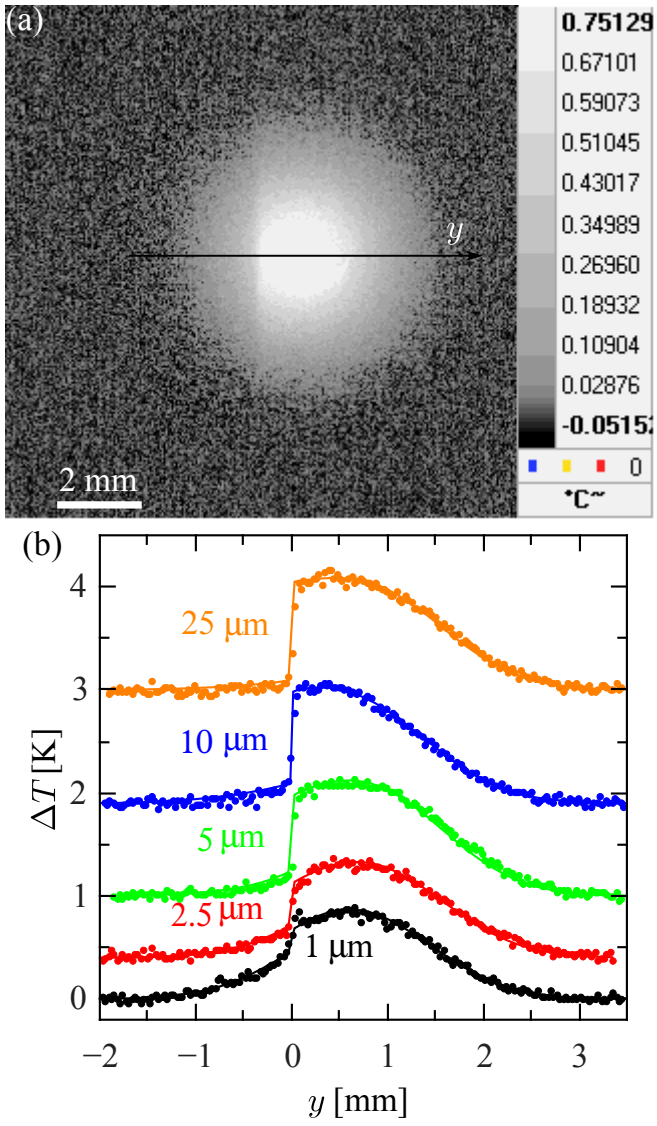

Figure 9.7: (a) Thermogram for two AISI-304 blocks put in contact to simulate an infinite vertical crack

1 $t = 70$ $d = 0.81$ $a = 0.78$

1 μm thick at $t = 70$ ms. We used the following experimental parameters: $d = 0.81$ mm, $a = 0.78$ mm and $D = 3.7$ mm^{2}s^{-1}. (b) Temperature profiles along the y-axis for several crack widths at $t = 70$ ms. Dots correspond to experimental data and continuous lines to the fits to Equation (9.10).

In Figure 9.7a we show the thermogram corresponding to a 1 μm thick crack on AISI-304 stainless steel, obtained 70 ms after the heating pulse. As can be seen, even such a small air gap is clearly visible in the thermal image. Following the method described above we measured $a = 0.78 \pm 0.04$ mm and $D = 3.70 \pm 0.08$ mm^{2}s^{-1}, which were kept constant for all crack thicknesses. On the other hand, we chose $d = 0.81$ mm for all cracked samples. Figure 9.7b shows the temperature profiles along the y-axis for the vertical cracks at $t = 70$ ms after the laser pulse (i.e. $\mu = 1$ mm, satisfying $d \approx 0.75\mu \approx 1.1a$). The temperature values are shifted in order to better show the jump at the crack position. Dots represent the experimental data and the continuous line the fit to Equation (9.10). A non-linear least square fit based on the Levenberg–Marquardt algorithm was implemented [63,112] with two free parameters (KR_{th} and I_0/ϵ). Table 9.1 shows the results obtained for the cracks thicknesses. Notice the good agreement between the estimated values and the tape thicknesses. We fitted data collected at five times, from 70 to 110 ms, to obtain the standard deviation of the estimated values.

Table 9.1: Results of the crack thickness obtained for AISI-304 and PEEK.

Calibrated thickness [μm]	AISI-304 crack thickness [μm]	PEEK crack thickness [μm]
1	0.74 ± 0.05	---
2.5	1.9 ± 0.1	---
5	5.4 ± 0.3	---
10	17 ± 3	10 ± 1
25	28 ± 4	24 ± 3
50	---	48 ± 4
100	---	90 ± 5

It is important to mention that lock-in thermography (LIT) measurements show

higher signal-to-noise ratio than pulsed laser spot thermography (PLST) ones, as can be seen by comparing Figure 9.7b with Figures 7.11c and 7.11d of Chapter 7. In Table 9.2 the relative error ($\varepsilon_{rel} = (L_{crack} - L_{measured})/L_{crack} \times 100$) is shown, calculated on AISI-304 stainless steel cracked samples, for both LIT and PLST. Clearly, the former gives more accurate results for the crack thicknesses. However, PLST values are accurate enough. Moreover, PLST is faster than lock-in thermography measurements.

Table 9.2: Relative errors on the crack thickness for AISI-304 measured with lock-in thermography (LIT) and pulsed laser spot thermography (PLST).

Calibrated thickness [μm]	PLST crack thickness [μm]	PLST ε_{rel} [%]	LIT crack thickness [μm]	LIT ε_{rel} [%]
1	0.74	26	0.9	10
2.5	1.9	24	2.8	12
5	5.4	8	5.2	4
10	17	70	12	20
25	28	12	27	8

Since narrow cracks are harder to characterize in thermal insulator materials, we performed measurements on calibrated cracks using two plates of polyether-ether ketone (PEEK) 1 cm thick. As this polymer is semitransparent, a thin matt black synthetic enamel layer of about 5 μm thick has been sprayed on the surface to make it opaque to the exciting wavelength. In this case, we placed strips of nickel tape of 10, 25, 50 and 100 μm thick, which correspond to thermal resistances of 4×10^{-4}, 10^{-3}, 2×10^{-3} and 4×10^{-3} W^{-1}m^{2}K.

In Figure 9.8a a thermogram corresponding to a 10 μm thick crack is shown, obtained 500 ms after the heating pulse. Note that this 10 μm (4×10^{-4} W^{-1}m^{2}K) thick crack is more difficult to distinguish than the 1 μm (4×10^{-5} W^{-1}m^{2}K) thick crack in AISI-304, in agreement with the theoretical predictions. In fact, the product KR_{th} is higher for a 1 μm thick crack in AISI-304 (6×10^{-4} m) than for a 10 μm thick crack in

PEEK (1×10^{-4} m). The measured values of the experimental parameters were: $D = 0.190 \pm 0.004$ mm^{2}s^{-1}, $a = 0.77 \pm 0.05$ mm and $d = 0.84$ mm. Notice that for the 100 μm thick crack, we chose $d \approx 1$ mm. This is because for smaller values of d, the laser light comes into the 'air gap' and the proposed model does not hold.

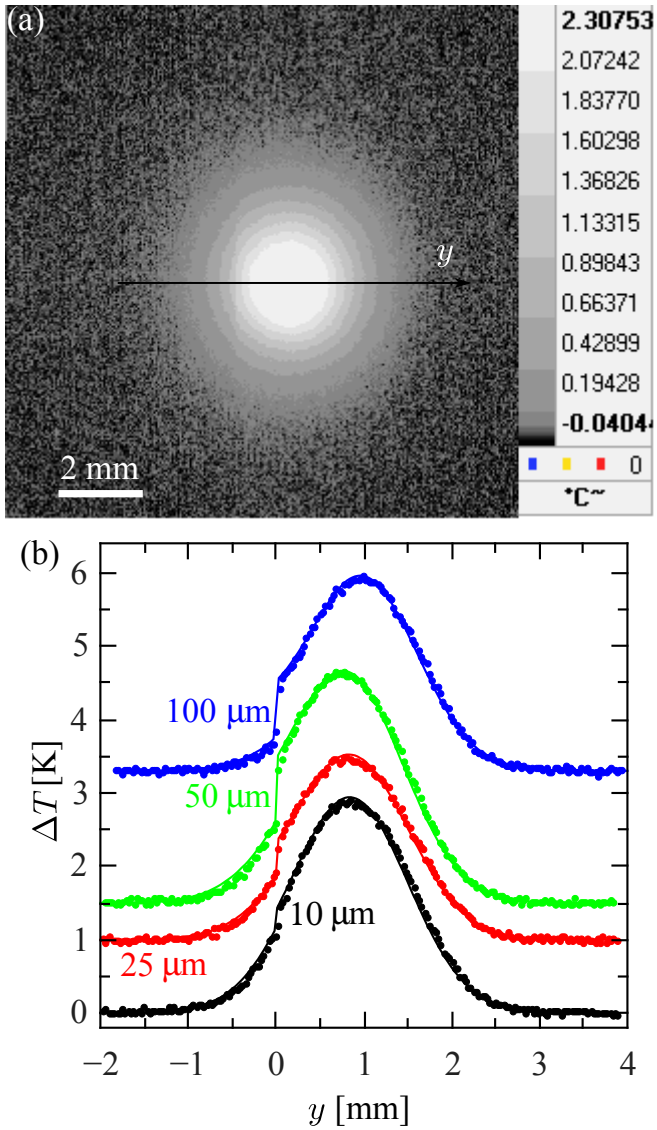

Figure 9.8: (a) Thermogram for two PEEK plates put in contact to simulate an infinite vertical crack 10 μm thick at $t = 500$ ms. We used the following experimental parameters: $d = 0.94$ mm, $a = 0.93$ mm and $D = 0.19$ mm^{2}s^{-1}. (b) Temperature profiles along the y-axis for several crack widths. Dots correspond to experimental data and continuous lines to the fits to Equation (9.10).

Figure 9.8b shows the temperature profiles along the y-axis for all vertical cracks studied in PEEK. As before, the values of the temperature are shifted in order to show the jump at the crack position. We use dots for the experimental results and continuous lines for the fittings to Equation (9.10). Table 1 shows the results obtained for the cracks thicknesses. Similarly to AISI-304 cracked samples, there is a good agreement between the estimated values and the tape thicknesses in PEEK. In this case, the uncertainty is the standard deviation corresponding to seven measurement times, from 500 to 800 ms.

Finally, we put the two AISI-304 blocks in direct contact, i.e. without nickel tape between them. As the surfaces in contact are polished, they simulate an extremely thin crack. The result obtained for the crack length depends slightly on the position in which the sample is excited, probably due to the different edge surface conditions. This result allows us to conclude that the upper limit for this thermal resistance is $R_{th} \leq 2.3 \times 10^{-5}$ W^{-1}m^{2}K ($L_{crack} \leq 600$ nm). Similarly, for the PEEK plates, we found that the upper limit for this thermal resistance is $R_{th} \leq 3.1 \times 10^{-4}$ W^{-1}m^{2}K ($L_{crack} \leq 8$ μm).

Note that in the experiments we used a 'flat-top' instead of the Gaussian laser assumed in the theory. Although at short times after the heating pulse, both spatial temperature distributions are very different, as times goes by, both temperature fields converge. In fact, when the thermal diffusion length fulfills the condition $\mu = \sqrt{4Dt} \geq 1.6a$, the difference between both temperatures is smaller than $1\,\%$ at each point. This means that for times satisfying $t \geq \frac{2.56a^2}{4D}$, predictions from a Gaussian laser and a "flat-top" one are indistinguishable, as explained in Section 6.5 of Chapter 6. In order to fulfill this condition, we chose $t \geq 70$ ms for AISI-304 and $t \geq 500$ ms for PEEK in the measurements.

It is worth noting that the experimental results shown in Figures 9.7b and 9.8b do not exhibit a sharp discontinuity at the crack, but a smooth transition involving around 4 pixels. This result is due to the imperfect imaging system of the IR camera (diffraction, multiple reflections, flare…). The so-called Point Spread Function (PSF) of

the optical system quantifies its effect, which depends on the lens quality [166]. However, as in our system the effect is quite small, we have not taken it into account in the fits.

Equation (9.10), which has been used for fitting, is only valid for infinite vertical cracks. All simulations and experiments shown in this work were performed on infinite cracks. However, real cracks have a limited area. For finite cracks there are no semi-analytical solutions, and sophisticated numerical methods must be used [158] that are outside the scope of this work. Nevertheless, a practical question arises: which is the minimum size of a crack whose width could be obtained accurately using Equation (9.10)? A rough answer to this question is that both length and depth of the crack should be higher than (at least twice) the thermal diffusion length. This means that tightly focusing the laser beam very close to the crack and using short times after the laser pulse, sub-millimetric cracks could be characterized. However, a tightly focused laser pulse could easily damage the sample. Keeping the experimental data used in this work, radius of the spot $a \approx 0.8$ mm and distance from the laser spot to the crack $d \approx 0.9$ mm, together with the optimal contrast condition proposed at the end of Section 9.3: $d \approx 0.75\mu \approx 0.85a$, a more realistic conclusion is that the model developed in this work can be used to size the width of open cracks larger than 4 mm in length and 2 mm in depth.

Before concluding, let us make some comments on the time consumption of the method. Once the laser radius is measured and the laser spot is placed close to the crack, the acquisition time of the temperature evolution of the sample surface after the laser pulse is about 2 s. Then, the data processing to obtain the temperature profile across the crack at a given time after the laser pulse takes about 3 min since it is done manually (15 min for five profiles). Finally, the fitting procedure to retrieve the crack width takes only 1 min. This means that the total duration could be drastically reduced by automating the data selection and processing procedure. Thus, a fast characterization of infinite vertical cracks with pulsed laser spot thermography could be implemented using the method presented in this work.

9.5 Summary

In this Chapter, we have presented a method for the characterization of the thickness of infinite vertical cracks using pulsed laser spot infrared thermography. First, we have found a semi-analytical expression for the surface temperature of a material containing such a crack when a Dirac-like pulse laser beam of Gaussian shape impinges close to the crack. The presence of the crack produces an abrupt jump in the surface temperature at the crack position. Numerical simulations indicate that the highest temperature contrast is produced when the radius of the spot a, the distance between the spot and the crack d and the thermal diffusion length μ satisfy $d \approx 0.75\mu \approx 0.85a$. However, in order to avoid the laser pulse from entering the crack we have used the following experimental rule: $d \approx 0.75\mu \approx 1.1a$. The validity of the model has been tested by performing pulsed infrared thermography measurements on AISI-304 stainless steel and PEEK samples containing calibrated cracks. The thickness of the crack was obtained by fitting the surface temperature along the profile perpendicular to the crack through the center of the Gaussian spot. The agreement between the optically calibrated width and the retrieved one is very good even for widths as narrow as 1 μm in stainless steel and 10 μm in PEEK. More effort has to be done in order to characterize semi-infinite and finite vertical cracks, which allows real application for industry.

Conclusions

Pulsed infrared thermography in the front-face configuration proved its versatility and good accuracy for determining the thermal transport properties as well as linear optical absorption coefficients in semitransparent and opaque solids. Several experimental setups were tested for studying the thermal diffusivity and thermal effusivity in semitransparent or opaque, thin or thick samples. Moreover, pulsed infrared thermography retrieved in-plane and in-depth thermal diffusivities, simultaneously, with good accuracy compared with literature values. Studies performed in several solid materials (polymers, ceramics, glasses, metals, metallic oxides, nanocomposites, etc.) covering a wide range of thermal conductivities and semitransparency validate the robustness of the method.

On the other hand, lock-in thermography was successfully applied for determining the width of infinite vertical cracks in semi-infinite calibrated opaque samples. Moreover, it was also implemented for characterization of the width and depth of semi-infinite vertical cracks. In both cases, good agreement between the obtained values and the calibrated ones was found, confirming the applicability of the proposed models.

Finally, pulsed laser spot thermography was successfully used to study the width of infinite vertical cracks in opaque semi-infinite solids. It was shown that this technique is not as accurate as lock-in thermography, but instead it is faster and provided accurate enough values of the crack widths compared to the calibrates ones.

1.- On the study of the thermal diffusivity of semitransparent slabs without coating using the front-face flash method:

(a) An almost complete one-dimensional heat conduction model was introduced in Chapter 3 in order to accurately retrieve the thermal diffusivity of semitransparent plates without coating. This model includes: multiple reflections of the incident light beam on the slab surfaces, heat losses to the surrounding atmosphere due to convective mechanisms, semi-transparency to IR wavelengths and also the temporal shape of the heating pulse.

(b) Curve fitting of the proposed model to experimental data, obtained using the thermographic setup shown in Figure 2.1a of Chapter 2, allowed to retrieve accurate thermal diffusivities of the semitransparent studied samples. Moreover, as by-products of the fits, the optical absorption coefficient to the incident wavelength and the effective optical absorption coefficient to IR wavelengths were also obtained. Both thermal diffusivities and optical absorption coefficients at the incident wavelength obtained in this work are in good agreement with literature values.

(c) A wide range of conducting materials was studied, ranging from poor thermal conductors (polymers, cardboard, polymeric composites, glass and ceramics) to highly conductive ones (metals and metallic oxides). Also, the studied materials cover a wide range of semi-transparency to both IR wavelengths and incident wavelength. This provides an experimental validation of the front-face flash method to study the thermal diffusivity of semitransparent slabs. However, this method is not adequate to study materials with a highly reflective surface (polished metals or glasses, etc.) and/or specimens which are transparent to the incident wavelength (glass, quartz, germanium, etc.), since in both cases the thermographic signal might be too low or negligible.

(d) Characterization of semitransparent plates without coating is faster using the front-face flash method introduced in Chapter 3 than with modulated methods. Moreover, the front-face flash method has an advantage with respect to the classical flash method, since it does not need access to the non-illuminated

surface. However, in both configurations of the flash method, the thickness of the studied sample must be known.

2.- About the enhancement of the thermal conductivity of polyester resin composites loaded with magnetized carbon nanofibers using the front-face flash method:

(a) Magnetized carbon nanofibers were aligned in a polyester matrix using a uniform magnetic field of moderate intensity, generated with a pair of Helmholtz coils. Significant increase in the thermal conductivity of those aligned composite films, along the direction of alignment, was obtained with respect to polyester composites with non-aligned carbon nanofibers, as shown in Figure 4.7 of Chapter 4.

(b) The front-face flash method, as applied in Chapter 4, provided fast and accurate values of the thermal diffusivities and thermal effusivities of the studied composites, which allowed to calculate their thermal conductivities.

(c) A theoretical model based on the interaction direct derivative was used to interpret the enhancement achieved on thermal conductivity. Moreover, the obtained values for the thermal mismatch between the carbon nanofibers and the polyester matrix are in good agreement with literature.

3.- Regarding the simultaneous measurements of the thermal diffusivity and thermal effusivity of opaque solid plates using the front-face flash method on a two-layer system:

(a) The surface temperature, considering one dimensional heat conduction, in a two-layer system consisting of an opaque solid slab in direct contact with a semi-infinite liquid layer was solved in order to study the thermal diffusivity and thermal effusivity of the solid, when the thermal properties of the liquid are known. Sensitivity analysis provided guidelines to select the cases in which it is possible to retrieve the thermal diffusivity and thermal effusivity of the slab, simultaneously (see Figure 5.3 of Chapter 5).

(b) A thermographic setup such as the one shown in Figure 2.1 of Chapter 2 was

used to obtain experimental data, which fitted to the proposed model retrieved accurate values of the thermal diffusivity and thermal effusivity of the studied solids. It is important to mention that the thermal effusivity retrieved was underestimated when its actual value was three times the thermal effusivity of the liquid (in most cases water) or larger. However, in all cases the thermal diffusivity was retrieved with good accuracy.

(c) A wide range of conductive solids was covered (polymers, glasses, ceramics and metals) in order to validate and to test the robustness of the proposed method. Good agreement between the retrieved values and literature was found.

(d) Since a restriction in the ratio of the thermal effusivities of the solid and liquid layers was found, this method is not well suited for materials with high thermal effusivities. However, it is very accurate for many materials of industrial interest such as polymers, metallic oxides, ceramics and many others.

4.- On the simultaneous measurement of the in-plane and in-depth thermal diffusivity of semitransparent solid slabs using focused laser spot thermography:

(a) A heat conduction model for solid slabs was successfully applied to study the in-plane and in-depth thermal diffusivities on isotropic and anisotropic materials. This model considers illumination using a Dirac-like delta pulse with circular Gaussian laser spot, it includes heat losses to the surrounding atmosphere by convective mechanisms, semi-transparency of the solid slab to both the incident wavelength and to IR wavelengths.

(b) In-plane thermal diffusivity of semitransparent, opaque, thin and/or thick (semi-infinite) can be retrieved by a linear fit of the time evolution of the Gaussian radius of the temperature profile. Moreover, the slope of the fit is not disturbed by heat losses, as shown in Subsection 6.4.1 of Chapter 6. Experimental measurements were performed with a thermographic setup (see Figure 2.6 of Chapter 2). Good agreement between the retrieved thermal diffusivities and literature values was found.

(c) It was shown that by spatially averaging the IR signal matching a Gaussian

illumination on an anisotropic semitransparent slab the IR signal response of a plane illumination is obtained, which allowed to retrieve the thermal diffusivity using the one-dimensional heat conduction model as in the front-face flash method. A test on an anisotropic polymeric composite confirmed the applicability of the method.

(d) Several opaque and semitransparent specimens, covering a wide range of thermal diffusivities were studied and good agreement between our results and literature was found, confirming the validity of the model.

5.- About the measured thickness of infinite vertical cracks with lock-in thermography:

(a) A semi-analytical expression for the surface temperature of a material which contains an infinite vertical crack and is excited with a modulated Gaussian laser beam close to the crack position was found, which allowed to study the width of calibrated infinite vertical cracks.

(b) Analysis of the amplitude and phase contrasts allowed to select the optimum conditions for the radius of the spot, the modulation frequency and the distance of the laser beam to the crack, in order to retrieve the width of infinite vertical cracks in semi-infinite specimens.

(c) Lock-in thermography measurements were performed on AISI-304 and glassy carbon specimens, using the setup shown in Figure 2.7 of Chapter 2. Curve fitting of the surface temperature profile along the center of the laser spot to the proposed model retrieved the crack thicknesses with good accuracy compared with the optically calibrated ones.

6.- On the study of finite vertical cracks with lock-in thermography:

(a) The surface temperature of semi-infinite samples which contain arbitrarily narrow cracks of any shape when the sample surface is illuminated by a modulated and focused Gaussian laser beam was numerically solved using a Bauman-Oden type discontinuous Galerkin finite element method. In particular, this model was successfully applied to characterize calibrated semi-infinite

vertical cracks on AISI-304.

(b) Lock-in thermography measurements were performed on AISI-304 samples containing calibrated semi-infinite cracks of several thicknesses and depths. The values retrieved from least square fittings are in good agreement with the nominal ones, confirming the validity of the model.

(c) A powerful method was established, which opens the possibility of characterizing real cracks of arbitrary shape, size and orientation using lock-in thermography as proposed in Chapter 8.

7.- Regarding the measurement of the width of infinite vertical cracks with pulsed laser spot thermography:

(a) A semi-analytical solution of the surface temperature of a material containing an infinite vertical crack, as shown in Figure 9.1 of Chapter 9 was found, considering a Dirac-like pulse of Gaussian beam focused close to the crack position. This model allowed to study, in a fast way and with enough accuracy, the width of infinite vertical cracks in semi-infinite samples.

(b) Numerical simulations of the temperature contrast revealed the optimum conditions under which vertical cracks can be measured with the highest accuracy allowed by this method.

(c) The validity of the model was tested by performing pulsed infrared thermography measurements, using the setup shown in Figure 2.6 of Chapter 2, on AISI-304 stainless steel and PEEK samples containing calibrated cracks. Curve fitting of the proposed model on the experimental data provided accurate enough values of cracks, in comparison with the calibrated ones.

(d) It was shown that even though lock-in measurements provided higher signal-to-noise ratio and the crack thicknesses retrieved with this technique are more accurate that those obtained with pulsed laser spot thermography, the latter is faster and sufficiently accurate for measuring the width of infinite vertical cracks in opaque materials, which makes it a very interesting technique for non-destructive testing in industrial applications.

Future work

According to the work performed in this thesis on infrared thermography, we could extend our future research to several fields of engineering and physics. Moreover, deeper understanding and application of the topics studied here, still remain a challenge for non-destructive testing in laboratories and industry. In the following, a few applications related to infrared thermography in both pulsed and lock-in modes are presented.

1.- *Curing of dental resins*. It is well known that dental resins usually cure by applying a blue light source. The curing of this kind of resins has been typically monitored using modulated photothermal radiometry. However, it only allows to monitor a localized region of the whole sample, depending on the size of the infrared detector, which is typically of 1 mm $\times$ 1 mm. Instead, we propose to use lock-in thermography to monitor the curing of dental resins, which will allow access to a bigger area and to serve as an inspection tool for the cured/uncured regions.

2.- *Granular media*. Heat conduction trough granular systems has been a challenging task for engineers and scientists. A few approaches have been reported in literature and most of them are based on finite element methods. This is a quite complex problem, thus, we propose to simplify it by considering a linear chain of spheres. Lock-in thermography with line illumination may allow us to study the heat conduction through

that chain of beads in the thermally thin limit, i.e., when the thermal diffusion length due to the modulation is larger than the diameter of a sphere conforming the linear chain.

3.- *Thermal conductivity of liquids and pasty materials*. It is quite interesting to develop a method which would be able to retrieve the thermal conductivity of liquids and/or pasty materials in a fast non-invasive way. It has been reported in literature that using a three-layer system makes it possible to retrieve the thermal diffusivity and thermal effusivity of a liquid using the classical flash method. Here, we propose to apply this idea to the front-face flash method and to explore the sensitivity of the method for each parameter (thermal effusivity and thermal diffusivity) in order to establish the limits of application.

4.- *Polymer composites with electrically aligned multi-walled carbon nanotubes*. It is well-known that multi-walled carbon nanotubes (MWCNTs) are good electrical conductors. Thus, it is interesting to use this property in order to build nanocomposites with enhanced thermal properties which can be useful for thermal management applications in electron components. It has been observed that MWCNTs can be aligned from surface to surface in liquids in a box with metallic parallel walls, by applying an oscillating voltage. It is possible to extend this phenomena to a polymer, i.e., align the MWCNTs in a monomer solution and then polymerize it. The front-face flash method would be a great technique to characterize this kind of samples.

5.- *In-plane thermal diffusivity of solids*. The flash method demands the use of a Dirac-like excitation source which can be, in some cases, dangerous for the sample surface (laser ablation). Thus, we propose to explore the possibility of using a low power heating source under continuous heating (Heaviside-like step). Since there is no analytical solution in this case, robust inversion algorithms should be used or developed in order to obtain the surface temperature at each instant of time.

6.- *Characterization of vertical cracks using Heaviside-like step*. There are just a few reports using this kind of illumination for crack detection and it is not all explored yet. Even when the model could become cumbersome, it is worth to try, due to fact that only a low power laser heating is needed. Thus, it is a challenging task for non-destructive testing of materials.

Resumen Extendido

La termografía infrarroja pulsada en la configuración frontal ha demostrado su versatilidad y buena precisión para determinar tanto las propiedades de transporte térmico, así como los coeficientes lineales de absorción óptica en sólidos semitransparentes y opacos. En este trabajo, varios arreglos experimentales han sido probados para estudiar la difusividad térmica y efusividad térmica en muestras semitransparentes u opacas, delgadas o gruesas. Además, la termografía infrarroja pulsada ha recuperado simultáneamente, las difusividades paralela y perpendicular al plano con buena precisión comparado con valores de literatura. Estudios realizados en varios materiales sólidos (polímeros, cerámicos, vidrios, metales, óxidos metálicos, nano-compuestos, etc.) que abarcan un amplio rango de conductividades térmicas y semitransparencia validan la robustez del método.

Por otra parte, la termografía modulada ha sido aplicada exitosamente para determinar el espesor de grietas verticales infinitas en muestras semi-infinitas opacas y calibradas. Además, este método se ha implementado para la caracterización del espesor y profundidad de grietas verticales semi-infinitas. En ambos casos, se ha obtenido buen acuerdo entre los valores obtenidos y los de calibración, confirmando la aplicabilidad de los modelos propuestos.

Finalmente, la termografía pulsada de láser enfocado fue exitosamente usada para estudiar el espesor de grietas verticales infinitas en sólidos semi-infinitos. Se ha mostrado que esta técnica no es tan precisa como la termografía modulada, pero en

cambio es más rápida y provee valores suficientemente precisos de los espesores de las grietas comparados con los valores calibrados. A continuación se presenta, en resumen, cada uno de los trabajos desarrollados.

Para el estudio de la difusividad térmica de placas semitransparentes sin recubrimientos usando el método flash en su configuración frontal:

- Un modelo de conducción de calor unidimensional casi completo se ha desarrollado en el Capítulo 3, con el fin de obtener la difusividad térmica de placas semitransparentes sin necesidad de recubrirlas. Este modelo incluye: reflexiones múltiples del haz de luz incidente sobre las superficies de la placa, pérdidas de calor hacia los alrededores debido a mecanismos de convección, semitransparencia al infrarrojo (IR) y también la forma temporal del pulso de excitación.
- Ajustes numéricos del modelo propuesto a los datos experimentales obtenidos usando el arreglo experimental mostrado en la Figura 2.1a del Capítulo 2, han permitido recuperar las difusividades térmicas de las muestras semitransparentes con buena precisión. Además, como subproductos de los ajustes, también se obtuvo el coeficiente de absorción óptica a la longitud de onda incidente y el coeficiente de absorción óptica efectivo a longitudes de onda en el IR. Todos los parámetros obtenidos mostraron buen acuerdo con valores de literatura.
- Un amplio rango de materiales conductores ha sido estudiado, desde conductores de calor pobres (polímeros, cartulinas, compuestos poliméricos, vidrios y cerámicos) hasta muy buenos conductores de calor (metales y óxidos metálicos). Los materiales estudiados también cubren un amplio rango de semitransparencia tanto al IR como a la longitud de onda del haz incidente. Esto proporciona una validación experimental del método flash en su configuración frontal para el estudio de la difusividad térmica de placas semitransparentes. Sin embargo, este método no es adecuado para el estudio de materiales cuyas superficies sean altamente reflectoras (metales pulidos o vidrios, etc.) y/o muestras que sean transparentes a la longitud de onda incidente (vidrio, cuarzo, germanio, etc.), ya que en ambos casos la señal termográfica podría ser muy

débil o nula.

- La caracterización de películas semitransparentes sin recubrimiento es más rápida utilizando el método flash en configuración frontal introducido en el Capítulo 3 que mediante métodos modulados. Además, tiene una ventaja con respecto al método flash clásico, ya que el primero no requiere acceso a la superficie no iluminada. Sin embargo, en ambas configuraciones del método flash, el espesor de la muestra estudiada debe ser conocido.

Acerca de la mejora en la conductividad térmica de compuestos de resina poliéster cargados con nanofibras de carbono magnetizadas usando el método flash en configuración frontal:

- Las nanofibras de carbono magnetizadas fueron alineadas en una matriz de resina poliéster mediante un campo magnético uniforme de intensidad moderada, generado por un par de bobinas Helmholtz. Se ha obtenido un incremento significativo en la conductividad térmica de las películas de compuestos alineados, en la dirección de alineamiento de las nanofibras, con respecto a los compuestos de resina poliéster no-alineados, como se muestra en la Figura 4.7 del Capítulo 4.
- El método flash en configuración frontal, como ha sido aplicado en el Capítulo 4, ha proporcionado valores precisos y de manera rápida, para las difusividades térmicas y efusividades térmicas de los compuestos estudiados, lo que ha permitido calcular sus conductividades térmicas.
- Un modelo teórico basado en la 'derivación de interacción directa' (IDD por sus siglas en inglés) ha sido utilizado para interpretar el incremento obtenido en la conductividad térmica. Cabe mencionar que los valores de resistencia térmica entre las nanofibras de carbono y la matriz de poliéster concuerdan muy bien con valores de literatura.

Con respecto a las medidas simultáneas de difusividad térmica y efusividad térmica de películas opacas usando el método flash en la configuración frontal para un

sistema de dos-capas:

- La temperatura superficial, considerando conducción de calor unidimensional, de un sistema de dos-capas que consiste de una placa de sólido opaco en contacto directo con una capa de líquido semi-infinita ha sido resuelta con el fin de estudiar la difusividad térmica y efusividad térmica del sólido, siempre que las propiedades térmicas del líquido sean conocidas. Un análisis de sensibilidad ha proporcionado guías para seleccionar los casos en los que es posible recuperar de manera simultánea la difusividad térmica y efusividad térmica de la placa (ver la Figura 5.3 del Capítulo 5).
- Un arreglo experimental termográfico como el mostrado en la Figura 2.1 del Capítulo 2 ha sido usado para obtener datos experimentales, que ajustados al modelo propuesto han recuperado valores precisos de las difusividades térmicas y efusividades térmicas de los sólidos estudiados. Es importante mencionar que la efusividad térmica obtenida es subestimada cuando su valor real es tres veces o más, la efusividad térmica del líquido (agua en la mayoría de los casos). Sin embargo, en todos los casos, la difusividad térmica es obtenida con buena precisión.
- Un amplio rango de sólidos conductores (polímeros, vidrios, cerámicos y metales) ha sido probado con el fin de validar y probar la robustez del método propuesto. Los valores recuperados de los ajustes numéricos concuerdan con valores encontrados en la literatura.
- Debido a que una restricción en la razón de las efusividades térmicas de la capa sólida y la capa líquida ha sido encontrada, este método no es muy adecuado para materiales con altas efusividades térmicas. Sin embargo, este método es muy preciso para muchos materiales de interés industrial, tales como polímeros, algunos óxidos metálicos, cerámicos entre otros.

Acerca de la medida simultánea de las difusividades térmicas paralela y perpendicular al plano de iluminación en placas sólidas semitransparentes utilizando termografía pulsada de láser enfocado:

- Un modelo de conducción de calor en las placas sólidas ha sido exitosamente aplicado al estudio de las difusividades paralela y perpendicular al plano, en materiales isotrópicos y anisotrópicos. Este modelo considera iluminación utilizando un pulso tipo delta de Dirac con un haz circular Gaussiano, incluye las pérdidas de calor a los alrededores debido a mecanismos convectivos, semitransparencia del sólido a la longitud de onda incidente y a longitudes de onda en el IR.
- La difusividad térmica paralela al plano de materiales semitransparentes, opacos, delgados o gruesos (semi-infinitos), puede ser recuperada con un ajuste lineal de la evolución temporal del radio Gaussiano del perfil central de la temperatura superficial. Además, la pendiente de dicho ajuste no es afectada por las pérdidas de calor, como es explicado en la Subsección 6.4.1 del Capítulo 6. Las medidas experimentales realizadas utilizando un arreglo termográfico como el mostrado en la Figura 2.6 del Capítulo 2 han concordado muy bien con valores reportados en la literatura.
- Se ha mostrado que promediando espacialmente la señal IR resultante de una iluminación Gaussiana en una placa semitransparente anisotrópica, la respuesta de una iluminación plana es obtenida, lo que permite recuperar la difusividad térmica usando un modelo de conducción de calor unidimensional como en el método flash en su configuración frontal. Una prueba hecha en un compuesto polimérico anisotrópico ha confirmado la aplicabilidad del método.
- Varias muestras opacas y semitransparentes, abarcando un amplio régimen de difusividades térmicas han sido estudiadas y se ha obtenido muy buena concordancia entre los valores recuperados y valores de la literatura, confirmando la validez del modelo.

En relación con la medida del espesor de grietas verticales infinitas usando termografía modulada:

- Una expresión semi-analítica de la temperatura superficial de un material que contiene una grieta vertical infinita y que es excitada mediante un láser de haz

circular Gaussiano modulado, localizado a una distancia cercana a la grieta has sido planteada, lo cual permite el estudio del espesor de grietas verticales infinitas calibradas.

- El análisis de los contrastes en amplitud y fase ha permitido seleccionar las condiciones óptimas para el tamaño del haz del láser, la frecuencia de modulación y la distancia del centro del haz a la grieta, con el fin de recuperar el espesor de grietas verticales infinitas en muestras semi-infinitas.
- Se han realizado medidas de termografía modulada en muestras calibradas de AISI-304 y carbono vítreo, utilizando un arreglo experimental como el mostrado en la Figura 2.7 del Capítulo 2. Ajustes numéricos entre el perfil central de temperatura superficial del modelo propuesto y los datos experimentales han permitido determinar espesores de grietas con muy buena precisión comparados con los espesores calibrados ópticamente.

Acerca del estudio de grietas verticales semi-infinitas con termografía modulada:

- La temperatura superficial de muestras semi-infinitas que contienen grietas arbitrariamente delgadas de cualquier geometría cuando la superficie de la muestra es iluminada con un láser Gaussiano modulado de haz enfocado ha sido resuelta numéricamente usando elementos finitos discontínuos de Galerkin de tipo Bauman-Oden. En particular, este modelo ha sido aplicado con éxito para caracterizar grietas verticales semi-infinitas calibradas en AISI-304.
- Se han hecho medidas de termografía modulada en muestras de AISI-304 que contienen grietas semi-infinitas calibradas de distintos espesores y profundidades. Los valores recuperados a partir de ajustes numéricos concuerdan con los valores nominales, lo que confirma la validez del modelo.
- El método establecido en el Capítulo 8, basado en termografía modulada, abre la posibilidad de caracterizar grietas reales de geometría arbitraria, de cualquier tamaño y orientación.

Sobre la medida del espesor de grietas verticales infinitas con termografía pulsada de láser enfocado:

- Se ha encontrado una solución semi-analítica para la temperatura superficial de un material que contiene una grieta vertical infinita, como se muestra en la Figura 9.1 del Capítulo 9. Se ha considerado un pulso tipo delta de Dirac de haz Gaussiano enfocado cerca de la grieta. Este modelo ha permitido el estudio, de una manera rápida y con buena precisión, del espesor de grietas infinitas verticales en muestras semi-infinitas.
- Simulaciones numéricas del contraste de temperatura han revelado las condiciones óptimas bajo la cuales es posible medir el espesor de grietas verticales con la máxima precisión permitida por este método.
- La validez del modelo ha sido probada realizando medidas de termografía infrarroja pulsada (utilizando un arreglo experimental como el mostrado en la Figura 2.6 del Capítulo 2), en muestras de AISI-304 y PEEK que contienen grietas calibradas. Los ajustes numéricos del modelo propuesto y los datos experimentales han proporcionado espesores lo suficientemente precisos con respecto a los valores calibrados.
- Se ha mostrado que aún cuando la termografía modulada provee mayor razón señal-ruido y que los espesores de la grietas son más precisos que los obtenidos mediante termografía pulsada, esta última es más rápida y lo suficientemente precisa para determinar el espesor de grietas verticales en materiales opacos, lo cual la sitúa como una técnica interesante para ensayos no-destructivos en aplicaciones industriales.

List of Publications

The following journal publications are product of this thesis:

- N. W. Pech-May, A. Oleaga, A. Mendioroz, A. J. Omella, R. Celorrio, and A. Salazar, "Vertical cracks characterization using lock-in thermography: I infinite cracks," *Meas. Sci. Technol.*, vol. 25, no. 11, p. 115601, Nov. 2014.
- R. Celorrio, A. J. Omella, N. W. Pech-May, A. Oleaga, A. Mendioroz, and A. Salazar, "Vertical cracks characterization using lock-in thermography: II finite cracks," *Meas. Sci. Technol.*, vol. 25, no. 11, p. 115602, Nov. 2014.
- N. W. Pech-May, A. Mendioroz, and A. Salazar, "Generalizing the flash technique in the front-face configuration to measure the thermal diffusivity of semitransparent solids," *Rev. Sci. Instrum.*, vol. 85, no. 10, p. 104902, Oct. 2014.
- N. W. Pech-May, Á. Cifuentes, A. Mendioroz, A. Oleaga, and A. Salazar, "Simultaneous measurement of thermal diffusivity and effusivity of solids using the flash technique in the front-face configuration," *Meas. Sci. Technol.*, vol. 26, no. 8, p. 085017, Aug. 2015.
- N. W. Pech-May, C. Vales-Pinzón, A. Vega-Flick, Á. Cifuentes, A. Oleaga, A. Salazar, and J. J. Alvarado-Gil, "Study of the thermal properties of polyester composites loaded with oriented carbon nanofibers using the front-face flash method," *Polym. Test.*, vol. 50, pp. 255–261, Apr. 2016.
- N. W. Pech-May, A. Mendioroz, and A. Salazar, "Simultaneous measurement of

the in-plane and in-depth thermal diffusivity of solids using pulsed infrared thermography with focused illumination," *NDT E Int.*, vol. 77, pp. 28–34, Jan. 2016.

- N. W. Pech-May, A. Oleaga, A. Mendioroz, and A. Salazar, "Fast Characterization of the Width of Vertical Cracks Using Pulsed Laser Spot Infrared Thermography," *J. Nondestruct. Eval.*, vol. 35, no. 2, pp. 1–10, Mar. 2016.

Also, the work developed in this thesis has been presented in the following international conferences:

- R. Celorrio, A. J. Omella, N. W. Pech-May, A. Mendioroz, A. Oleaga and A. Salazar, Development of a discontinuous finite element method to characterize vertical cracks using lock-in thermography, The 12th International Conference on Quantitative InfraRed Thermography, Bordeaux (France), 2014, Oral
- N. W. Pech-May, A. Mendioroz, E. Apiñaniz and A. Salazar, Thermal and Optical Characterization of Semitransparent Slabs by the Flash Method, 20th European Conference on Thermophysical Properties, Porto (Portugal), 2014, Oral
- A. Oleaga, R. Celorrio, A. J. Omella, N. W. Pech-May, A. Mendioroz and A. Salazar, Recent Advances in the Characterization of Vertical Cracks Using Lock-in Thermography, International School of Quantum Electronics: 3rd Mediterranean International Workshop on Photoacoustic and Photothermal Phenomena Focus on Biomedical, Nanoscale Imaging and Non-Destructive Evaluation, Erice (Italy), 2014, Oral
- N. W. Pech-May, A. Mendioroz and A. Salazar, Extending the Flash Method for Semitransparent Materials, International School of Quantum Electronics: 3rd Mediterranean International Workshop on Photoacoustic and Photothermal Phenomena Focus on Biomedical, Nanoscale Imaging and Non-Destructive Evaluation, Erice (Italy), 2014, Oral

- A. Oleaga, N. W. Pech-May, C. Vales-Pinzón, A. Vega-Flick, A. Cifuentes, A. Salazar and J. J. Alvarado-Gil, Transport Thermal Properties of Polyester/Magnetized Carbon Nanofibers (mCNF) Composites, Energy Materials Nanotechnology Meeting, Phuket (Thailand), 2015 Oral: Invited
- N. W. Pech-May, A. Mendioroz, A. Oleaga and A. Salazar, Characterization of Vertical Cracks by Pulsed Thermography, 18th International Conference on Photoacoustic and Photothermal Phenomena, Novi Sad (Serbia), 2015, Oral
- N. W. Pech-May, A. Cifuentes, A. Mendioroz, A. Oleaga and A. Salazar, Development of the Flash Method to Measure the Thermal Diffusivity and Effusivity of Solids Simultaneously, 18th International Conference on Photoacoustic and Photothermal Phenomena, Novi Sad (Serbia), 2015, Oral
- N. W. Pech-May, C. Vales-Pinzón, A. Vega-Flick, A. Cifuentes, A. Oleaga, A. Salazar and J. J. Alvarado-Gil, Enhancement of Transport Thermal Properties in Polyester Based Composites with Aligned Magnetized Carbon Nanofibers, 18th International Conference on Photoacoustic and Photothermal Phenomena, Novi Sad (Serbia), 2015, Oral
- N. W. Pech-May, A. Oleaga, A. Mendioroz and A. Salazar, Sizing the Thermal Resistance of Vertical Cracks Using Pulsed Infrared Thermography with Laser Spot Excitation, 13th Quantitative Infrared Thermography Conference, Gdansk, (Poland), 2016, Oral

References

[1] W. Herschel, “Experiments on the Refrangibility of the Invisible Rays of the Sun. By William Herschel, LL. D. F. R. S.,” *Philos. Trans. R. Soc. Lond.* **90**, 284–292 (1800).

[2] W. Minkina and S. Dudzik, *Infrared Thermography: Errors and Uncertainties* (John Wiley & Sons, United Kingdom, 2009).

[3] R. Eisenberg and R. Resnick, *Quantum Physics of Atoms, Molecules, Solids, Nuclei, and Particles,* 2nd edition (John Wiley & Sons, New York, 1985).

[4] Z. Zou, Y. Hu, B. Gao, W. L. Woo, and X. Zhao, “Temperature recovery from degenerated infrared image based on the principle for temperature measurement using infrared sensor,” *J. Appl. Phys.* **115**, 043522 (2014).

[5] V. Vavilov, “Thermal non-destructive testing: short history and state of the art,” in *QIRT Conf.* **1**, (QIRT, Paris, 1992).

[6] V. Vavilov, “Thermal NDT: historical milestones, state-of-the-art and trends,” *Quant. InfraRed Thermogr. J.* **11**, 66–83 (2014).

[7] C. Meola and G. M. Carlomagno, “Recent advances in the use of infrared thermography,” *Meas. Sci. Technol.* **15**, R27 (2004).

[8] C. Ibarra-Castanedo and X. P. V. Maldague, “Infrared Thermography,” in *Handb. Tech. Diagn.*, H. Czichos, Ed. (Springer Berlin Heidelberg, 2013).

[9] J. D. Jackson, *Classical Electrodynamics*, 3rd ed. (John Wiley & Sons, 1998).

[10] A. Rogalski, “Infrared detectors: an overview,” *Infrared Phys. Technol.* **43**, 187–

210 (2002).

[11] A. Rogalski, “Infrared detectors: status and trends,” *Prog. Quantum Electron.* **27**, 59–210 (2003).

[12] A. Rogalski and K. Chrzanowski, “Infrared devices and techniques,” *Opto - Electron. Rev.*, 111–136 (2002).

[13] A. Rogalski, “Recent progress in infrared detector technologies,” *Infrared Phys. Technol.* **54**, 136–154 (2011).

[14] “Teledyne Judson Technologies: Dewars and Coolers,” http://www.judsontechnologies.com/dewars.html (accessed: 10 January 2016).

[15] O. Breitenstein, W. Wilhelm, and M. Langenkamp, *Lock-in Thermography - Basics and Use for Evaluating Electronic Devices and Materials*, 2nd ed. (Springer Berlin Heidelberg, 2010).

[16] G. M. Carlomagno and P. G. Berardi, “Unsteady Thermotopography in Non-Destructive Testing,” in *Proc III Infrared Inf. Exch.*, (C. Warren, St Louis, 1976).

[17] G. Busse, D. Wu, and W. Karpen, “Thermal wave imaging with phase sensitive modulated thermography,” *J. Appl. Phys.* **71**, 3962–3965 (1992).

[18] D. Almond and P. Patel, *Photothermal Science and Techniques* (Chapman & Hall, 1996).

[19] H. S. Carslaw and J. J. C. Jaeger, *Conduction of Heat in Solids*, 2nd ed. (Clarendon Press, 1986).

[20] A. Ocariz, A. Sanchez-Lavega, and A. Salazar, “Photothermal study of subsurface cylindrical structures. I. Theory,” *J. Appl. Phys.* **81**, 7552–7560 (1997).

[21] F. Garrido and A. Salazar, “Thermal wave scattering by spheres,” *J. Appl. Phys.* **95**, 140 (2004).

[22] J. Liu, W. Yang, and J. Dai, “Research on thermal wave processing of lock-in thermography based on analyzing image sequences for NDT,” *Infrared Phys. Technol.* **53**, 348–357 (2010).

[23] R. Montanini, “Quantitative determination of subsurface defects in a reference specimen made of Plexiglas by means of lock-in and pulse phase infrared thermography,” *Infrared Phys. Technol.* **53**, 363–371 (2010).

[24] J. C. Krapez, “Compared performances of four algorithms used for modulation thermography,” in *QIRT Conf.* **4**, (QIRT, Lodz, 1998).

[25] D. Wu and G. Busse, “Lock-in thermography for nondestructive evaluation of materials,” *Rev. Générale Therm.* **37**, 693–703 (1998).

[26] D. L. Balageas, “Defense and illustration of time-resolved pulsed thermography for NDE,” *Quant. InfraRed Thermogr. J.* **9**, 3–32 (2012).

[27] C. Ibarra-Castanedo, N. P. Avdelidis, M. Grenier, X. Maldague, and A. Bendada, “Active thermography signal processing techniques for defect detection and characterization on composite materials,” in *Proc SPIE* **7661**, (SPIE, Orlando, 2010).

[28] S. M. Shepard, J. R. Lhota, B. A. Rubadeux, T. Ahmed, and D. Wang, “Enhancement and reconstruction of thermographic NDT data,” in *Proc SPIE* **4710**, (SPIE, Orlando, 2002).

[29] C. Ibarra-Castanedo and X. P. V. Maldague, “Interactive Methodology for Optimized Defect Characterization by Quantitative Pulsed Phase Thermography,” *Res. Nondestruct. Eval.* **16**, 175–193 (2005).

[30] S. M. Shepard, J. Hou, J. R. Lhota, and J. M. Golden, “Automated processing of thermographic derivatives for quality assurance,” *Opt. Eng.* **46**, 051008–051008 – 6 (2007).

[31] D. Balageas, B. Chapuis, G. Deban, and F. Passilly, “Improvement of the detection of defects by pulse thermography thanks to the TSR approach in the case of a smart composite repair patch,” *Quant. InfraRed Thermogr. J.* **7**, 167–187 (2010).

[32] D. L. Balageas and J.-M. Roche, “Common tools for quantitative time-resolved pulse and step-heating thermography – part I: theoretical basis,” *Quant. InfraRed Thermogr. J.* **11**, 43–56 (2014).

[33] F.-H. L. J. -M. Roche, “Images of Thermographic Signal Reconstruction Coefficients: A Simple Way for Rapid and Efficient Detection of Discontinuities,” *Mater. Eval.* **72**, 73–82 (2014).

[34] W. J. Parker, R. J. Jenkins, C. P. Butler, and G. L. Abbott, “Flash Method of

Determining Thermal Diffusivity, Heat Capacity, and Thermal Conductivity," *J. Appl. Phys.* **32**, 1679–1684 (1961).

[35] D. L. Balageas, "Thermal diffusivity measurement by pulsed methods," *High Temp. High Press.* **21**, 85–96 (1989).

[36] "SC7000 MWIR Datasheet" http://www.flir.com/instruments/display/?id=18092 (FLIR systems AB, 2011).

[37] L. Fabbri and E. Scafè, "Nonuniform heating effects on thermal diffusivity measurements by the laser-pulse method: Influence of detector position," *Rev. Sci. Instrum.* **63**, 2008–2013 (1992).

[38] T. Baba and A. Ono, "Improvement of the laser flash method to reduce uncertainty in thermal diffusivity measurements," *Meas. Sci. Technol.* **12**, 2046 (2001).

[39] E. Apiñaniz, A. Mendioroz, N. Madariaga, A. Oleaga, R. Celorrio, and A. Salazar, "Thermal characterization of rods, tubes and spheres using pulsed infrared thermography," *J. Phys. D: Appl. Phys.* **41**, 015403 (2008).

[40] A. Mendioroz, R. Fuente-Dacal, E. Apiñaniz, and A. Salazar, "Thermal diffusivity measurements of thin plates and filaments using lock-in thermography," *Rev. Sci. Instrum.* **80**, 074904 (2009).

[41] A. Salazar, A. Mendioroz, R. Fuente, and R. Celorrio, "Accurate measurements of the thermal diffusivity of thin filaments by lock-in thermography," *J. Appl. Phys.* **107**, 043508 (2010).

[42] A. Salazar, A. Mendioroz, and R. Fuente, "The strong influence of heat losses on the accurate measurement of thermal diffusivity using lock-in thermography," *Appl. Phys. Lett.* **95**, 121905 (2009).

[43] A. Rosencwaig and A. Gersho, "Theory of the photoacoustic effect with solids," *J. Appl. Phys.* **47**, 64–69 (1976).

[44] U. Zammit, F. Mercuri, S. Paoloni, M. Marinelli, and R. Pizzoferrato, "Simultaneous absolute measurements of the thermal diffusivity and the thermal effusivity in solids and liquids using photopyroelectric calorimetry," *J. Appl. Phys.* **117**, 105104 (2015).

[45] C. Vales-Pinzon, J. Ordonez-Miranda, and J. J. Alvarado-Gil, "Photothermal characterization of the thermal properties of materials using four characteristic modulation frequencies in two-layer systems," *J. Appl. Phys.* **112**, 064909 (2012).

[46] M. Chirtoc and G. Mihilescu, "Theory of the photopyroelectric method for investigation of optical and thermal materials properties," *Phys. Rev. B* **40**, 9606–9617 (1989).

[47] M. Depriester, P. Hus, S. Delenclos, and A. H. Sahraoui, "New methodology for thermal parameter measurements in solids using photothermal radiometry," *Rev. Sci. Instrum.* **76**, 074902 (2005).

[48] A. Salazar and A. Sánchez-Lavega, "Measurements of the Thermal Diffusivity Tensor of Polymer–Carbon Fiber Composites by Photothermal Methods," *Int. J. Thermophys.* **19**, 625–636 (1998).

[49] R. Fuente, E. Apiñaniz, A. Mendioroz, and A. Salazar, "Simultaneous measurement of thermal diffusivity and optical absorption coefficient using photothermal radiometry. I. Homogeneous solids," *J. Appl. Phys.* **110**, 033515–033515 – 9 (2011).

[50] J.-F. Bisson, D. Fournier, M. Poulain, O. Lavigne, and R. Mévrel, "Thermal Conductivity of Yttria–Zirconia Single Crystals, Determined with Spatially Resolved Infrared Thermography," *J. Am. Ceram. Soc.* **83**, 1993–1998 (2000).

[51] F. Cernuschi, A. Russo, L. Lorenzoni, and A. Figari, "In-plane thermal diffusivity evaluation by infrared thermography," *Rev. Sci. Instrum.* **72**, 3988–3995 (2001).

[52] A. Degiovanni, J. C. Batsale, and D. Maillet, "Mesure de la diffusivité longitudinale de matériaux anisotropes," *Rev. Générale Therm.* **35**, 141–147 (1996).

[53] D. Demange, P. Beauchêne, M. Bejet, and R. Casulleras, "Mesure simultanée de la diffusivité thermique selon les deux directions principales d'un matériau," *Rev. Générale Therm.* **36**, 755–770 (1997).

[54] J.-C. Krapez, L. Spagnolo, M. Frieß, H.-P. Maier, and G. Neuer, "Measurement of in-plane diffusivity in non-homogeneous slabs by applying flash thermography," *Int. J. Therm. Sci.* **43**, 967–977 (2004).

[55] P. G. Bison, F. Cernuschi, and E. Grinzato, “Ageing evaluation of thermal barrier coating: comparison between pulsed thermography and thermal wave interferometry,” *Quant. InfraRed Thermogr. J.* **3**, 169–181 (2006).

[56] A. Salazar, A. Mendioroz, E. Apiñaniz, C. Pradere, F. Noël, and J.-C. Batsale, “Extending the flash method to measure the thermal diffusivity of semitransparent solids,” *Meas. Sci. Technol.* **25**, 035604 (2014).

[57] R. E. Imhof, D. J. S. Birch, F. R. Thornley, J. R. Gilchrist, and T. A. Strivens, “Optothermal transient emission radiometry,” *J. Phys. [E]* **17**, 521 (1984).

[58] R. E. Imhof, F. R. Thornley, J. R. Gilchrist, and D. J. S. Birch, “Opto-thermal study of thermally insulating films on thermally conducting substrates,” *J. Phys. D: Appl. Phys.* **19**, 1829 (1986).

[59] H. G. Walther, U. Seidel, W. Karpen, and G. Busse, “Application of modulated photothermal radiometry to infrared transparent samples,” *Rev. Sci. Instrum.* **63**, 5479–5480 (1992).

[60] H. Stehfest, “Algorithm 368: Numerical Inversion of Laplace Transforms [D5],” *Commun ACM* **13**, 47–49 (1970).

[61] X. P. Maldague, *Theory and Practice of Infrared Technology for Nondestructive Testing* (Wiley, New York, 2001).

[62] J. Abate and W. Whitt, “A Unified Framework for Numerically Inverting Laplace Transforms,” *Inf. J. Comput.* **18**, 408–421 (2006).

[63] D. W. Marquardt, “An Algorithm for Least-Squares Estimation of Nonlinear Parameters,” *J. Soc. Ind. Appl. Math.* **11**, 431–441 (1963).

[64] K. Madsen, H. B. Nielsen, and O. Tingleff, *Methods for non-linear least squares problems*, 2nd ed. (Technical University of Denmark DTU, Denmark, 2004).

[65] H. P. Gavin, “The Levenberg-Marquardt method for nonlinear least squares curve-fitting problems” (Duke University, 2016).

[66] S. A. Prahl, I. A. Vitkin, U. Bruggemann, B. C. Wilson, and R. R. Anderson, “Determination of optical properties of turbid media using pulsed photothermal radiometry,” *Phys. Med. Biol.* **37**, 1203 (1992).

[67] A. Matvienko, A. Mandelis, and S. Abrams, “Robust multiparameter method of

evaluating the optical and thermal properties of a layered tissue structure using photothermal radiometry," *Appl. Opt.* **48**, 3192 (2009).

[68] M. Marinelli, F. Mercuri, U. Zammit, R. Pizzoferrato, F. Scudieri, and D. Dadarlat, "Photopyroelectric study of specific heat, thermal conductivity, and thermal diffusivity of Cr_2O_3 at the N'eel transition," *Phys. Rev. B* **49**, 9523–9532 (1994).

[69] R. Fuente, A. Mendioroz, E. Apiñaniz, and A. Salazar, "Simultaneous Measurement of Thermal Diffusivity and Optical Absorption Coefficient of Solids Using PTR and PPE: A Comparison," *Int. J. Thermophys.* **33**, 1876–1886 (2012).

[70] H. Watanabe, "Thermal constants for Ni, NiO, MgO, MnO and CoO at low temperatures," *Thermochim. Acta* **218**, 365–372 (1993).

[71] Y. S. Touloukian, R. W. Powell, C. Y. Ho, and M. C. Nicolaou, *Thermal Diffusivity*, Softcover reprint of the original 1st ed. 1973 edition (Springer, New York, 2013).

[72] Y. A. Cengel, *Heat Transfer: A Practical Approach* (Mcgraw-Hill, Boston, 2002).

[73] N. K. Mahanta, A. R. Abramson, M. L. Lake, D. J. Burton, J. C. Chang, H. K. Mayer, and J. L. Ravine, "Thermal conductivity of carbon nanofiber mats," *Carbon* **48**, 4457–4465 (2010).

[74] Z. Han and A. Fina, "Thermal conductivity of carbon nanotubes and their polymer nanocomposites: A review," *Prog. Polym. Sci.* **36**, 914–944 (2011).

[75] J. Philip, P. D. Shima, and B. Raj, "Enhancement of thermal conductivity in magnetite based nanofluid due to chainlike structures," *Appl. Phys. Lett.* **91**, 203108–203108 – 3 (2007).

[76] A. M. Marconnet, N. Yamamoto, M. A. Panzer, B. L. Wardle, and K. E. Goodson, "Thermal Conduction in Aligned Carbon Nanotube–Polymer Nanocomposites with High Packing Density," *ACS Nano* **5**, 4818–4825 (2011).

[77] K. Kurabayashi, "Anisotropic Thermal Properties of Solid Polymers," *Int. J. Thermophys.* **22**, 277–288 (2001).

[78] Y. Mamunya, A. Boudenne, N. Lebovka, L. Ibos, Y. Candau, and M. Lisunova,

"Electrical and thermophysical behaviour of PVC-MWCNT nanocomposites," *Compos. Sci. Technol.* **68**, 1981–1988 (2008).

[79] R. A. Medina-Esquivel, M. A. Zambrano-Arjona, J. A. Mendez-Gamboa, J. M. Yanez-Limon, J. Ordonez-Miranda, and J. J. Alvarado-Gil, "Thermal characterization of composites made up of magnetically aligned carbonyl iron particles in a polyester resin matrix," *J. Appl. Phys.* **111**, 054906 (2012).

[80] H. Huang, C. H. Liu, Y. Wu, and S. Fan, "Aligned Carbon Nanotube Composite Films for Thermal Management," *Adv. Mater.* **17**, 1652–1656 (2005).

[81] M. J. Biercuk, M. C. Llaguno, M. Radosavljevic, J. K. Hyun, A. T. Johnson, and J. E. Fischer, "Carbon nanotube composites for thermal management," *Appl. Phys. Lett.* **80**, 2767–2769 (2002).

[82] P. M. Ajayan and J. M. Tour, "Materials Science: Nanotube composites," *Nature* **447**, 1066–1068 (2007).

[83] K. Enomoto, S. Fujiwara, T. Yasuhara, H. Murakami, J. Teraki, and N. Ohtake, "Effect of Filler Orientation on Thermal Conductivity of Polypropylene Matrix Carbon Nanofiber Composites," *Jpn. J. Appl. Phys.* **44**, L888 (2005).

[84] G. G. Tibbetts, M. L. Lake, K. L. Strong, and B. P. Rice, "A review of the fabrication and properties of vapor-grown carbon nanofiber/polymer composites," *Compos. Sci. Technol.* **67**, 1709–1718 (2007).

[85] S. Agarwal, M. M. K. Khan, and R. K. Gupta, "Thermal conductivity of polymer nanocomposites made with carbon nanofibers," *Polym. Eng. Sci.* **48**, 2474–2481 (2008).

[86] J. Liang, M. C. Saha, and M. C. Altan, "Effect of Carbon Nanofibers on Thermal Conductivity of Carbon Fiber Reinforced Composites," *Procedia Eng.* **56**, 814–820 (2013).

[87] J. C. Maxwell, *A treatise on electricity and magnetism* (Dover Publications, 1954).

[88] J. E. Gubernatis and J. A. Krumhansl, "Macroscopic engineering properties of polycrystalline materials: Elastic properties," *J. Appl. Phys.* **46**, 1875–1883 (2008).

[89] D. a. G. Bruggeman, “Berechnung verschiedener physikalischer Konstanten von heterogenen Substanzen. I. Dielektrizitätskonstanten und Leitfähigkeiten der Mischkörper aus isotropen Substanzen,” *Ann. Phys.* **416**, 636–664 (1935).

[90] C.-W. Nan, R. Birringer, D. R. Clarke, and H. Gleiter, “Effective thermal conductivity of particulate composites with interfacial thermal resistance,” *J. Appl. Phys.* **81**, 6692–6699 (1997).

[91] R. Pal, “New Models for Thermal Conductivity of Particulate Composites,” *J. Reinf. Plast. Compos.* **26**, 643–651 (2007).

[92] L. E. Nielsen, “The thermal and electrical conductivity of two-phase systems,” *Ind. Eng. Chem. Fundam.* **13**, 17–20 (1974).

[93] J. Ordonez-Miranda, R. Yang, and J. J. Alvarado-Gil, “On the thermal conductivity of particulate nanocomposites,” *Appl. Phys. Lett.* **98**, 233111 (2011).

[94] L. E. Nielsen, “Thermal conductivity of particulate-filled polymers,” *J. Appl. Polym. Sci.* **17**, 3819–3820 (1973).

[95] L. Gao, X. Zhou, and Y. Ding, “Effective thermal and electrical conductivity of carbon nanotube composites,” *Chem. Phys. Lett.* **434**, 297–300 (2007).

[96] F. Deng, Q.-S. Zheng, L.-F. Wang, and C.-W. Nan, “Effects of anisotropy, aspect ratio, and nonstraightness of carbon nanotubes on thermal conductivity of carbon nanotube composites,” *Appl. Phys. Lett.* **90**, 021914 (2007).

[97] G. Buonanno and A. Carotenuto, “The effective thermal conductivity of a porous medium with interconnected particles,” *Int. J. Heat Mass Transf.* **40**, 393–405 (1997).

[98] D.-X. Du and Q.-S. Zheng, “A further exploration of the interaction direct derivative (IDD) estimate for the effective properties of multiphase composites taking into account inclusion distribution,” *Acta Mech.* **157**, 61–80 (2002).

[99] Q.-S. Zheng and D.-X. Du, “An explicit and universally applicable estimate for the effective properties of multiphase composites which accounts for inclusion distribution,” *J. Mech. Phys. Solids* **49**, 2765–2788 (2001).

[100] F. Deng and Q. Zheng, “Interaction models for effective thermal and electric conductivities of carbon nanotube composites,” *Acta Mech. Solida Sin.* **22**, 1–17

(2009).

[101] D. Maillet, S. André, J. C. Batsale, A. Degiovanni, and C. Moyne, *Thermal quadrupoles: solving the heat equation through integral transforms* (Wiley, Chichester; New York, 2000).

[102] P. Bevington and D. K. Robinson, *Data Reduction and Error Analysis for the Physical Sciences*, 3rd ed. (McGraw-Hill Higher Education, Boston, 2002).

[103] M. H. Al-Saleh and U. Sundararaj, "A review of vapor grown carbon nanofiber/polymer conductive composites," *Carbon* **47**, 2–22 (2009).

[104] M. Idicula, A. Boudenne, L. Umadevi, L. Ibos, Y. Candau, and S. Thomas, "Thermophysical properties of natural fibre reinforced polyester composites," *Compos. Sci. Technol.* **66**, 2719–2725 (2006).

[105] A. Salazar, "On thermal diffusivity," *Eur. J. Phys.* **24**, 351 (2003).

[106] E. Marín, "The role of thermal properties in periodic time-varying phenomena," *Eur. J. Phys.* **28**, 429 (2007).

[107] M. Murabayashi, Y. Takahashi, and T. Mukaibo, "Measurement of Heat Capacity at High Temperatures by Laser Flash Method Heat Capacity of Alumina," *J. Nucl. Sci. Technol.* **7**, 312–316 (1970).

[108] Y. Takahashi, H. Yokokawa, H. Kadokura, Y. Sekine, and T. Mukaibo, "Laser-flash calorimetry I. Calibration and test on alumina heat capacity," *J. Chem. Thermodyn.* **11**, 379–394 (1979).

[109] K. Shinzato and T. Baba, "A Laser Flash Apparatus for Thermal Diffusivity and Specific Heat Capacity Measurements," *J. Therm. Anal. Calorim.* **64**, 413–422 (2001).

[110] S.-K. Kim and Y.-J. Kim, "Improvement of specific heat measurement by the flash method," *Thermochim. Acta* **455**, 30–33 (2007).

[111] H. Stehfest, "Remark on Algorithm 368: Numerical Inversion of Laplace Transforms," *Commun ACM* **13**, 624 – (1970).

[112] K. Levenberg, "A Method for the Solution of Certain Non-Linear Problems in Least Squares," *Q. Appl. Math.* **2**, 164–168 (1944).

[113] Y. Plevachuk, V. Sklyarchuk, S. Eckert, G. Gerbeth, and R. Novakovic,

"Thermophysical Properties of the Liquid Ga–In–Sn Eutectic Alloy," *J. Chem. Eng. Data* **59**, 757–763 (2014).

[114] P. G. Bison, F. Cernuschi, E. Grinzato, S. Marinetti, and D. Robba, "Ageing evaluation of thermal barrier coatings by thermal diffusivity," *Infrared Phys. Technol.* **49**, 286–291 (2007).

[115] L. Fabbri and P. Fenici, "Three-dimensional photothermal radiometry for the determination of the thermal diffusivity of solids," *Rev. Sci. Instrum.* **66**, 3593–3600 (1995).

[116] J. C. Krapez and G. Gardette, "Characterization of anisotropic materials by steady state and modulated thermal ellipsometry," *High Temp. High Press.* **30**, 567 (1998).

[117] J. F. Bisson and D. Fournier, "Influence of diffraction on low thermal diffusivity measurements with infrared photothermal microscopy," *J. Appl. Phys.* **83**, 1036–1042 (1998).

[118] C. S. Welch, D. M. Heath, and W. P. Winfree, "Remote measurement of in-plane diffusivity components in plates," *J. Appl. Phys.* **61**, 895–898 (1987).

[119] P. Bison, F. Cernuschi, and S. Capelli, "A thermographic technique for the simultaneous estimation of in-plane and in-depth thermal diffusivities of TBCs," *Surf. Coat. Technol.* **205**, 3128–3133 (2011).

[120] A. B. Donaldson and R. E. Taylor, "Thermal diffusivity measurement by a radial heat flow method," *J. Appl. Phys.* **46**, 4584–4589 (1975).

[121] P. Cielo, L. A. Utracki, and M. Lamontagne, "Thermal-diffusivity measurements by the converging-thermal-wave technique," *Can. J. Phys.* **64**, 1172–1177 (1986).

[122] S. Alterovitz, G. Deutscher, and M. Gershenson, "Heat capacity and thermal conductivity of sintered Al2O3 at low temperatures by the heat pulse technique," *J. Appl. Phys.* **46**, 3637–3643 (1975).

[123] I. Philippi, J. C. Batsale, D. Maillet, and A. Degiovanni, "Measurement of thermal diffusivities through processing of infrared images," *Rev. Sci. Instrum.* **66**, 182–192 (1995).

[124] C. Welch and J. Johnson, "Thermographic measurement of in-plane diffusivity in

very thin plates using diffusion of thermal patterns," in *AIP Conf. Proc.* **509**, (AIP Publishing, 2000).

[125] A. D. Poularikas, Ed., *Transforms and Applications Handbook*, 3rd ed. (CRC Press, Boca Raton, Fla, 2010).

[126] R. N. Bracewell, *Fourier Transform and Its Applications*, New edition (McGraw-Hill Inc.,US, New York, 1978).

[127] A. Sánchez-Lavega, A. Salazar, A. Ocariz, L. Pottier, E. Gomez, L. M. Villar, and E. Macho, "Thermal diffusivity measurements in porous ceramics by photothermal methods," *Appl. Phys. A* **65**, 15–22 (1997).

[128] "Goodfellow - Catalogue," http://www.goodfellow.com/catalogue/GFCatalogue.php?Language=E (accessed: 16 May 2016).

[129] E. J. Kubiak, "Infrared Detection of Fatigue Cracks and Other Near-Surface Defects," *Appl. Opt.* **7**, 1743 (1968).

[130] J. Rantala, D. Wu, and G. Busse, "Amplitude-modulated lock-in vibrothermography for NDE of polymers and composites," *Res. Nondestruct. Eval.* **7**, 215–228 (1996).

[131] L. D. Favro, X. Han, Z. Ouyang, G. Sun, H. Sui, and R. L. Thomas, "Infrared imaging of defects heated by a sonic pulse," *Rev. Sci. Instrum.* **71**, 2418–2421 (2000).

[132] J.-M. Piau, A. Bendada, X. Maldague, and J.-G. Legoux, "Nondestructive testing of open microscopic cracks in plasma-sprayed-coatings using ultrasound excited vibrothermography," *Nondestruct. Test. Eval.* **23**, 109–120 (2008).

[133] J. Renshaw, J. C. Chen, S. D. Holland, and R. Bruce Thompson, "The sources of heat generation in vibrothermography," *NDT E Int.* **44**, 736–739 (2011).

[134] A. Mendioroz, A. Castelo, R. Celorrio, and A. Salazar, "Characterization of vertical buried defects using lock-in vibrothermography: I. Direct problem," *Meas. Sci. Technol.* **24**, 065601 (2013).

[135] M. Morbidini, P. Cawley, T. Barden, D. Almond, and P. Duffour, "Prediction of the thermosonic signal from fatigue cracks in metals using vibration damping

measurements," *J. Appl. Phys.* **100**, 104905 (2006).

[136] B. Weekes, P. Cawley, D. P. Almond, and T. Li, "The Effect of Crack Opening on Thermosonics and Laser-Spot Thermography," in *AIP Conf. Proc.* **1211**, (AIP Publishing, 2010).

[137] Y. Q. Wang, P. K. Kuo, L. D. Favro, and R. L. Thomas, "A Novel 'Flying-Spot' Infrared Camera for Imaging Very Fast Thermal-Wave Phenomena," in *Photoacoust. Photothermal Phenom. II*, P. J. C. Murphy, J. W. M. S. P. D, L. C. A. P. D, and P. B. S. H. Royce, Eds. (Springer Berlin Heidelberg, 1990).

[138] J. L. Bodnar, M. Egée, C. Menu, R. Besnard, A. Le Blanc, M. Pigeon, and J. Y. Sellier, "Cracks detection by a moving photothermal probe," *J. Phys. IV* **04**, C7–C591 – C7–C594 (1994).

[139] C. Gruss, F. Lepoutre, and D. Balageas, "Nondestructive evaluation using a flying-spot camera," *ONERA TP* **1** (1993).

[140] J.-C. Krapez, "Résolution spatiale de la caméra thermique à source volante," *Int. J. Therm. Sci.* **38**, 769–779 (1999).

[141] T. Li, D. P. Almond, and D. A. S. Rees, "Crack imaging by scanning laser-line thermography and laser-spot thermography," *Meas. Sci. Technol.* **22**, 035701 (2011).

[142] J. Schlichting, M. Ziegler, A. Dey, C. Maierhofer, and M. Kreutzbruck, "Efficient data evaluation for thermographic crack detection," *Quant. InfraRed Thermogr. J.* **8**, 119–123 (2011).

[143] T. Li, D. P. Almond, and D. A. S. Rees, "Crack imaging by scanning pulsed laser spot thermography," *NDT E Int.* **44**, 216–225 (2011).

[144] S. E. Burrows, S. Dixon, S. G. Pickering, T. Li, and D. P. Almond, "Thermographic detection of surface breaking defects using a scanning laser source," *NDT E Int.* **44**, 589–596 (2011).

[145] J. Schlichting, C. Maierhofer, and M. Kreutzbruck, "Crack sizing by laser excited thermography," *NDT E Int.* **45**, 133–140 (2012).

[146] M. Streza, Y. Fedala, J. P. Roger, G. Tessier, and C. Boue, "Heat transfer modeling for surface crack depth evaluation," *Meas. Sci. Technol.* **24**, 045602

(2013).

[147] K. Friedrich and H.-G. Walther, “The effect of edges on photothermal imaging,” *J. Appl. Phys.* **70**, 4697–4701 (1991).

[148] A. Sánchez-Lavega and A. Salazar, “Photothermal measurements near a 90° edge. I. Mirage deflection by a free edge,” *J. Appl. Phys.* **74**, 536–547 (1993).

[149] K. R. Grice, L. J. Inglehart, L. D. Favro, P. K. Kuo, and R. L. Thomas, “Thermal wave imaging of closed cracks in opaque solids,” *J. Appl. Phys.* **54**, 6245–6255 (1983).

[150] A. M. Mansanares, T. Velinov, Z. Bozoki, D. Fournier, and A. C. Boccara, “Photothermal microscopy: Thermal contrast at grain interface in sintered metallic materials,” *J. Appl. Phys.* **75**, 3344–3350 (1994).

[151] F. Lepoutre, D. Balageas, P. Forge, S. Hirschi, J. L. Joulaud, D. Rochais, and F. C. Chen, “Micron-scale thermal characterizations of interfaces parallel or perpendicular to the surface,” *J. Appl. Phys.* **78**, 2208–2223 (1995).

[152] A. Ocariz, A. Sanchez-Lavega, A. Salazar, D. Fournier, and A. C. Boccara, “Photothermal characterization of vertical and slanted thermal barriers: A quantitative comparison of mirage, thermoreflectance, and infrared radiometry,” *J. Appl. Phys.* **80**, 2968–2982 (1996).

[153] F. A. McDonald, G. C. Wetsel Jr., and G. E. Jamieson, “Photothermal beam-deflection imaging of vertical interfaces in solids,” *Can. J. Phys.* **64**, 1265–1268 (1986).

[154] NIST, “NIST Digital Library of Mathematical Functions,” DLMF, 25 April 2014, http://dlmf.nist.gov/ (accessed: 26 May 2016).

[155] C. Johnson, *Numerical Solution of Partial Differential Equations by the Finite Element Method* (Dover Publications, Mineola, N.Y, 2009).

[156] J. T. Oden, I. Babuŝka, and C. E. Baumann, “A Discontinuous hp Finite Element Method for Diffusion Problems,” *J. Comput. Phys.* **146**, 491–519 (1998).

[157] D. Arnold, F. Brezzi, B. Cockburn, and L. Marini, “Unified Analysis of Discontinuous Galerkin Methods for Elliptic Problems,” *SIAM J. Numer. Anal.* **39**, 1749–1779 (2002).

[158] A. J. Omella and R. Celorrio, "Discontinuous Galerkin Method Applied to Photothermal Inspection of Cracked materials," in *Monogr Semin Mat Garcia Galdeano* **40**, (2015).

[159] R. Celorrio, A. J. Omella, A. Mendioroz, A. Oleaga, and A. Salazar, "Advances in Crack Characterization by Lock-In Infrared Thermography," *Int. J. Thermophys.* **36**, 1202–1207 (2015).

[160] A. Logg, K.-A. Mardal, and G. Wells, Eds., *Automated Solution of Differential Equations by the Finite Element Method* (Springer Berlin Heidelberg, Berlin, Heidelberg, 2012).

[161] F. Hecht, "New development in freefem++," *J. Numer. Math.* **20**, 251–266 (2013).

[162] J. E. Parrot and A. D. Stuckes, *Thermal conductivity of solids* (London: Pion, 1975).

[163] A. Mendioroz, R. Celorrio, and A. Salazar, "Characterization of rectangular vertical cracks using burst vibrothermography," *Rev. Sci. Instrum.* **86**, 064903 (2015).

[164] J. L. Bodnar and M. Egée, "Wear crack characterization by photothermal radiometry," *Wear* **196**, 54–59 (1996).

[165] G. B. Arfken and H. J. Weber, *Mathematical Methods for Physicists*, 6th ed. (Academic Press, Boston, 2005).

[166] J. C. Heigel and E. P. Whitenton, "The Effects of Emissivity and Camera Point Spread Function on the Temperature Measurement of Segmented Chip Formation Using Infrared Thermography," in *Proc. ASME 2010 Int. Manuf. Sci. Eng. Conf.*, (Pennsylvania, 2010).